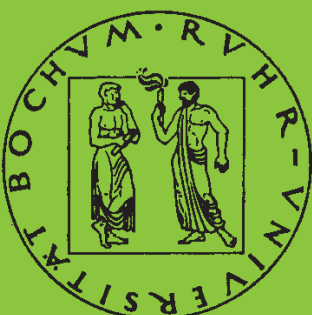


Mitteilungen aus dem Institut für Mechanik

Christian Grabe

**Experimental testing and parameter
identification on the
multidimensional material behavior of
shape memory alloys**

Heft Nr. 142



RUHR-UNIVERSITÄT BOCHUM

**Experimental testing
and parameter identification
on the multidimensional material behavior
of shape memory alloys**

Dissertation

zur

**Erlangung des Grades
Doktor-Ingenieur**

der

**Fakultät für Maschinenbau
der Ruhr-Universität Bochum**

von

Dipl.-Ing. Frank Christian Grabe

aus Hagen

Bochum 2007

Dissertation eingereicht am: 16.04.2007

Tag der mündlichen Prüfung: 15.06.2007

Erster Referent: Prof. Dr.-Ing. O.T. Bruhns

Zweiter Referent: Prof. Dr.-Ing. G. Eggeler

Zusammenfassung

Diese Arbeit behandelt die mehraxiale, thermomechanische Charakterisierung einer binären NiTi-Formgedächtnislegierung. Zur Realisierung der Versuche wird ein Versuchsstand mit einem neuartigen, aktiven Temperaturregelungskonzept und einem biaxialen Dehnungsmesssystem, das für einen großen Temperaturbereich und große Verdrehungen geeignet ist, entwickelt. Die experimentellen Aufgabenstellungen lassen sich in drei Themenkomplexe unterteilen. Dies sind Versuche zum viskosen und dehnratenabhängigen Materialverhalten im pseudoelastischen Temperaturbereich, die Untersuchung der Materialantwort auf biaxiale Dehnpfade in allen vier Quadranten des Normal-/Scherdehnungsraums und die Identifikation des Materialverhaltens bezüglich biaxialer Spannungspfade hinsichtlich des Einwegeffektes. Bei den Versuchen zum letztgenannten Bereich wird die Probe im martensitischen Zustand belastet und eine Entlastung wird sowohl an der martensitischen als auch der austenitischen Mikrostruktur durchgeführt.

Im Hinblick auf das zur Parameteridentifikation verwendete kontinuumsmechanische Materialmodell wird eine Erweiterung zur Beschreibung der Zug/Torsions-Asymmetrie vorgeschlagen. Mit Hilfe eines parallelisierten, evolutionären Optimierungsalgorithmus unter Verwendung verschiedener Minimierungsstrategien werden die Modellparameter identifiziert. Daraufhin findet ein Vergleich zur Evaluierung und Validierung des Modells zwischen experimentell ermittelten Messdaten und mit dem Modell und den identifizierten Parametern berechneten Daten statt.

Contents

List of Figures	iv
List of Tables	viii
Conventions and Notations	ix
1 Introduction	1
1.1 Motivation	1
1.2 Outline	3
2 Illustration of NiTi shape memory behavior	5
2.1 Microscopic properties	5
2.2 Thermomechanical properties	8
2.3 Terminology	10
3 Continuum mechanical and thermodynamic frame	12
3.1 Continuum mechanical framework	12
3.1.1 Kinematics	12
3.1.2 Kinetics	15
3.1.3 Objectivity and objective rates	17
3.2 Balance laws	18
3.2.1 Mass conservation	18
3.2.2 Balance of linear momentum	19
3.2.3 Balance of angular momentum	19
3.2.4 Conservation of energy/first law of thermodynamics	19
3.2.5 Balance of entropy/second law of thermodynamics	20
3.3 Thermomechanical coupling	21
4 Phenomenological modeling	22
4.1 R_L -model for finite deformations	22
4.2 Discussion of the R_L -model and modification	29
5 Experimental setup	35
5.1 Specimen material and geometry	35
5.2 Heating of the specimen	37
5.3 Cooling of the specimen	41

5.3.1	Pressure system	43
5.3.2	Heat exchanger	44
5.3.3	Nozzle system	46
5.4	Temperature measurement	47
5.5	Temperature control	52
5.5.1	Calculation of the mean temperature	52
5.5.2	Temperature chamber	53
5.5.3	Temperature control algorithm/procedure	53
5.6	Mechanical loading	56
5.6.1	Measuring of stress	58
5.7	Clamping of the specimen	58
5.8	Strain measuring	59
5.8.1	Axial displacement measuring	61
5.8.2	Twist measuring	62
5.9	Complete system	63
6	Experiments	65
6.1	Pretests and preparatory experiments	65
6.1.1	Heat treatment	65
6.1.2	Mechanical tests on specifically heat treated specimens	66
6.1.3	DSC results	70
6.1.4	TEM results	74
6.1.5	Effect of temperature on the stress-induced transformation behavior	77
6.2	Characterization of viscous and rate dependent material behavior	80
6.2.1	Comparison between non-isothermal and isothermal tests	82
6.2.1.1	Simple tension	82
6.2.1.2	Simple torsion	86
6.2.1.3	Combined box tests	86
6.2.1.4	Conclusions	89
6.2.2	Relaxation behavior	96
6.2.3	Creep behavior	99
6.3	Complex loading paths in the tension/compression/torsion subspace	106
6.3.1	Combined circle test spanning all four axial/torsional strain quadrants	107
6.3.2	Combined box tests spanning all four axial/torsional strain quadrants	109
6.3.3	Combined butterfly tests spanning all four axial/torsional strain quadrants	112
6.4	One-way effect under different loading conditions	115
6.4.1	One-way effect under uniaxial loading conditions	117
6.4.1.1	One-way effect for simple tension	117
6.4.1.2	One-way effect for simple torsion	119
6.4.2	One-way effect under complex loading conditions	121

6.4.2.1	Unloading in the martensitic state	122
6.4.2.2	Unloading in the austenitic state	126
7	Numerical methods for the parameter identification	134
7.1	Direct problem	134
7.2	Inverse problem	137
7.2.1	Probability density and l_p -norm	138
7.3	Optimization procedures	141
7.3.1	Newton's and damped Newton method	142
7.3.2	The NEWUOA algorithm	144
7.3.3	Evolutionary algorithms	145
7.3.3.1	Simple evolutionary algorithm	145
7.3.3.2	Extended evolutionary algorithm	148
7.3.3.3	Classification of evolutionary algorithms	149
7.4	Implementation and realization	150
7.4.1	Formulation of the objective function	150
7.4.2	Implementation of the evolutionary algorithm	152
7.4.3	Parallelization of the evolutionary algorithm	152
8	Determination of material parameters	156
8.1	Basic considerations	156
8.1.1	Results of the parameter identification	162
8.2	Comparison between calculated and measured data sets	168
8.2.1	Proportional experiments	168
8.2.2	Nonproportional experiments	169
9	Conclusions and possible extensions	175
9.1	Summary	175
9.2	Conclusions	176
9.3	Outlook	178
A	Implementation of the modified R_L-model	179
B	Additional experiments concerning the one-way effect	182
C	Results of the parameter identification	188
C.1	Identified material parameters	188
C.2	Additional nonproportional experiments and comparison	188
	Bibliography	192

List of Figures

1.1	NiTi devices and implants	2
2.1	Lattice invariant shear	6
2.2	Shape memory effects and deformation mechanisms	7
2.3	Regions of pseudoelasticity and the one-way shape memory effect	9
2.4	One-way effect, pseudoelastic, and plastic material behavior	10
2.5	Intrinsic two-way effect	10
3.1	Body and particle in reference and current configuration	13
4.1	Comparison of stress curves for different values of b	32
5.1	DSC curve of the as-received material	36
5.2	Simple tension tests of the as-received material	37
5.3	Specimen geometry	38
5.4	Polished micrograph section of specimen wall	38
5.5	Applied heating concept	40
5.6	Temperature changes for different heating powers	41
5.7	Cooling concept	43
5.8	Pressure system	44
5.9	Heat exchanger system	45
5.10	Nozzle system	47
5.11	Inward fluid feed	48
5.12	Thermocouple bead	49
5.13	Thermocouple (top) / specimen (bottom) join patch	50
5.14	Inner thermocouple	51
5.15	Arrangement of the thermocouples	51
5.16	Temperature chamber	54
5.17	Tension tests with and without temperature control	55
5.18	Tension tests with and without temperature control, not averaged	55
5.19	Mechanical loading setup	57
5.20	Photograph of the clamping device	59
5.21	Drawing of the aluminum disks	61
5.22	Axial strain measurement	62
5.23	Details of the torsional strain measurement	63

5.24 Schematic of the complete experimental system	64
6.1 Uniaxial tests for a HT 1 specimen	67
6.2 Simple torsion tests for a HT 2 specimen	68
6.3 Repeated simple tension tests, HT 2	69
6.4 Repeated isothermal tension tests, HT 2	71
6.5 Repeated isothermal tension tests, HT 1	72
6.6 DSC curves for HT 1, HT 2, and as-received specimen material .	72
6.7 Comparison of two different DSC cycles for HT 1	73
6.8 Schematic of the ordering of lenticular Ni ₄ Ti ₃ precipitates	74
6.9 Bright field TEM images of an HT 1 specimen at 70°C	75
6.10 Bright field TEM images of an HT 1 specimen at 26°C	76
6.11 Various SADPs of an HT 1 specimen at different temperatures .	77
6.12 Isothermal tension tests for different temperatures, HT 1	78
6.13 Transformation stress and apparent Young's modulus	79
6.14 Uniaxial tension tests for different strain rates	83
6.15 Uniaxial isothermal tension tests for different strain rates	85
6.16 Uniaxial torsion tests for different strain rates	87
6.17 Uniaxial isothermal torsion tests for different strain rates	88
6.18 Strain-strain, stress-stress diagrams for combined box tests . . .	90
6.19 Axial and torsional stress-strain diagrams for combined box tests	91
6.20 Temperature response for combined box tests	92
6.21 Strain-strain, stress-stress diagrams for isothermal box tests . . .	93
6.22 Axial and torsional stress-strain diagrams for isothermal box tests	94
6.23 Temperature response for isothermal box tests	95
6.24 Stress-strain diagram for isothermal relaxation tests	96
6.25 Temperature proceeding for an isothermal relaxation test	97
6.26 Stress and strain for an isothermal relaxation test with $\epsilon_{\max} = 3.5\%$	98
6.27 Stress progressions for a relaxation test with $\epsilon_{\max} = 3.5\%$	99
6.28 Stress-strain diagram for isothermal creep tests	100
6.29 Stress and strain for the isothermal creep tests	101
6.30 Specimen temperatures for a creep test	101
6.31 Strain progressions for the creep test	102
6.32 Stress-strain diagram for an isothermal creep test	103
6.33 Stress and strain for the isothermal creep test	103
6.34 Strain progressions for the creep test	104
6.35 Specimen temperatures as functions of time	105
6.36 Strain-strain, stress-stress diagrams for an isothermal circle test .	108
6.37 Axial and torsional stress-strain diagrams for an isothermal circle test	110
6.38 Strain-strain, stress-stress diagrams for isothermal box tests . . .	111
6.39 Axial and torsional stress-strain diagrams for isothermal box tests	113
6.40 Strain-strain, stress-stress diagrams for isothermal butterfly tests	114

6.41	Axial and torsional stress-strain diagrams for isothermal butterfly tests	116
6.42	Simple tension one-way effect; stress-strain-temperature diagram	118
6.43	Simple tension one-way effect; strain-temperature diagram . . .	118
6.44	Simple tension one-way effect; stress-strain diagram	119
6.45	Simple torsion one-way effect; stress-strain-temperature diagram	120
6.46	Simple torsion one-way effect; strain-temperature diagram . . .	120
6.47	Simple torsion one-way effect; stress-strain diagram	121
6.48	Control path of a box test in the pseudoplastic temperature regime	122
6.49	Pseudoplastic temperature/strain response on the box stress path	123
6.50	Pseudoplastic strain response on the box stress path	124
6.51	Strain recovery of the pseudoplastic box test	124
6.52	Stress-strain diagrams for the pseudoplastic box test	125
6.53	Pseudoplastic control path of an interrupted box test	127
6.54	Pseudoplastic temperature/strain response on the interrupted box stress path	127
6.55	Pseudoplastic strain response on the interrupted box stress path	128
6.56	Temperature/strain for the interrupted pseudoplastic box test . .	128
6.57	Stress-strain diagrams for the interrupted pseudoplastic box test	129
6.58	Pseudoplastic control path of an interrupted box test with compression	130
6.59	Strain response on the interrupted box stress path with compression as a function of temperature	131
6.60	Strain response on the interrupted box stress path with compression	131
6.61	Strain as function of temperature for the interrupted pseudoplastic box test with compression	132
6.62	Stress-strain diagrams for the interrupted pseudoplastic box test with compression	133
7.1	Modified R_L -model specified for small deformations	135
7.2	Specification of stress quantities for special load cases	136
7.3	Simple evolutionary algorithm	147
7.4	Extended evolutionary algorithm	148
7.5	Master-slave paradigm	153
7.6	Speedup due to a parallelization of the algorithm	154
8.1	Phenomenological interpretation of selected material parameters	159
8.2	Physical interpretation of selected material parameters	161
8.3	Comparison of typical, tensile stress-strain curves	162
8.4	Comparison of typical, torsional stress-strain curves	163
8.5	Computed and measured simple tension tests	166
8.6	Computed and measured simple torsion tests	167
8.7	Strain-strain, stress-stress diagrams for isothermal proportional tests	170

8.8	Axial and torsional stress-strain diagrams for isothermal proportional tests	171
8.9	Strain-strain, stress-stress diagrams for isothermal box test . . .	172
8.10	Axial and torsional stress-strain diagrams for isothermal box test	173
B.1	Pseudoplastic control path of an interrupted box test	183
B.2	Pseudoplastic strain response on the interrupted box stress path as a function of temperature	183
B.3	Pseudoplastic strain response on the interrupted box stress path	184
B.4	Strain as function of temperature for the interrupted pseudoplastic box test	184
B.5	Stress-strain diagrams for the interrupted pseudoplastic box test	185
B.6	Pseudoplastic control path of an interrupted box test with compression	185
B.7	Pseudoplastic strain response on the interrupted box stress path with compression as a function of temperature	186
B.8	Strain response on the interrupted box stress path with compression	186
B.9	Temperature/strain for the pseudoplastic box test with compression	187
B.10	Stress/strain for the pseudoplastic box test with compression . .	187
C.1	Strain-strain, stress-stress diagrams for isothermal butterfly test .	189
C.2	Axial and torsional stress-strain diagrams for isothermal butterfly test	190

List of Tables

- 5.1 Requirements for the strain measuring device 60
- 6.1 Applied heat treatments HT 1 and HT 2 66
- 7.1 Computation effort for several optimization procedures 141
- 7.2 Classification of optimization algorithms 142
- 7.3 Correspondence table and nomenclature 146
- 8.1 Material parameters of the modified R_L -model 156
- 8.2 Material parameters that are taken from the literature and identified in advance 157
- 8.3 Admissible domain of the material parameters for the modified R_L -model 160
- 8.4 Identified material parameters 164
- C.1 Identified material parameters 188

Conventions and Notations

Scalars (italics)

a	Time shift
a_α	Longitudinal weighting factor
A	Area
A_f	Austenite finish temperature
A_p	Austenite peak temperature
A_s	Austenite start temperature
b_β	Circumference weighting factor
c_p	Specific heat at constant pressure
d	Difference function
B	Body
da	Area element in current configuration
E_g	Internally generated, thermal energy
E_{st}	Internal energy
f	Function for phase transformation
f	Probability density
g	Specific Gibbs free energy
g^*	Potential according to Raniecki, B. & Lexcellent, C. (1998)
h	Equivalent Hencky strain
h^*	Equivalent strain of von-Mises type
h_c	Convection heat coefficient
\dot{h}_{lat}	Energy generation per unit volume
h_r	Radiation heat coefficient
H_2	Invariant of strain deviator according to equation (4.50)
I	Current
J	Jacobian (determinant)
k	Thermal conductivity
k	Function for phase transformation
l	Number of cluster nodes
m	Mass
M_f	Martensite finish temperature
M_p	Martensite peak temperature
M_s	Martensite start temperature
n	Number of computation tasks
N_2^g	Gaseous nitrogen

N_2^1	Liquid nitrogen
q	Quadratic model
q	Specific heat, $[q] = \text{W/kg}$
Q	Heat
r	Internal heat source
R	Resistance
s	Specific entropy
S	Entropy
S	Estimator of dispersion
S_1	Invariant of stress tensor according to equation (4.56)
S_2	Invariant of stress tensor according to equation (4.56)
t	Time
T_2	Invariant of stress deviator according to equation (4.14)
T_3	Invariant of stress deviator according to equation (4.55)
u	Specific internal energy
U	Voltage
v	Trust region step
v	Volume in the current configuration
V	Volume (in the reference configuration)
w	Specific energy
X	Particle

Scalars (Greek characters)

α	Proportionality coefficient
γ	Internal entropy production
γ	Shear component of engineering strain
Γ	Gamma function
ε	Axial component of engineering strain
η	Amplitude of pseudoelastic strain
$\hat{\eta}$	Modified amplitude of pseudoelastic strain
Θ	Temperature
$\bar{\Theta}$	Mean temperature
$\bar{\Theta}_\alpha$	Mean temperature at longitudinal position α
$\bar{\Theta}_{\alpha\beta}$	Mean temperature at longitudinal, circumference position α, β
$\Theta_{\alpha\beta_{\text{in}}}$	Inside temperature at longitudinal, circumference position α, β
$\Theta_{\alpha\beta_{\text{out}}}$	Outside temperature at longitudinal, circumference position α, β
Θ_s	Temperature at a surface
Θ_0	Reference temperature
Θ_∞	Ambient temperature
κ	Bulk modulus
λ	Lamé constant
μ	Lamé constant
ξ	Mass fraction of martensite

π^f	Thermodynamic driving force
π_0^f	Phase chemical potential
ρ	Current mass density
ρ_0	Referential mass density
σ	Axial component of engineering stress
σ	Equivalent engineering stress
τ	Equivalent stress
τ	Shear component of engineering stress
τ^*	Equivalent stress of von-Mises type
$\hat{\tau}$	Modified equivalent stress
ψ	Specific Helmholtz free energy
ψ_{it}	Free energy of interaction

Vectors (boldface roman)

a	Internal variables
da	Area element in current configuration
dA	Area element in reference configuration
dk	Force element in current configuration
dx	Line element in the current configuration
dX	Line element in the reference configuration
e_i	Unit vector
c	Translation
q	Heat flux vector
t	Traction
x	Position in the current configuration
X	Position in the reference configuration

Vectors (Greek characters)

χ	Deformation
--------	-------------

Second order tensors (boldface roman)

1	Unit tensor
B	Left Cauchy-Green tensor
C	Right Cauchy-Green tensor
D	Stretching tensor
e	Euler-Almansi strain tensor
E	Green-Lagrange strain tensor
F	Deformation gradient
h	Hencky strain in current configuration
H	Hencky strain in reference configuration
P₁	First Piola-Kirchhoff stress tensor
P₂	Second Piola-Kirchhoff stress tensor

Q	Rotation tensor
R	Rotation tensor (polar decomposition)
T	Cauchy stress tensor
U	Right stretching tensor
V	Left stretching tensor
W	Spin tensor

Second order tensors (Greek characters)

α	Tensor of thermal expansion
κ	Intrinsic phase distortion
τ	Kirchhoff stress tensor
τ^*	Modified Kirchhoff stress tensor

Fourth order tensors (boldface roman)

C	Elastic stiffness tensor
D	Elastic compliance tensor
I	Symmetric fourth order unit tensor
I _{dev}	Deviatoric unit tensor
Z	Tensorial function

Other symbols

\mathcal{B}	Current configuration
\mathcal{B}_0	Reference configuration
Δ	Increment, trust region
$\Delta\theta_t$	Temperature difference between inside and outside of specimen

Special symbols & functions

$A \rightarrow M$	Austenite-martensite transformation
$M \rightarrow A$	Martensite-austenite transformation
det	Determinant
div	Divergence
grad	Gradient with respect to \mathbf{x}
Grad	Gradient with respect to \mathbf{X}
skw(\cdot)	Skew-symmetric part of a tensor
sym(\cdot)	Symmetric part of a tensor
tr(\cdot)	Trace of a tensor
$(\cdot)^T$	Transpose of a tensor
$(\cdot)^{-1}$	Inverse
$\dot{(\cdot)}$	Material time derivative
$\overset{\circ}{(\cdot)}^{\log}$	Logarithmic time rate
\cdot	Scalar product

:	Double contraction
\times	Vector product
\otimes	Dyadic product

Superscripts

$(\cdot)^e$	Elastic
$(\cdot)^i$	Inelastic
$(\cdot)^{tr}$	Transformation induced
$(\cdot)^*$	Transformed
$(\cdot)'$	Deviator of tensorial quantity

Subscripts

$(\cdot)_0$	Quantity associated with reference configuration
$(\cdot)_{cond}$	Quantity associated with conduction
$(\cdot)_{conv}$	Quantity associated with convection
$(\cdot)_{eq}$	Equivalent
$(\cdot)_{mech}$	Mechanical
$(\cdot)_{obj}$	Quantity associated with the objective function
$(\cdot)_{rad}$	Quantity associated with radiation
$(\cdot)_{ten}$	Tension
$(\cdot)_{th}$	Thermal
$(\cdot)_{tor}$	Torsion

1 Introduction

1.1 Motivation

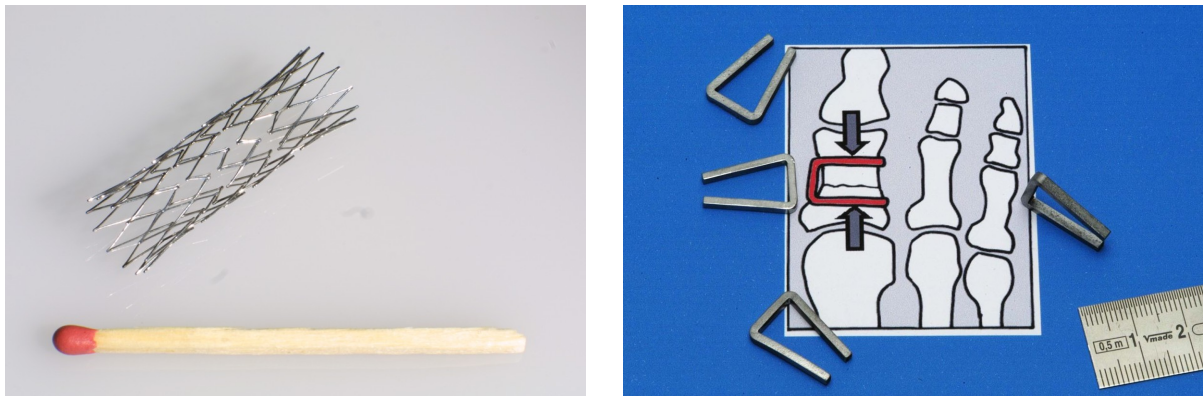
During the last decades, a steadily increasing trend to miniaturize technical components has been noticeable. Today, this is even more an issue than ever before. However, miniaturization is not an aim in itself. Moreover, it is frequently the prerequisite for efficiency enhancements, for instance, in the aerospace and automotive industry. Another example is medical technology, where minimally invasive surgery is more and more gaining ground, since the patients' recovery times can be significantly reduced due to less damage to tissue and muscle and less blood loss. In this regard, newly found materials or fluids, which exhibit special properties are highly challenging. Oftentimes, those materials are referred to as *intelligent*, *functional* or *smart* materials and fluids. Amongst others, this field comprises semiconductors, piezoceramics, magnetorheological fluids and shape memory alloys. The existence of microcomputers and cellular phones would be unthinkable without semiconductors. Piezoceramics are used in state of the art diesel fuel injectors whereas some automakers use magnetorheological fluids for realizing adaptive suspension systems.

Shape memory alloys, which will be the key issue in this treatise, combine multiple effects that are highly absorbing. The most prominent effects are pseudoelasticity and the one-way and two-way shape memory effect. Furthermore, what makes shape memory alloys additionally fascinating, is the possibility to use them as sensors and actuators simultaneously, so that two classical components can be substituted by one single shape memory element.

Referring to the unique effects, pseudoelasticity is fundamentally characterized by extremely large recoverable strains¹ upon loading and unloading. In comparison to pseudoelasticity, the one-way shape memory or, simply, shape memory effect can be observed at the same alloy at lower temperatures. Here, the material may be deformed so that apparently plastic deformations are existent on unloading, which is why this part of the one-way effect is also termed pseudoplasticity. Upon heating this apparently plastic deformation is completely eliminated. The term two-way effect indicates the switching between two particular strain states by means of changing the temperature of the material. All three effects will be explained in more detail in Chapter 2.

Figure 1.1 shows some typical samples for applications of NiTi shape memory alloys. A peripheral stent, which is designed to support the walls of blood vessels

¹Recoverable strains in the order of 11% and 7% are reported for NiTi single crystals and polycrystals, respectively, cf. Saburi, T. (1998).



(a) Peripheral stent (Photograph courtesy of Memory-Metalle GmbH, Germany) (b) Staples for foot surgery (Photograph courtesy of Research Centre Jülich in the Helmholtz Association of National Research Centres, Germany)

Figure 1.1: NiTi devices and implants

making use of the pseudoelastic effect, is depicted in Figure 1.1(a). Figure 1.1(b) illustrates the working principle of a staple for foot surgery, which is based on the one-way effect, see Krone, L. et al. (2005). Here, a compressive force acts on the fracture zone to assist the healing process.

In order to save development costs and time, today, it is mandatory, to compute the mechanical behavior beforehand, optimizing the shape of new components with reference to functionality, reliability and costs. Consequently, if complex geometries are considered, like in the case of stents, it is of paramount importance to be able to perform three-dimensional structural analyses. In this regard, a continuum mechanical material model for shape memory alloys incorporating large deformations was thermodynamically consistently derived by Müller, C. (2003) based on the R_L -model by Raniecki, B. et al. (1992). Several material parameters were introduced with this phenomenological approach. Since some of those material parameters are specific to the model and others are different for distinct microstructures or heat treatments, a consistent set of model parameters is not at hand. Hence, a parameter identification would have to be realized on one single NiTi alloy.

The identification of model parameters for a shape memory alloy is one of the major topics in this work. Furthermore, multidimensional validation experiments are projected to show the capabilities and limitations of the given material model. In addition, to allow for a further amendment of material models and a deeper understanding of the thermodynamically coupled mechanical material behavior, multidimensional axial/torsional experiments should be conducted. Concomitantly, the material temperature should be controlled so that different thermodynamic effects may be decoupled and thus may be interpreted more easily.

1.2 Outline

The present thesis is structured in nine chapters. Subsequent to this introduction, the basic properties of shape memory alloys are presented. First, the microscopic effects are treated, simultaneously elucidating the martensitic phase transformation on shape memory alloys, which gives rise to the specific shape memory behavior. Furthermore, the notion of lattice invariant shear is briefly introduced. Thereafter, the particular material behavior of shape memory alloys is schematically illustrated on the macroscale.

Chapter 3 establishes the basic notations concerning the continuum mechanical and thermodynamic framework, which are used in this treatise. More specifically, different stress and strain measures are derived, and the concept of work conjugacy is illustrated, leading to work conjugated pairs of stress and strain. Consecutively, special focus is on the concept of objectivity, which results in some reflections with respect to objective rates, and which yields the work conjugated pair of stress and strain used later on. Additionally, the fundamental balance laws and conservation equations are accounted with the Clausius-Duhem inequality being the representation of the second law of thermodynamics. Finally, the thermomechanical coupling is very briefly inferred.

A sketch of the basic structure of the material model as derived by Müller, C. (2003) is presented in the first part of Chapter 4. Here, the train of thought is analogous to the concept presented in Müller, C. (2003). The second part treats possible extensions of the R_L -model and a short survey of the respective literature. Furthermore, a modification of the given material model is proposed incorporating the tension/shear asymmetry.

Since one of the principal topics of this work is the execution of experiments, a comparably large part, namely Chapter 5, addresses the experimental setup. At this juncture, special importance is attached to the concepts of heating and cooling of the specimen, which furnish, together with the temperature measurement, the integrated system of temperature control. Furthermore, a new biaxial strain measuring device is developed, which is compatible to the overall temperature control setup.

Thereupon, the experimental examinations are outlined. Foremost, the given specimen material is characterized and the specimen preparation is exemplified. Here, the microstructure and the mechanical behavior are explored. In the following, the rate dependence of the mechanical material behavior is determined. Several isothermal tests with varying deformation rates and strain- and stress-hold periods are conducted. Thereafter, Section 6.3 is about complex loading paths in the tension/compression/torsion subspace presenting tests that span all four strain quadrants. Finally, complex multidimensional experiments are performed on different crystallographic microstructures, in order to examine the one-way effect for the given material. Thereby, the temperature is varied within a large interval.

A second key issue is the identification of the model parameters for the R_L -

and modified R_L -model, respectively. On this account, Chapter 7 deals with numerical methods for the parameter identification. In this connection, the notions of the direct and inverse problem are discussed. Besides, different optimization procedures are surveyed with special focus on the comparison between deterministic and stochastic search algorithms. As a conclusion, the performed implementation and realization of the parameter identification is given.

The determination of material parameters is the topic of Chapter 8. After some basic considerations concerning reasonable constraints in order to increase the convergence rate, the material parameters are identified. Subsequently, the experiments, which are used for the identification, are recalculated using the identified parameters and compared to the measurements. For validation purposes, new, multidimensional experiments are computed and checked against actually measured, multidimensional data.

Concluding this thesis, the last chapter summarizes the main results of this work and gives an outlook with reference to a further amendment of the experimental database.

2 Illustration of NiTi shape memory behavior

In order to be able to investigate the mechanical and thermodynamically coupled material behavior of shape memory alloys, it is of high importance to understand the basic mechanisms, which are responsible for the unique phenomenological effects. On this account, this chapter is meant to give a short overview of some microscopic considerations and the impact thereof on the macroscopic material behavior. It is pointed out that only a simplified view on the crystallography of shape memory alloys will be given here. In this connection, the main focus is on polycrystals. Furthermore, even though most of the following statements concerning shape memory alloys hold true in general, the key issue in this work are binary, nearly equiatomic NiTi alloys.

In this connection, NiTi is chosen as specimen material for this treatise, since it is the most prominent and most widely-used shape memory alloy. The reasons therefor are higher transformation stresses and strains, a superior biocompatibility, and an improved mechanical stability in comparison to other shape memory alloys, cf. [Miyazaki, S. \(1996\)](#); [Melton, K.N. \(1998\)](#); [Miyazaki, S. \(1998\)](#).

2.1 Microscopic properties

Fundamentally, the different features of shape memory alloys can be traced back to the *martensitic* transformation behavior of shape memory alloys. This specific type of phase transformation was termed “martensitic” in honor of the eminent German metallurgist Adolf Martens (1850-1914) who conducted his research in the field of microstructural steel characterization at the end of the 19th century. [Otsuka, K. & Wayman C. M. \(1998\)](#) define the martensitic phase transformation as being “a diffusionless phase transformation in solids, in which atoms move cooperatively, and often by a shear-like mechanism. Usually the parent phase (a high temperature phase) is cubic, and the martensite (a lower temperature phase) has a lower symmetry”. Sometimes, the martensitic transformation is referred to as displacive due to the cooperative movement of the atoms. By virtue of the lower degree of symmetry, a large number of distinct martensite variants¹ may form upon phase transformation. However, only one single austenite variant is existent for NiTi. In this regard, a volumetric change of -0.34% can be observed for a NiTi austenite-martensite phase transformation, [Shimizu, K. & Tadaki, T. \(1984\)](#).

The aforementioned shear-like deformation of the crystal lattice is called *Bain* strain and is depicted in a simplified form for a single crystal in Figure 2.1a),

¹12 martensite variants exist. All of them are crystallographically equivalent.

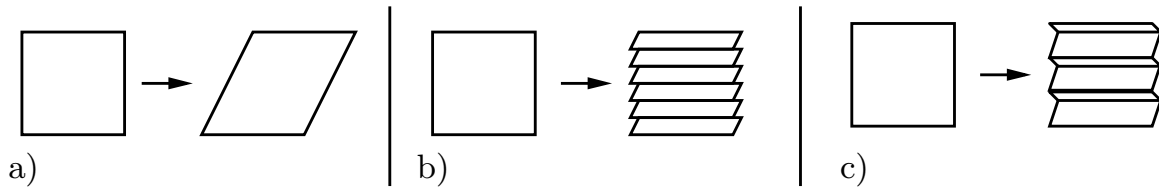
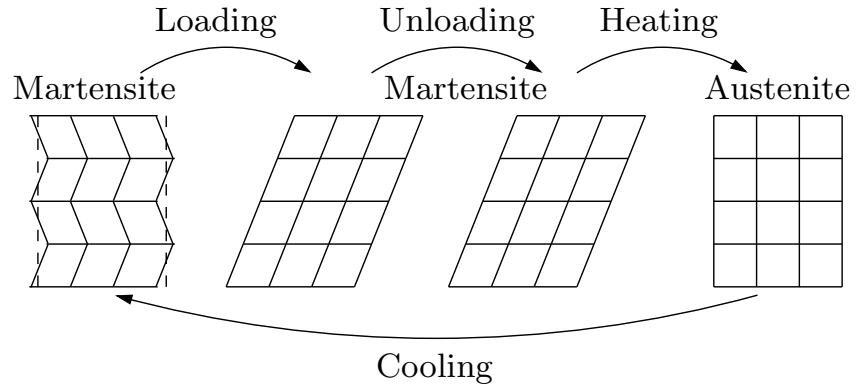


Figure 2.1: a) Shape change upon martensitic transformation; accommodation of strain due to b) slip and c) twinning

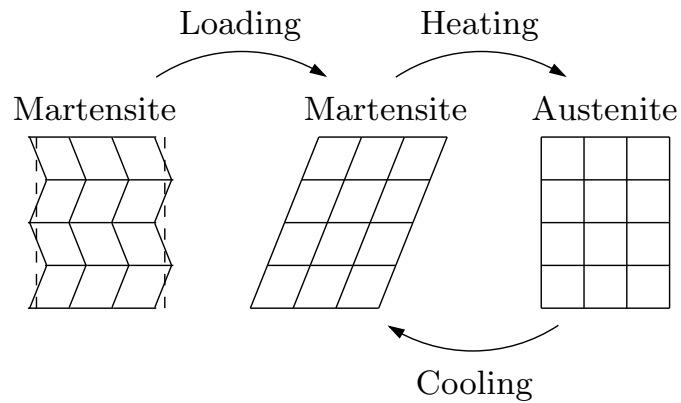
Otsuka, K. & Wayman C. M. (1998). On the left, the parent phase, austenite, is shown while on the right the distorted lattice of martensite is evident. It is obvious that due to the shearing deformation a large shape change occurs around the martensite. However, an overall shape change of the material cannot be observed in reality for a temperature induced phase transformation. The reason is that it is essential for the nucleation and growth of martensite to minimize the strain energy, thus, to reduce the strain. The mechanism to achieve this is called *lattice invariant shear*. Two different types of this mechanism, namely *slip* and *twinning*, are known. They are sketched for a single crystal and only two different martensite variants in Figures 2.1b) and 2.1c). Slip comes along with the introduction and movement of dislocations and is, thus, an irreversible step. This is not the case for twinning, as the movement of twin boundaries is reversible. Which kind of lattice invariant shear appears, depends on the particular alloy. Nevertheless, the mechanism of twinning plays a major role for NiTi, which is why twinning is, here and henceforth, considered as the primary lattice invariant shear effect.

Ortín, J. & Planes, A. (1989) state that, from a thermodynamic viewpoint, temperature and externally applied stress play equivalent roles for the phase transformation. Against this background, Figure 2.2 elucidates the different effects inherent in shape memory alloys for two martensite variants, cf. Helm, D. (2001). Fundamentally, in the case of temperature-induced phase transformation, self-accommodated martensite forms due to the absence of external stresses, as can be seen in the upper two schematic drawings. Here, the starting point of the particular effects is temperature-induced martensite being the stable phase at the present material temperature. Advancing from top to bottom, pseudo-plasticity is the isothermal part of the one-way effect. It occurs upon loading of the self-accommodated martensitic microstructure. Since twin boundaries are quite mobile, detwinning and variant reorientation takes place in order to accommodate the external stress. The growing of one variant at the expense of other variants is frequently referred to as variant coalescence, cf. Miyazaki, S. (1996). If the external stress is high enough, the microstructure will become one single variant. However, the microstructure is almost completely sustained upon unloading so that an apparently plastic deformation of the material is evident. Basically, only elastic unloading takes place but no repeated twinning. If

Pseudoplasticity and one-way effect



Pseudoplasticity and two-way memory effect



Pseudoelasticity

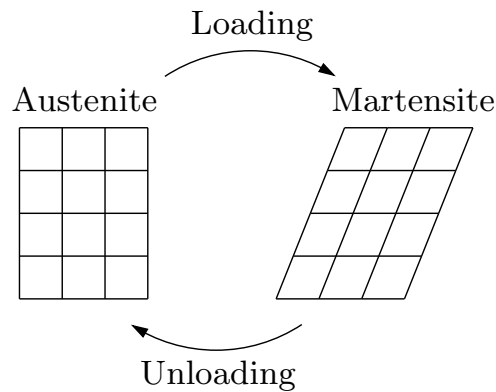


Figure 2.2: Shape memory effects and deformation mechanisms on the microscale

the alloy is subsequently heated, resulting in austenite being the stable phase, the initial shape is recovered due to the higher symmetry of the parent phase. Upon cooling, self-accommodated martensite is regained. The one-way effect comprises the whole process including heating and cooling.

Regarding the two-way effect, the stable martensite phase is loaded by externally applied or eigenstresses. These eigenstresses may result from the existence of dislocations or precipitates. Consequently, it is referred to the extrinsic or intrinsic two-way effect. The crystallographic material response is similar for both cases. First, as the crystal lattice is loaded, the stress is accommodated. The initial shape is regained upon heating due to the aforementioned reasons resulting in

an austenitic microstructure. In contrast to the one-way effect, the stresses are still present so that a preferentially oriented microstructure is retrieved upon cooling.

Pseudoelasticity can be observed, if austenite is the only stable phase under zero applied stress at the actual material temperature. Then, martensite can be formed by the application of external stress. Since the material accommodates the external stress state, oriented martensite is the result of this process leading to an overall deformation of the material. The energetically most beneficial variants develop. However, upon unloading the parent phase which shows a higher degree of symmetry reappears. Under the assumption that no irreversible slip is introduced, the resulting austenite microstructure is identical to the initial one, since only one single austenite variant exists.

While fully annealed NiTi alloys transform from austenite, $B2$, directly to the monoclinic $B19'$ martensite phase, for thermomechanically treated alloys, this is frequently not the case, as those feature oftentimes a two-stage martensitic $B2 \rightarrow R \rightarrow B19'$ phase transformation. In this context, the martensitic R -phase is characterized by a trigonal structure, cf. [Saburi, T. \(1998\)](#). Considerably smaller hystereses are associated with the transformation between the $B2$ - and the R -phase so that in the case of mechanical material modeling this phase transformation is usually neglected.

2.2 Thermomechanical properties

The aforementioned effects on the microscale provoke distinct stress-strain curves on the macroscale. The macroscopically phenomenological material behavior is addressed in the following.

In the context of martensitic transformations the start and finish temperatures of the respective phase transitions are of high importance. Here, the martensite and austenite temperatures are denoted by M and A with the start and finish points signified by the indices “s” and “f”. Since these transformation temperatures differ, a hysteretic material behavior can be observed in the stress-strain space. The respective size depends strongly on the specific alloy.

Generally, pseudoelasticity and the one-way effect may occur at the same alloy, see Figure 2.3 after [Shimizu, K. & Tadaki, T. \(1984\)](#); [Miyazaki, S. \(1996\)](#). That is, the shape memory effect is existent for temperatures below A_s followed by heating above A_f . By contrast, if the critical stress to induce irreversible slip is high enough, the pseudoelastic range is above A_f where martensite is completely unstable for vanishing external stresses. Within the temperature regime between A_s and A_f a mixed material behavior may be noted. The straight line featuring a positive slope characterizes the necessary stress to induce martensite as described by a Clausius-Clapeyron-like equation, cf. [Ortín, J. & Planes, A. \(1989\)](#). The two other straight lines exhibiting negative slopes indicate two arbitrary, critical stress progressions for the induction of slip. Following the ideas explained in

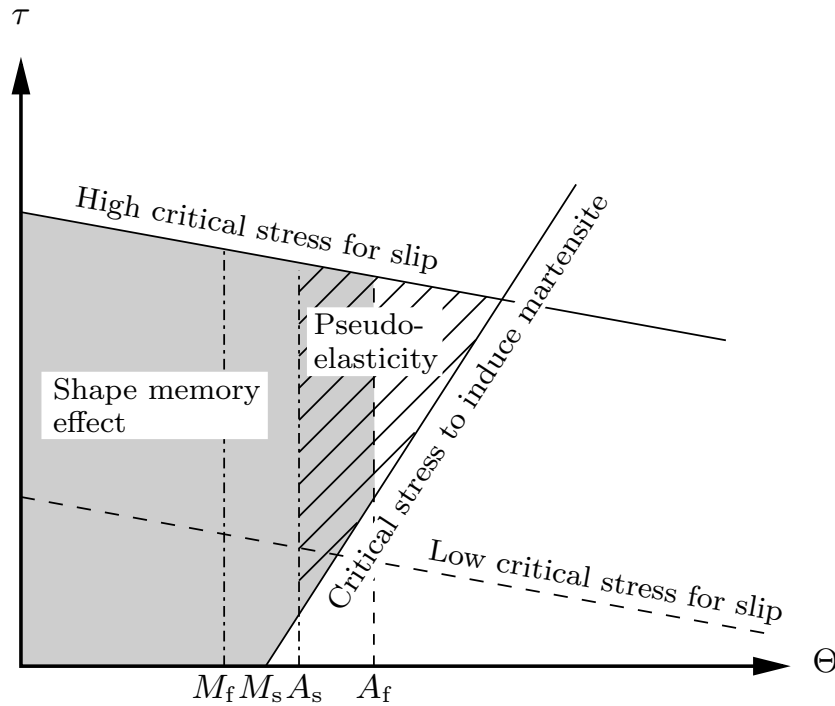


Figure 2.3: Schematic diagram showing the regions of pseudoelasticity and of the one-way shape memory effect

Section 2.1, a reversible, pseudoelastic material behavior is impossible, if slip occurs, since slip is not recovered upon unloading or heating. However, against the background of physical metallurgy, the critical line for slip can be shifted by means of solution hardening, precipitation hardening, or work hardening, refer to [Otsuka, K. & Wayman C. M. \(1998\)](#).

Figure 2.4 presents the phenomenological stress-strain behavior for the cases of plastic austenite, pseudoelasticity, and the one-way effect. Above a certain temperature, M_d , the introduction of plastic slip is energetically preferred over the formation of stress-induced martensite. Consequently, the austenite is plastically deformed. When temperatures between A_f and M_d are considered, stress-induced martensite as described in Section 2.1 is formed upon loading. Finally, since martensite is unstable at this elevated temperature level, the complete strain is recovered as the stress is released.

Below M_f , martensite is the stable phase featuring a self-accommodated crystallographic microstructure. Due to variant coalescence the applied external stress is accommodated leading to an overall strain. Only elastic unloading is observed upon unloading but during heating, austenite develops starting at A_s . This process is concluded at A_f . After cooling below M_f , a twinned martensitic microstructure is regained.

The intrinsic two-way memory effect is sketched schematically in Figure 2.5. The term “intrinsic” applies, since no external stresses are present. However, due to local stress fields by virtue of eigenstresses a preferred martensitic microstructure

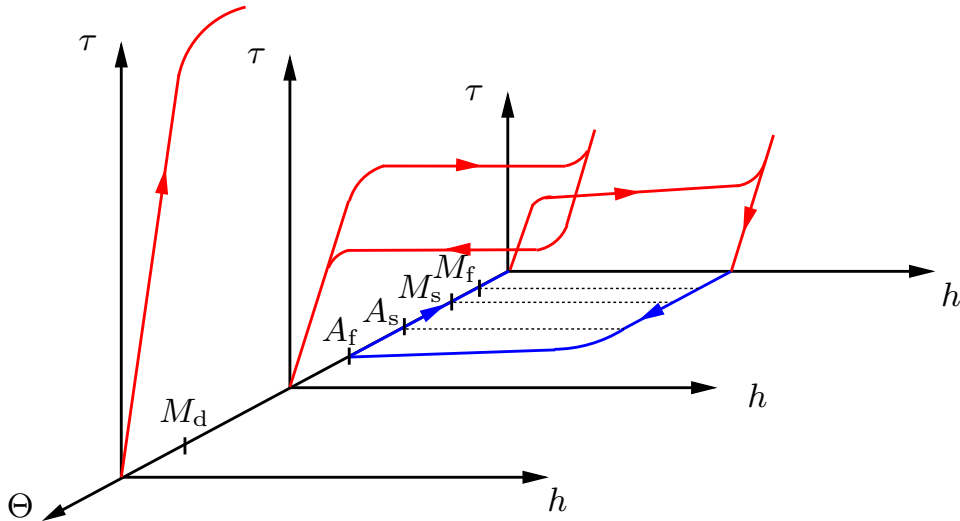


Figure 2.4: Schematic drawing of the one-way shape memory effect, pseudoelastic, and plastic material behavior (rear to front) with the respective transformation temperatures

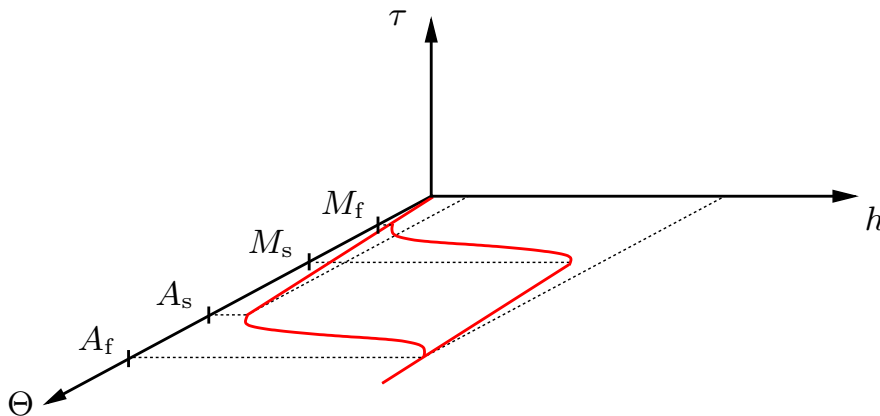


Figure 2.5: Sketch of the intrinsic two-way shape memory relation between temperature and strain, heat expansion is included

exists. Because of the higher degree of symmetry of the austenitic lattice and the constant local stress fields, it can be switched between two strain states by changing the material temperature. A similar temperature-strain relationship can be observed, if the load is externally applied.

2.3 Terminology

In this chapter, only transformation pseudoelasticity has been considered. As this term implies, the origin of this effect is a phase transformation between a parent and a martensitic phase. However, other types of pseudoelasticity exist,

such as twinning pseudoelasticity (Hornbogen, E. (1995)) or rubber-like behavior (Otsuka, K. & Wayman C. M. (1998)). Both terms are attributed to an effect which may be observed on particular twinned martensitic microstructures. Here, detwinning takes place upon loading but the twinned microstructure is regained upon unloading. Consequently, it describes the reversible movement of twin boundaries, Otsuka, K. & Wayman C. M. (1998). The reasons for this material behavior are subject to ongoing research. In Section 6.1.5, this effect is revisited. The term “superelasticity” is proposed for transformation pseudoelasticity by Otsuka, K. & Wayman C. M. (1998) whereas Hornbogen, E. (1995) suggests to use the latter in order to avoid misunderstandings. However, the term “transformation pseudoelasticity” is used in this work whenever confusion seems possible.

3 Continuum mechanical and thermodynamic frame

This chapter gives a short glance on some basic principles of continuum mechanics and thermodynamics. It is not exhaustive nor it is meant to be. Moreover, the intention is to establish a consistent nomenclature and to introduce the basic assumptions and laws needed in the subsequent parts of this work.

This chapter is organized as follows. The first section gives some fundamentals on kinematics and kinetics, i.e. strain and stress measures and the respective material rates are introduced. Section 3.2 treats the first and second law of thermodynamics additionally to conservation and balance laws.

For a more detailed view on these subject matters the interested reader is referred to the works [Truesdell, C. & Noll, W. \(2003\)](#); [Ogden, R.W. \(1997\)](#); [Stein, E. & Barthold, F.-J. \(1996\)](#); [Altenbach, J. & Altenbach, H. \(1994\)](#); [Xiao, H. et al. \(2006\)](#).

3.1 Continuum mechanical framework

3.1.1 Kinematics

In the following sections a body B as a set of particles or material points is considered. Therein, a generic particle is labeled by X . Fundamentally, different configurations of the body may exist which shall be denoted by \mathcal{B} . Now, assuming a fixed referential configuration \mathcal{B}_0 which coincides, for the sake of simplicity, with the initial configuration of the body, the reference position of the generic particle X is designated by the position vector \mathbf{X} . Thus, a mapping of the particle onto its position in the reference (Euclidean) point space is realized so that the material point can be identified by the local position in the reference configuration. Accordingly, the position of the particle in the current configuration \mathcal{B} is indicated by \mathbf{x} . In this context, different coordinate systems with different origins may be chosen for reference and current configuration.

Then, the following equation can be used for describing the deformation of the body B :

$$\mathbf{x} = \chi(\mathbf{X}). \tag{3.1}$$

It follows from the physics that this is supposed to be a one-to-one mapping between current and reference configuration which is said to be bijective. Figure 3.1 depicts the aforementioned interrelations.

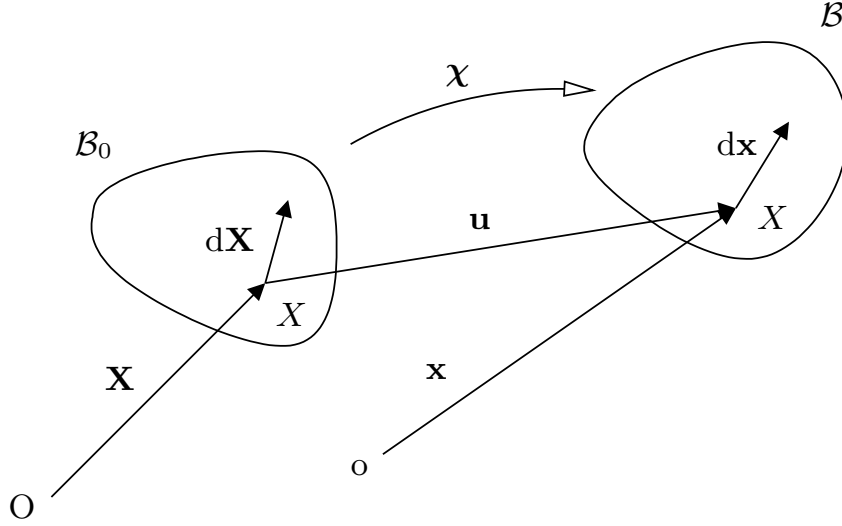


Figure 3.1: Body and particle in reference and current configuration

Consequently, physical observations can be expressed as a function of the reference or the current configuration, respectively resulting in the *Lagrangian* (or material) and the *Eulerian* (or spatial) description, the latter being of special interest in this work.

The material *deformation gradient* mapping a line element in the reference configuration $d\mathbf{X}$ onto the corresponding line element in the current configuration $d\mathbf{x}$ is given by

$$d\mathbf{x} = \mathbf{F}d\mathbf{X}. \quad (3.2)$$

In order to calculate the deformation gradient which is a two-point second-order tensor field, use of the following equation is made,

$$\mathbf{F} = \text{Grad } \mathbf{x} \quad \text{with} \quad \text{Grad} = \frac{\partial}{\partial \mathbf{X}}. \quad (3.3)$$

Furthermore, stipulating consistency of the current configuration and accounting that $\det \mathbf{F} = 1$ for the special case of coincidence of reference and current configuration the inverse mapping,

$$\mathbf{F}^{-1} = \text{grad } \mathbf{X} \quad \text{with} \quad \text{grad} = \frac{\partial}{\partial \mathbf{x}} \quad (3.4)$$

follows, with

$$J := \det \mathbf{F} > 0. \quad (3.5)$$

J is called the *Jacobian* (determinant) and can be interpreted in anticipation of the conservation of mass in Section 3.2 as the ratio of the mass densities in the reference and current configuration,

$$J = \frac{dV}{dv} = \frac{\rho_0}{\rho}, \quad (3.6)$$

with dV and dv being the respective element volumes. Since the deformation gradient comprehends the total motion of the body between reference and current configuration including rigid body rotations¹, the deformation gradient \mathbf{F} is not well-suited for describing the distortion of the body. But, as the deformation gradient is non-singular, a polar decomposition as shown below is always possible

$$\mathbf{F} = \mathbf{R} \mathbf{U} = \mathbf{V} \mathbf{R}, \quad (3.7)$$

with the proper orthogonal *rotation tensor* \mathbf{R} and the uniquely determinable symmetric and positive definite *right* and *left stretch tensor*, \mathbf{U} and \mathbf{V} , respectively. Evidently, the tensors \mathbf{U} and \mathbf{V} are independent of rigid body rotations. Nevertheless, the stretch tensors \mathbf{U} and \mathbf{V} are complicated irrational functions of the deformation gradient \mathbf{F} and as a consequence, for special cases, it proves advantageous to use the *right* and *left Cauchy-Green tensor*,

$$\mathbf{C} = \mathbf{F}^T \mathbf{F} = \mathbf{U} \mathbf{U} \quad (3.8)$$

and

$$\mathbf{B} = \mathbf{F} \mathbf{F}^T = \mathbf{V} \mathbf{V}, \quad (3.9)$$

respectively. By contrast, for handling general considerations, \mathbf{U} and \mathbf{V} are rather used, see [Truesdell, C. & Noll, W. \(2003\)](#).

Albeit the independence of rigid body motions, for an unstrained body the identity $\mathbf{U} = \mathbf{V} = \mathbf{C} = \mathbf{B} = \mathbf{1}$ holds. However, often a strain measure is desired which exhibits a value of zero for an unstrained body instead of the identity, [Altenbach, J. & Altenbach, H. \(1994\)](#). On this account, a set of general strain measures can be established following Equations (3.10), cf. [Ogden, R.W. \(1997\)](#).

	Lagrange	Euler	
$m \neq 0$	$\frac{1}{m}(\mathbf{U}^m - \mathbf{I})$	$\frac{1}{m}(\mathbf{V}^m - \mathbf{I})$	(3.10)
$m = 0$	$\ln \mathbf{U}$	$\ln \mathbf{V}$	

For the special cases of $m = 2$ and $m = -2$ the *Green-Lagrangian* and *Almansi-Eulerian strain tensor*,

$$\mathbf{E} = \frac{1}{2}(\mathbf{C} - \mathbf{1}) \quad (3.11)$$

and

$$\mathbf{e} = \frac{1}{2}(\mathbf{I} - \mathbf{B}^{-1}) \quad (3.12)$$

¹Rigid body translations have no effect on the deformation gradient due to the differentiation with respect to \mathbf{X} .

are obtained.

Besides, the logarithmic strain measures

$$\mathbf{H} = \frac{1}{2} \ln(\mathbf{C}) \quad \text{and} \quad \mathbf{h} = \frac{1}{2} \ln(\mathbf{B}), \quad (3.13)$$

also called *Hencky* strains and obtained for $m = 0$, play a special role because of some intrinsic features. One of those is that they can be decomposed additively into two parts which are associated with the change of the volume and the change of the shape of the body. Due to numerous reasons stated later on, the Eulerian Hencky strain \mathbf{h} is of particular interest in this work.

The fundamental base of the analysis of strain velocities is the velocity gradient tensor \mathbf{L} defined as

$$d\dot{\mathbf{x}} = \dot{\mathbf{F}}\mathbf{F}^{-1}d\mathbf{x} = \mathbf{L}d\mathbf{x}. \quad (3.14)$$

It can be interpreted as the spatial gradient of the velocity $\dot{\mathbf{x}}$, hence, relating an Eulerian line element $d\mathbf{x}$ to its material time derivative $d\dot{\mathbf{x}}$. \mathbf{L} can be additively decomposed into a symmetric and a skew-symmetric part furnishing the *Eulerian strain rate* or *stretching tensor* \mathbf{D} and the *spin tensor* \mathbf{W} given by

$$\mathbf{L} = \text{sym}(\mathbf{L}) + \text{skw}(\mathbf{L}) = \mathbf{D} + \mathbf{W} \quad (3.15)$$

with

$$\mathbf{D} = \frac{1}{2} (\mathbf{L} + \mathbf{L}^T) \quad \text{and} \quad \mathbf{W} = \frac{1}{2} (\mathbf{L} - \mathbf{L}^T). \quad (3.16)$$

3.1.2 Kinetics

Due to a system of applied forces on the current configuration \mathcal{B} of a body, at every imaginary cut surface of the body, a vector field exists, which is called the stress vector \mathbf{t} . With the resultant contact force $d\mathbf{k}$ and the area element da it follows

$$d\mathbf{k} = \mathbf{t} da. \quad (3.17)$$

As a result from *Cauchy's fundamental postulate*, one may find that the stress vectors at two opposing faces of an assumed cut are equal but oppositely oriented. Additionally accounting *Cauchy's theorem*, a second-order tensor \mathbf{T} exists with

$$\mathbf{t} = \mathbf{T} \mathbf{n} \quad \text{and} \quad d\mathbf{k} = \mathbf{T} da, \quad (3.18)$$

and \mathbf{n} being the normal vector to the actual area a . \mathbf{T} is an Eulerian stress measure and is called *Cauchy* or *true stress tensor*.

Consistent to the above remarks concerning strain measures, different Eulerian and Lagrangian stress measures may be established. Weighted by the Jacobian

or the ratio of mass densities for referential and current configuration in the case of closed systems, \mathbf{T} can be transformed into the *Kirchhoff stress tensor* $\boldsymbol{\tau}$,

$$\boldsymbol{\tau} = J \mathbf{T}. \quad (3.19)$$

If the contact forces are associated with face elements in the referential configuration $d\mathbf{A}$, the *first Piola-Kirchhoff stress tensor* can be derived, which is a two-point tensor, yielding

$$d\mathbf{k} = \mathbf{P}_1 d\mathbf{A}. \quad (3.20)$$

By means of *Nanson's formula*, cf. [Stein, E. & Barthold, F.-J. \(1996\)](#),

$$d\mathbf{a} = \det(\mathbf{F}) \mathbf{F}^{-T} d\mathbf{A}, \quad (3.21)$$

the first Piola-Kirchhoff tensor can be calculated from

$$\mathbf{P}_1 = \det(\mathbf{F}) \mathbf{T} \mathbf{F}^{-T}. \quad (3.22)$$

If a Lagrangian stress measure is needed, a fictitious referential contact force can be imagined, which associated with a referential face element yields the symmetric *second Piola-Kirchhoff stress tensor* \mathbf{P}_2 ,

$$d\mathbf{K} = \mathbf{P}_2 d\mathbf{A}, \quad (3.23)$$

with

$$\mathbf{P}_2 = \det(\mathbf{F}) \mathbf{F}^{-1} \mathbf{T} \mathbf{F}^{-T}. \quad (3.24)$$

\mathbf{P}_2 has no physical meaning and is therefore only used for calculation purposes. Beyond, for the constitutive modeling of material behavior, in anticipation of Section 3.2, the stress power \dot{w} is utilized to determine appropriate pairs of stress and strain measures. Fundamentally, the stress power is calculated from

$$\dot{w} = \boldsymbol{\tau} : \mathbf{D}. \quad (3.25)$$

Notwithstanding this fundamental relationship between Kirchhoff stress, Eulerian stretching and stress power other stress/strain rate pairs can be found which fulfill this *work conjugacy* equation. Some of them are \mathbf{P}_1 and $\dot{\mathbf{F}}$ or \mathbf{P}_2 and $\dot{\mathbf{E}}$ while by contrast \mathbf{D} could not be associated with a time derivative of a strain tensor for a long time.

The closure of this problem will be readdressed in the course of this section after some additional considerations concerning *frame of reference* or *observer indifference*.

3.1.3 Objectivity and objective rates

If two independent observers are considered who are in relative motion to one another, the following relationship for the description of the motion of a body is evident

$$\mathbf{x}^* = \mathbf{Q}(t)\mathbf{x} + \mathbf{c}(t) \quad \text{and} \quad t^* = t - a, \quad (3.26)$$

with the relative rotation and translation of the two observers $\mathbf{Q}(t)$, $\mathbf{c}(t)$ and the time shift a . In contrast to their kinematical description, physical phenomena do not depend on the choice of observer. Therefore, mathematical formulations of physical interrelations must reflect this independence, see [Ogden, R.W. \(1997\)](#). Physical quantities, which are independent of the choice of observer, are termed objective. The transformation rule for an objective second-order tensor reads

$$\mathbf{A}^*(\mathbf{x}^*) = \mathbf{Q}(t)\mathbf{A}(\mathbf{x})\mathbf{Q}^T(t). \quad (3.27)$$

Objective tensor fields are for example \mathbf{D} , \mathbf{E} , \mathbf{T} , $\boldsymbol{\tau}$, and \mathbf{P}_2 . In this regard, special attention has to be paid on time derivatives. For Lagrangian tensors the material time derivative is objective. Contrastively, for Eulerian measures this is not the case, so that modified time derivatives have to be used. The material time derivative for the (objective) Cauchy stress is given below,

$$\begin{aligned} \dot{\mathbf{T}}^* &= \overline{\dot{\mathbf{Q}}\mathbf{T}\mathbf{Q}^T} \\ &= \dot{\mathbf{Q}}\mathbf{T}\mathbf{Q}^T + \mathbf{Q}\dot{\mathbf{T}}\mathbf{Q}^T + \mathbf{Q}\mathbf{T}\dot{\mathbf{Q}}^T. \end{aligned} \quad (3.28)$$

As evident, the material time derivative of an objective Eulerian second-order tensor does not transform objectively. Prominent classical objective time derivatives are according to [Xiao, H. et al. \(2000a\)](#) the *Oldroyd* and *Truesdell* rates and the *Zaremba-Jaumann* and *Green-Naghdi* rate. Just recently, it was shown in [Xiao, H. et al. \(2000b\)](#) that the logarithmic rate of the Eulerian Hencky² strain yields the stretching tensor,

$$\overset{\circ}{\mathbf{h}}^{\log} = \mathbf{D}. \quad (3.29)$$

Hereby, it can be shown that the Hencky strain and the Kirchhof stress form a work conjugated pair, which is the work conjugated pair of choice for all further considerations.

For the modeling of elastoplastic and akin material behaviors, the decomposition of a strain or deformation measure into a reversible and irreversible part is essential, due to the different modeling approaches for reversible and irreversible processes. It was shown in [Xiao, H. et al. \(2006\)](#) that, motivated by a split of the stress power into a reversible and irreversible part,

$$\dot{w} = \boldsymbol{\tau} : \mathbf{D} = \dot{w}^e + \dot{w}^i, \quad (3.30)$$

²Only by use of this combination, logarithmic rate and Eulerian Hencky strain, the stretching tensor can be interpreted as a corotational time derivative of a strain tensor.

with

$$\dot{w}^e = \boldsymbol{\tau} : \mathbf{D}^e \quad \text{and} \quad \dot{w}^i = \boldsymbol{\tau} : \mathbf{D}^i, \quad (3.31)$$

associated with elastic and inelastic deformation, the stretching tensor and its additive decomposition should be taken for elastoplastic and related material models,

$$\mathbf{D} = \mathbf{D}^e + \mathbf{D}^i. \quad (3.32)$$

3.2 Balance laws

In this section, a general overview of the five fundamental balance equations and conservation laws is given. This section is just meant to show the basic concepts, results, and implications from those laws. It is not intended to give a detailed derivation of each. Furthermore, only *Boltzmann* continua are treated which results in the neglect of volume-distributed moments.

Basically, the considered balance laws can be written in the following form according to [Altenbach, J. & Altenbach, H. \(1994\)](#)

$$\frac{d}{dt} \int_{\mathcal{B}} \boldsymbol{\Psi}(\mathbf{x}, t) \rho \, dv = \int_{\partial \mathcal{B}} \boldsymbol{\Phi}(\mathbf{x}, t) \mathbf{n} \, da + \int_{\mathcal{B}} \boldsymbol{\Xi}(\mathbf{x}, t) \rho \, dv. \quad (3.33)$$

In this equation, $\boldsymbol{\Psi}$ are tensor-valued balance quantity densities. $\boldsymbol{\Phi}$ and $\boldsymbol{\Xi}$ are the respective fluxes through the surface area $\partial \mathcal{B}$ of the current configuration \mathcal{B} of the body and mass specific generation or annihilation due to external influences or internal sources or sinks, respectively.

Sufficient smoothness of all solutions is assumed so that in all subsequent sections the local forms of the balance equations are given.

3.2.1 Mass conservation

Assuming that mass is not annihilated or generated within the body, and that no mass transfer takes place throughout the surface of the body, the conservation equation of mass can be written as

$$m = \int_{\mathcal{B}} \rho \, dv = \int_{\mathcal{B}_0} \rho_0 \, dV \quad (3.34)$$

with $\boldsymbol{\Psi} = 1$ and $\boldsymbol{\Phi} = \boldsymbol{\Xi} = 0$. By means of the deformation gradient \mathbf{F} , the *first local form of mass conservation* follows,

$$\frac{\rho_0}{\rho} = \det \mathbf{F} = J. \quad (3.35)$$

Besides, differentiation of the global form with respect to time yields the *continuity equation* or *second local form of mass conservation*, cf. [Stein, E. & Barthelemy, F.-J. \(1996\)](#),

$$\dot{\rho} + \rho \operatorname{div} \dot{\mathbf{x}} = 0. \quad (3.36)$$

3.2.2 Balance of linear momentum

The conservation of linear momentum states that the velocity of change of linear momentum is equal to the applied surface- and body-forces. The balance law can be inferred from the general balance equation, (3.33), for $\Psi = \dot{\mathbf{x}}$, $\Phi = \mathbf{T}$, and $\Xi = \mathbf{b}$

$$\frac{d}{dt} \int_{\mathcal{B}} \dot{\mathbf{x}} \rho \, dv = \int_{\partial \mathcal{B}} \mathbf{T} \mathbf{n} \, da + \int_{\mathcal{B}} \mathbf{b} \rho \, dv. \quad (3.37)$$

Here, \mathbf{T} is the Cauchy stress tensor, and \mathbf{b} is the body-force density. Application of the divergence theorem leads to the local form, which is also known as *Cauchy's first law of motion*

$$\operatorname{div} \mathbf{T} + \rho(\mathbf{b} - \ddot{\mathbf{x}}) = \mathbf{0}. \quad (3.38)$$

3.2.3 Balance of angular momentum

The essence of the balance of angular momentum is, that the vectorial sum of moments resulting from the applied surface- and body-forces, with reference to an arbitrarily chosen point, is equal to the velocity of change of angular momentum. The respective balance law reads

$$\frac{d}{dt} \int_{\mathcal{B}} (\mathbf{x} - \mathbf{x}_0) \times \dot{\mathbf{x}} \rho \, dv = \int_{\partial \mathcal{B}} (\mathbf{x} - \mathbf{x}_0) \times (\mathbf{T} \mathbf{n}) \, da + \int_{\mathcal{B}} (\mathbf{x} - \mathbf{x}_0) \times \mathbf{b} \rho \, dv, \quad (3.39)$$

with \mathbf{x}_0 being an arbitrarily chosen reference point. Reference is given to Equation (3.33) by $\Psi = (\mathbf{x} - \mathbf{x}_0) \times \dot{\mathbf{x}}$, $\Phi \mathbf{n} = (\mathbf{x} - \mathbf{x}_0) \times (\mathbf{T} \mathbf{n})$, and $\Xi = (\mathbf{x} - \mathbf{x}_0) \times \mathbf{b}$. By means of the continuity equation, (3.36), the divergence theorem, and stipulating smoothness of the solution, the essence of the conservation of angular momentum can be given by the symmetry of the true stress tensor,

$$\mathbf{T} = \mathbf{T}^T. \quad (3.40)$$

This is not to be confused with the fact that all stress measures may be symmetric, which is beyond doubt not the case.

3.2.4 Conservation of energy/first law of thermodynamics

For all considered bodies, the velocity of change of total energy is equal to the velocity of heat supply and the power of the applied external forces. Herein, the total energy can be split into the internal and kinetic energy. Thus, the change of internal energy equals the internal stress power and the supplied heat, resulting in

$$\frac{d}{dt} \int_{\mathcal{B}} u \rho \, dv = \int_{\partial \mathcal{B}} (\mathbf{T} \dot{\mathbf{x}} - \mathbf{q}) \cdot \mathbf{n} \, da + \int_{\mathcal{B}} r \rho \, dv. \quad (3.41)$$

Here, u denotes the internal energy. \mathbf{q} and r are the heat flux and heat sources, respectively. Consequently, Equation (3.41) results from the general form of balance equation, (3.33), by $\Psi = u$, $\Phi = \mathbf{T}\dot{\mathbf{x}} - \mathbf{q}$, and $\Xi = r$. By means of the moment of angular momentum, utilizing the symmetry of the Cauchy stress tensor, the local form of the *first law of thermodynamics* is given by

$$\dot{u} = r - \frac{1}{\rho} \operatorname{div} \mathbf{q} + \frac{1}{\rho} \mathbf{T} : \mathbf{D}. \quad (3.42)$$

3.2.5 Balance of entropy/second law of thermodynamics

The existence of *entropy* S and absolute temperature Θ is assumed. Furthermore, the entropy has its minimum with $S = 0$ at $\Theta = 0$. This is sometimes referred to as the *third law of thermodynamics*, see [Altenbach, J. & Altenbach, H. \(1994\)](#). Now, the balance of entropy states that the velocity of change of entropy is equal to the sum of internal entropy production and entropy supply due to internal heat sources and heat fluxes through the surface. Hence, the balance of entropy can be written as

$$\frac{d}{dt} \int_{\mathcal{B}} s \rho \, dv = - \int_{\partial \mathcal{B}} \frac{1}{\Theta} \mathbf{q} \cdot \mathbf{n} \, da + \int_{\mathcal{B}} \left(\frac{r}{\Theta} + \dot{\gamma} \right) \rho \, dv, \quad (3.43)$$

with the mass specific entropy s and the internal entropy production rate $\dot{\gamma}$. Formally, this can be ascribed to Equation (3.33) with $\Psi = s$, $\Phi = -\frac{1}{\Theta} \mathbf{q}$, and $\Xi = \frac{r}{\Theta} + \dot{\gamma}$. Realizing that the internal entropy production is always non-negative, with the border case of reversible processes for which $\dot{\gamma} = 0$, it follows that

$$\dot{\gamma} \geq 0. \quad (3.44)$$

Incorporating this into Equation (3.43), and stipulating smoothness of the solutions, Equation (3.44) yields

$$\Theta \rho \dot{\gamma} = \rho \dot{s} - \frac{\rho r}{\Theta} + \operatorname{div} \frac{\mathbf{q}}{\Theta} \geq 0. \quad (3.45)$$

Consecutive rearranging then gives the *Clausius-Duhem inequality* with

$$\dot{s} \geq \frac{r}{\Theta} - \frac{1}{\rho} \operatorname{div} \frac{\mathbf{q}}{\Theta}. \quad (3.46)$$

Substituting the term of internal heat sources by means of the balance of energy (3.42), and establishing the notion of the *specific Helmholtz free energy*

$$\psi = u - \Theta s, \quad (3.47)$$

the Clausius-Duhem inequality can be reformulated to yield

$$\Theta \rho \dot{\gamma} = \mathbf{T} : \mathbf{D} - \rho \left(\dot{\psi} + s \dot{\Theta} \right) - \frac{1}{\Theta} \mathbf{q} \cdot \operatorname{grad} \Theta \geq 0. \quad (3.48)$$

3.3 Thermomechanical coupling

Since thermal and mechanical effects are strongly interrelated in the context of thermodynamic consistent material modeling, it has to be accounted for the thermomechanical coupling, when deriving governing equations for deformation and temperature.

By means of the principle of conservation of energy and a *Legendre* transformation reflection on different representations of energy, noting that

$$\frac{\partial g}{\mathbf{a}} = \frac{\partial \psi}{\mathbf{a}}, \quad (3.49)$$

the governing equation for the thermomechanical coupling is inferred as

$$c_p \dot{\Theta} = -\frac{1}{\rho} \operatorname{div} \mathbf{q} + \frac{1}{\rho} \dot{h}_{\text{lat}}, \quad (3.50)$$

cf. Müller, C. (2003) for further details. In this context, \dot{h}_{lat} denotes the latent heat generation per unit volume as a function of the *specific Gibbs free energy* g . Recalling that for scalar valued functions the following identity holds

$$\dot{g} = \overset{\circ}{g}{}^{\text{log}}, \quad (3.51)$$

and for isotropic tensorial functions the chain rule for corotating rates can be applied, Xiao, H. et al. (1999), the determining equation for \dot{h}_{lat} reads

$$\frac{1}{\rho} \dot{h}_{\text{lat}} = \frac{1}{\rho_0} \boldsymbol{\tau} : \mathbf{D}^{\text{tr}} + r - \frac{\partial g}{\partial \mathbf{a}} \cdot \overset{\circ}{\mathbf{a}}{}^{\text{log}} + \Theta \frac{\partial^2 g}{\partial \Theta \partial \boldsymbol{\tau}} : \overset{\circ}{\boldsymbol{\tau}}{}^{\text{log}} + \Theta \frac{\partial^2 g}{\partial \Theta \partial \mathbf{a}} : \overset{\circ}{\mathbf{a}}{}^{\text{log}}. \quad (3.52)$$

Here, \mathbf{a} represents the set of internal variables of the respective material model.

4 Phenomenological modeling

As this work is partly concerned with the identification of material parameters, the respective material model is presented in this chapter. The material model was developed in original form for small deformations by [Raniecki, B. et al. \(1992\)](#), and extended to finite deformations by [Müller, C. \(2003\)](#); [Müller, C. & Bruhns, O.T. \(2004, 2006\)](#). Additionally, special attention was paid by Müller to the thermodynamic frame.

The fundamentals of the R_L -model for finite deformations are demonstrated in the first section of this chapter. As a matter of fact, the purpose of this chapter is to offer an introduction to the R_L -model. Nevertheless, in order to gain a detailed insight, the disposed reader is referred to the aforementioned treatises. Afterwards, some remarks are made with respect to several shortcomings of the material model, which prove the parameter identification for tension/torsion tests cumbersome. Finally, after some comments about different approaches in the literature, a modification of the extended R_L -model is suggested, which incorporates the “tension/torsion” asymmetry.

4.1 R_L -model for finite deformations

Fundamental base of the presented material model is the additive decomposition of the stretching tensor, which can be motivated from the split of the stress power, (3.30). Since only elastic and pseudoelastic material behavior is considered here, the latter being associated with phase transformations, inelasticity in terms of plastic material behavior is not accounted. Moreover, the dissipative deformations are completely linked to phase transitions. Thus, Equation (3.32) becomes

$$\mathbf{D} = \mathbf{D}^e + \mathbf{D}^{\text{tr}}, \quad (4.1)$$

with \mathbf{D}^{tr} denoting the inelastic stretching tensor due to recoverable phase transformations. Starting thereof, and recalling Equation (3.29), the following split of the Hencky strain is used

$$\mathbf{h} = \mathbf{h}^e + \mathbf{h}^{\text{tr}}. \quad (4.2)$$

For the elastic material behavior, it is assumed that the stress admits a hyperelastic potential¹ according to

$$\Sigma(\boldsymbol{\tau}) = \frac{1}{2} \boldsymbol{\tau} : \mathbb{D} : \boldsymbol{\tau} + (\Theta - \Theta_0) \boldsymbol{\alpha} : \boldsymbol{\tau}. \quad (4.3)$$

¹Due to the axiom of material symmetry this is an isotropic tensor function with \mathbb{D} and $\boldsymbol{\alpha}$ being isotropic material properties.

Here, \mathbb{D} and $\boldsymbol{\alpha}$ are the fourth-order *elastic compliance tensor* and second-order *tensor of thermal expansion*, respectively. Additionally, a reference temperature Θ_0 is introduced.

Based on Equation (4.3), it is straightforward to derive the stress in terms of the elastic strain and the absolute temperature Θ , i.e.

$$\boldsymbol{\tau} = \mathbf{h}^e : \mathbb{C} - (\Theta - \Theta_0)\boldsymbol{\alpha} : \mathbb{C}. \quad (4.4)$$

Herein, an additional tensorial quantity \mathbb{C} is established, which is the inverse of the elastic compliance tensor, and which is termed *elastic stiffness tensor*.

In order to characterize the phase composition of the material, the mass fraction of martensite ξ is introduced,

$$\xi = \frac{m^M}{m}, \quad m = m^A + m^M. \quad (4.5)$$

Here and in the course of this work, the superscripts A and M respectively denote the austenite and martensite specific quantities. Accordingly, as only austenite-martensite and martensite-austenite two-stage phase transitions are considered, the mass fraction of austenite is given by

$$\frac{m^A}{m} = 1 - \xi. \quad (4.6)$$

In contrast to several other phenomenological material models, cf. for example [Qidwai, M.A. & Lagoudas, D.C. \(2000\)](#); [Juhász, L. et al. \(2002\)](#), the mass fraction instead of the volume fraction is taken in accord to the conservation of mass, (3.34). Nevertheless, with the assumption of constant and equal mass densities for austenite and martensite the two different formulations coincide.

Henceforth, the only internal variable of the material model shall be the martensite mass fraction, thus

$$\mathbf{a} = \{\xi\}. \quad (4.7)$$

As the material model is to be formulated in terms of the state variables \mathbf{h}^e , Θ , and \mathbf{a} , the specific Helmholtz free energy has to be considered as governing measure.

The overall Helmholtz free energy can be calculated from the energies of the single phases by using the following mixing rule,

$$\psi = (1 - \xi)\psi^A + \xi\psi^M + \xi(1 - \xi)\psi_{it}, \quad (4.8)$$

cf. [Müller, C. \(2003\)](#). Here, the *internal interaction* ψ_{it} is given by

$$\psi_{it}(\Theta) = \bar{u}_0 - \Theta\bar{s}_0 \geq 0, \quad (4.9)$$

with the material parameters \bar{u}_0 and \bar{s}_0 as *configurational internal energy* and *entropy*. An analogous type of mixing rule, which is motivated by micromechanical considerations, is chosen for the calculation of the macroscopic strain

$$\mathbf{h} = (1 - \xi) \mathbf{h}^A + \xi \mathbf{h}^M, \quad (4.10)$$

with

$$\mathbf{h}^\alpha = \mathbf{h}^{e\alpha} + \mathbf{h}^{\text{tr}\alpha}, \quad \alpha = \{A, M\}. \quad (4.11)$$

In order to characterize the transformation strain, which is associated with the generation of martensite, the *intrinsic phase distortion* $\boldsymbol{\kappa}$ is introduced,

$$\boldsymbol{\kappa} : \boldsymbol{\kappa} = \eta^2 = \text{const}. \quad (4.12)$$

$\boldsymbol{\kappa}$ is chosen to have properties of a strain like quantity.

Though the intrinsic phase distortion itself is subject to changes, the respective *Frobenius* norm is constant. The value of this norm, η , is termed *amplitude of pseudoelastic strain* or *pseudoelastic flow*, and can be interpreted as the length of the pseudoelastic hysteresis.

Since the martensitic transformation is assumed to be volume preserving, volumetric changes of only -0.34% are reported in the literature, see [Shimizu, K. & Tadaki, T. \(1984\)](#) in [Funakubo, H. \(1984\)](#), $\boldsymbol{\kappa}$ is taken to be deviatoric. The fact, that the considered transformation is induced by stress, suggests that the phase distortion may be proportional to the stress deviator,

$$\boldsymbol{\kappa} = \eta \frac{\boldsymbol{\tau}'}{\tau}, \quad \tau = \sqrt{T_2}, \quad (4.13)$$

with T_2 being the second invariant of the stress deviator, defined by

$$T_2 = \text{tr}(\boldsymbol{\tau}' \cdot \boldsymbol{\tau}') = \boldsymbol{\tau}' : \boldsymbol{\tau}'. \quad (4.14)$$

In other words, the orientation of the martensitic phase is equal to the load or stress direction.

Resulting from the definition of $\boldsymbol{\kappa}$, the transformation strain of the martensite phase with respect to the parent phase, namely austenite, is determined by

$$\mathbf{h}^{\text{tr}M} = \boldsymbol{\kappa} \quad \Rightarrow \quad \text{tr}(\mathbf{h}^{\text{tr}M}) = 0. \quad (4.15)$$

Accordingly, it follows

$$\mathbf{h}^{\text{tr}A} = \mathbf{0}. \quad (4.16)$$

Now, incorporating Equations (4.15) and (4.16) into the mixing rule, (4.10), the overall transformation strain can be derived straightforward in terms of the martensite fraction and phase distortion, yielding

$$\mathbf{h}^{\text{tr}} = \xi \boldsymbol{\kappa} \quad \Rightarrow \quad \text{tr}(\mathbf{h}^{\text{tr}}) = 0. \quad (4.17)$$

Then, assuming constant and equal elastic stiffness and thermal dilatation for the two phases, $\mathbb{C}^A = \mathbb{C}^M = \mathbb{C} = \mathbb{C}_0$, $\boldsymbol{\alpha}^A = \boldsymbol{\alpha}^M = \boldsymbol{\alpha} = \boldsymbol{\alpha}_0$, the resultant specific Helmholtz free energy reads

$$\begin{aligned} \psi(\mathbf{h}^e, \Theta, \xi) &= \frac{1}{2\rho_0} \mathbf{h}^e : \mathbb{C}_0 : \mathbf{h}^e - (\Theta - \Theta_0) \frac{1}{\rho_0} \boldsymbol{\alpha}_0 : \mathbb{C}_0 : \mathbf{h}^e \\ &+ c_v \left(\Theta - \Theta_0 - \Theta \ln \left(\frac{\Theta}{\Theta_0} \right) \right) \\ &+ u_0^{*A} - \Theta s_0^{*A} - \xi \pi_0^f(\Theta) + \xi(1 - \xi) \psi_{\text{it}}(\Theta). \end{aligned} \quad (4.18)$$

Here, $u_0^{*\alpha}$ and $s_0^{*\alpha}$, with $\alpha = \{A, M\}$, denote the phase specific internal energy and entropy, respectively.

π_0^f is defined as the difference between the two phase specific Helmholtz free energies,

$$\pi_0^f(\Theta) = \psi^A - \psi^M, \quad (4.19)$$

and is called *phase chemical potential*. With the incorporation of the equations for the phase specific Helmholtz energies, given for example in Müller, C. & Bruhns, O.T. (2004, 2006), π_0^f can be recast to

$$\pi_0^f(\Theta) = \Delta u^* - \Theta \Delta s^*, \quad (4.20)$$

with the differences of internal energy Δu^* and entropy Δs^* ,

$$\Delta u^* = u_0^{*A} - u_0^{*M} \quad (4.21)$$

$$\Delta s^* = s_0^{*A} - s_0^{*M}. \quad (4.22)$$

Beyond the principle of conservation of energy, the second law of thermodynamics stating the direction of thermomechanical processes must be satisfied as well. Recalling the Clausius-Duhem inequality (Equation (3.48)), computing the total differential of ψ , and noting that the only internal variable is the martensite fraction, resulting in $\mathbf{a} = \mathbf{a}_{\text{mech}}$, the internal entropy production rate can be decomposed additively into independent mechanically and thermally induced parts

$$\Theta \rho \dot{\gamma} = \Theta \rho \dot{\gamma}_{\text{mech}} + \Theta \rho \dot{\gamma}_{\text{th}} \geq 0. \quad (4.23)$$

Then, the two addenda on the right side are defined by

$$\Theta \rho \dot{\gamma}_{\text{mech}} = \frac{\rho}{\rho_0} \dot{w}^{\text{tr}} - \rho \frac{\partial \psi}{\partial \mathbf{a}} \cdot \overset{\circ}{\mathbf{a}}^{\log} \quad (4.24)$$

$$\Theta \rho \dot{\gamma}_{\text{th}} = -\frac{1}{\Theta} \mathbf{q} \cdot \text{grad} \Theta. \quad (4.25)$$

Under the assumption that *Fourier's law*, cf. [Mills, A.F. \(1999\)](#), holds and for non-negative values of the *thermal conductivity* k , the thermally induced part of the Clausius-Duhem inequality is always non-negative, i.e.

$$\Theta \rho \dot{\gamma}_{\text{th}} = \frac{k}{\rho \Theta^2} (\text{grad } \Theta)^2 \geq 0. \quad (4.26)$$

Subsequently as a consequence, the mechanically induced part of the entropy production has to be non-negative as well,

$$\Theta \rho \dot{\gamma}_{\text{mech}} \geq 0. \quad (4.27)$$

This can be further specified to yield

$$\boldsymbol{\tau} : \overset{\circ}{\mathbf{h}}^{\text{tr log}} - \rho_0 \frac{\partial \psi}{\partial \xi} \dot{\xi} \geq 0. \quad (4.28)$$

With the governing equation for the transformation strain, Equation (4.17), the first addendum in Equation (4.28) can be calculated to give

$$\boldsymbol{\tau} : \overset{\circ}{\mathbf{h}}^{\text{tr log}} = \dot{\xi} \boldsymbol{\tau} : \boldsymbol{\kappa} + \xi \boldsymbol{\tau} : \overset{\circ}{\boldsymbol{\kappa}}^{\text{log}}. \quad (4.29)$$

Now, for the very special case that the Frobenius norm of $\boldsymbol{\kappa}$ is constant (Equation (4.12)) and that $\boldsymbol{\kappa}$ is not only coaxial to but also linearly dependent on $\boldsymbol{\tau}'$ (Equation (4.13)) the second addendum of Equation (4.29) vanishes. Hence, Equation (4.28) can be written as product of a *thermodynamic driving force* π^f and a *thermodynamic flux*, which is in this case the time derivative of the martensite fraction,

$$\pi^f \dot{\xi} \geq 0, \quad (4.30)$$

with

$$\pi^f = \frac{1}{\xi} \boldsymbol{\tau} : \mathbf{h}^{\text{tr}} - \rho_0 \frac{\partial \psi}{\partial \xi}. \quad (4.31)$$

Equation (4.30) implies that

$$\begin{aligned} \dot{\xi} &> 0 & \text{for } \pi^f > 0 \\ \dot{\xi} &< 0 & \text{for } \pi^f < 0. \end{aligned} \quad (4.32)$$

For the evolution of the thermodynamic driving force, it is assumed that a yield-surface-like function may exist, for which the following equations hold

$$\begin{aligned} f^{\text{A} \rightarrow \text{M}} &= \text{const} & \text{for } \dot{\xi} > 0 \\ f^{\text{M} \rightarrow \text{A}} &= \text{const} & \text{for } \dot{\xi} < 0. \end{aligned} \quad (4.33)$$

A simple evolution equation is adopted with a new function $k^\alpha(\xi)$, $\alpha = \{A \rightarrow M, M \rightarrow A\}$, which proves crucial for the behavior of the material law, i.e.,

$$\begin{aligned} f^{A \rightarrow M}(\pi^f, \xi) &= \pi^f - \rho_0 k^{A \rightarrow M}(\xi) \leq 0 \\ f^{M \rightarrow A}(\pi^f, \xi) &= -\pi^f + \rho_0 k^{M \rightarrow A}(\xi) \leq 0. \end{aligned} \quad (4.34)$$

Straightforward, the rate of the thermodynamic force π^f may be calculated based on Equations (4.33) and (4.34)

$$\begin{aligned} \dot{\pi}^f &= \rho_0 \dot{k}^{A \rightarrow M} \quad \text{for } \dot{\xi} > 0 \\ \dot{\pi}^f &= \rho_0 \dot{k}^{M \rightarrow A} \quad \text{for } \dot{\xi} < 0. \end{aligned} \quad (4.35)$$

In [Raniecki, B. et al. \(1992\)](#), the following form of the phase transformation function is proposed

$$\begin{aligned} \rho_0 k^{A \rightarrow M}(\xi) &= -(A_1 + B_1 \xi) \ln(1 - \xi) + C_1 \xi \geq 0 \\ \rho_0 k^{M \rightarrow A}(\xi) &= (A_2 - B_2(1 - \xi)) \ln \xi - C_2(1 - \xi) \leq 0, \end{aligned} \quad (4.36)$$

with the constants A_i , B_i , and C_i , $i = \{1, 2\}$, which are further specified by

$$\begin{aligned} A_1 &= \frac{\Delta s^* - \bar{s}_0}{a_1} & B_1 &= \frac{2r_1 \bar{s}_0}{a_1} & C_1 &= 2r_1 \psi_{it}(M_s^0) \\ A_2 &= \frac{\Delta s^* + \bar{s}_0}{a_2} & B_2 &= \frac{2r_2 \bar{s}_0}{a_2} & C_2 &= 2r_2 \psi_{it}(A_s^0). \end{aligned} \quad (4.37)$$

Thereupon, by means of the consideration of so-called neutral processes, meaning that the martensite fraction is kept constant, and, similar to the theory of plasticity, building the total differential of the thermodynamic force, the rate of the martensite fraction can be deduced as

$$\dot{\xi}^\alpha = \frac{\dot{\pi}^f|_{\xi=\text{const}}}{\left(\rho_0 \frac{\partial k^\alpha}{\partial \xi} - \frac{1}{\xi} \boldsymbol{\tau} : \frac{\partial \mathbf{h}^{\text{tr}}}{\partial \xi} + \frac{1}{\xi^2} \boldsymbol{\tau} : \mathbf{h}^{\text{tr}} - 2\rho_0 \psi_{it} \right)}. \quad (4.38)$$

For a detailed derivation of Equation (4.38), the interested reader is referred to [Müller, C. \(2003\)](#).

In what follows, the hyperelastic potential $\Sigma(\boldsymbol{\tau})$ being isotropic in respect of the Kirchhoff stress $\boldsymbol{\tau}$, see Footnote 1 on page 22, is further specified. The isotropic tensor of thermal expansion and elastic stiffness tensor are taken as

$$\boldsymbol{\alpha}_0 = \alpha_0 \mathbf{1} \quad (4.39)$$

$$\mathbb{C}_0 = \kappa \mathbf{1} \otimes \mathbf{1} + 2\mu \left(\mathbb{I} - \frac{1}{3} \mathbf{1} \otimes \mathbf{1} \right). \quad (4.40)$$

Furthermore, the *bulk modulus* κ can be expressed in terms of the *Lamé constants* μ and λ :

$$\kappa = \lambda + \frac{2}{3}\mu. \quad (4.41)$$

Altogether, (4.4), (4.39), (4.40), (4.41), the Kirchhoff stress can be easily calculated from the elastic Hencky strain

$$\boldsymbol{\tau} = \lambda \operatorname{tr}(\mathbf{h}^e) \mathbf{1} + 2\mu \mathbf{h}^e - 3\kappa (\Theta - \Theta_0) \alpha_0 \mathbf{1}. \quad (4.42)$$

Moreover, it can be shown that the stress deviator $\boldsymbol{\tau}'$, the elastic strain deviator $\mathbf{h}^{e'}$, the transformation strain \mathbf{h}^{tr} , and thus the overall strain deviator \mathbf{h}' are coaxial, see Müller, C. (2003).

For further simplifications, a new quantity is introduced, termed as equivalent Hencky strain, which is defined as

$$h = \sqrt{\mathbf{h}' : \mathbf{h}'}. \quad (4.43)$$

The equivalent strain is an isotropic tensor function. Thus, its time derivative can be calculated by means of the chain rule for corotating rates to yield

$$\dot{h} = \frac{1}{h} \mathbf{h}' : \mathbf{D}. \quad (4.44)$$

This, together with $\boldsymbol{\tau}'$, $\mathbf{h}^{e'}$, \mathbf{h}^{tr} , \mathbf{h}' being coaxial is used for deriving the rate of \mathbf{h}^{tr} , i.e.

$$\overset{\circ}{\mathbf{h}}^{\text{tr log}} = \mathbf{D}^{\text{tr}} = \frac{\eta}{h} \left(\mathbf{h}' \dot{\xi} + \xi \left(\mathbb{I} - \frac{1}{3} \mathbf{1} \otimes \mathbf{1} - \frac{1}{h^2} (\mathbf{h}' \otimes \mathbf{h}') \right) : \mathbf{D} \right). \quad (4.45)$$

Finally, after substantial calculations, cf. Müller, C. (2003), Equation (4.38) can be specified to give a scalar expression for the formation of martensite

$$\dot{\xi}^a = \frac{2\mu\eta\dot{h} + \rho_0(-\Delta s^* + (1 - 2\xi)\bar{s}_0)\dot{\Theta}}{\rho_0 \frac{\partial k^\alpha}{\partial \xi} - 2\rho_0\psi_{\text{it}} + 2\mu\eta^2}. \quad (4.46)$$

Additionally, also the thermodynamic driving force derived in Equation (4.31), playing a major role for the material model, can be further particularized. Thus, π^{f} reads for the aforementioned special case with Equations (4.9), (4.18), and (4.20)

$$\pi^{\text{f}} = \tau\eta + \rho_0 (\Delta u^* - \Theta\Delta s^*) - \rho_0 (1 - 2\xi) (\bar{u}_0 - \Theta\bar{s}_0). \quad (4.47)$$

By means of Equation (4.18) furnishing the overall Helmholtz free energy, and under the assumption of an isotropic hyperelastic potential, the governing equation for the latent heat, (3.52), is obtained as

$$\frac{1}{\rho} \dot{h}_{\text{lat}} = \frac{1}{\rho_0} \boldsymbol{\tau} : \mathbf{D}^{\text{tr}} + (\Delta u^* - \bar{u}_0(1 - 2\xi))\dot{\xi} - \frac{1}{\rho_0} \Theta \alpha_0 : \overset{\circ}{\boldsymbol{\tau}}^{\text{log}}. \quad (4.48)$$

4.2 Discussion of the R_L -model and modification

In this section, a modification of the presented R_L -model for finite deformations is proposed. The main focus of this modification is on the description of asymmetric effects concerning the tension/torsion behavior. It is not intended to modify the material model to describe the well-known tension/compression asymmetry, though this effect may be incorporated in the same straightforward manner shown below. Before the new approach is described in detail, some shortcomings of the existing material model are discussed in order to give a motivation for the applied changes.

As can be observed by Equation (4.47), the R_L -model is based on a *von-Mises* type equivalent stress τ and according to Equations (4.43), (4.44), and (4.46) an equivalent strain of the same type with

$$\tau = \sqrt{T_2} = \sqrt{\boldsymbol{\tau}' : \boldsymbol{\tau}'}, \quad (4.49)$$

$$h = \sqrt{H_2} = \sqrt{\mathbf{h}' : \mathbf{h}'}, \quad (4.50)$$

respectively.

Albeit, the equivalent strain cannot be termed as being of von-Mises type² because of the different weighting factors for shear stress and strain in the von-Mises frame, which result from the requirement of strain energy equivalence

$$w = \boldsymbol{\tau} : \mathbf{h} = \tau^* h^*. \quad (4.51)$$

Here, τ^* and h^* are a von-Mises equivalent stress and strain, respectively.

This condition is not fulfilled for the R_L -model specific equivalent stress and strain, i.e.

$$w = \boldsymbol{\tau} : \mathbf{h} \neq \tau h. \quad (4.52)$$

Moreover, it can be shown that the tension/torsion material behavior of conventional shape memory alloys cannot be predicted accurately by material models which are based on a von-Mises type equivalent stress. This can be substantiated for example by the works of [Lexcellent, C. et al. \(2006\)](#); [Helm, D. \(2001\)](#); [Lexcellent, C. & Rejzner, J. \(2000\)](#); [Raniecki, B. & Lexcellent, C. \(1998\)](#); [Lim, T.J. & McDowell, D.L. \(1999\)](#) for NiTi, but which is also observed for Cu-based shape memory alloys, cf. [Tokuda, M. et al. \(1998\)](#); [Šittner, P. et al. \(1995\)](#). In

²In [Tokuda, M. et al. \(2002\)](#); [Lim, T.J. & McDowell, D.L. \(1999\)](#) von-Mises equivalent stress and strain are defined by the following equations

$$\sigma_{\text{eq}} = \sqrt{\sigma^2 + (\sqrt{3}\tau)^2} \quad \varepsilon_{\text{eq}} = \sqrt{\varepsilon^2 + \left(\frac{\gamma}{\sqrt{3}}\right)^2},$$

with σ , τ and ε , γ being the normal and shear components of the stress, strain tensor, respectively.

many cases, this is not stated explicitly but can be verified directly by analyzing the published experimental data, see e.g. Helm, D. (2001). This is in particular interesting, since the “tension/torsion asymmetry” is not as well-known and discussed as extensively in the literature as the tension/compression asymmetry, although the effect is supposed to be at least as important.

In this context, different approaches exist for covering the special tension/torsion relationship. Šittner and co-workers, for example, who use a micromechanical material model, deal with the tension/torsion behavior outside the actual model, refer to Šittner, P. et al. (1997, 1996). In this ad-hoc approach, two material parameters are introduced, which are similar to the von-Mises weighting factors $\sqrt{3}$ and $\frac{1}{\sqrt{3}}$ but exhibit different and variable values. Those parameters are to be identified for each alloy so that the stress responses of two simple uniaxial tension, torsion tests coincide. Hence, modified stress and strain tensors are generated from the original ones by weighting normal and shear components differently. Afterwards, the so-modified stress and strain tensors are used as input to the micromechanical material model.

The approach presented by Raniecki, B. & Lexcellent, C. (1998); Lexcellent, C. & Rejzner, J. (2000), points into a different direction. Here, a modification or generalization of the R_L -model is proposed. A new potential, $g^*(\boldsymbol{\tau}) \geq 0$, is introduced, and it is assumed that the intrinsic phase distortion admits this potential and is calculated thereof (compare to plasticity),

$$\boldsymbol{\kappa} = \rho_0 \frac{\partial g^*(\boldsymbol{\tau})}{\partial \boldsymbol{\tau}}. \quad (4.53)$$

A general form of the potential is proposed, which is subject to further specification

$$g^*(\boldsymbol{\tau}) = \frac{\eta}{\rho_0} \tau f(y), \quad y = \frac{3\sqrt{6}T_3}{\tau^3}, \quad (4.54)$$

with

$$T_3 = \det(\boldsymbol{\tau}). \quad (4.55)$$

Then, specific potentials are calculated for the cases of pure tension, compression, and pure shear. Finally, the effective potential of a proportional loading path is calculated as a linear combination of the simple cases. Herein, the weighting factors are proportional to the respective strain components.

By contrast, a slightly different approach is suggested in this work. It is intended to modify the governing equation of the intrinsic phase distortion so that the thermodynamic driving force π^f describes the observed asymmetry of the tension/torsion behavior. In order to be able to formulate the material model with respect to finite deformations using the logarithmic rate, the thermodynamic driving force has to be an isotropic tensor function. Only in this case, the chain rule for corotational rates can be utilized for the calculation of the total

differential of the thermodynamic force, cf. [Xiao, H. et al. \(1999\)](#). The obvious and self-evident first approach to decompose the stress deviator additively into an axial and a shear component part proves inappropriate, since the resultant tensor function representing the thermodynamic force is non-isotropic. To account for this, a new equivalent stress measure is introduced, which is based on the first and second invariant of the stress tensor,

$$\hat{\tau} = \sqrt{b^2(S_2 - S_1^2) + \frac{2}{3}S_1^2}, \quad (4.56)$$

with

$$S_1 = \text{tr}(\boldsymbol{\tau}) \quad \text{and} \quad S_2 = \text{tr}(\boldsymbol{\tau} \cdot \boldsymbol{\tau}) = \boldsymbol{\tau} : \boldsymbol{\tau}, \quad (4.57)$$

and the material parameter b . Hereby, the phase distortion $\boldsymbol{\kappa}$ is assumed as

$$\boldsymbol{\kappa} = \eta \frac{\hat{\tau}}{\tau^2} \boldsymbol{\tau}'. \quad (4.58)$$

With Equation (4.17), the governing equation for the transformation induced strain reads

$$\mathbf{h}^{\text{tr}} = \xi \eta \frac{\hat{\tau}}{\tau^2} \boldsymbol{\tau}'. \quad (4.59)$$

Analogous to Section 4.1, the thermodynamic driving force can be specialized under the assumption of an isotropic potential $\Sigma(\boldsymbol{\tau})$, yielding

$$\tau^{\text{f}} = \hat{\tau} \eta + \rho_0 (\Delta u^* - \Theta \Delta s^*) - \rho_0 (1 - 2\xi) (\bar{u}_0 - \Theta \bar{s}_0). \quad (4.60)$$

The only difference between Equations (4.60) and (4.47) lies in the definition of the equivalent stress. Consequently, the governing equation for the martensite fraction is given by Equation (4.38), which leads for this special case to

$$\dot{\xi}^\alpha = \frac{\frac{\eta}{\tau^2} [\boldsymbol{\tau}' : \mathbb{Z}(\boldsymbol{\tau}) + \hat{\tau} \boldsymbol{\tau}'] : \overset{\circ}{\boldsymbol{\tau}}^{\text{log}} + \rho_0 (-\Delta s^* + (1 - 2\xi) \bar{s}_0) \dot{\Theta}}{\rho_0 \frac{\partial k^\alpha}{\partial \xi} - 2\rho_0 \psi_{\text{it}}}, \quad (4.61)$$

with the fourth-order tensorial function $\mathbb{Z}(\boldsymbol{\tau})$ given by

$$\mathbb{Z}(\boldsymbol{\tau}) = \frac{\boldsymbol{\tau}' \otimes \boldsymbol{\tau}^*}{\hat{\tau}} + \hat{\tau} \left(\mathbb{I}_{\text{dev}} - \frac{2}{\tau^2} \boldsymbol{\tau}' \otimes \boldsymbol{\tau}' \right). \quad (4.62)$$

Furthermore, the second-order tensor field $\boldsymbol{\tau}^*$ and the fourth-order deviatoric unit tensor \mathbb{I}_{dev} are introduced for simplification purposes,

$$\boldsymbol{\tau}^* = b^2 \boldsymbol{\tau} + \left(\frac{2}{3} - b^2 \right) \text{tr}(\boldsymbol{\tau}) \mathbf{1} \quad (4.63)$$

$$\mathbb{I}_{\text{dev}} = \mathbb{I} - \frac{1}{3} \mathbf{1} \otimes \mathbf{1}. \quad (4.64)$$

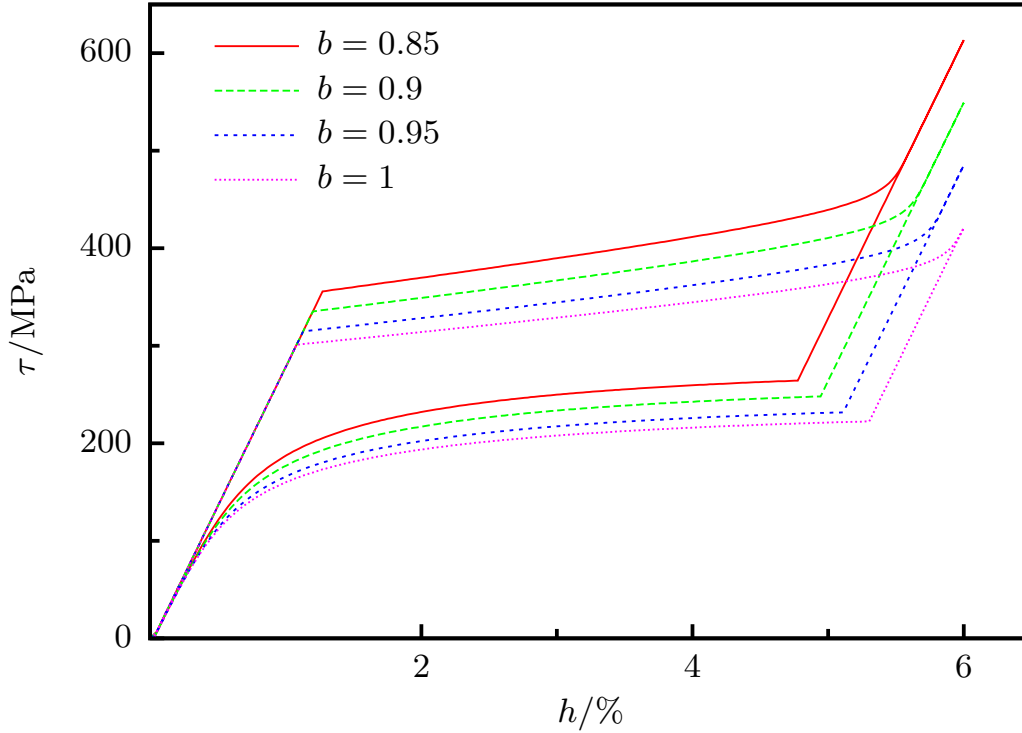


Figure 4.1: Comparison of the simple torsion stress-strain behavior for different values of the material parameter b

In this context, the rate of the transformation induced strain $\mathbf{h}^{\circ \text{tr log}}$ can be derived as well, so that

$$\mathbf{h}^{\circ \text{tr log}} = \mathbf{D}^{\text{tr}} = \frac{\eta}{\tau^2} \left(\dot{\xi} \hat{\tau} \boldsymbol{\tau}' + \xi \mathbb{Z}(\boldsymbol{\tau}) : \overset{\circ}{\boldsymbol{\tau}}^{\text{log}} \right). \quad (4.65)$$

Altogether, one additional material parameter is introduced in order to capture the tension/torsion asymmetry and moreover, it can be seen from Equations (4.60) and (4.56) that the scalar-valued tensor function π^{f} is isotropic, as it is formulated in terms of invariants of the stress tensor.

Accordingly, Figure 4.1 shows a comparison of simple torsion test computations for different values of the material parameter b . It can be seen that the hysteresis shifts to higher stresses for lower values of b . Furthermore, the height of the hysteresis is increased for a decreasing parameter b . For the special case of $b = 1$, the modified R_L -model and the R_L -model presented in Section 4.1 coincide, with

$$\hat{\tau}(b = 1) = \sqrt{S_2 - \frac{1}{3}S_1^2} = \sqrt{T_2} = \tau. \quad (4.66)$$

Thus, in the h - τ -space the stress curves for a simple torsion test with $b = 1$ and a simple tension test regardless of the parameter b are identical. Consequently, for $b = 1$, torsion and tension curves coincide in the h - τ -space.

If Equations (4.58) and (4.60) are compared to the findings in Raniecki, B. & Lexcellent, C. (1998), an alternative interpretation of the material parameter b comes into mind, and Equations (4.58) and (4.60) can be reformulated, resulting in

$$\kappa = \hat{\eta} \frac{\tau'}{\tau} \quad (4.67)$$

and

$$\pi^f = \tau \hat{\eta} + \rho_0 (\Delta u^* - \Theta \Delta s^*) - \rho_0 (1 - 2\xi) (\bar{u}_0 - \Theta \bar{s}_0) \quad (4.68)$$

with

$$\hat{\eta} = \eta \frac{\hat{\tau}}{\tau}. \quad (4.69)$$

The analogy to the unmodified R_L -model, separated by Equations (4.13) and (4.47), is obvious.

Now, two particular but simple cases are considered, on the one hand a simple tension test and on the other hand a simple torsion test. In the simple tension case the resulting amplitude of pseudoelastic flow $\hat{\eta}_{\text{ten}}$ is identical to η

$$\hat{\eta}_{\text{ten}} = \eta, \quad (4.70)$$

whereas for simple torsion the resulting amplitude of pseudoelastic flow reads

$$\hat{\eta}_{\text{tor}} = b \eta. \quad (4.71)$$

Consequently, b can be interpreted as the ratio of the amplitudes of pseudoelastic strain in the simple torsion and tension case,

$$b = \frac{\hat{\eta}_{\text{tor}}}{\hat{\eta}_{\text{ten}}}. \quad (4.72)$$

This can be further clarified after recalling Figure 4.1. Here, it is obvious that the lengths of the hystereses correlate with the values of b . As pointed out before and immanent in Equation (4.72), smaller values of b result in smaller hysteresis lengths. Again, it is reminded of the coincidence of tension and torsion curves for $b = 1$.

At the end of this chapter, special attention is drawn to the Clausius-Duhem inequality. As pointed out on page 26, just for one special case, the Clausius-Duhem inequality can be split multiplicatively into a scalar thermodynamic force and flux. It is seen that the Frobenius norm of the intrinsic phase distortion κ is not constant within the modified model deduced in this section. Accordingly, the second addendum of Equation (4.29) can not be neglected for arbitrary loading paths. Nevertheless, if the material model is restricted to loading paths without reorientation, as is done by Qidwai, M.A. & Lagoudas, D.C. (2000), the Clausius-Duhem inequality can be fulfilled in advance. On this account, at most

proportional loading paths are shown in [Raniecki, B. & Lexcellent, C. \(1998\)](#); [Lexcellent, C. & Rejzner, J. \(2000\)](#). Above all, the magnitude of the resultant error, if nonetheless loading paths with reorientation are considered, is subject to further examination and specific to the particular load case. This topic will be revisited in context of the parameter identification in [Chapter 8](#).

5 Experimental setup

For the thermomechanical characterization of NiTi and the parameter identification of a respective material model, it is necessary to be able to realize well-defined and, within certain limitations, freely configurable thermomechanical experiments. Here, the physically relevant temperature range, which is between -100°C and $+100^{\circ}\text{C}$ in this work, has to be covered by a temperature control, which is to be implemented. Due to the abrupt generation and absorption of latent heat, the temperature control procedure has to exhibit a highly dynamic behavior.

Moreover, stresses and strains are to be applied and to be measured. Beyond that, the specimen geometry has to be chosen with reference to the testing material and to the testing machine. The fact that strain values up to 10% are desired, poses a significant challenge to the projected measuring devices.

This chapter is subdivided into nine sections. Firstly, the specimen material and specimen geometry are presented. This is followed by a detailed review of heating and cooling mechanisms and the applied heating and cooling concepts. Subsequently, general temperature measuring by means of thermocouples and the specific temperature measuring, which is implemented in this work are introduced. Section 5.5 states the temperature control scheme, which is based on the concepts illustrated in the preceding sections while Sections 5.6, 5.7, and 5.8 deal with the mechanical part of the experimental setup. Finally, this chapter is concluded by a presentation of the complete testing system.

5.1 Specimen material and geometry

The shape memory alloy, which is used in all experiments within this work is a special NiTi alloy¹, exhibiting pseudoelastic behavior at room temperature. The nominal composition is 50.7 at.% NiTi. Figure 5.1 shows a typical DSC² curve³ of the as-received material. Typical values of the peak temperatures A_p ⁴, M_p ⁵ are -20°C , -60°C , respectively.

In the as-received state, the alloy features a single step forward and reverse transformation. In spite of the existence of two distinct transformation peaks and

¹Co. Euroflex GmbH, Nitinol SE 508 tubing

²Differential Scanning Calorimetry, a thermoanalytical technique for characterizing materials by which the amount of energy that is absorbed or released by a sample and a reference during cooling and heating are measured as a function of temperature.

³Co. TA Instruments, 2920 CE, differential scanning calorimeter

⁴Austenite peak temperature

⁵Martensite peak temperature

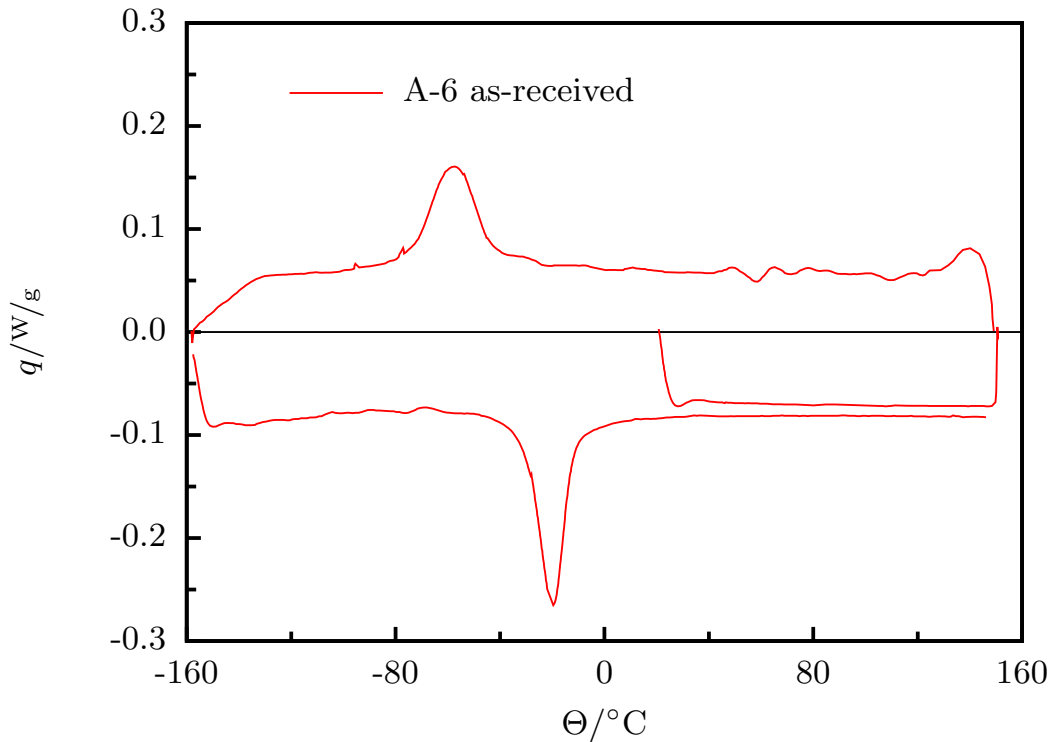


Figure 5.1: DSC curve of the as-received material

a testing temperature above the endothermic peak, the material shows hardly any mechanically pseudoelastic behavior in the as-received state, as evident in Figure 5.2 showing the stress-strain relation for three simple tension tests at different temperatures. In order to “improve” the mechanical behavior, a special thermomechanical treatment has to be found. This procedure is explained in detail in Chapter 6.1.

The specimens are cut from tubular stock⁶ of one single charge of material as to minimize any potential variation in the material behavior.

A special geometry is chosen for the specimens as shown in Figure 5.3. An hour-glass shape is selected so that a stress concentration and thus, the beginning of phase transition, is localized in the gage section of the specimen. The length of the gage section is a consequence of a compromise between the objective that no buckling and kinking may occur during compression and torsion tests and that the temperature profile is as uniform as possible without large boundary effects. Incorporating a radius-to-wall-thickness ratio of 5:1 resulting from an outer, inner diameter of 9.6 mm, 7.92 mm, respectively, the specimen can be considered as thin-walled, Lim, T.J. & McDowell, D.L. (1999); Li, Z.Q. & Sun, Q.P. (2002).

Figure 5.4 shows a polished micrograph section of the specimen wall within the

⁶Inner diameter 7.92 mm, outer diameter 12.7 mm

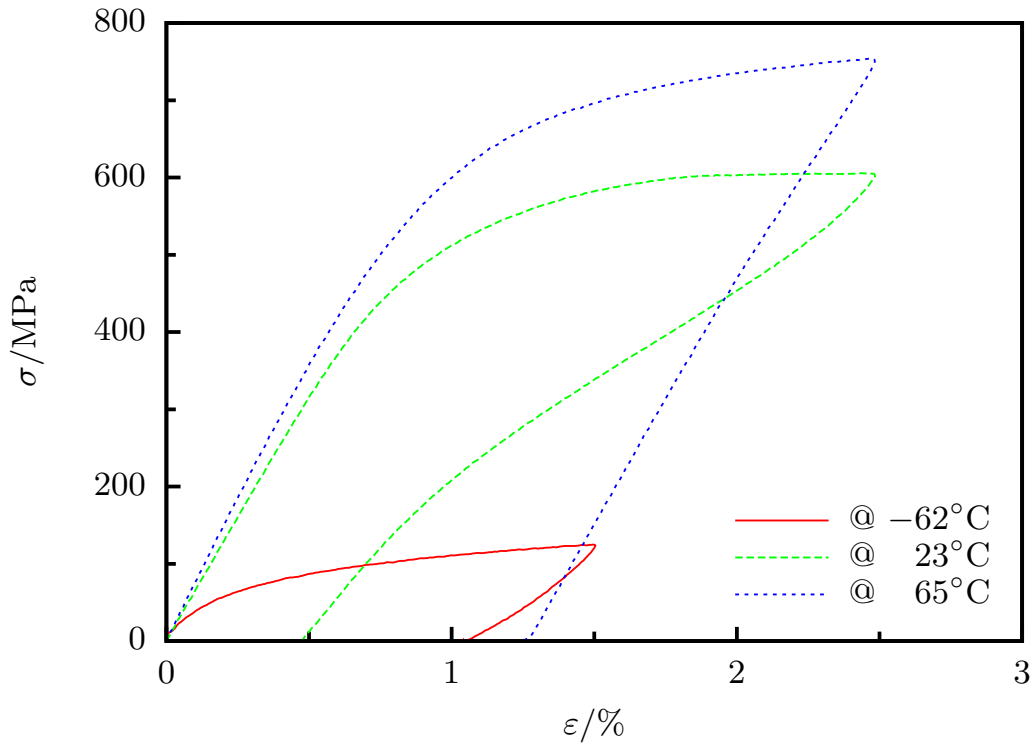


Figure 5.2: Simple tension tests of the as-received material for different start temperatures, strain rate $\dot{\epsilon} = 10^{-4} \text{ s}^{-1}$

gage section. It can be recognized that the grains are comparatively large, cf. [Sun, Q.P. & Li, Z.Q. \(2002\)](#). Nevertheless, with a grain size of approximately $150 \mu\text{m}$, considering a gage length of 20 mm, and a perimeter of 27.5 mm, one ends up with a rough estimate of 150,000 grains within the gage section. As a consequence, according to [Rogueda, C. et al. \(1996\)](#), grain size effects can be neglected.

5.2 Heating of the specimen

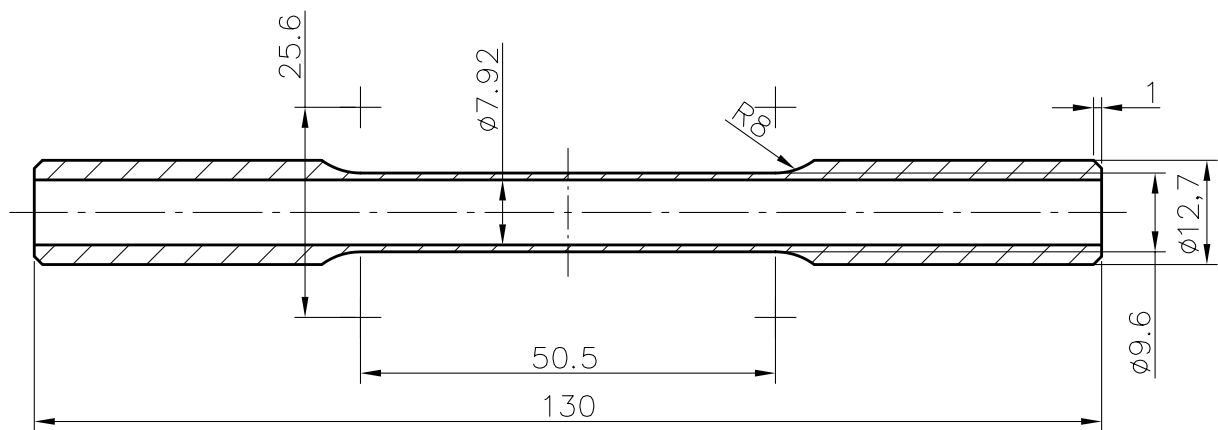
Specimen heating can be realized in numerous ways. This is depicted by Equation (5.1) showing the heat balance of an arbitrary specimen.

$$\dot{E}_{\text{st}} = \dot{Q}_{\text{cond}} + \dot{Q}_{\text{conv}} + \dot{Q}_{\text{rad}} + \dot{E}_{\text{g}} \quad (5.1)$$

Here, \dot{Q}_{cond} , \dot{Q}_{conv} , \dot{Q}_{rad} represent the heat flow resulting from conduction, convection, and radiation, respectively. Furthermore, \dot{E}_{g} stands for thermal energy generation, also known as internal heat sources, and E_{st} is the internal energy, which is to be increased in order to raise the temperature of the specimen. Consequently, a specimen can be heated using convection, conduction, radiation, or internal heat sources. Actually, most of those effects are used for heating



(a) Photograph of the specimen



(b) Engineering drawing of the specimen geometry

Figure 5.3: Specimen geometry



Figure 5.4: Polished micrograph section of the wall within the gage section, magnification of 100x

specimens. However, not all of those are appropriate for special demands. Hence, the most suitable method has to be found.

Usually, the heating of specimens is realized by inductive or resistance heating furnaces representing heating by internal heat sources and convective heating, respectively. Conceptually, the former type of furnace has certain advantages, i.e., an amount of energy can be allotted very efficiently, since no surrounding medium has to be heated. In addition to that, heat is generated at near-surface layers inside the specimen and not only at the outer surface. This results in very low radiation losses. Thus, inductive heating is very fast. Nevertheless, it has to be pointed out that inductive heating comes with high-frequency electromagnetic fields, which is unproblematic for annealing or heat treatment purposes, but which is not admissible when using highly sensible electrical sensors in the immediate vicinity. Complex shielding and measuring filters would be necessary to prevent or reduce resulting artifacts, simultaneously worsening the measuring dynamics. In respect of electrical sensors, another disadvantage of inductive heating is the direct heating of metal-based components in the same magnitude as for the specimen.

Convection heating can be subdivided into two different types. One of those uses air as a convective medium whilst the other uses a different ambient medium such as oil or water. In the first case, air is usually heated by resistance heating. Both convective methods are comparatively slow, with time constants of several decades of minutes, since heat transfer takes place just at the specimen surface. Furthermore, before the specimen is heated the temperature of the medium has to be raised, resulting in an indirect heating of the specimen. However, considering certain limitations, convective heating using e.g. oil as ambient medium is capable of realizing isothermal conditions, see [Shaw, J.A. & Kyriakides, S. \(1995\)](#).

For special applications, even radiation is used to heat up specimens. This procedure is mainly utilized in the semiconductor industry for rapid thermal processing of wafers using halogen lamps. Very high temperature rates can be realized that way because the surrounding medium is not heated. Since heat transfer takes place only at the surface, radiation heating is especially interesting when considering thin specimens. However, when shadowing effects cannot be neglected, radiation heating should not be the method of choice.

For this work, heating is realized using the ohmic loss. This method of heating is called *Joule* heating. The basic effect is as follows. As current flows through an electrical conductor, a part of the electrical energy is converted into thermal energy. The conductor gets warmer. This is due to the driven current and the conductor's resistivity,

$$\dot{E}_g = R \cdot I^2 = U \cdot I. \quad (5.2)$$

Thus, knowing the effective resistivity of the conductor, the heating power can be directly controlled by changing the driven current. In this manner, the heat is generated throughout the whole cross-sectional area. In doing so, the heating of

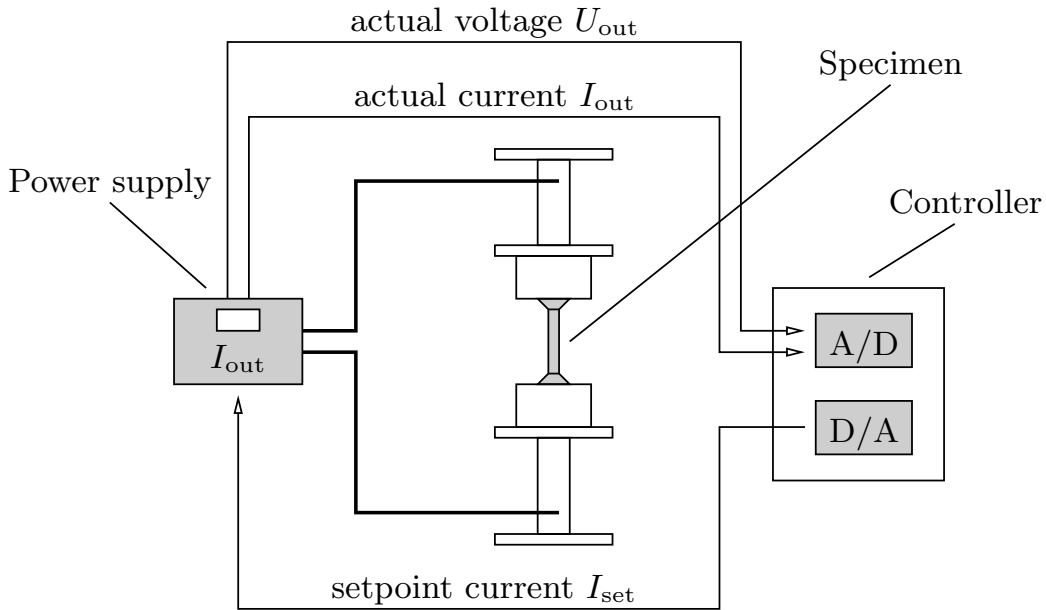


Figure 5.5: Applied heating concept

the ambient medium is just a by-product and not the means for heat transfer. In contrast to most other heating mechanisms, which are using just a small part of the specimen for heat transfer, the *Joule* heating produces heat homogeneously throughout the specimen material.

Figure 5.5 shows the applied heating concept. Here, an adjustable DC power supply is connected to the specimen. Thus, the sample can be electrically energized. A digital controller supervises and monitors the actual current and voltage of the power supply. This allows for variations in the electrical resistance of the specimen due to temperature changes during experiments. Hence, not only the current is controlled but also the heating power, which is the governing variable for temperature manipulations. A DC power supply is chosen instead of an AC power supply because of the same reasons, which ruled out the inductive heating procedure, namely high-frequency electro-magnetic fields leading to corrupted measurements due to the alternating direction of the current flow.

As a power supply two cascaded precision bench power supplies⁷ are used, which belong to the manufacturer's 3 kW-series. The maximum output voltage and current are 15 V, 200 A, respectively. For the two possible cascade configurations, this results in an effective output voltage and current of 30 V and 200 A for the serial, or 15 V and 400 A for the parallel setup, which is used in this work.

The maximum heating power is limited in all experiments to 250 W. Figure 5.6 shows the resulting heating curves for some typical values of \dot{E}_g . Furthermore, a comparison of different starting temperatures for each value of the heating power

⁷Co. Delta Elektronika BV, SM 15-200 D, ripple + noise (rms/p-p) < 100/250 mA

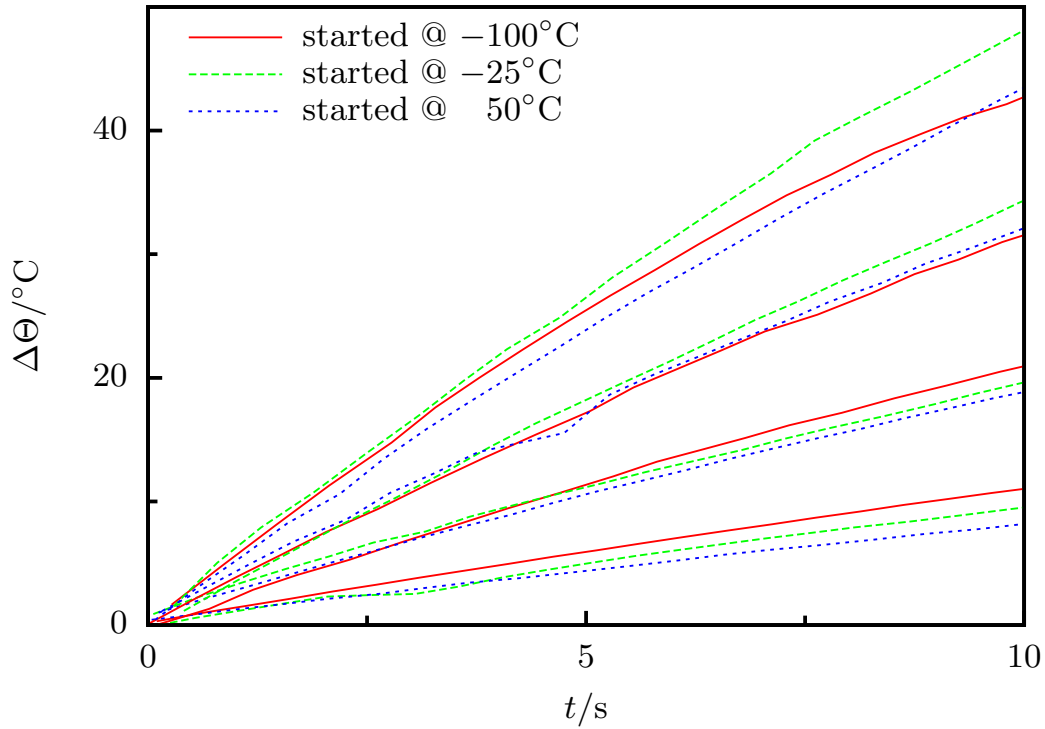


Figure 5.6: Temperature changes for heating powers \dot{E}_g of 38 W, 75 W, 113 W and 150 W, comparison for different starting temperatures

is depicted. This shows that the heating behavior is independent of the starting point. Besides, the gradients can be considered linear for the observed period of time.

With respect to the practical realization of the test rig, it has to be accounted for an effective electrical insulation from the energized parts. This means that on the one hand the drive shaft and the machine frame as on the other hand any measurement device, which is sensitive to electrical current have to be electrically decoupled. The insulation of the drive shaft and the machine frame is realized by means of *PEEK*⁸-bushings and two *PTFE*⁹-shims. Additionally, the insulation of the measurement devices is illustrated in the respective sections.

5.3 Cooling of the specimen

The temperature and the temperature distribution inside the specimen depend on several external factors. In general, heat transfer is driven by temperature gradients and temperature variations. According to [Incropera, F.P. & DeWitt,](#)

⁸Polyetheretherketone

⁹Polytetrafluorethylene

D.P. (1996); Mills, A.F. (1999), the assumption, that the specimen is gray¹⁰ and small in comparison to the surroundings, leads to the following form of Equation (5.1) in the context of specimen cooling

$$\begin{aligned}\dot{E}_{\text{st}} &= \dot{Q}_{\text{cond}} + \dot{Q}_{\text{conv}} + \dot{Q}_{\text{rad}} \\ &= \int_{\Omega} \text{div}(k \text{grad}\Theta) dV - \int_{\partial\Omega} h_c \Delta\Theta dA - \int_{\partial\Omega} h_r \Delta\Theta dA,\end{aligned}\quad (5.3)$$

with

$$\Delta\Theta = \Theta_s - \Theta_{\infty}, \quad (5.4)$$

where k is the *thermal conductivity* and Θ_s and Θ_{∞} are defined as the temperature at the surface and as the temperature of the surroundings. The coefficients h_c and h_r are called convection and radiation heat transfer coefficient, respectively. Here, h_r is strongly dependent on the temperature difference $\Delta\Theta$.

Obviously, radiation cannot be used for cooling down the specimen, since the governing parameters for h_r , namely material parameters like the thermal emissivity or the temperature of the surrounding body, are very difficult to modify. Also, the thermal conductivity k is an intrinsic parameter of the specimen material, which cannot be influenced without changing the overall material behavior. In order to increase the heat flow due to conduction, the temperature gradient $\text{grad}\Theta$ has to be increased. This leads again to a solid body cooling problem. Thus, controlled cooling of a specimen using conduction seems in this context impracticable.

In contrast, it is very easy to increase the convection heat transfer coefficient h_c in the case of forced convection. This can be achieved by applying a higher volume flow of the fluid, resulting in higher flow rates. Besides, using a different fluid also changes h_c . Furthermore, a different temperature of the fluid does not only contribute to the convective heat transfer by the temperature difference $\Delta\Theta$ but also modifies h_c .

Since cooling of a specimen can only take place at surfaces or through cross-sectional areas, forced convection is the method of choice in this work.

Figure 5.7 gives an overview of the cooling concept. Here, the volume flow is controlled via controlling the dynamic pressure by means of the *pressure system* (A), see 5.3.1. The desired temperature of the fluid is adjusted within the *heat exchanger system* (B), cf. 5.3.2. Afterwards, the cooling fluid is blown through the *nozzle system* (C) onto the gage section of the *specimen* (D). Additionally, some part of the cooling fluid is blown through an *inward fluid feed* (E) into the interior of the specimen in order to use every free surface of the specimen for heat transfer.

¹⁰ *Gray* in terms of radiation heat transfer means that the absorptivity and emissivity of the body are equal. Furthermore, the absorptivity and emissivity are independent of the wavelength of the incident and emitted radiation, respectively.

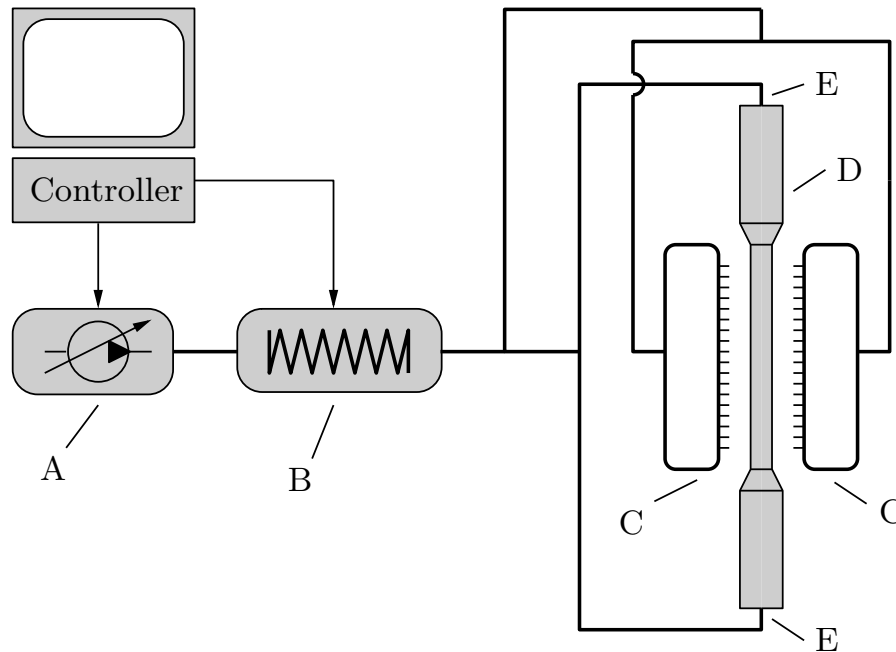


Figure 5.7: Cooling concept: A) Pressure system; B) Heat exchanger system; C) Nozzle system; D) Specimen; E) Inward fluid feed

5.3.1 Pressure system

The pressure system is used to control the volume flow of the cooling fluid. Cooled, gaseous nitrogen is chosen therefor as convective medium. It is assumed that for the pressure range of concern, 0 – 0.5 bar, a proportional relationship between the volume flow and the dynamic pressure of the fluid exists, neglecting different friction losses for different fluid velocities. Figure 5.8 illustrates the operation principles.

Compressed gaseous nitrogen is stored within a *gas bottle* (A)¹¹. At the outlet of the bottle, the nitrogen pressure is reduced and set to a specific and fixed value by the manually operated *pressure-regulation valve* (B). Subsequently, the gaseous nitrogen flows into a *storage tank* (D) where it is pressed through liquid nitrogen¹². That way, the gaseous nitrogen is cooled down. Because of the positive pressure inside the storage tank, cooled-down gasiform nitrogen is forced out of the container and streams through the *nozzle feed* (G) to the system of nozzles, cf. 5.3.3, where it is blown onto the specimen. The actual value of the internal container pressure is measured by means of a *pressure gage* (C)¹³ and supervised by a digital controller, which is connected to the gage. With the aid of *proportional valves* (E,F) at the inlet and at the outlet of the storage

¹¹The maximum pressure for the completely filled bottle is 200 bar.

¹²Due to the perpetual vaporization the liquid nitrogen is kept at a temperature of $-196\text{ }^{\circ}\text{C}$.

¹³Co. American Sensor Technologies, Inc., AST4000, pressure range 0-25 psi, analog output 1-6 V

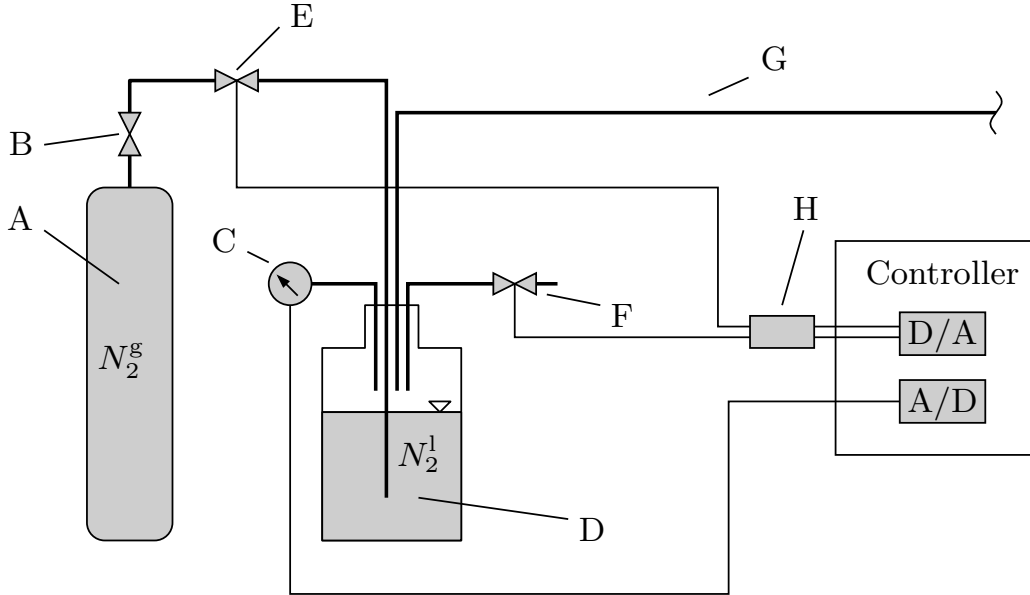


Figure 5.8: Pressure system: A) Supply bottle, N_2^g ; B) Pressure-regulation valve, 0 – 10 bar; C) Pressure gage, 0 – 0.5 bar; D) Storage tank N_2^l ; E) Proportional inlet valve, 0 – 100 %; F) Proportional outlet valve, 0 – 100 %; G) nozzle feed; H) I/O valve control module

tank, the pressure inside the container can be digitally controlled. In doing so, a classical closed loop control can be implemented, which shows a nice control behavior even for a simple PI-algorithm¹⁴. This is particularly advantageous, since a PI-controller can be tuned very easily.

For the implementation of the digital controller a positional algorithm is used,

$$u(k) = K_p \left(e(k) + K_i \sum_{i=1}^k \frac{e(i) - e(i-1)}{2} \Delta t \right), \quad (5.5)$$

with K_p , K_i , $u(k)$ and $e(k)$ being the proportional gain, integral gain and the time discrete values for the controller output and the error between setpoint and process variable, see [Unbehauen, H \(1997\)](#); [Isermann \(1988\)](#).

5.3.2 Heat exchanger

As mentioned earlier, the heat exchanger is used to keep the fluid temperature at the specimen at a desired setpoint. This is mainly necessary in conjunction

¹⁴Proportional-Integral control algorithm, see equation below: The controller output is calculated from the error and the integral of the error, realizing zero offset behavior.

$$u(t) = K_p \left(e(t) + K_i \int_0^t e(t) dt \right)$$

Here, $u(t)$, $e(t)$, K_p and K_i represent controller output, error/difference between setpoint and process variable, proportional and integral gain, respectively.

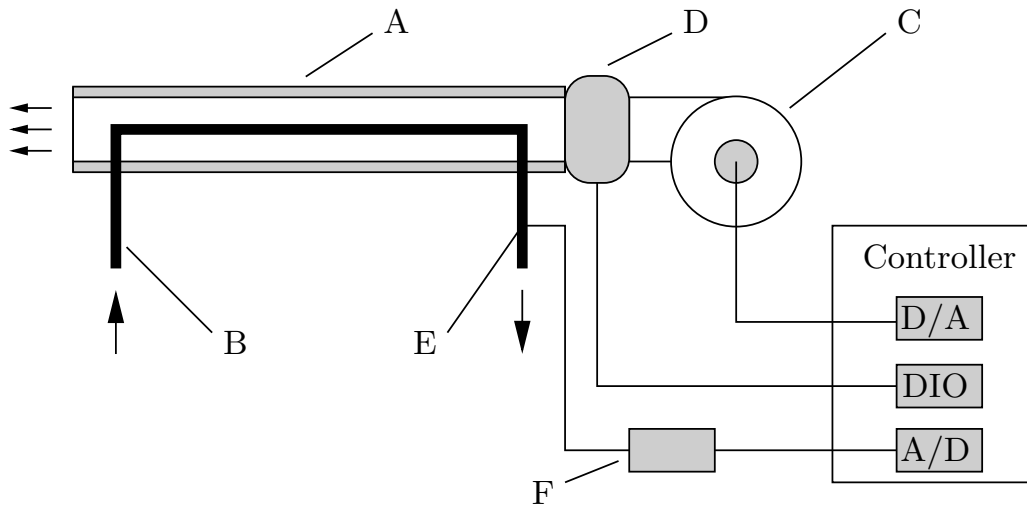


Figure 5.9: Heat exchanger system: A) Exchanger tubing; B) N_2 tubing; C) Radial blower; D) Heating wire element; E) Outlet thermocouple; F) Measuring amplifier

with long-lasting experiments, since without active control, a temperature balancing between the cooling fluid and the tubing takes place leading to a creeping decrease of the fluid temperature at the nozzles. In turn, this results in a change of the temperature conditions at the specimen worsening the interpretability of the conducted experiments and the control behavior.

To circumvent this difficulty, a heat exchanger system is designed, which allows for long-lasting experiments without any significant change in the temperature of the cooling fluid.

Figure 5.9 shows a sketch of the applied heat exchanger concept. Here, the cooling medium temperature can only be raised. Thus, the heat exchanger is just used for heating the cooling fluid. There is no need for further cooling of the fluid within the exchanger device, since supercooled nitrogen is already utilized for the cooling concept.

The described system consists of the exchanger itself, a heating wire element, a blower, two *type K* thermocouples¹⁵¹⁶, and a digital controller. Two tubes with different diameters form the exchanger which is designed as a concentric tube heat exchanger. It is operated in counterflow mode in order to maximize the heat exchanger effectiveness, see Incropera, F.P. & DeWitt, D.P. (1996). The cooling medium streams through the *smaller-diameter-tube* whereas warm air is blown through the surrounding *larger-diameter-tube*. The large tube is thermally insulated at the outer surface to prevent any heat losses apart from

¹⁵Co. Conatex, TM12K02GG2, wire diameter 0.2 mm, class 1 according to DIN 43722 (1994)

¹⁶Co. Omega Engineering, Inc., IEC-TFCY-003/IEC-TFAL-003, wire diameter 0.08 mm, class 1 according to DIN 43722 (1994)

the heat transfer between the two tubes. By means of the heating wire element¹⁷ the temperature of the warm air can be raised. 16 different heating stages can be digitally addressed by the controller. It can be shown that the number of 16 stages is sufficient for changing the temperature of the nitrogen smoothly.

The volume flow of the warm air is produced by a radial blower¹⁸, which is connected to the 16 bit D/A converter board¹⁹ of the digital controller. Thus, the fan speed can be adjusted between standstill and maximum speed almost continuously. Nevertheless, for the applied temperature control of the cooling fluid, the fan is driven with the highest possible speed.

The two *type K* thermocouples are installed inside the nitrogen tube at two different locations, one of which is at the outlet of the heat exchanger and the other at the inlet of the nozzle system. Due to the extremely small dimensions of the sensors, changes of the temperature of the surrounding medium are detected almost instantaneously.

This system is operated by two cascaded digital PI-controllers, see 5.3.1 for the general implementation of the simple PI-control algorithm. The inner, fast control loop controls the temperature at the outlet of the heat exchanger. The controller output determines the stage of the heating wire element. The setpoint temperature at the outlet of the heat exchanger is governed by the superordinate, outer controller. Its process variable is the cooling medium temperature at the nozzles. Because of the applied setup, it can be accounted for the large dead time within the system and hence, large overshoots are inhibited and the overall control behavior is improved. As a consequence, the temperature of the cooling medium is kept within a range of 2 K around the setpoint.

5.3.3 Nozzle system

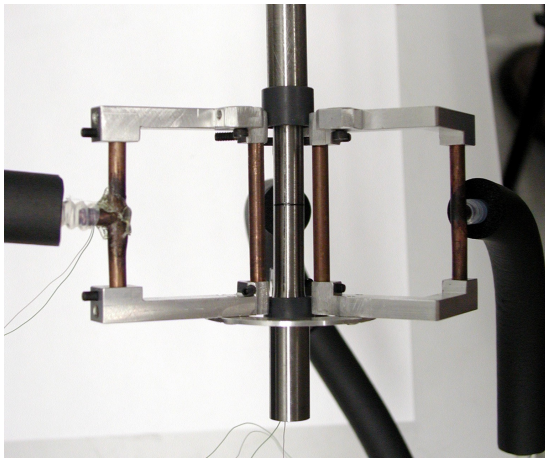
In this section, the inward fluid feed and the nozzle system, which spreads gasiform nitrogen onto the outer surface of the specimen's gage section are specified.

The nozzle system consists of three identical, perforated, tubular copper nozzles, which are arranged equally around the specimen, resulting in an angular shift of 120° between each of the nozzles. The nozzles and the supply tubing are designed to allow for sufficient space for the deformation and distortion measurement devices described later, see Section 5.8. The nozzle system and the hole pattern are depicted by the photography shown in Figure 5.10. In order to achieve an optimal nitrogen covering of the gage section, the pattern and the size of the holes are specifically chosen. It can be seen that in every other row two holes are situated, which are offset from the middle line. That way, the nitrogen exhalation region is widened at both sides of the nozzle.

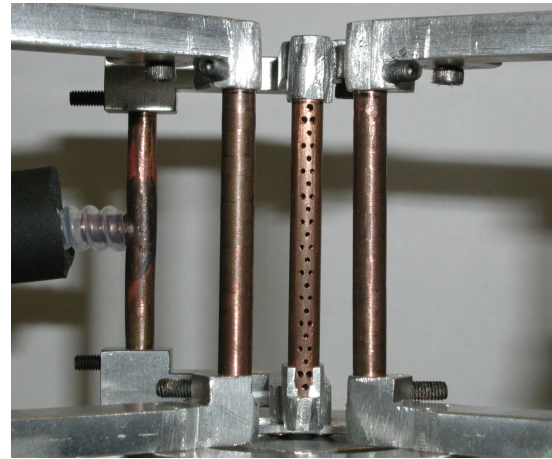
¹⁷Co. Steinel GmbH, HL1810S, $\Theta_{max} = 600^\circ\text{C}$ at $\dot{V} = 500 \text{ l/min}$

¹⁸Co. Micronel AG, U97EM-012KK-3, speed 10650 r.p.m., air flow rate 575 l/min

¹⁹Co. Meilhaus Electronic GmbH, ME-4670i, galvanically isolated, 500kHz/16bit A/D-conversion



(a) General view of the nozzle system mounted on specimen



(b) Magnified view of the nozzle system and nozzle hole pattern

Figure 5.10: Nozzle system

Since a large part of the free surface area, namely the interior of the specimen, cannot be cooled down using the copper nozzles, nitrogen has to be supplied to the interior using an additional supply line. Herein, this is called *inward fluid feed*. However, in the same amount as cooling fluid is supplied to the inside of the specimen, nitrogen has to be drained to avoid overpressure. Furthermore, the supply and drain setup has to be symmetrical in favor of an optimal temperature field. Altogether, this leads to the special design of the clamping core shown in the drawing in Figure 5.11.

5.4 Temperature measurement

In this work, temperature measurements are conducted using thermocouples. The working principle is the thermoelectric (*Seebeck*) effect, meaning that an electromotive force (EMF) is generated due to the temperature difference between two junctions of two conductors of different material or alloy, which are part of the same electronic circuit, [DIN EN 60584-2 \(1994\)](#).

Consequently, when an electrical conductor is exposed to a temperature gradient, it will generate an electric voltage. There, the value of the voltage strongly depends on the material of the conductor. In order to measure the voltage, the electronic circuit has to be completed. This is done by means of a second conductor. Likewise, this conductor is subjected to the same temperature gradient as the other one, leading to a measured voltage of 0 V, if both conductors are of the same material. This results from the fact that at locations with equal temperatures two conductors of the same material exhibit identical electrical potentials. Consequently, a pair of wires is chosen so that the measurable voltage is maximized. Thus, knowing the type of the pairing and knowing the voltage,

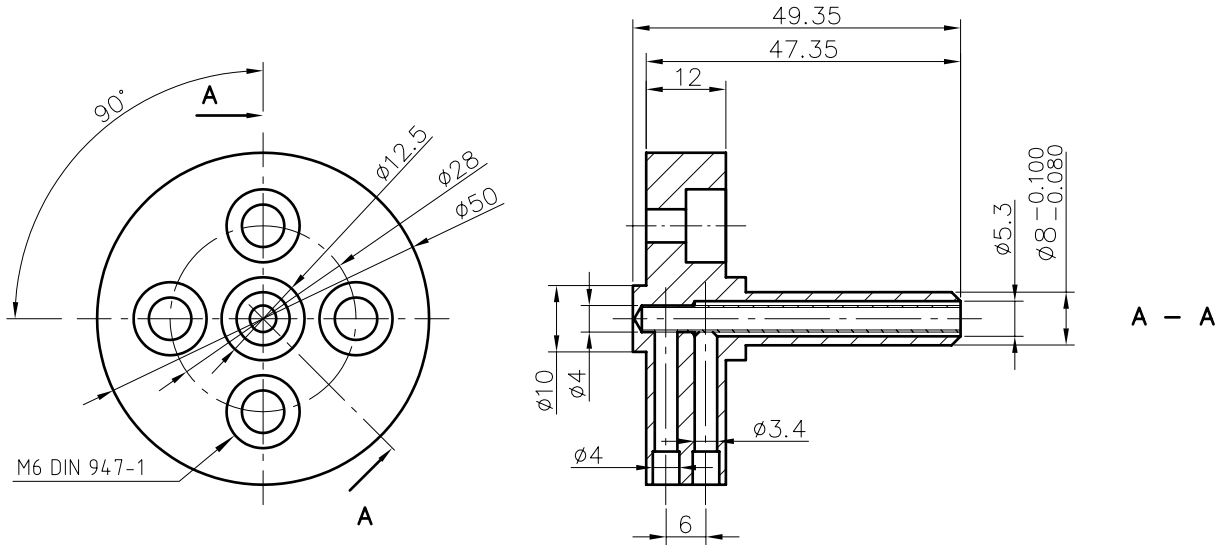


Figure 5.11: Inward fluid feed

the temperature gradient can be calculated.

As usually not the temperature gradient itself but the absolute value of the temperature is to be measured, one junction, the *cold junction*, of the thermocouple has to be kept at a constant temperature, known as the reference temperature. Often, in temperature measuring amplifiers this cold junction is simulated by electrical, temperature sensitive components. Then, this electronic circuit is called *cold junction compensation*.

In what follows, *type K* thermocouples are used for all applications. These are composed of a Chromel²⁰ and an Alumel²¹ wire. They are widely used because of their large temperature range²² and the moderate costs. Nevertheless, one has to take into account the comparatively low accuracy of thermocouples²³. However, several advantages let thermocouples outperform other standard temperature measuring devices for the described applications of concern.

The objective of the temperature measurement is to measure the temperature at each location within the gage length, inside and outside. Naturally, a thermo-optical procedure seems to be the first choice. On the other hand, a thermocamera, for example, can only be used if it has an unobstructed view onto the specimen. This cannot be guaranteed as a cold nitrogen exhalation is used for the cooling, a thick, small window²⁴ is situated between camera and specimen, and the specimen itself is shadowed by large parts of the deformation measuring device. *PT100*- and *resistance*-thermometers, whereas more accurate, are also rejected due to the limited available space.

²⁰Ni-Cr alloy

²¹Ni-Al alloy

²²-200°C to +1200°C according to [DIN EN 60584-2 \(1994\)](#)

²³±1.5°C between -40°C and +375°C according to [DIN EN 60584-2 \(1994\)](#)

²⁴Additionally, a temperature chamber is used, see [5.5.2](#)

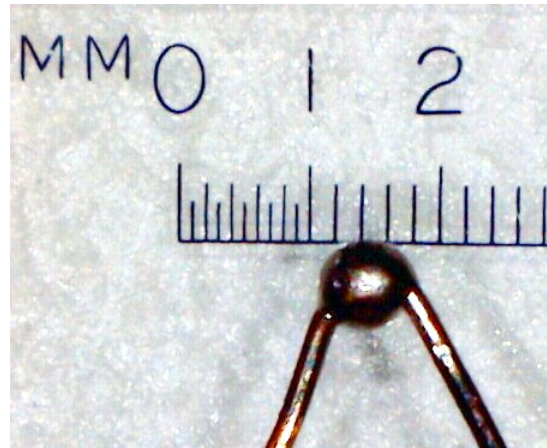


Figure 5.12: Thermocouple bead

Due to the desired high local resolution of the temperature measurements, multiple temperature sensors have to be utilized. Two different sets of type K thermocouples are used^{25,26}. As a matter of fact, many different techniques concerning the mode of thermal connection between sensor and specimen exist. Furthermore, the shape and the type of the junction of the two thermo wires is crucial. Thorough studies have been conducted by [Körtvélyessy, L. \(1998\)](#). Besides, [Vogelsang, H. \(2001\)](#) reported a new and very efficient way of using type K thermocouples with high accuracy.

It was shown that the frequently used twisting of the two thermo wires to create the measuring tip, after being attached to the specimen, leads to a virtual measuring point, which does not lie on the surface of the specimen, thus, resulting in a faulty measuring of the temperatures. Moreover, when a current is driven in order to energize and heat up the specimen, step voltages might occur at the thermocouples due to the not exactly defined contact points with the specimen. Corrupted measurements and hence, unstable control behavior are the probable consequences.

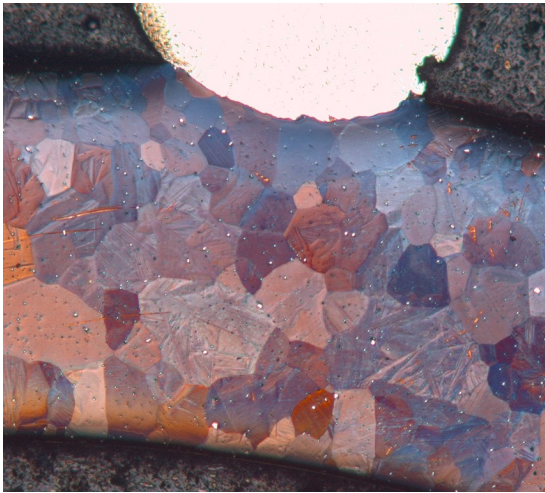
As a matter of fact, [Vogelsang, H. \(2001\)](#) presented a new way to create significantly improved thermocouple junctions, see [Figure 5.12](#). After a well-defined twisting²⁷, the junction of the two wires is arc welded within an argon atmosphere to an almost perfect sphere.

Thermal contact is most frequently realized by gluing or clamping the sensor onto the specimen. The disadvantage of gluing is the comparatively poor thermal contact resulting in slow measurements. Also clamping is not the appropriate choice for the experiments within this work, since an additional clamping device

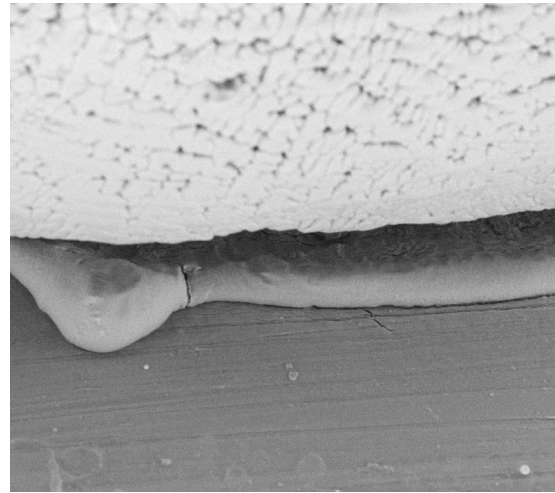
²⁵Co. Conatex, TM12K02GG2, wire diameter 0.2 mm, class 1 according to [DIN 43722 \(1994\)](#)

²⁶Co. Omega Engineering, Inc., IEC-TFCY-005/IEC-TFAL-005, wire diameter 0.13 mm, class 1 according to [DIN 43722 \(1994\)](#)

²⁷The twisted portion has to contain always the same amount of material.



(a) Polished micrograph section, magnification of 100x



(b) SEM picture, magnification of 500x

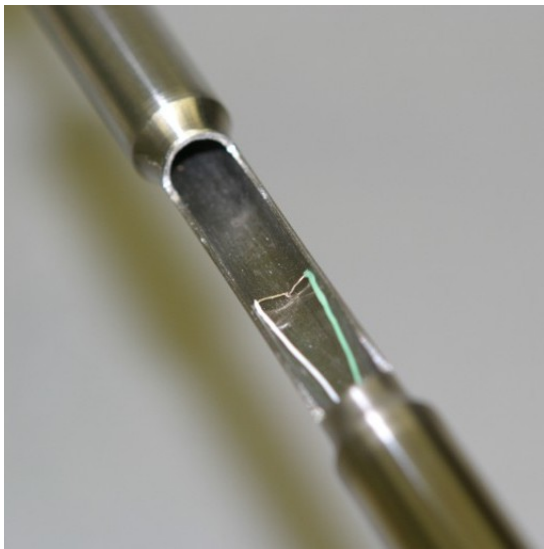
Figure 5.13: Thermocouple (top) / specimen (bottom) join patch

would be required, which consumes additional space being unavailable.

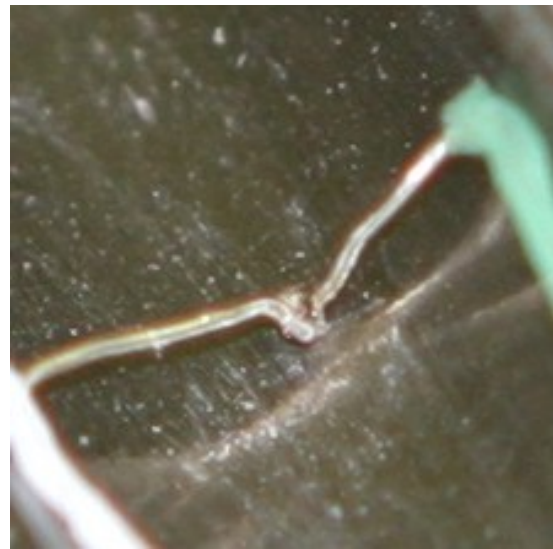
In order to circumvent those complications, the thermocouples are welded onto the specimens using the single-pulse welding procedure presented and discussed in detail in [Vogelsang, H. \(2001\)](#). Typical join patches are shown in [Figure 5.13](#). It can be observed that the microstructure of the specimen is not altered due to the welding process. The reason is the very small heat affected zone. The welding setup was improved and modified to achieve an even higher accuracy and repeatability. Furthermore, a new device was added so that thermocouples can be welded actually onto the inner surface of the specimen.

Seven thermocouples are applied onto the outer and one additional thermocouple onto the inner surface of the specimen within the gage length. For the inner thermocouple, the aforementioned small diameter thermo wires are used. [Figure 5.14](#) shows a picture of the inner thermocouple.

The main reason for using these small cross-sectional area wires is that the wires have to be transferred out of the inside of the specimen. The only possible way of doing so, is to use the already limited cross-sectional area of the supply, drain lines of the inward fluid feed, respectively, which explains the need for reducing the cross section of the wires themselves, cf. [5.3.3](#). Though it seems appropriate to lead each of the two thermo wires through a different inward feed, in order to block as few as possible of the draining nitrogen, unfortunately, this turns out to be impracticable. The reason is that the electromagnetic field, generated by the heating of the specimen, induces measuring artifacts when the two thermo wires are led through different inward feeds. Drawing attention to the arrangement of the thermocouples, the application pattern is depicted in [Figure 5.15](#).



(a) General view of a showcase specimen whose gage section is opened in order to allow an unobstructed view of the inner thermocouple



(b) Magnified view of the inner thermocouple

Figure 5.14: Inner thermocouple

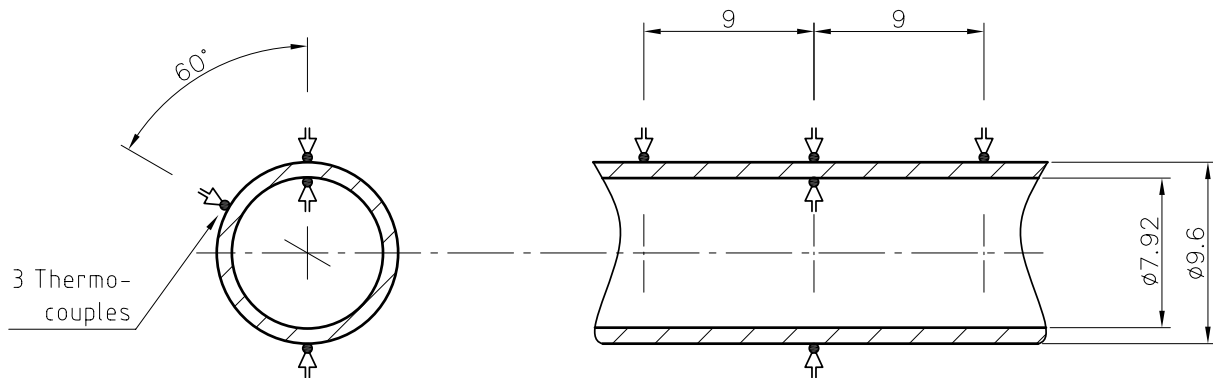


Figure 5.15: Arrangement of the thermocouples

Two multiple channel thermocouple measuring amplifiers²⁸ are used for the temperature measurements. Cold junction compensation and calculation of the temperature values are realized within this digital device.

²⁸Co. Hottinger Baldwin Messtechnik GmbH, 2xML801/AP409, galvanically isolated, being part of the digital amplifier system MGCplus

5.5 Temperature control

5.5.1 Calculation of the mean temperature

As the temperature field is measured at eight different locations and as it is not possible to change the temperature at each location independently, a mean temperature has to be calculated. This may be done in numerous ways e.g. in the simplest form by using the arithmetic average. Nevertheless, an algorithm, which incorporates the spacing and the local arrangement, seems more promising.

The temperature has to be averaged in three directions. That are the longitudinal, circumferential, and thickness direction. Averaging in longitudinal direction leads to

$$\bar{\Theta} = \sum_{\alpha=1}^3 a_{\alpha} \bar{\Theta}_{\alpha}, \quad (5.6)$$

with $\bar{\Theta}$ and $\bar{\Theta}_{\alpha}$ being the overall and circumferential mean temperatures, respectively. Here, $\alpha = 1, 2, 3$ denote the top, middle, and bottom values of the in circumference direction already averaged temperatures. These circumferential mean values are calculated using

$$\bar{\Theta}_{\alpha} = \sum_{\beta=1}^3 b_{\beta} \bar{\Theta}_{\alpha\beta}, \quad (5.7)$$

where the averaged temperature at longitudinal position α and circumferential position β , with $\beta = 1, 2, 3$ representing the circumference positions at $0^{\circ}, 60^{\circ}, 180^{\circ}$, is given by $\bar{\Theta}_{\alpha\beta}$. Since the wall thickness within the gage length is relatively small, cf. Figure 5.3, and a rough calculation of the heat diffusion equation shows that the temperature developing is almost linear, averaging in thickness direction is realized by simply taking the arithmetic average of the inside and outside temperatures

$$\bar{\Theta}_{\alpha\beta} = \frac{1}{2} (\Theta_{\alpha\beta_{\text{out}}} + \Theta_{\alpha\beta_{\text{in}}}). \quad (5.8)$$

Now, assuming that the temperature difference between inside and outside $\Delta\Theta_{\alpha\beta_t}$ is constant throughout the whole gage section, the equation for $\Theta_{\alpha\beta_{\text{in}}}$ reads

$$\Theta_{\alpha\beta_{\text{in}}} = \Theta_{\alpha\beta_{\text{out}}} + \Delta\Theta_t \quad \text{with} \quad \Delta\Theta_t = \Theta_{\text{mid}0^{\circ}_{\text{in}}} - \Theta_{\text{mid}0^{\circ}_{\text{out}}}. \quad (5.9)$$

Additionally, the temperature difference between circumference position $\beta = 60^{\circ}$ and $\beta = 180^{\circ}$ is supposed to be constant for each longitudinal position, thus, resulting in

$$\bar{\Theta}_{\alpha 180^{\circ}} = \bar{\Theta}_{\alpha 60^{\circ}} + \Delta\Theta_{\alpha 180^{\circ}} \quad \text{with} \quad \Delta\Theta_{\alpha 180^{\circ}} = \Theta_{\text{mid}180^{\circ}} - \Theta_{\text{mid}60^{\circ}}. \quad (5.10)$$

As the three nozzles are equally distributed around the specimen, a 120° spacing is evident. Presuming that all temperature conditions apart from the position

of the nozzles are equal for all circumference positions, it is reasonable to set the weighting factors b_β to

$$\begin{aligned} b_{0^\circ} &= 0.50 \\ b_{60^\circ} &= 0.25 \\ b_{180^\circ} &= 0.25. \end{aligned} \tag{5.11}$$

Hence, the arithmetic average between positions *facing* and *between* two nozzles is calculated.

The values for the weighting factors a_α follow from the longitudinal spacing of the thermocouples

$$\begin{aligned} a_{\text{top}} &= 0.275 \\ a_{\text{mid}} &= 0.450 \\ a_{\text{bottom}} &= 0.275. \end{aligned} \tag{5.12}$$

Thereupon, Equation (5.6) yields for the overall mean temperature

$$\begin{aligned} \bar{\Theta} &= +0.1375 \cdot \Theta_{\text{top}0^\circ_{\text{out}}} - 0.275 \cdot \Theta_{\text{mid}0^\circ_{\text{out}}} + 0.1375 \cdot \Theta_{\text{bottom}0^\circ_{\text{out}}} \\ &\quad + 0.1375 \cdot \Theta_{\text{top}60^\circ_{\text{out}}} - 0.025 \cdot \Theta_{\text{mid}60^\circ_{\text{out}}} + 0.1375 \cdot \Theta_{\text{bottom}60^\circ_{\text{out}}} \\ &\quad + 0.25 \cdot \Theta_{\text{mid}180^\circ_{\text{out}}} + 0.5 \cdot \Theta_{\text{mid}0^\circ_{\text{in}}}. \end{aligned} \tag{5.13}$$

5.5.2 Temperature chamber

In addition to the fast and direct heating and cooling approaches already described in this chapter, a temperature chamber²⁹ is used to control the temperature of the whole setup including the clamping and the deformation measuring devices, see Figure 5.16. In so doing, the surrounding temperature of the specimen can be varied and set to a particular value. Naturally, the temperature chamber is comparatively slow. Hence, it is used to shift the starting or base temperatures for certain experiments. Also, it can be used if the time constant for temperature changes is not critical and if it is desired to guarantee almost no temperature gradients within the specimen resulting from the bulky steel clamping shown in Figure 5.20.

5.5.3 Temperature control algorithm/procedure

As already mentioned in Paragraph 5.5.2, the temperature chamber is used to realize the baseline temperature. In addition to that, heating by the ohmic loss described in detail in Section 5.2 and cooling by exhaling cold nitrogen, see 5.3, is used for fast and local temperature control.

²⁹Co. Fresenberger, TK 18.400.100, temperature range -100°C to $+400^\circ\text{C}$, heating/cooling rates for empty chamber: $+20^\circ\text{C}$ to $+400^\circ\text{C}$ in 22 min, $+20^\circ\text{C}$ to -100°C in 10 min

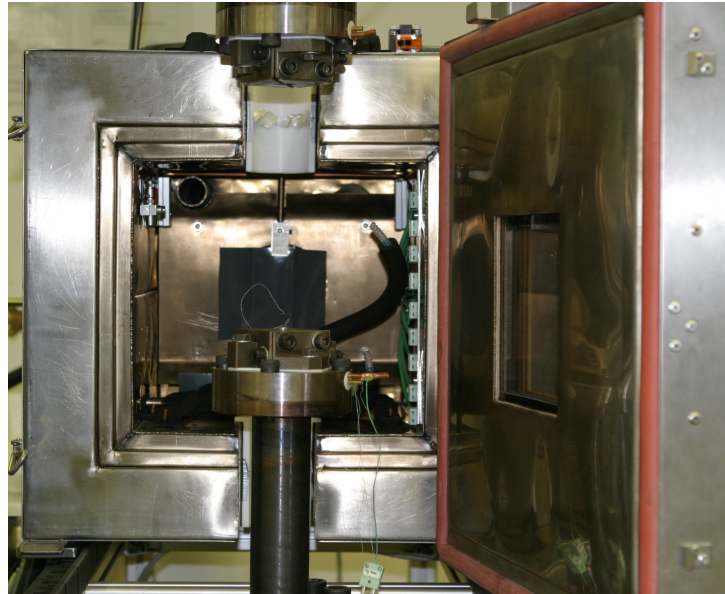


Figure 5.16: Temperature chamber

Now, the task is as follows. One parameter, which is temperature, is to be controlled and four parameters, which are heating power, volume flow, and temperature of nitrogen, and setpoint temperature of the temperature chamber, can be adjusted. In this regard, a theoretically possible though adverse control scheme with one single control and multiple output variables is avoided, since it tends to exhibit an unstable control behavior. By contrast, it proves successful to set the nitrogen volume flow and the nitrogen temperature to predefined, fixed levels so that only the heating power is subject to adjustment in order to realize the projected temperature control.

Again, a simple PI-algorithm is sufficient for achieving a very good control performance as well for disturbance reaction as for reference action. In this context, Figure 5.17 shows two averaged temperature progressions for two similar but, according to the thermal conditions, significantly different simple tension tests, as one experiment is carried out with active temperature control whereas for the other case the temperature of the specimen is not manipulated at all. Here, only a basic setup with four independent thermocouples is used whose measured temperatures are averaged accordingly. The high frequency oscillations, which can be observed at the temperature curve for the case with enabled temperature control, originate from the aggressive tuning of the control algorithm. This is necessary as to guarantee a good disturbance behavior of the applied control scheme so that disturbances are immediately compensated.

In order to evaluate the overall control performance, also the individual temperature readings are shown, Figure 5.18. Here, it can be seen that, naturally, because of the heterogeneous transformation behavior of the specimen material, the experiment cannot be performed in a locally isothermal way. If this was re-

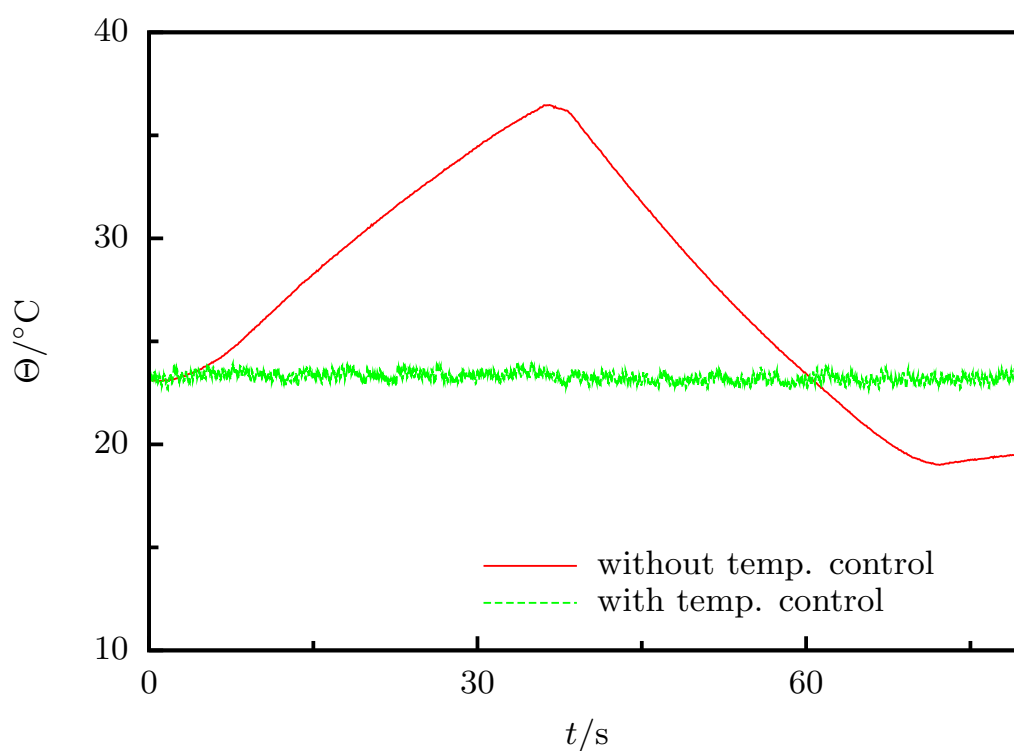


Figure 5.17: Two identical tension tests, with and without temperature control

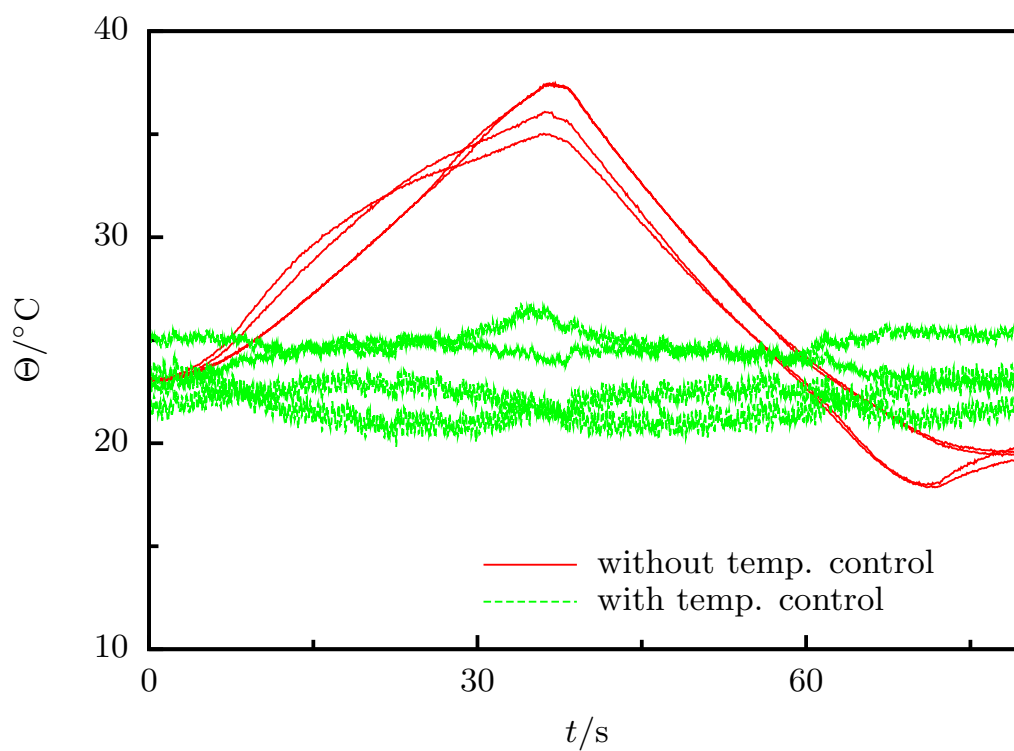


Figure 5.18: Two identical tension tests, with and without temperature control, the readings of four thermocouples are given without averaging

quired, a locally infinitely high resolution heating and cooling procedure would be necessary, which proves infeasible due to heat flow effects, space limitations etc. Nevertheless, it remains subject of further examination to what degree the realized macroscopically isothermal conditions imply effectively isothermal conditions for the performed experiments, see Chapter 6.

5.6 Mechanical loading

A sketch of the mechanical loading setup is shown in Figure 5.19. The core of the mechanical experimental rig is the electromechanical tension/torsion testing machine³⁰. It consists of a mechanical loading frame³¹ (A), an analog machine control (C), and a loading cell³² (B). The maximal loading in axial, torsional direction is ± 50 kN, ± 300 Nm, respectively. Furthermore, traverse paths up to 1500 mm from peak to peak are generally possible, even though some restrictions exist for the applied setup due to the height of the temperature chamber (L). In rotary direction, no limitations are present so that the maximum allowable torque can be realized for angles $\alpha = \pm\infty^\circ$. This is due to the drive concept of the machine.

As mentioned above, the testing machine is electromechanically driven, i.e., two braced spindles, moving the crosshead, are driven by an electric motor with disc-shaped rotor. Consequently, the natural control mode of the machine is displacement rate control. By contrast, the commonly used servo-hydraulic testing machines are intrinsically force-controlled.

The second control axis is driven by a similar motor. Again, two drive shafts are braced in order to minimize the reversal clearance. Via a form-closed connected rotary disc a specimen can be loaded in torsional direction.

The machine can be operated in two ways, manually and programmatically. Hence, preparing an experiment can be realized by using the manual control of the machine while for the actual experiment an afore coded program is executed. The digital governing of the analog control is implemented by means of a freely configurable control system³³, which is connected to a PC. A parallel IEEE-488 digital communications bus is used for the connection between PC and digital machine control. Through a freely programmable software front-end, more complex control paths are possible than with the analog curve generator, which is part of the analog machine control.

Besides displacement rate control, additional control modes are possible utilizing a cascaded control scheme, [Unbehauen, H. \(1997\)](#). Force, torque and displacement (rate), rotation (rate) control, respectively, are already hard-wired configured within the analog machine control. The actual value is measured

³⁰Co. Schenck Trebel GmbH, RM 50

³¹Co. Schenck Trebel GmbH, RME

³²Co. Lebow Products, Inc., 6467-110, $F_{max} = 50$ kN, Nonlinearity $< 0.01\%$, $M_{max} = 300$ Nm, Nonlinearity $< 0.05\%$

³³Co. HuDe Datenmesstechnik GmbH, Interfacer 4

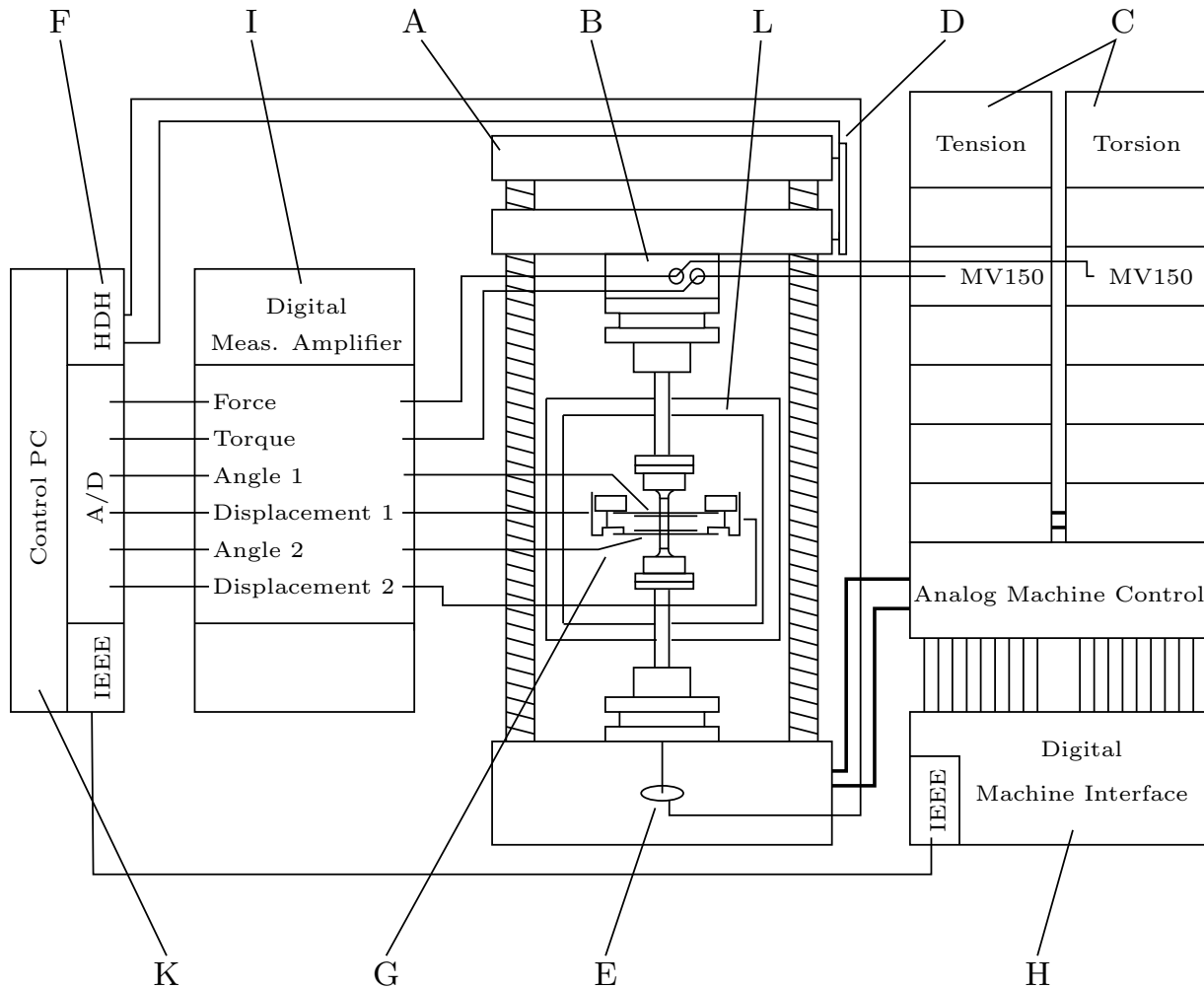


Figure 5.19: Mechanical loading setup: A) Machine frame; B) Tension/Torsion load cell; C) Analog machine control; D) Incremental linear encoder; E) Incremental angle encoder; F) PC counter card; G) Deformation measuring system; H) Digital machine interface; I) Digital, modular measuring amplifier; K) Control PC; L) Temperature chamber

by the load cell (B) or internal potentiometric transducers for displacement or angle. Furthermore, displacement and angle can be measured very accurately using additionally integrated incremental encoders³⁴ (D,E) and a PC counter card³⁵ (F). However, in so doing, an analog signal is not generated, which could be used within the control loop. Nevertheless, the two incremental devices are used for supervision purposes in order to have a certain degree of redundancy within the system so that in cases of breakdown or malfunction of the primary transducers the system can be halted. Furthermore, the calibration of inductive

³⁴Co. Dr. Johannes Heidenhain GmbH,
 Angle: RON 255, line count 18000, measuring step 0.001° , system accuracy $\pm 5''$
 Displacement: ULS 300, grating period $20 \mu\text{m}$, measuring step $0.5 \mu\text{m}$, system accuracy $0.5 \mu\text{m}$

³⁵Co. Dr. Johannes Heidenhain GmbH, IK 220

or strain gage based displacement measuring devices is carried out utilizing these highly linear and accurate encoders.

In addition to the hard-wired measuring transducers other sensors can be used for the machine control, too. For the integration of other measuring devices the actual measuring signal has to be converted or amplified to an analog signal in the range of ± 10 V, which serves as input for the analog control loop^{36,37}. The amplification of the measuring signal is performed by a modular digital 24 bit measuring amplifier³⁸ (I). Moreover, the measurement data of all connected sensors is provided by the amplifier through different digital interfaces like IEEE-488 and RS232 so that the data can be stored or further processed by PCs.

By using this alternative approach, the deformation measuring system (G) presented in Section 5.8 can be integrated into the analog control loop, thus, resulting in a control of engineering strain in axial and torsional direction.

5.6.1 Measuring of stress

Since the lateral deformation cannot be measured, see Section 5.8 for a detailed explanation thereof, only engineering stress is used in the context of experimental observations within this work. Consequently the measuring of stress reduces to a measuring of axial force F and torque M_t using the aforementioned load cell. Finally, the governing equations for axial and shearing stress (σ , τ) as a consequence of axial force and torque read

$$\sigma = \frac{F}{A} \quad (5.14)$$

and

$$\tau = M_t \frac{16 d_o}{\pi (d_o^4 - d_i^4)}, \quad (5.15)$$

with A , d_i , and d_o respectively representing the cross-sectional area, inner and outer diameter of the specimen.

5.7 Clamping of the specimen

A four-jaw clamping device depicted in Figure 5.20 is constructed so that the clamping forces are equally distributed and well-repeatable. In order to prevent the specimen from buckling within the clamping region, reusable clamping mandrels are used, which are already shown in Figure 5.11 and which additionally serve as inward fluid feed.

³⁶Co. Schenck Trebel, MV 150, accuracy class 0.05

³⁷Co. Schenck Trebel, MV 154

³⁸Co. Hottinger Baldwin Messtechnik GmbH, MGCplus, accuracy class 0.03, max. sample rate 19.2 kHz, 24 bit A/D converter for each measuring channel

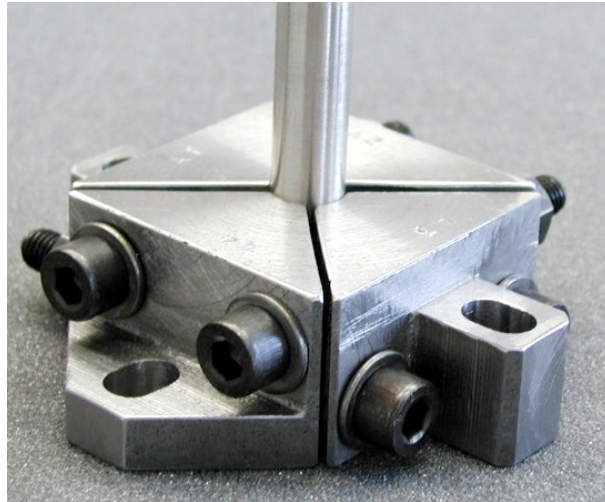


Figure 5.20: Photograph of the clamping device

The clamping devices are fixed to the machine by screws, which are guided by slotted holes so that during the mounting process the clamping devices are free to move in lateral direction with respect to the specimen axis and bending moments on the specimen due to a possible misalignment are minimized.

PTFE³⁹-panels are used to implement some thermal decoupling between the clamping device and the machine flange.

5.8 Strain measuring

Whenever referring to experiments or experimental data in this work, engineering strain is used. This is due to the fact that the measuring of the lateral deformation is quite crucial for a tubular specimen because of the mandatory measurement of the deformation at the inner surface. Additionally, boundary effects cannot be neglected. Thus, the lateral deformation is not necessarily and most unlikely uniform throughout the gage section. As a consequence, a local high-resolution procedure such as the laser speckle interferometry or other optical techniques would have to be chosen, lacking in most cases the ability to generate analog signals, which could be used as input for the control of the testing machine. Furthermore, the exhalation of cold nitrogen resulting in local density gradients and the window of the temperature chamber interfere with optical methods. Hence, for now, direct strain control cannot be realized for true strain within the shown experimental concept.

Consequently, the problem of strain measuring reduces to the measuring of axial displacement and angle, i.e.,

$$\varepsilon = \frac{\Delta l}{l} \quad (5.16)$$

³⁹Polytetrafluorethylene

and

$$\gamma = \frac{\Delta\varphi r}{l}, \quad (5.17)$$

with Δl and $\Delta\varphi$ being elongation and twist. r and l denote the effective radius and initial gage length of the specimen.

Moreover, only a local measuring of displacement and angle guarantees a good quality and interpretability of experimental data. This is in sharp contrast to the measurement of displacement and angle of the crosshead and rotary disk of the testing machine, respectively.

Several standard procedures exist for the task of strain/displacement measuring, some of which are for instance strain gauges, extensometers or the already ruled-out optical techniques. Table 5.1 gives a short overview of the requirements for the desired strain measurement system.

Temperature range	:	$-100^{\circ}\text{C} < \Theta < +100^{\circ}\text{C}$
Gage length	:	$l_0 = 20 \text{ mm}$
Maximum strain	:	$\varepsilon_{\max} = \gamma'_{\max}{}^{40} = 10\%$
Axial range	:	$-2 \text{ mm} < \Delta l < +2 \text{ mm}$
Torsional range	:	$-45^{\circ} < \Delta\varphi < +45^{\circ}$
Direction	:	Axial/Torsional

Table 5.1: Requirements for the strain measuring device, axial and torsional range result from gage length and maximum strain

At first sight, strain gauges seem to be the device of choice. Nevertheless, two problems arise when utilizing strain gauges. This is on the one hand the resultant shielding of the specimen. Nitrogen cannot be blown onto the specimen surface but is blown onto the strain gauge, thus, thermally insulating the specimen. Furthermore, strain gauges are, with some exceptions, intentionally localized measuring devices, meaning that, for example, temperature cannot be measured within the gage length of the gauge.

These limitations do not exist for extensometers. Nevertheless, the necessity of measuring axial and torsional deformation poses significant problems to this technique. Even though biaxial tension/torsion extensometers exist, the requirement that the device may cover a torsional range between -45° and $+45^{\circ}$ cannot be fulfilled by standard biaxial extensometers. Altogether, this leads to the consequence that a custom-made strain measuring device has to be constructed.

The basis of the new strain measuring device are two aluminum disks. Figure 5.21 presents an engineering drawing thereof. Three holders are mounted equally

⁴⁰ von-Mises equivalent strain, see Section 4.2

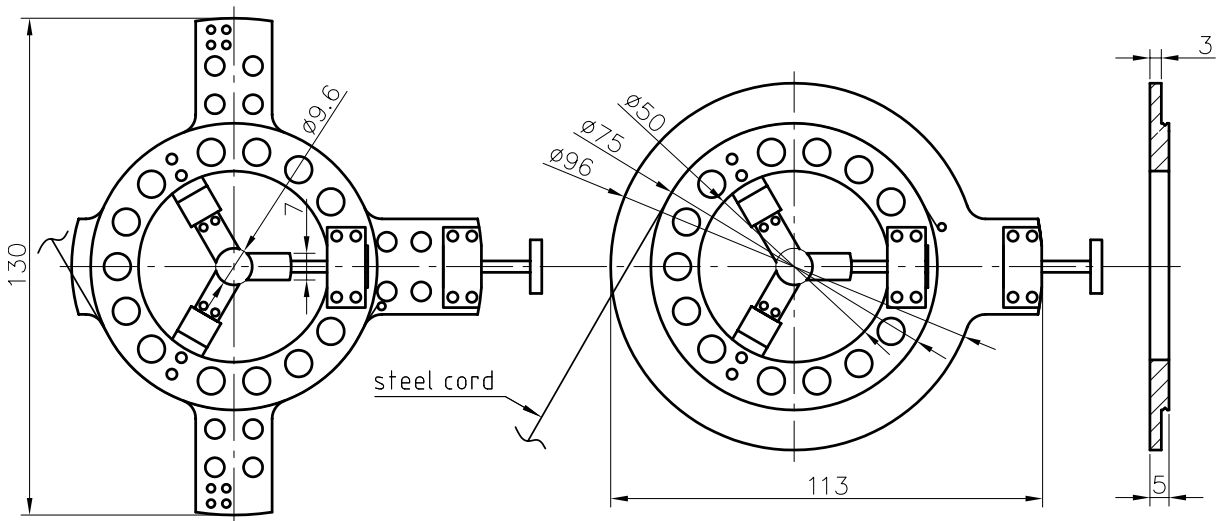


Figure 5.21: Drawing of the aluminum disks

distributed⁴¹ on each of the disks, two of which are fixedly attached while the third one is, supported by linear bearings, movable in radial direction. This third holder has a cutting-edge-like shape. Furthermore, in order to implement an effective electrical insulation between the disks and the energized specimen, PEEK-bushings and -shims are utilized at the contact surfaces between holders and disks additional to ceramic carrier elements of the fixed holders.

By virtue of a spring, which implements a radial force onto the movable edge with respect to the specimen, each disk is clamped onto the specimen so that the rotation axes of the specimen and the disks coincide. Hence, each disk is self-supportingly fixed on the specimen. The axial distance between the two disks equals the gage length.

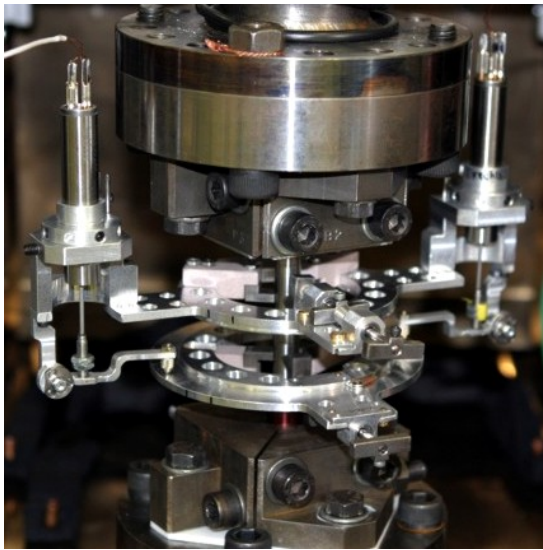
Because of the edge-like shape of the movable holder and the corrugated contact surface of the two counterholders, the disks are prevented from slippage in axial and circumferential direction. Consequently, by measuring the relative movement of the disks, the gage length elongation and twist can be directly deduced.

5.8.1 Axial displacement measuring

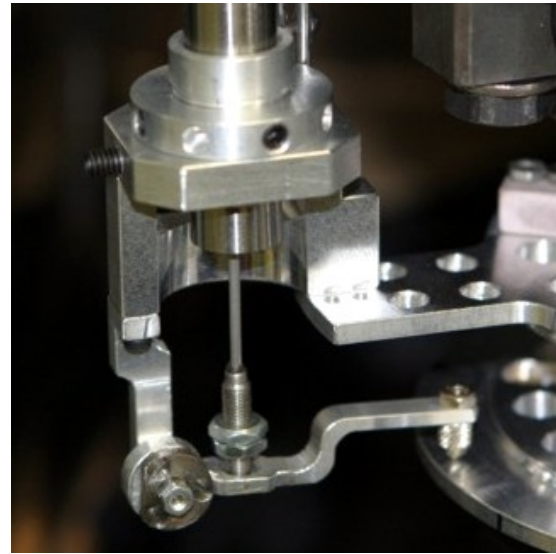
The measurement of the relative, axial movement of the two discs is performed by means of two inductive transducers⁴². These are located so that the center line of the specimen is intersected by the connecting line of the two transducers. In so doing, only two sensors are needed to fully measure the axial elongation, compensating any rotation of the disks perpendicular to the longitudinal axis of

⁴¹Resulting in a 120° degree shift

⁴²Co. Hottinger Baldwin Messtechnik GmbH, W 2 AK, accuracy class 0.4, nominal range ± 2 mm



(a) General view of the strain measuring device



(b) Magnified view of the lever system which is used to transfer the axial displacement to the inductive transducer

Figure 5.22: Axial strain measurement

the specimen. Figure 5.22(a) shows a photograph of the strain measuring system with the two axial transducers.

The axial movement is measured by a gliding feeler head and transferred to the sensors via a lever system, which is shown in a magnified photograph in Figure 5.22(b). This setup allows for any rotational movement of the disks with respect to its center line. Thus, the axial transducers are decoupled from any circumferential motion. The arithmetic mean of the two measurements, weighted by the leverage, gives the elongation of the gage length of the specimen and thus, the axial strain.

5.8.2 Twist measuring

Also in the circumference direction, two inductive transducers⁴³ are utilized for quantifying the relative motion of the two disks.

Steel cords with a diameter of 0.45 mm are attached to each of the disks. A small guideway groove leads the cords around the disks. Besides, each cord is stressed by a weight of $m = 40$ g so that the tension force is always constant. Figure 5.23(b) gives an impression of the guideway groove and the cord attachment. Here, the fixing points are indicated by white circles.

By virtue of two deflection rollers the movement of the steel cords is transferred to the inductive transducers. In Figure 5.23(a) the transducer system including

⁴³Co. Hottinger Baldwin Messtechnik GmbH, W 50 K, accuracy class 0.4, nominal range ± 50 mm



(a) General view of the strain measuring device, outside the temperature chamber on the left: deflection rollers and inductive transducer system for the twist measuring

(b) Magnified view of the disks, the fixing points of the steel cords (indicated by white circles) and the guideway grooves

Figure 5.23: Details of the torsional strain measurement

the rollers can be viewed outside the temperature chamber on the left. Through a differential measurement of the two sensors and by knowing the effective radius, the twist within the gage section can be easily calculated.

5.9 Complete system

By means of the presented experimental setup, freely configurable thermomechanical tests can be conducted. The schematic of the complete system is presented in Figure 5.24. Here, the temperature closed loop control is realized by a PC. This PC operates the temperature chamber and the cooling fluid system consisting of the pressure/volume flow control and the fluid temperature control including the heat exchanger system. Additionally, the Joule heating is managed by this digital PC-based controller.

A second PC is used for implementing the control of the mechanical loading system. Both controllers are interconnected within an Ethernet⁴⁴-based network so that each controller is capable of reacting to the respective counterpart. As a consequence, thermomechanically coupled experiments are possible. Based on an IEEE-488⁴⁵ bus system, the fast data acquisition is performed by the

⁴⁴Ethernet, standardized as IEEE 802.3, stands for a large family of frame-based computer networking technologies for local area networks (LANs)

⁴⁵IEEE-488, also known as HP-IB (Hewlett-Packard Instrument Bus) or GPIB (General Purpose Interface Bus) is an 8-bit parallel bus which can be used to connect up to 15 devices.

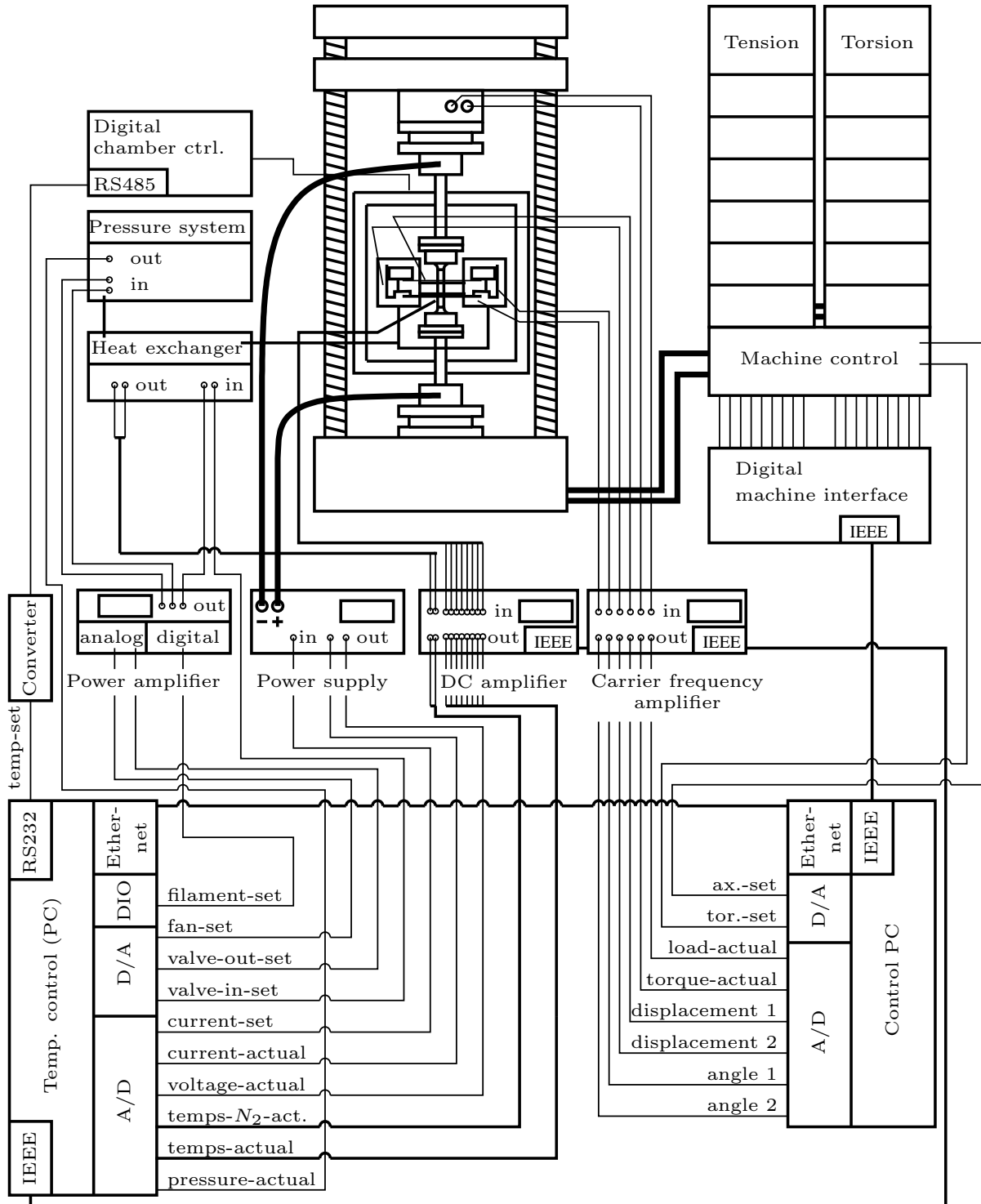


Figure 5.24: Schematic of the complete experimental system

temperature control PC in connection with the digital amplifier system.

Because of a handshake procedure the slowest device governs the data transfer rate

6 Experiments

6.1 Pretests and preparatory experiments

This section treats the conducted pretests, which are necessary in order to characterize the material, and in order to prepare the specimen material for the consecutive multiaxial, mechanical tests. Furthermore, these preparatory tests are essential to facilitate the interpretation of later experiments.

As already mentioned in Section 5.1, the specimen material cannot be used for mechanical testing in the as-received state. This is based on the following observations.

Indeed, the shape memory alloy exhibits a thermally “pseudoelastic” behavior at room temperature as can be observed in the respective DSC curve, Figure 5.1, since two well-defined peaks according to a martensitic transformation are evident. But nevertheless, a mechanically pseudoelastic behavior, which is expressed by a hysteresis in the stress-strain space cannot be noticed, see Figure 5.2. Accordingly, the plastic deformation and the transformation region are not well-separable. Usually, this is also the case for solutionized NiTi, Miyazaki, S. et al. (1982).

Moreover, on account of the comparatively large grains, cf. Figure 5.4, it would be also expedient, if the grain size could be reduced, even though this is not mandatory according to the train of argument in Section 5.1.

Altogether, this leads to the consequence that a thermomechanical treatment is to be performed prior to the actual mechanical experiments. By means of a plastic deformation process, such as rolling or forging, the grain size can be in fact significantly reduced. But, as the shape of the tubular stock is close to the projected specimen geometry, and an even smaller specimen size is not suitable for the testing machine at hand, due to the given range of mechanical loading, Section 5.6, an antecedent mechanical forming process is abandoned. Consequently, the preceding thermomechanical treatment reduces to a preceding heat treatment process. However, therewith a reduction of the grain size cannot be achieved.

6.1.1 Heat treatment

As in standard heat treatment procedures, the first step is a solution annealing process. Here, the existing dislocations and the present precipitates are annihilated. That way, a well-defined initial state can be attained. Contrastively to few other works in the literature in which the specimen material is cooled down

within the furnace, cf. Tanaka, K. et al. (1999); Lexcellent, C. & Tobushi, H. (1995); Lin, P. et al. (1996b); Lim, T.J. & McDowell, D.L. (1995), the specimen material used in this work is quenched in water after each annealing step. In so doing, the state achieved at the end of the heating process is frozen, regardless of the specific furnace so that the microstructure is well-repeatable and well-reproducible. This procedure is in accord to the treatises of Brinson, L.C. et al. (2004); Gall, K. et al. (2000); Khalil Allafi, J. (2002); Otsuka, K. (1990).

Subsequently, an aging or precipitation annealing step is conducted, again followed by a quenching in water, given that as aforementioned in the solutionized state usually no pseudoelasticity is observed, Miyazaki, S. et al. (1982). Thanks to finely dispersed Ni_4Ti_3 precipitates the plastic deformation and the transformation region can be shifted respectively to higher, lower stresses, hence, resulting in a well-defined and distinct transformation region within the stress-strain space. This is due to the fact that Ni_4Ti_3 precipitates act as nucleation sites for martensite, concomitantly impeding dislocation motion, Treppmann, D. & Hornbogen, E. (1995). For this reason the pseudoelastic stress-strain response can be stabilized, Miyazaki, S. et al. (1986). In this regard, the size and the amount of Ni_4Ti_3 precipitates are crucial. This is directly connected to the aging temperature and the duration of aging, which are still subject to further research, cf. Khalil Allafi, J. (2002), for example.

Two different heat treatments are chosen, which shall be denoted in the course of this work by *HT 1* and *HT 2*. It is clear from Table 6.1 that the solution an-

annealing step	HT 1	HT 2
solution annealing	1h @ 850°C	1h @ 850°C
aging	1h @ 350°C	0.5h @ 350°C

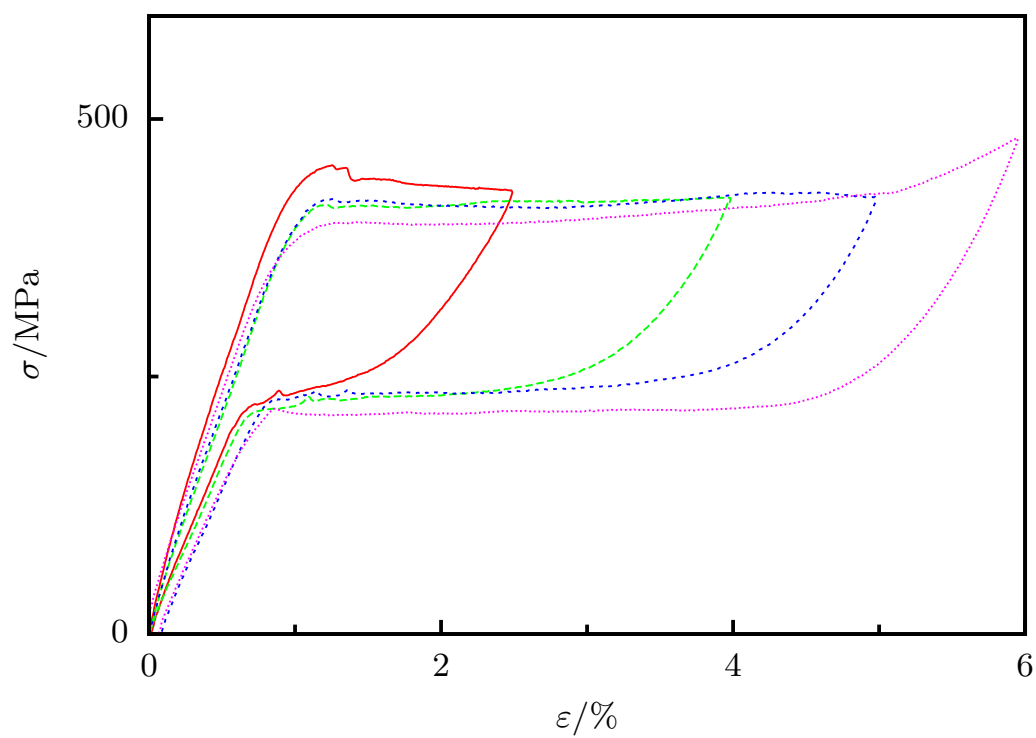
Table 6.1: Applied heat treatments HT 1 and HT 2

nealing step is equal for both heat treatments, while the only difference between the two types of heat treatment is the duration of aging.

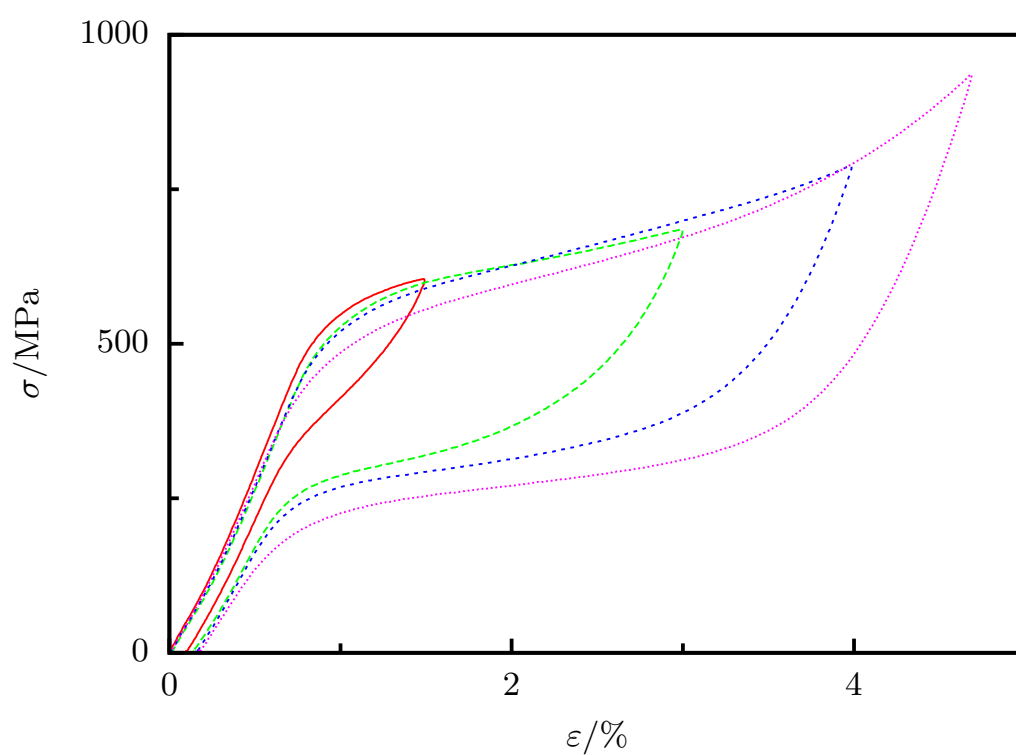
6.1.2 Mechanical tests on specifically heat treated specimens

Different types of strain controlled, uniaxial tests are performed on HT 1 and HT 2 specimens at room temperature in order to find out if the material behaves pseudoelastically after the respective heat treatment.

Figures 6.1(a) and 6.1(b) show simple tension and compression experiments for a HT 1 specimen. Here, for each experiment the stress-strain hysteresis is almost perfectly closed. Also in the case of torsion tests for a HT 2 specimen, Figure 6.2, an almost ideally pseudoelastic behavior can be observed. Von-Mises equivalent



(a) Simple tension



(b) Simple compression

Figure 6.1: Uniaxial tests for a HT 1 specimen with $\dot{\epsilon} = 10^{-4}\text{s}^{-1}$, starting at room temperature

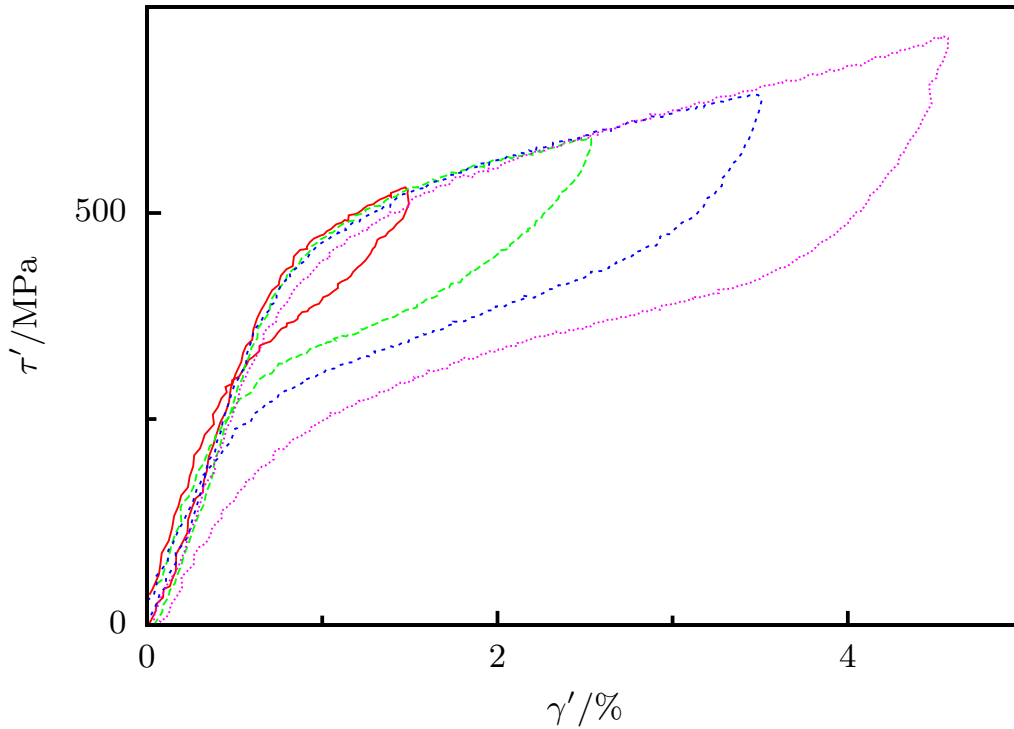


Figure 6.2: Simple torsion tests for a HT 2 specimen with $\dot{\gamma}' = 10^{-4} \text{s}^{-1}$, starting at room temperature

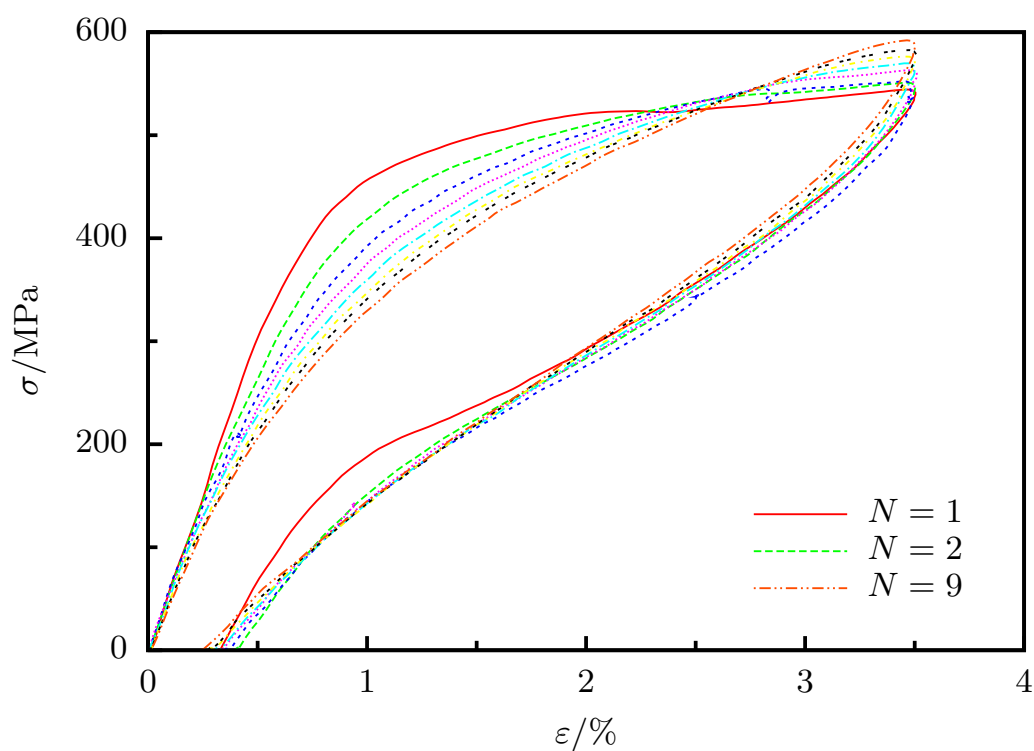
stress and strain¹ are used in this diagram.

Noting that the specimen material is pseudoelastic at room temperature for the applied heat treatments, it is of particular interest to determine the degree of degradation of the stress-strain behavior for multiple consecutive experiments, Miyazaki, S. et al. (1986). This knowledge is in particular essential, since it gives rise to the number of experiments that can be conducted on one single specimen without deteriorating the final conclusions. In this connection repeated strain controlled simple tension tests are carried out on HT 2 specimens at room temperature, see Figure 6.3.

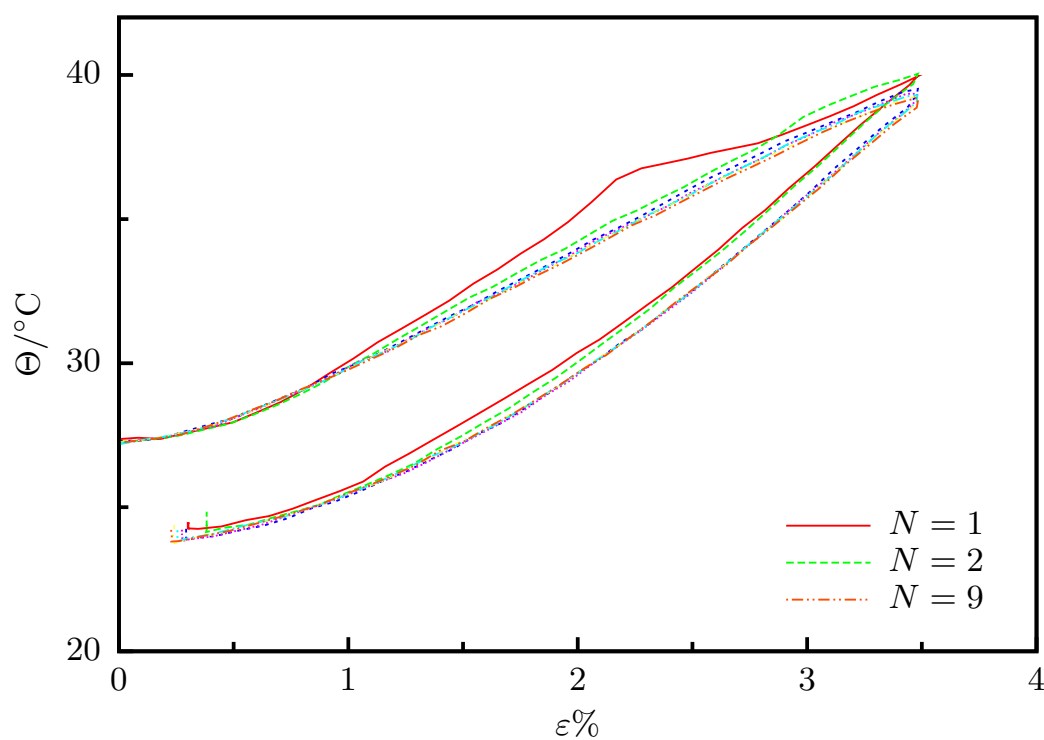
A maximum strain of 3.5% is chosen, which is well within the maximum possible hysteresis². The strain rate is $\dot{\epsilon} = 10^{-3} \text{s}^{-1}$. It is obvious from Figure 6.3(a) that the hystereses degrade, which means that the shape of the curves is subject to change. For higher cycle indices the slope of the stress developing gets steeper, concomitantly reducing the size of the hysteresis. Furthermore, residual strains are evident. In this regard, it is worthwhile taking a closer look at the temperature-strain curve. It can be recognized that large temperature dif-

¹See Section 4.2 for a definition thereof.

²It is well-known that at the end of the hysteresis the martensitic transformation is most unlikely accomplished. Additionally, a martensitic fraction of 100% has to be assumed as an unrealizable limiting case.



(a) Stress-strain diagram



(b) Temperature-strain diagram

Figure 6.3: Repeated simple tension tests, HT 2

ferences with respect to the ambient atmosphere occur during the experiment. Moreover, the temperature at the end of the experiment is well below the starting temperature, which is simultaneously the ambient temperature as well. The residual strain can be attributed to this negative temperature difference at the end of the tests shifting the transformation stress to lower values so that local eigenstresses may impede the complete reverse transformation. This explanation is substantiated by the diminishment of the residual strains, as the difference between ambient and specimen temperature is decreased. Consequently, isothermal³ tension tests might prove better suited in order to reduce the degradation process.

Those experiments are shown in Figure 6.4. Here, the residual strain is significantly reduced. Beyond that, the slope of the stress curve does not vary as much as in the non-isothermal case. Nevertheless, an evolution of the stress-strain behavior is still recognizable resulting in a flattening of the curves, if the region between the elastic and the transformation regime is considered.

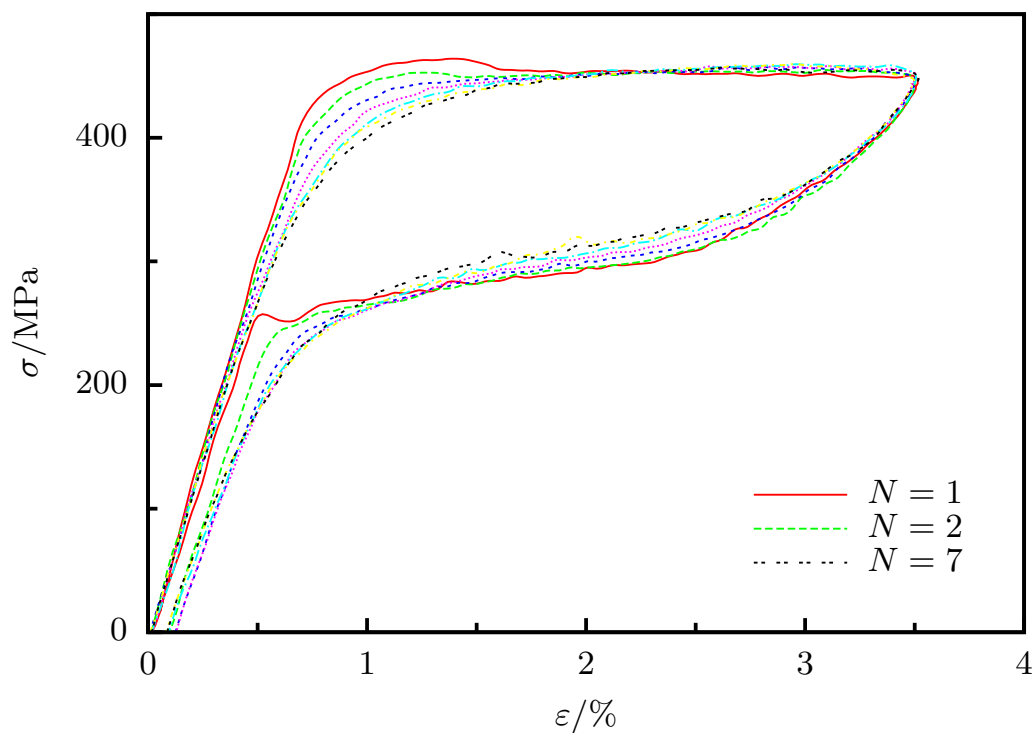
In this connection, the behavior of a HT 1 specimen must also be examined. As a result of the foregoing observations, isothermal uniaxial tension tests are performed as well, Figure 6.5. Again, a further improvement of the degradation behavior is noticed. Almost no evolution can be spotted for the different cycle indices. But the stress-strain curves are quantitatively different from the HT 2 curves. This is expressed by a different stress level of the stress plateau and a smaller slope in the elastic region. However, as a consequence of this improved “fatigue” behavior, for all further mechanical experiments, the heat treatment denoted by HT 1 is applied, unless stated otherwise.

6.1.3 DSC⁴ results

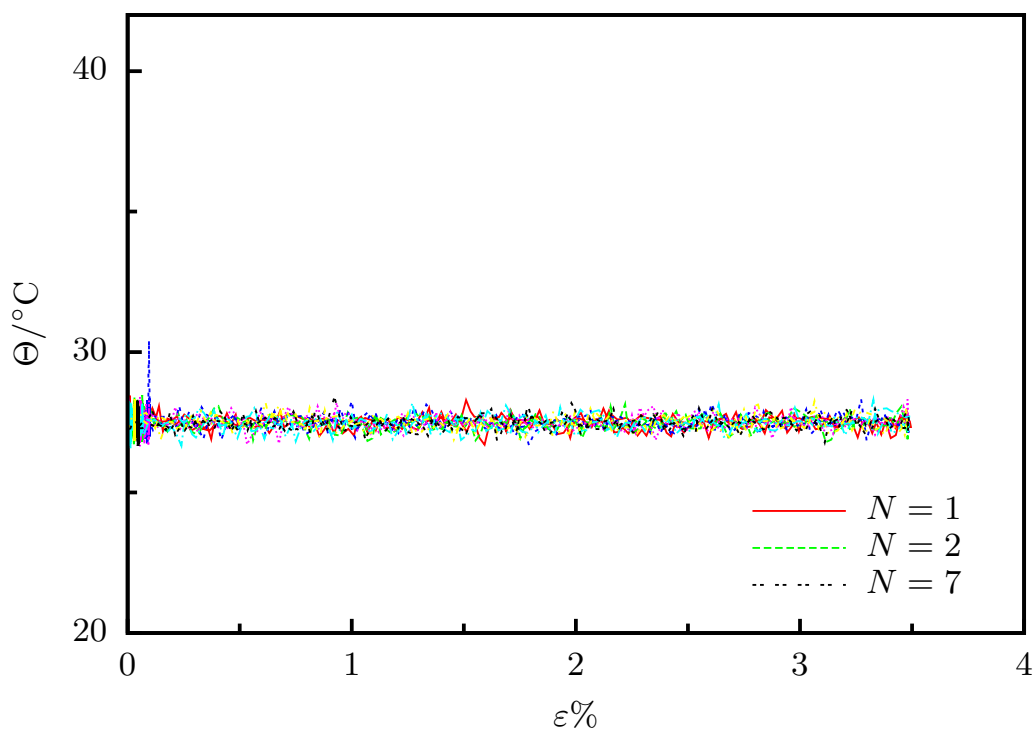
Irrespective of the first mechanical tests, further examinations are performed in order to characterize the material. In Figure 6.6, the DSC curves for the two different heat treatments are shown together with the DSC curve of the as-received material. It is obvious that the differences between the two heat treatments according to the DSC curves are marginal in spite of the large differences, which are observed in the stress-strain space, Section 6.1.2. In comparison to the as-received material, it is evident that instead of a one-step transformation the material passes through two steps as well for the forward as for the reverse transformation. This is partly in accord with the findings in Khalil Al-lafi, J. (2002), even though the DSC curves in this work correspond best with the respective curves for precipitation temperatures of 500°C. Furthermore, it can be observed that the endothermic austenite peak at -20°C shifts to higher temperatures for the two heat treatments. The reason for the peak shift might

³In Section 6.2, isothermal conditions and the possible realization are thoroughly discussed. As mentioned earlier (Section 5.5), completely isothermal conditions cannot be achieved.

⁴Differential Scanning Calorimetry, see Footnote 2 on page 35



(a) Stress-strain diagram



(b) Temperature-strain diagram

Figure 6.4: Repeated isothermal tension tests, HT 2

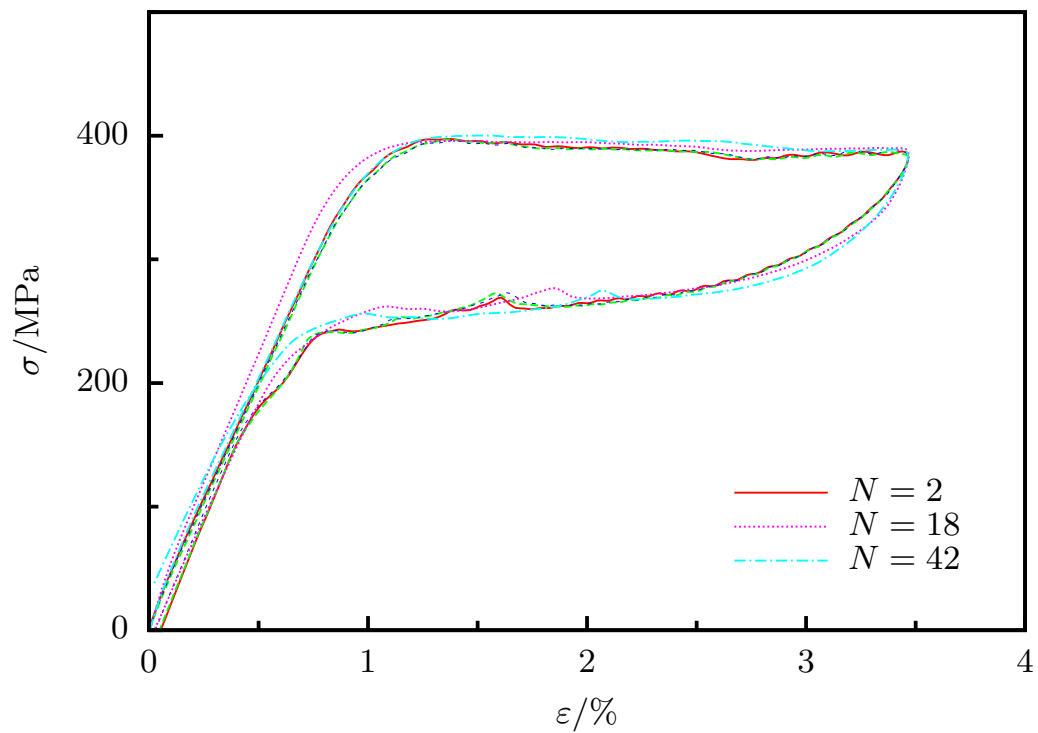


Figure 6.5: Repeated isothermal tension tests, HT 1

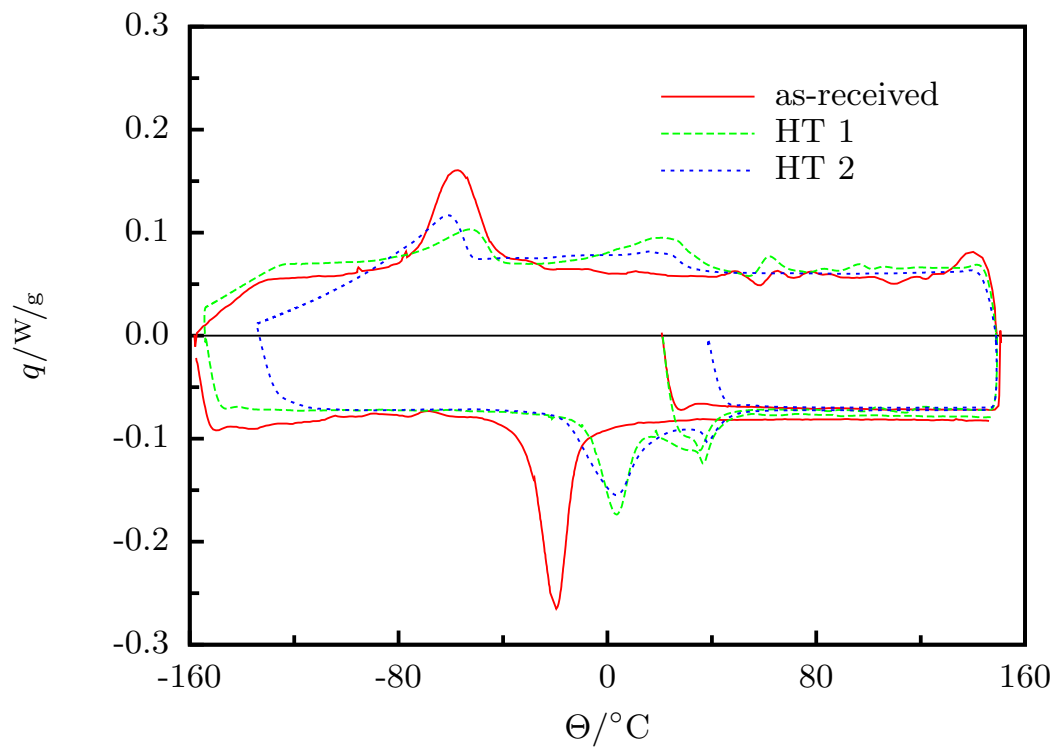


Figure 6.6: DSC curves for HT 1, HT 2, and as-received specimen material

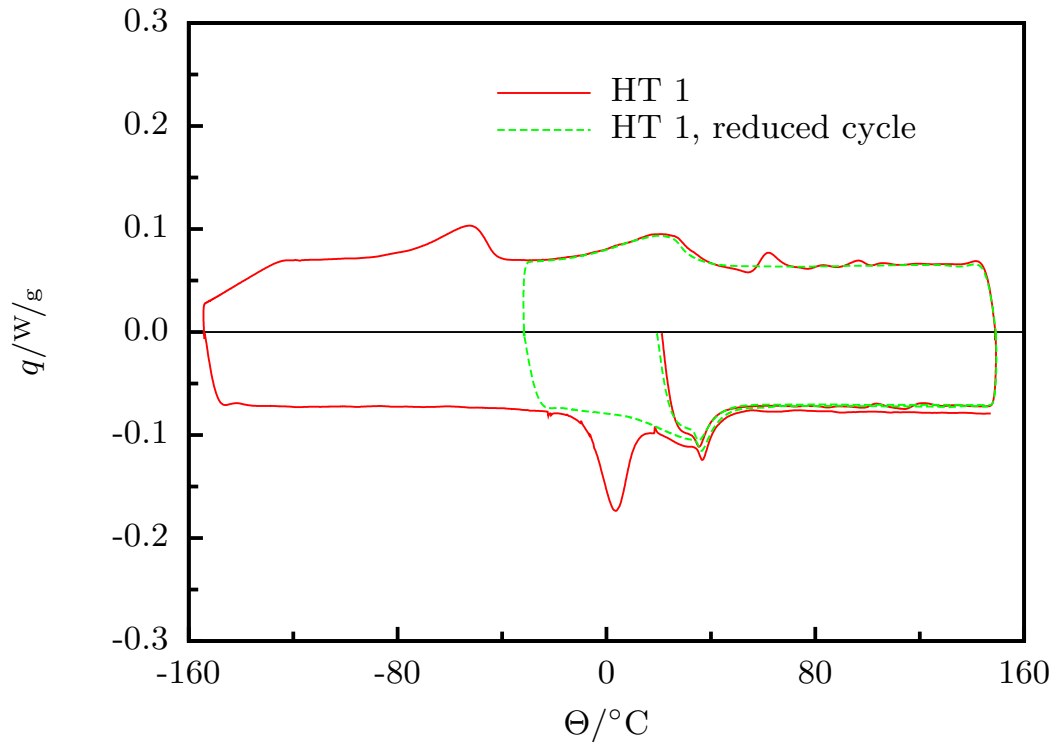


Figure 6.7: Comparison of two different DSC cycles for HT 1

be the depletion of Ni in the NiTi matrix due to the precipitation of Ni_4Ti_3 . Comparing the two heat treatments, it can be stated that for the longer precipitation duration, HT 1, the additional peaks are slightly more pronounced than in the case of the second heat treatment, HT 2.

In order to identify the origin of the additional peaks, further experiments are requisite. [Khalil Allafi, J. \(2002\)](#) identifies for a similar alloy the origin of the first exothermic peak as a $B2 \rightarrow R$ transformation at the grain boundaries due to heterogeneous Ni_4Ti_3 precipitates whereas the two peaks on heating are both assigned to a $B19' \rightarrow B2$ transformation. In this regard, an additional DSC cycle is realized on HT 1 specimen material. Here, the cycle is limited by temperatures just below the first exothermic transformation peak upon cooling, see Figure 6.7. A similar procedure is proposed in [Tanaka, K. et al. \(1999\)](#) in order to identify the start and finish temperatures for a two step transforming NiTi alloy whose reverse transformation peaks on heating partially overlap one another in the DSC measurements. By accounting these two DSC curves, it stands to reason that the two right peaks in the cooling and heating path belong together so that the origin of the respective peaks might be $B2 \rightarrow R$ and $R \rightarrow B2$ transformations. This can be explained by the fact that if on the cooling path no $B19'$ is generated, which is the case for the small DSC cycle according to [Khalil Allafi, J. \(2002\)](#), a transformation from $B19'$ is not possible upon heating because only $B2$ - and R -phase may be present.

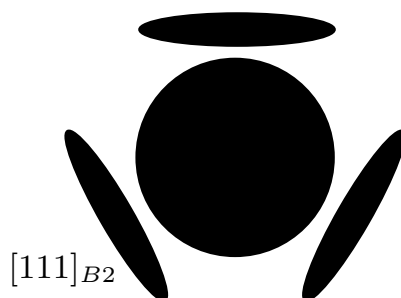


Figure 6.8: Schematic of the ordering of lenticular Ni_4Ti_3 precipitates according to [Michutta, J. \(2005\)](#)

6.1.4 TEM⁵ results

For a further characterization of the microstructure and the transformation behavior, especially for the classification of the two additional peaks in the DSC curves, TEM examinations are conducted on HT 1 specimen material. Here, for all TEM measurements in this work the same electron microscope is used⁶. For a detailed description of the fundamentals on TEM, refer to [Eggeler, G. \(2001b\)](#). Specifically, it is also intended to get a deeper insight in the distribution and size of Ni_4Ti_3 precipitates.

Before microscopy images of the grain and precipitate structure are presented, the schematic ordering of Ni_4Ti_3 precipitates is recalled, see Figure 6.8 from [Michutta, J. \(2005\)](#), which is of major importance for the interpretation of the respective TEM micrographs. Here, the lenticular shape of the Ni_4Ti_3 precipitates is obvious. Four different orientations exist, which is why three of the four projections of precipitates are shown as ellipses in the two-dimensional picture in Figure 6.8.

Now, in order to analyze the Ni_4Ti_3 precipitates, bright field TEM images are taken at 70°C, Figure 6.9. Images with a larger and a smaller magnification are shown. It is quite difficult to spot the elliptical precipitates at first sight within Figure 6.9(b) and impossible within Figure 6.9(a). But a closer view reveals that a vast number of precipitates in different variants is present whose characteristic length scale is even below 10 nm, substantiating the notion of finely dispersed Ni_4Ti_3 precipitates stated earlier in this chapter. Some of those are indicated by white arrows in Figure 6.9(b). In this context, it is very difficult to estimate the volumetric amount of Ni_4Ti_3 precipitates due to the smallness of the precipitates. For the characterization of the origin of the right hand side exothermic peak with reference to the DSC curves, a cooling test is performed within the electron microscope. Here, the temperature is decreased from a start value of 70°C.

⁵Transmission Electron Microscopy

⁶Co. Philips, CM 20, transmission electron microscope featuring a 200 kV high voltage electron beam and equipped with a LaB₆ electron emitting cathode. For cooling tests a Gatan, Inc. 636 double tilt holder is utilized.

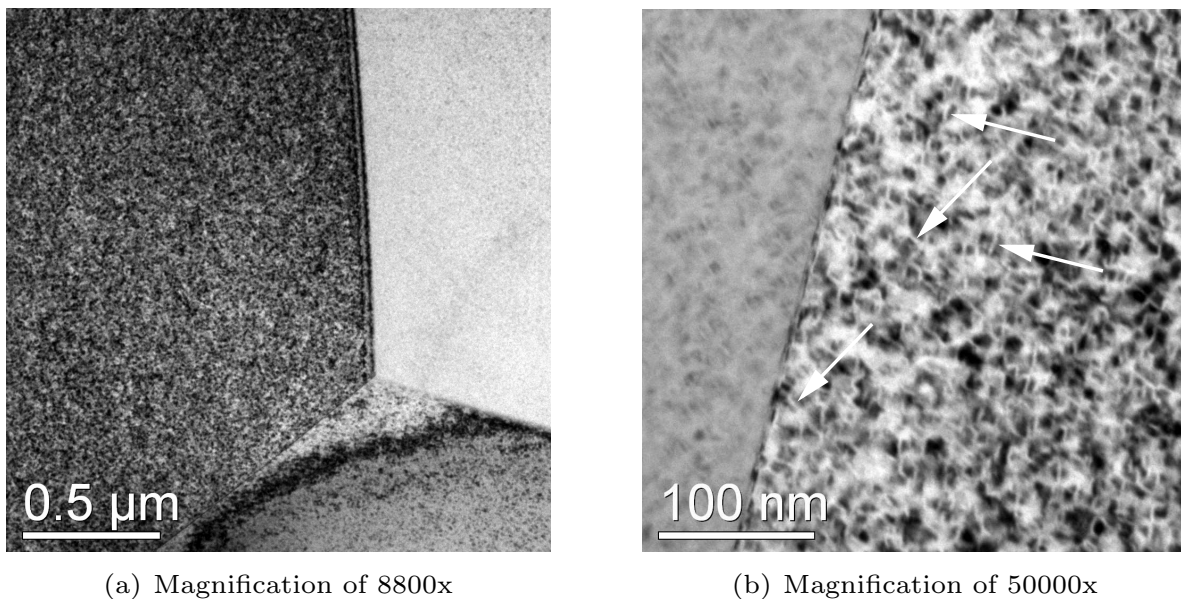


Figure 6.9: Bright field TEM images of an HT 1 specimen at 70°C

The respective experiment finish temperature is 26°C, which is approximately the temperature corresponding to the maximum heat flow. Consequently, the exothermic process is not completely accomplished at this point. In this regard, a second set of bright field images is taken showing the microstructure at 26°C, Figure 6.10. In doing so, bright field images are given for the experiment start and finish temperatures. It has to be highlighted that no difference in the microstructure can be recognized simply from the bright field images. That is why a set of SAD⁷ measurements is conducted. In so doing, the lattice structure is visualized so that different phases can be identified unambiguously in general. Figure 6.11 depicts four SADPs at four distinct temperatures in the direct vicinity of the aforementioned exothermic peak. Again, two images are shown corresponding to the start and finish values of the experiment temperature, see Figures 6.11(a) and 6.11(d). Additionally, two further SAD images are taken at 48°C and 39°C, Figures 6.11(b) and 6.11(c). Beginning with Figure 6.11(a), the classical austenite *B2* pattern can be observed, which is characterized by the clear hexagonal structure of the reflections without any additional superlattice reflections, cf. Heckmann, A. (2003), for example. This observation is in good accord with the DSC curves, since a temperature of 70°C is well above the last endothermic peak upon heating, implying that the microstructure is completely austenitic under the assumption that the amount of the untransformed portions of the specimen can be neglected. Figure 6.11(b) presents a similar picture.

⁷Selected Area Diffraction: The diffraction image exhibiting a certain selected area diffraction pattern, SADP, is a by-product of the TEM, as due to size effects a part of the electron beam gets diffracted and can be made visible afterwards, see Eggeler, G. (2001b) for a detailed introduction.

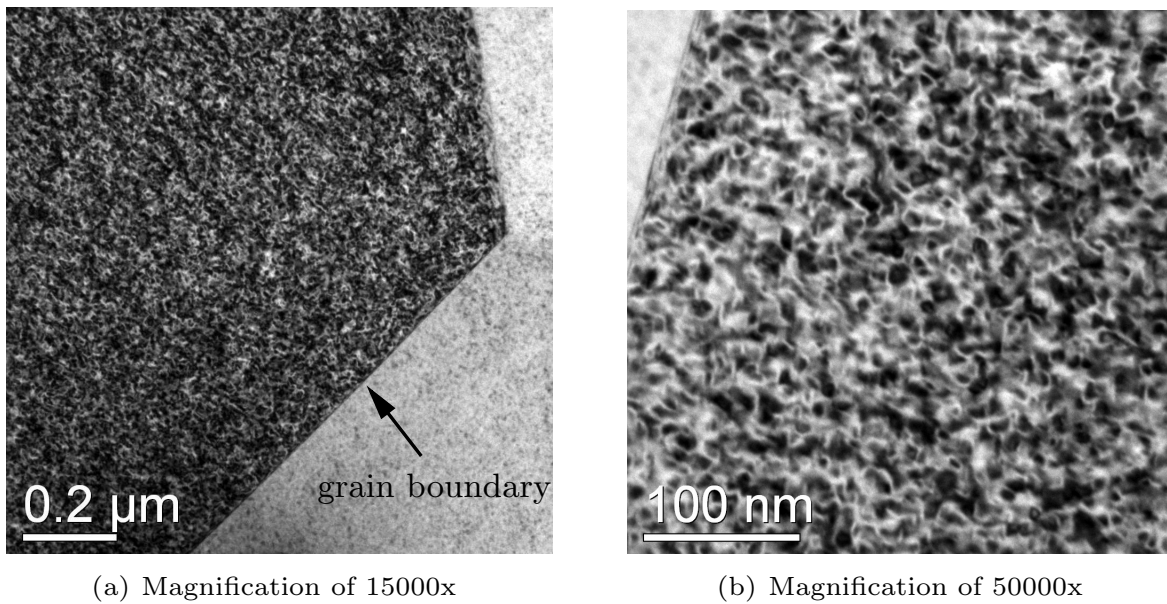


Figure 6.10: Bright field TEM images of an HT 1 specimen at 26°C

Again, the microstructure is clearly austenitic, which is also concluded from the DSC curves. This can be explained by the fact that the SAD image in Figure 6.11(b) is taken on a cooling path, well before the first tails of the exothermic peak are encountered according to Figure 6.7. However, the interpretation of Figure 6.11(c) is not as evident. Here, some additional extra spots might be anticipated but this is far from being unambiguous. This can be explained as the respective temperature, 39°C, lies just at the onset of the exothermic process, see Figure 6.7. By contrast, the SADP of Figure 6.11(d) clearly features superlattice reflections some of which are indicated by white arrows. These small $1/3^8 \langle 110 \rangle^9$ superlattice reflections are characteristic for the lattice structure of the *R*-phase, cf. Khalil Allafi, J. (2002); Michutta, J. (2005); Hara, T. et al. (1997). Nevertheless, only one single variant can be observed, since all $1/3 \langle 110 \rangle$ reflections are oriented from the upper left to the lower right. A possible reason might be the production process of the tubular stock resulting in a slightly textured microstructure, Hara, T. et al. (1997).

As a conclusion from the reduced DSC cycle and the TEM measurements, it stands to reason that the two right hand side peaks in the DSC curves correspond to $B2 \rightarrow R$ and $R \rightarrow B2$ phase transitions.

⁸This parameter states that the small extra reflections are positioned at every multiple of one third of the distance between two large reflections.

⁹ $\langle 110 \rangle$ denotes a direction of $\langle 110 \rangle$ type. Various $\langle 110 \rangle$ directions exist, Eggeler, G. (2001a)

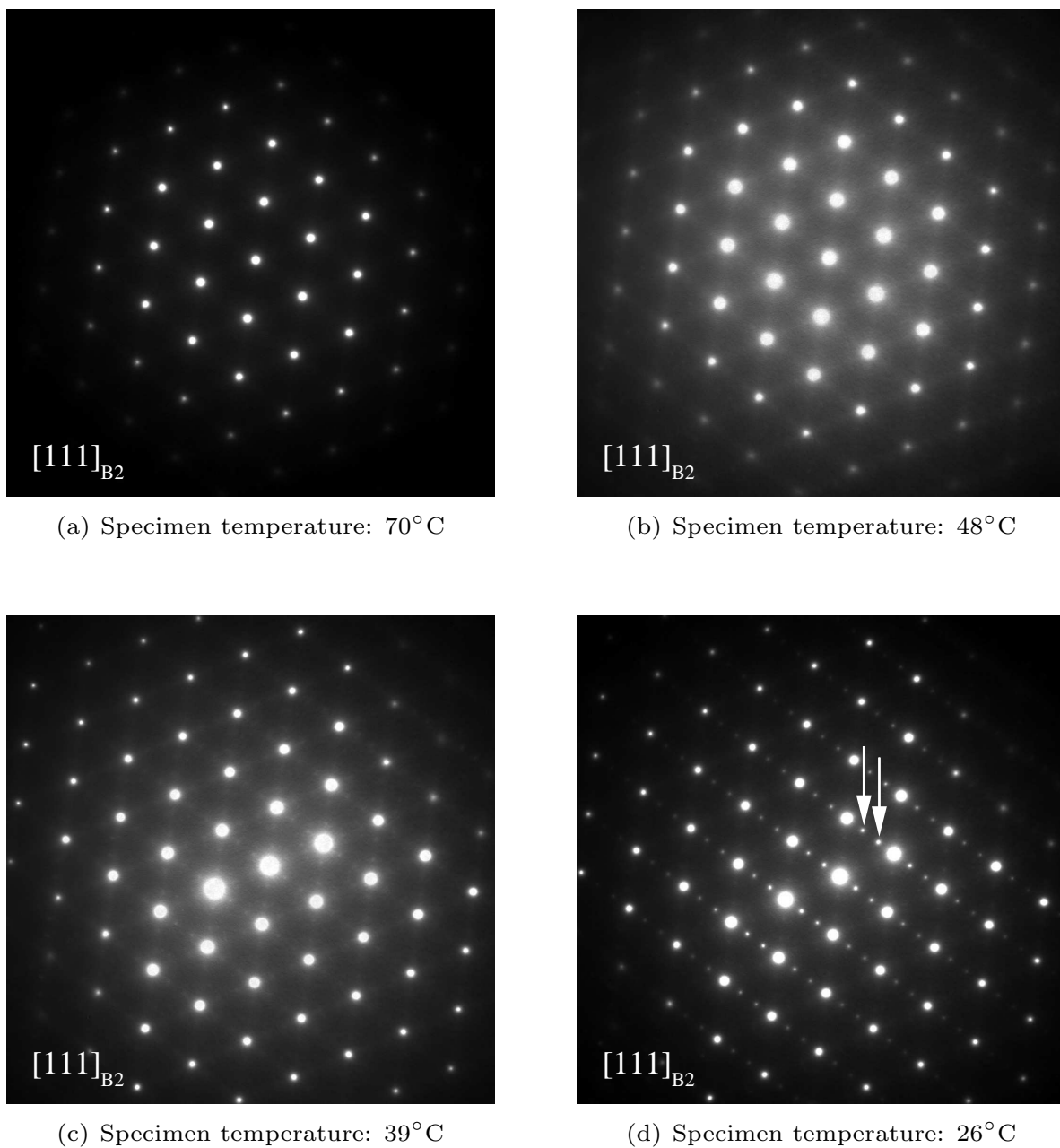


Figure 6.11: Various SADPs of an HT 1 specimen at different temperatures, diffraction images in direction of the $[111]$ zone axis

6.1.5 Effect of temperature on the stress-induced transformation behavior

A set of simple isothermal tension tests is performed on HT 1 specimens at different temperatures. Temperatures between 0°C and 65°C are chosen, which is motivated by the positions of the reverse transformation peaks in the earlier discussed DSC curves, Fig. 6.7. It is assumed that above a temperature of 50°C the

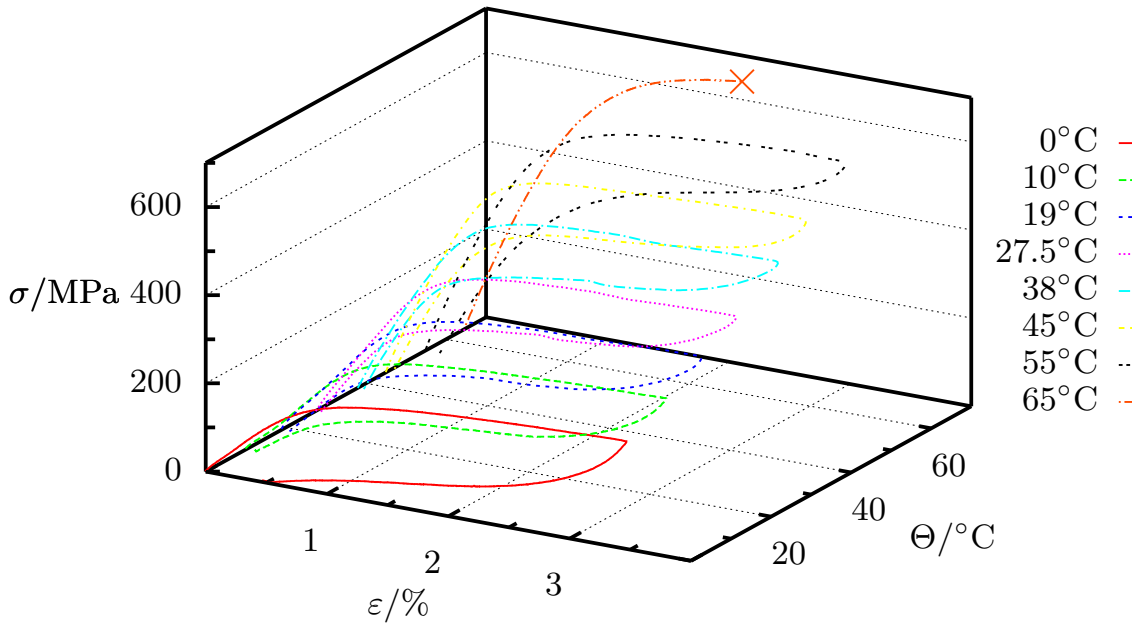


Figure 6.12: Isothermal tension tests for different temperatures on a HT 1 specimen; experiment temperatures are 0°C, 10°C, 19°C, 27.5°C, 38°C, 45°C, 55°C, 65°C

specimen material is completely austenitic, hence, resulting in the best possible pseudoelastic behavior for the performed heat treatment. In the temperature range between 0°C and 40°C, a mixed $B2/R$ -phase microstructure is supposed with a presumably different pseudoelastic behavior than that observed above a temperature of 50°C. Figure 6.12 depicts the measured stress-strain behavior for the different temperatures.

Fundamentally, pseudoelastic material behavior can be noticed for almost all temperatures under investigation. Obviously, the lower limit of the pseudoelastic domain is in the vicinity of 0°C, since a remaining strain of 0.5% is evident from the stress response at this temperature. The fact that, irrespective of the curves for 0°C and 65°C, a qualitatively similar pseudoelastic stress-strain behavior can be noticed for all experiments is especially surprising as the lower temperature tests are carried out within a supposedly mixed $B2/R$ -phase regime, as mentioned before. In this context, it is noteworthy that for several tested specimens fracture occurs at 65°C around 2% axial strain, which is presumably well within the pseudoelastic stress-strain hysteresis. Actually, around that particular temperature an almost ideally pseudoelastic material behavior is expected, since this temperature is just above the second endothermic peak in the DSC curve (Fig. 6.7), which was ascribed to a $R \rightarrow B2$ phase transition. The reason

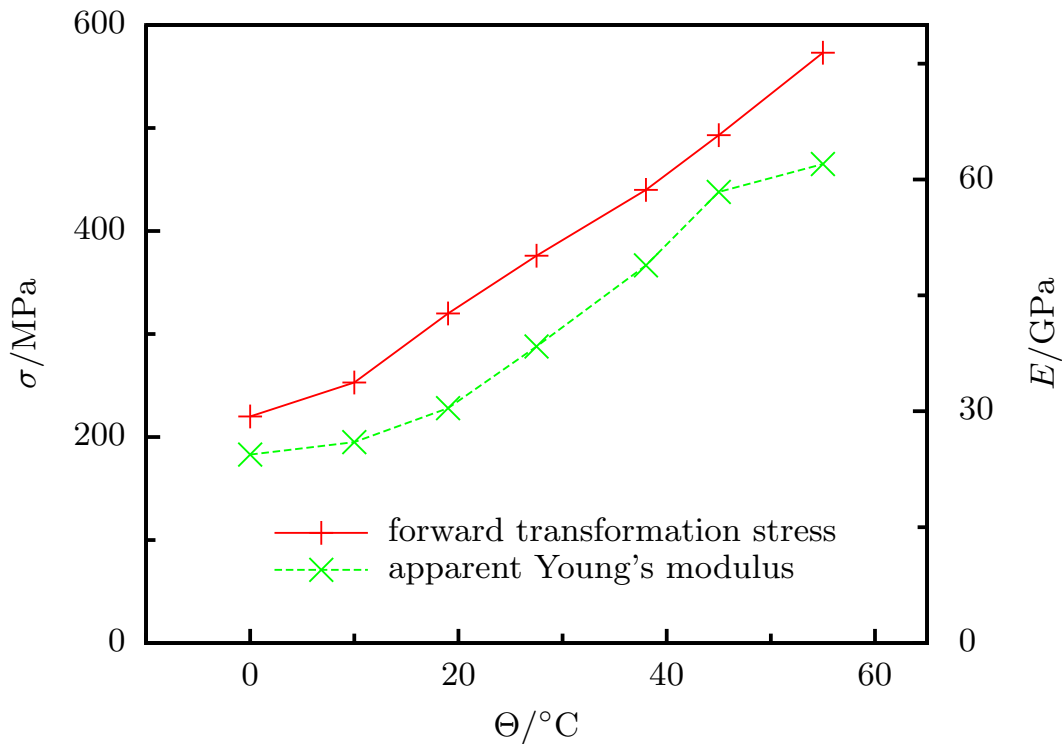


Figure 6.13: Effect of temperature on transformation stress and apparent Young's modulus

for the reproducible occurrence of fracture might be the high transformation stress level resulting from the high temperature as described by the Clausius-Clapeyron equation, see [Ortín, J. & Planes, A. \(1989\)](#). Additionally, the method of heat treatment may play its part, since the specimen, being enwrapped in a foil, is heated in air. In this vein, small oxide particles may be introduced into the specimen, which might cause brittle fracture above a specific stress limit. By contrast a heat treatment using an inert gas atmosphere or an airtight quartz covering of the specimen might be used to avoid this effect. Consequently, the temperature range between 10°C and 55°C is considered the pseudoelastic domain in the following as defined by [Otsuka, K. & Wayman C. M. \(1998\)](#) and discussed in Section 2.3.

Figure 6.13 shows the temperature effect on the forward transformation stress and the apparent Young's modulus. The term “apparent” Young's modulus is defined later in this paragraph. Since distinctive stress plateaus for the reverse transformation cannot be identified from the stress-strain curves in Figure 6.12, the reverse transformation stress function is not given in Figure 6.13.

An almost linear progression of the transformation stress, which has a slope in the range of 8.5 MPa/K is evident. This is in good accord with the reported values in the literature. For nearly equiatomic NiTi, [Honma, T. \(1984\)](#); [Shaw, J.A. & Kyriakides, S. \(1995\)](#) present values of 7.5 MPa/K and 8 MPa/K, for example.

Evidently, the apparent Young's modulus is strongly dependent on temperature. In this connection, the term "apparent" Young's modulus is used in reference to [Šittner, P. et al. \(2006\)](#). There, it is accounted that for NiTi a Young's modulus below 60 GPa indicates the existence of the R -phase. The reorientation process of the twinned R -phase, which occurs at low stress values, degrades the elastic modulus. Furthermore, the temperature dependence of the slope in the linear range is attributed to the increasing R -phase distortion for decreasing temperatures. In this way, the strong temperature dependence of the, otherwise reported, temperature insensitive Young's modulus of NiTi can be explained for the considered material. In this regard, the absence of residual strains upon unloading is noteworthy. This may be elucidated by the process of "twinning pseudoelasticity" as established by [Hornbogen, E. \(1995\)](#). There, it is claimed that as dislocations or eigenstresses due to coherent particles are given, which is the case for the performed heat treatment, a preferred twinning microstructure may exist, which is reestablished after the release of external stresses, hence, resulting in a shape memory of the specimen material and a full recovery of the strains.

Finally, it is supposed that for the considered material and heat treatment, the pseudoelastic material behavior may be attributed mainly to R -phase reorientation and $R \rightarrow B19'$ phase transition processes. However, it is assumed that the initial microstructure in the pseudoelastic temperature range is a mixture of $B2$ - and primarily R -phase with varying proportions depending on the specific temperature. In this connection, it has to be noted that further experiments would be necessary for a profound investigation of the origin of the observed pseudoelasticity, which is beyond the scope of this work.

6.2 Characterization of viscous and rate dependent material behavior

Throughout the last years, more and more experimental data on shape memory alloys and NiTi in particular have been accumulated. In this context, the thermomechanical coupling of the material behavior is especially intriguing. Extensive studies have been performed with reference thereof to the connection between specimen temperature and transformation stress, which can be defined as the critical stress that is needed for the triggering of a stress-induced transformation of the microstructure. The description of these phenomena using the Clausius-Clapeyron relation is meanwhile well adopted, see [Ortín, J. & Planes, A. \(1989\)](#), for instance.

Moreover, as a large amount of mechanical experiments is performed under strain control, multiple works have been dedicated to the characterization and determination of the strain rate effect on the stress-strain behavior. [Mukherjee, K. et al. \(1985\)](#) have been among the first to report a direct connection between higher strain rates and higher transformation stress levels. Similar findings have been

made by [Shaw, J.A. & Kyriakides, S. \(1995\)](#); [Leo, P.H. et al. \(1993\)](#); [McCormick, P.G. et al. \(1992\)](#). Herein, it is shown that a rise of the specimen temperature is observed during the loading process, which depends on the magnitude of the strain rate. Furthermore, [Shaw, J.A. & Kyriakides, S. \(1995\)](#); [McCormick, P.G. et al. \(1992\)](#) present experimental data for different ambient media, thus, resulting in different heat transfer conditions, i.e., different specimen temperatures and different stress-strain curves due to the temperature dependence of the transformation stress, cf. [Ortín, J. & Planes, A. \(1989\)](#).

It is well accepted today that the transformation process results in the production of latent heat leading to an exchange of heat between the specimen and the environment. Hence, the specimen temperature is changed. Consequently, different specimen geometries and different surrounding media lead to different experimental results. Finally, the outcome of the experiments strongly depends on the particular setup, which renders experimental data from distinct experimental setups incomparable. This is why it is highly important to realize an experimental setup, which is independent of the specific geometry and the external conditions, thus, allowing for a decoupled examination of strain rate and temperature effects on the material behavior.

Referring to the modeling part of material characterization, [Leo, P.H. et al. \(1993\)](#); [McCormick, P.G. et al. \(1993\)](#) use a one-dimensional material model, which incorporates heat transfer due to conduction, convection, and radiation, yielding a satisfactory agreement between modeled and material behavior observed on wire. [Lexcellent, C. & Rejzner, J. \(2000\)](#) arrives for a three-dimensional model and two-dimensional experiments conducted by [Lim, T.J. & McDowell, D.L. \(1999\)](#) at a similar result.

Although these modeling efforts give a first lead concerning the rate dependency of the mechanical material behavior, together with the awareness that part of the increase of the transformation stress can be attributed to the increase of the specimen temperature, the reverse, implying that the material behavior is independent of strain rate, is far from being a stringent conclusion. Moreover, it is questionable to what extent it is possible to render a material model the “true” model just by the fact that a certain effect can be fitted well.

On this account, temperature controlled experiments are imperative. Some such experiments are conducted by the research group around Tobushi and Lin ([Lin, P. et al. \(1996a,b\)](#); [Tobushi, H. et al. \(1998, 1999\)](#)) on 0.1 mm wire. Consequently, only uniaxial tension tests are possible. The specimen temperature is measured using one single thermocouple, which is pressed on the central part of the specimen. Based on the results of these tests, it is reported that the material behavior is independent of strain rate.

In order to generalize these findings and to determine whether this holds true even for bulk material, isothermal multidimensional experiments are to be carried out on three-dimensional specimens. The next section is dealing therewith. Preliminary results were published in [Grabe, C. & Bruhns, O.T. \(2006, 2007\)](#). Throwing a glance at a different field of viscous material behavior, some non-

isothermal relaxation and creep experiments have been presented by Helm, D. (2001) recently. Similar to the experimental data published by Lim, T.J. & McDowell, D.L. (1999), it is stated for relaxation experiments that during strain hold periods the specimen temperature decreases, which results in a stress drop. Nevertheless, Helm goes even further by claiming that the material unambiguously exhibits a viscous behavior. He also states that for higher strain rates¹⁰ this effect might be even more distinctive. However, the obligatory proof thereof is still missing, since the respective experiments were not conducted. The reason may lay in the fact that the superimposed temperature effect gets predominant for higher strain rates, and a temperature control scheme was not implemented in Helm's experimental setup. By contrast, it is argued by Tobushi, H. et al. (2003); Matsui, R. et al. (2004) that the pseudoviscoelastic material behavior, which is observed for creep and relaxation tests, might be completely assigned to the temperature variation as described by the Clausius-Clapeyron equation, due to latent heat effects during transformation processes. In order to give proof for the former or the latter assumption, isothermal creep and relaxation experiments are presented subsequent to the section dealing with isothermal mechanical tests at different strain rates.

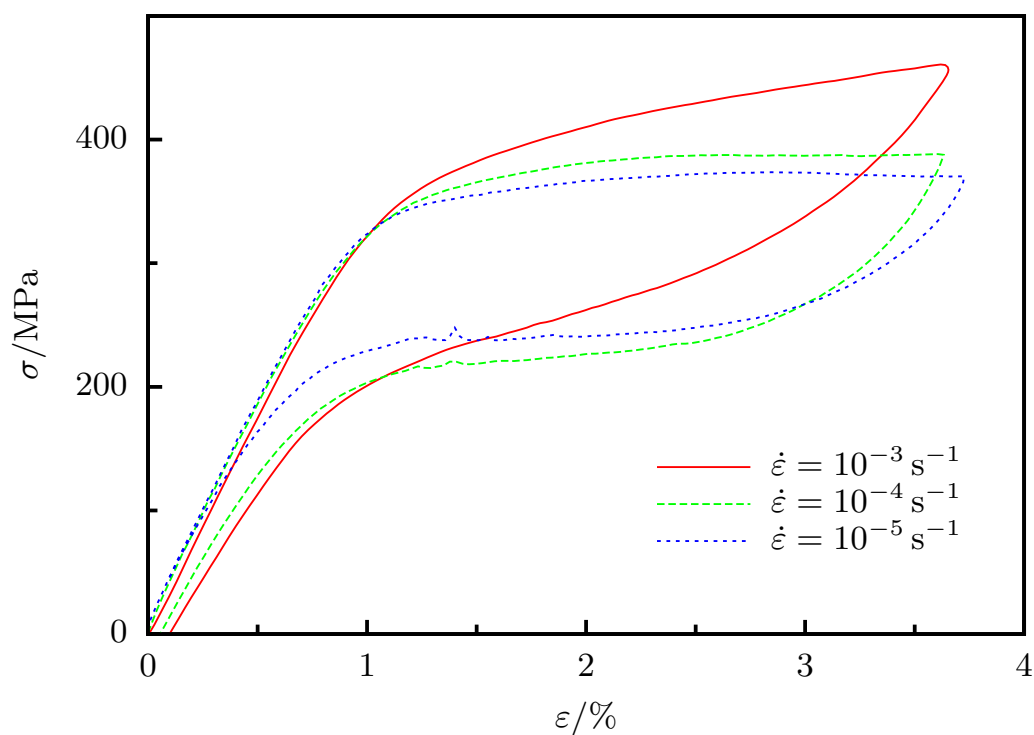
6.2.1 Comparison between non-isothermal and isothermal tests

In this section, three different types of experiments are discussed, two of which are simple uniaxial tests and the third one is a combined or two-dimensional test. For each experiment type, the isothermal and non-isothermal material behavior are compared. The given data pertains mechanical and thermal data so that, for each stress-strain or akin diagram, the respective temperature diagram is shown. At the beginning, the uniaxial tension tests are presented. These experiments can be directly linked to the aforementioned uniaxial wire experiments of Lin and Tobushi (Lin, P. et al. (1996b); Tobushi, H. et al. (1998)) representing a generalization of their findings, which, in anticipation of the following section, are rendered valid even for three-dimensional specimen geometries. Consecutively, some simple torsion tests are depicted while at the end of this section, two-dimensional box experiments are treated.

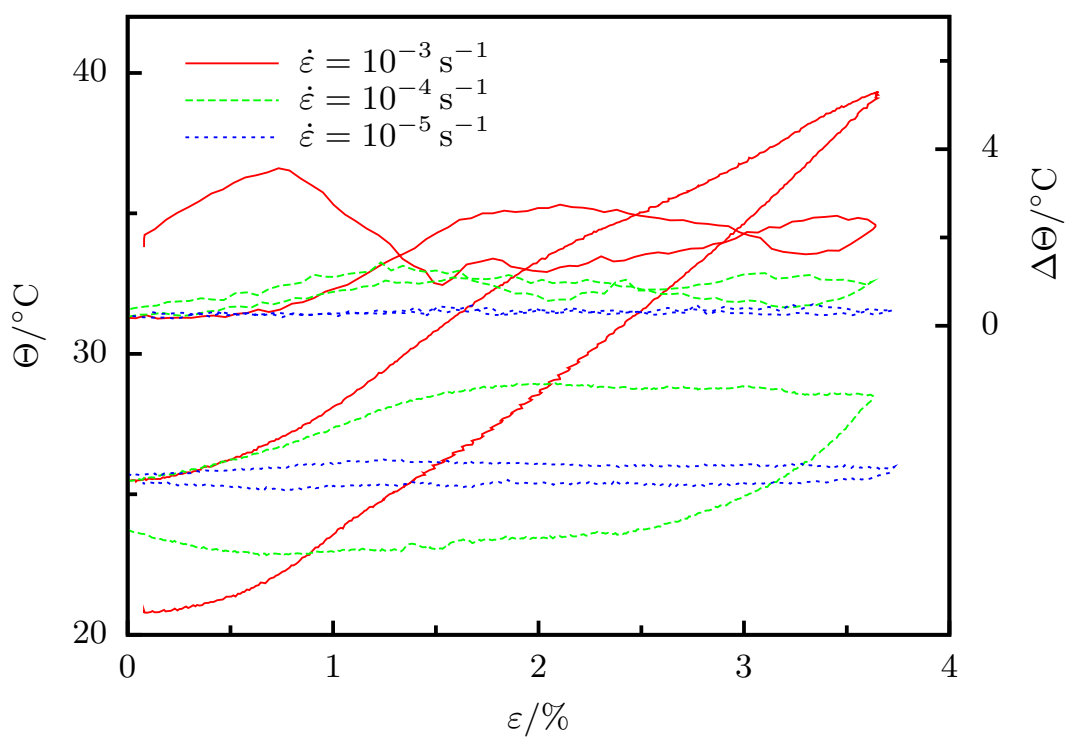
6.2.1.1 Simple tension

Three different strain rates are applied for the simple tension experiments ranging from $\dot{\epsilon} = 10^{-5} \text{ s}^{-1}$ via $\dot{\epsilon} = 10^{-4} \text{ s}^{-1}$ to $\dot{\epsilon} = 10^{-3} \text{ s}^{-1}$. Thus, two decades of strain rates are considered. In this regard, mechanical processes, which feature the lowest applied strain rate ($\dot{\epsilon} = 10^{-5} \text{ s}^{-1}$) are commonly regarded as being quasi-static. The maximum strain is chosen to be $\epsilon_{\max} = 3.5\%$, which is well below the end of the pseudoelastic hysteresis, see Figure 6.5.

¹⁰ A strain rate of $\dot{\epsilon} = 10^{-4} \text{ s}^{-1}$ is applied by Helm.



(a) Stress-strain diagram



(b) Temperature-strain diagram

Figure 6.14: Uniaxial tension tests for different strain rates, starting at room temperature

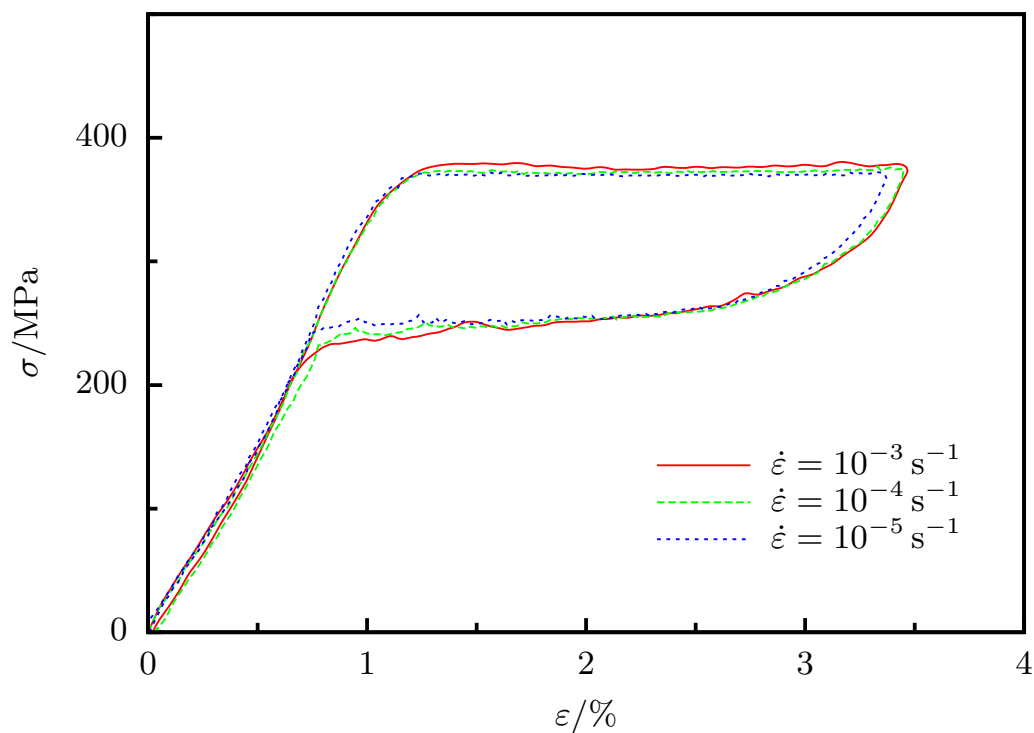
The material response under non-isothermal conditions is illustrated by Figure 6.14. Here, Figure 6.14(a) comprehends the stress-strain curves for the different strain rates while Figure 6.14(b) represents the respective temperature-strain diagram. Furthermore, as a measure of the local heterogeneity of the specimen temperature field, the temperature difference between highest and lowest temperature reading of the utilized thermocouples ($\Delta\Theta$) is given as a function of time, 6.14(b). Consequently, this curve immanently features positive values. As announced in Section 5.5, the ideal control provoking locally isothermal conditions, hence, leading to a $\Delta\Theta$ -curve, which coincides with the zero line, is infeasible so that, for temperature controlled tests, these curves can be used for an estimation of the quality of the applied setup.

It is evident from Figure 6.14(a) that the slope of the stress “plateau” steepens for higher strain rates. Simultaneously, the reverse transformation stress values are shifted to lower values with respect to the forward transformation stress curve, thus, yielding a larger hysteresis for larger strain rates. This cannot be directly distinguished from the curve for $\dot{\epsilon} = 10^{-3} \text{ s}^{-1}$ but it is obvious for the two other stress progressions.

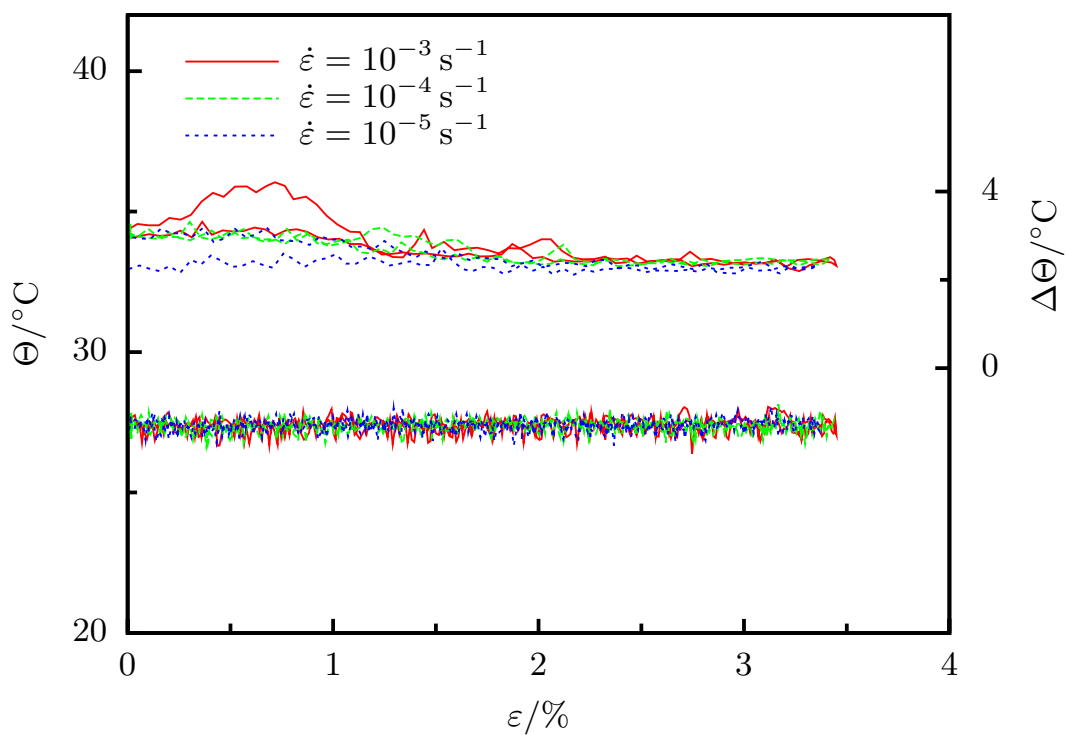
Naturally, a higher rate of latent heat is generated for higher strain rates. Since the amount of heat transfer per unit time between the specimen and the environment is finite, the specimen gets significantly warmer for the higher strain rates, leading to a maximum heating of 13 K for the case of $\dot{\epsilon} = 10^{-3} \text{ s}^{-1}$ and only a slight increase of approximately 1 K for the lowest strain rate ($\dot{\epsilon} = 10^{-5} \text{ s}^{-1}$). Due to the strong heterogeneity of the transformation process, the local temperature heterogeneity is largest for the case of a high strain rate. Furthermore, the local temperature heterogeneity occurs most pronounced at the end of the reverse transformation.

In Figure 6.15, the respective diagrams for the isothermal test conditions are given. Figures 6.15(a) and 6.15(b) illustrate the stress-strain and temperature-strain behavior, respectively. It is obvious from the temperature-strain diagram that the mean specimen temperature is kept constant at 27.5°C. In this context, it is of further interest to inspect the $\Delta\Theta$ -curves in detail in order to estimate the quality of the temperature control, as stated before. Different from the respective curves for the non-isothermal conditions, the $\Delta\Theta$ -curves in Figure 6.15(b) are almost identical for the different strain rates, neglecting the larger local temperature heterogeneity at the end of the reverse transformation for the case of $\dot{\epsilon} = 10^{-3} \text{ s}^{-1}$. A qualitatively similar heterogeneity can be observed for the same strain rate under non-isothermal conditions as well. However, the local heterogeneity for the macroscopically isothermal conditions can be quantified as being in the order of 3 K.

It is evident in Figure 6.15(a) that the stress-strain curves are identical for the different strain rates. The plateaus exhibit the same slope and the hystereses coincide. Consequently, under the applied isothermal conditions the material behavior is independent of strain rate for the given strain rate range. Moreover, it is straightforward to claim that the achieved, macroscopically isothermal con-



(a) Stress-strain diagram



(b) Temperature-strain diagram

Figure 6.15: Uniaxial isothermal tension tests for different strain rates

ditions are effectively isothermal for the transformation process. Consistently, the quality of the temperature control is approved.

6.2.1.2 Simple torsion

For the torsional tests, three different strain rates in the non-isothermal case and two strain rates for the isothermal case are applied. The experiments are strain controlled. Together with the usage of a timed sequence of strain setpoints, the tests are strain rate controlled. As measures of strain and stress, von-Mises equivalent quantities are used, see Footnote 2 on page 29. The maximum strain is $\gamma' = 3.5\%$ for each experiment.

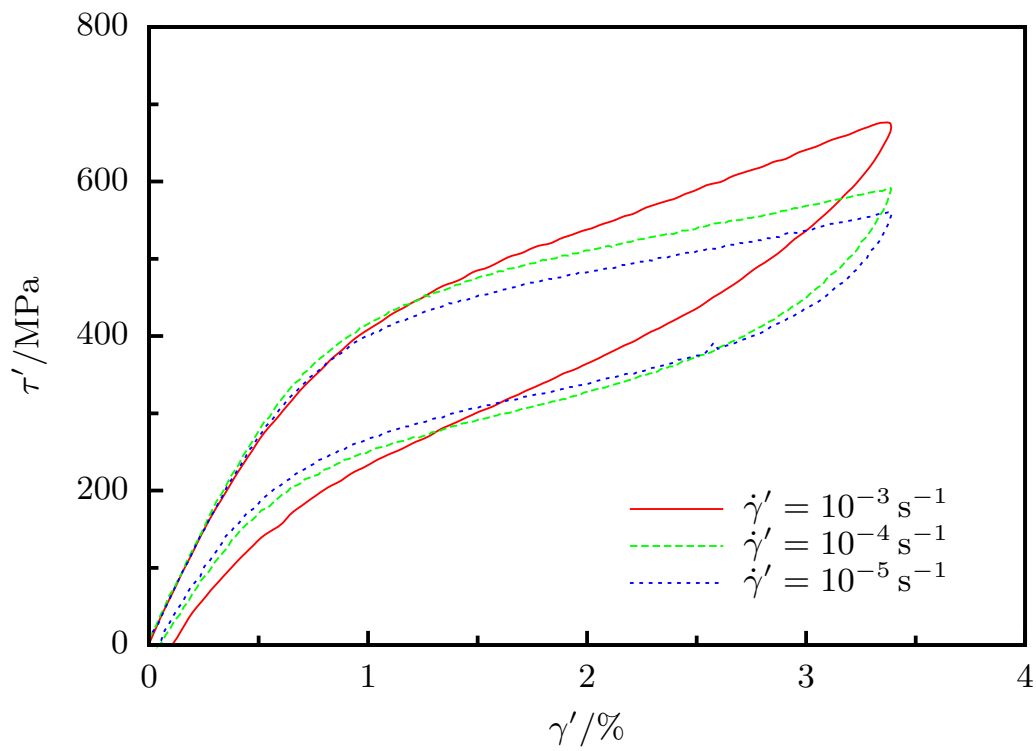
The material response is displayed in Figure 6.16. Analogous to the tensile case, high strain rates effectuate a high temperature increase (up to 13K) and a transformation stress shift. Again, hystereses get larger due to the strong temperature sensitivity of the material, which can be observed best for the cases featuring the lower strain rates, since for the highest strain rate the complete hysteresis is steepened so that the respective comparison is rendered impossible at a first glance. Other than in the tensile case, the largest local temperature heterogeneity occurs at the end of the forward transformation.

The isothermal behavior of simple torsion tests is given in Figure 6.17. This time, only two distinct strain rates are applied. Nevertheless, the chosen strain rates lead to significantly different stress-strain curves under non-isothermal conditions. For each experiment, the specimen temperature is held constant at 23°C with the local temperature heterogeneity being in the range of 5 K. The reason for the larger temperature heterogeneity with respect to the tensile tests is the usage of a different hole pattern of the nitrogen nozzles, which are used for cooling¹¹. Nevertheless, even for such a large local temperature variation, the stress-strain curves in Figure 6.17(a) coincide, leading to the notion that, also under these circumstances, effectively isothermal conditions are provided, and the mechanical material behavior is independent of the applied strain rate for the case of torsional loading as well.

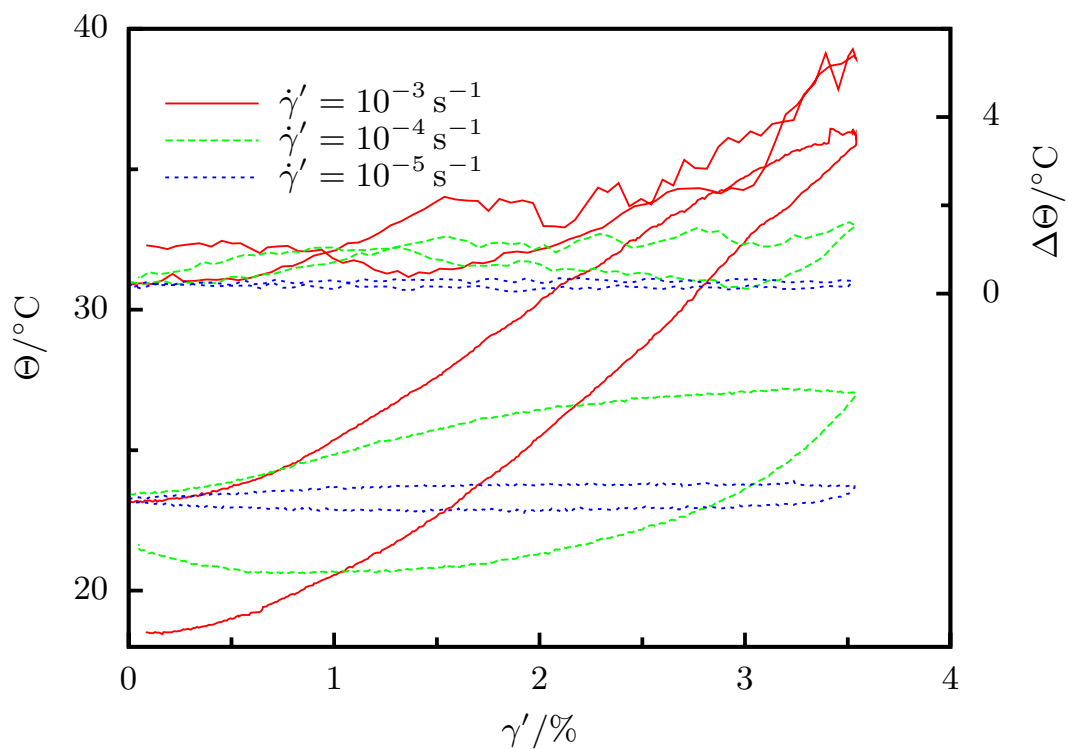
6.2.1.3 Combined box tests in the first axial/torsional strain-strain quadrant

A box-shaped loading path in the first axial/torsional strain-strain quadrant is chosen as representative of two-dimensional experiments. Again, von-Mises equivalent quantities are used. The loading path is implemented so that the maximum torsional and axial equivalent strains are equal and the maximum is given by $\varepsilon_{\max} = \gamma'_{\max} = 2.0\%$ resulting in a square in the von-Mises equivalent strain-strain space. First, the specimen is loaded in axial direction until the maximum strain value is reached. Subsequently, the axial strain is held constant while the specimen is distorted up to the maximum shear strain. The unloading is realized accordingly in the following order, first, axial, then torsional unloading.

¹¹See Section 5.3 for further details on the application of nitrogen.

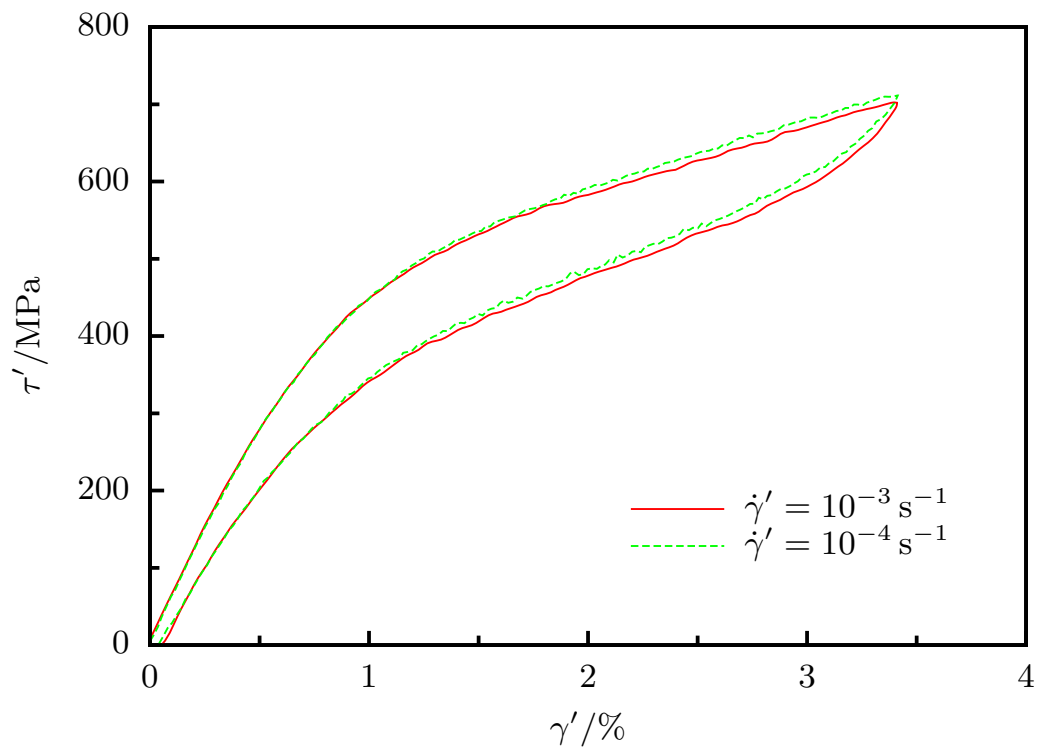


(a) Stress-strain diagram

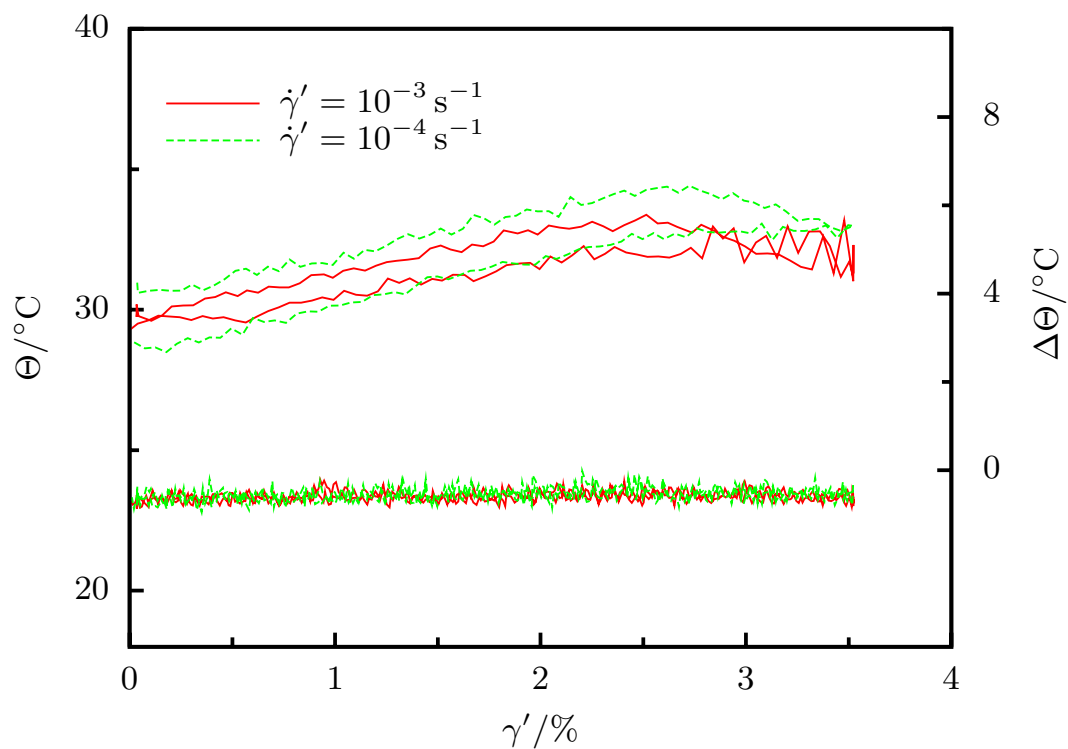


(b) Temperature-strain diagram

Figure 6.16: Uniaxial torsion tests for different strain rates on a HT 2 specimen, started at room temperature



(a) Stress-strain diagram



(b) Temperature-strain diagram

Figure 6.17: Uniaxial isothermal torsion tests for different strain rates on a HT 2 specimen

Loading velocities, which span two decades of strain rate, are applied with $\dot{\epsilon} = 10^{-5} \dots 10^{-3} \text{ s}^{-1}$.

Figures 6.18, 6.19, and 6.20 present the mechanical and thermal behavior of the specimen material for the box test under non-isothermal conditions. While Figure 6.18(a) illustrates the control path, i.e., the strain-strain progression, Figure 6.18(b) shows the respective stress-stress response. The stress-strain behavior in axial and torsional direction can be viewed in the subsequent figure (6.19).

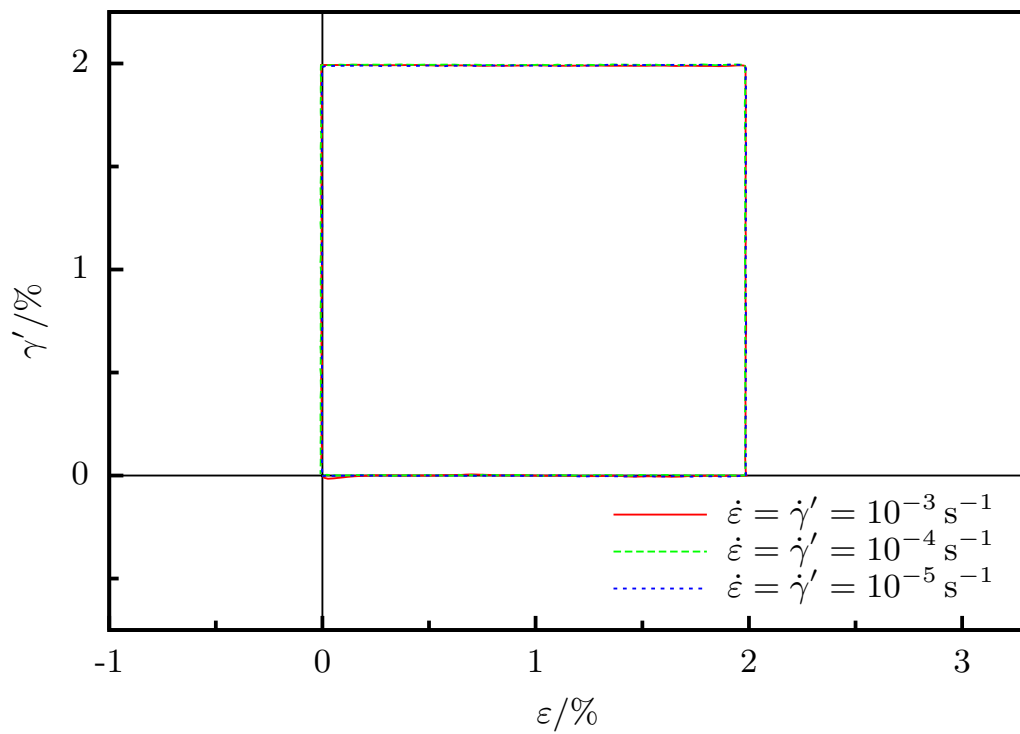
Similar curves for non-isothermal conditions have been reported by Helm, D. (2001). In the first part of the box test, the loading corresponds to the uniaxial case of simple tension exhibiting the behavior discussed in Section 6.2.1.1. Afterwards, when the specimen is loaded in torsional direction, the axial stress continuously decreases, which motivates the notion that the forward transformation may be ascribed to an equivalent stress measure, since one stress component reduces while the other is increased. At the beginning of the axial unloading process, a shear stress dip is obvious. Different from the findings in Helm, D. (2001), the renewed increase of the shear stress does not correspond to a change of the axial stress direction. However, during axial unloading the normal stress indeed migrates into the compression domain. A continuous increase of the shear stress after the dip is evident until the shear strain is reduced, resulting in a concurrent decrease of the shear and the compressive stress.

These diagrams show that the conclusions drawn in the case of uniaxial experiments can be analogously applied to the two-dimensional test. Once more, the higher the strain rates, the larger is the specimen temperature rise, Figure 6.20(a). Consequently, a transformation stress shift takes place so that hystereses get larger for higher strain rates even though this behavior is not as pronounced as in the uniaxial cases due to the lower overall strain level. Moreover, the local temperature heterogeneity is larger for the higher strain rates.

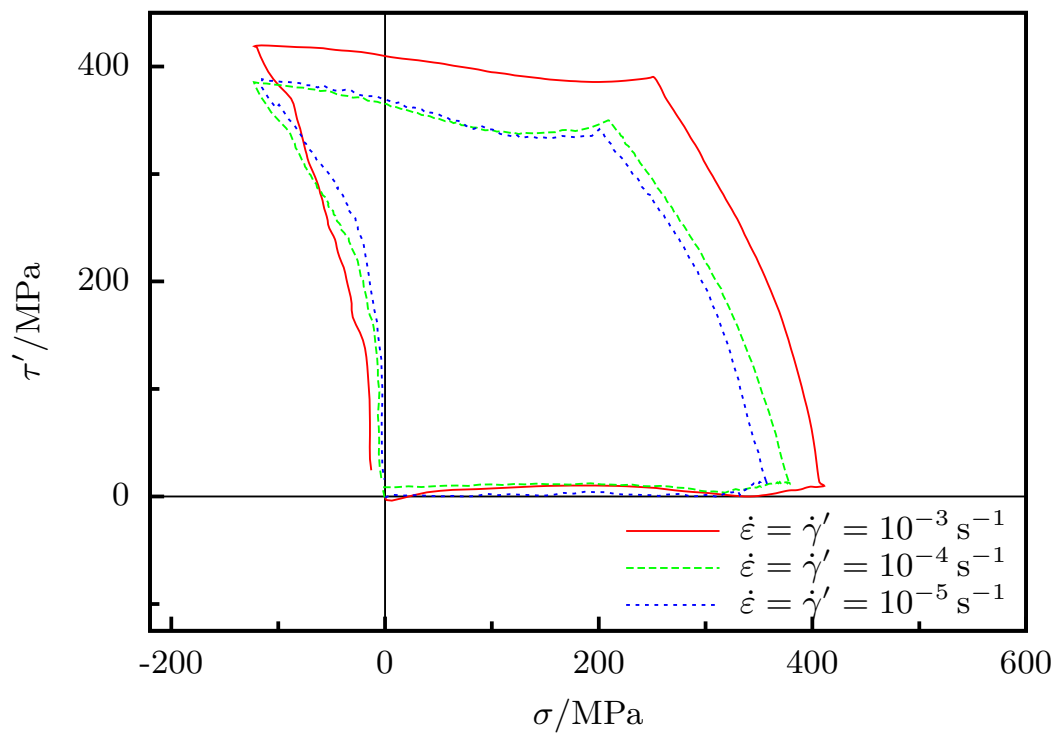
The material behavior of the respective isothermal experiments is examined in the following, see Figures 6.21 - 6.23. Clearly, the stress response is identical for the different strain rates. Analogous to the uniaxial cases, this is ascribed to the isothermal conditions with the macroscopic mean temperature being constantly kept at 27.5°C. Irrespective of two outliers, the local temperature heterogeneity (Figure 6.23(b)) is constant for all three experiments featuring an order of 2 K. Due to the stress response and the constant temperature heterogeneity, the macroscopically isothermal conditions can be regarded as effectively isothermal.

6.2.1.4 Conclusions

As a concluding remark, it can be accounted that the specimen material shows no strain rate dependence within the examined strain rate range. This does not hold true only for uniaxial cases and one-dimensional wire-like specimens but also for complex loading paths and complex specimen geometries. Moreover, the applied temperature control scheme, though only capable of realizing macroscopically isothermal conditions, can be used for implementing thermal

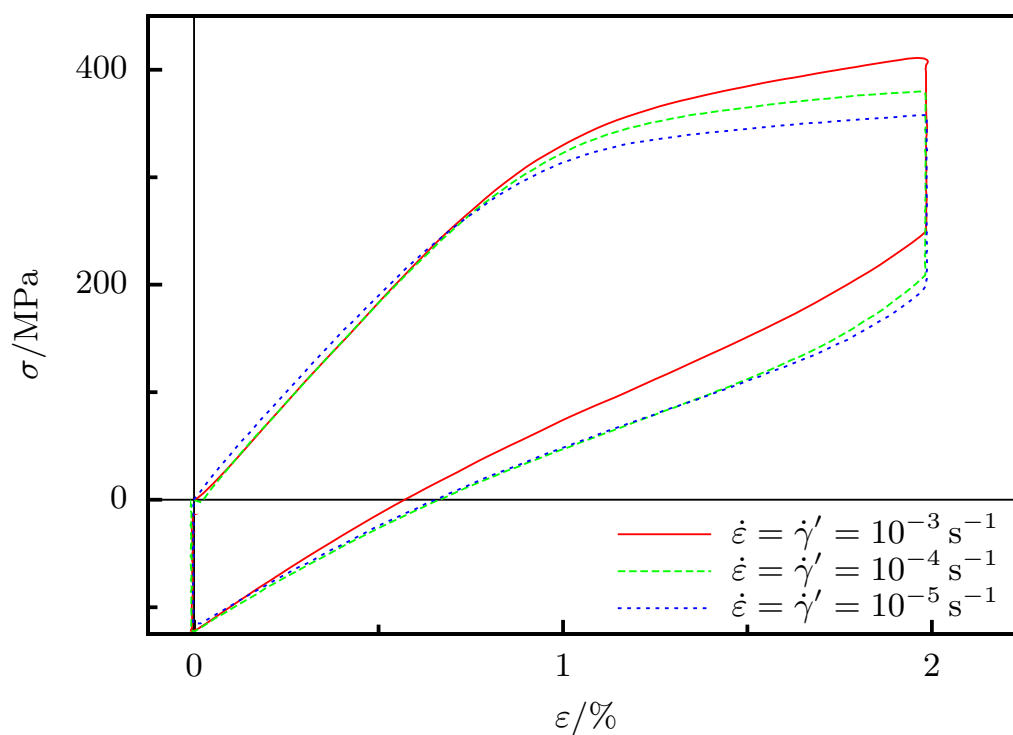


(a) Strain-strain diagram

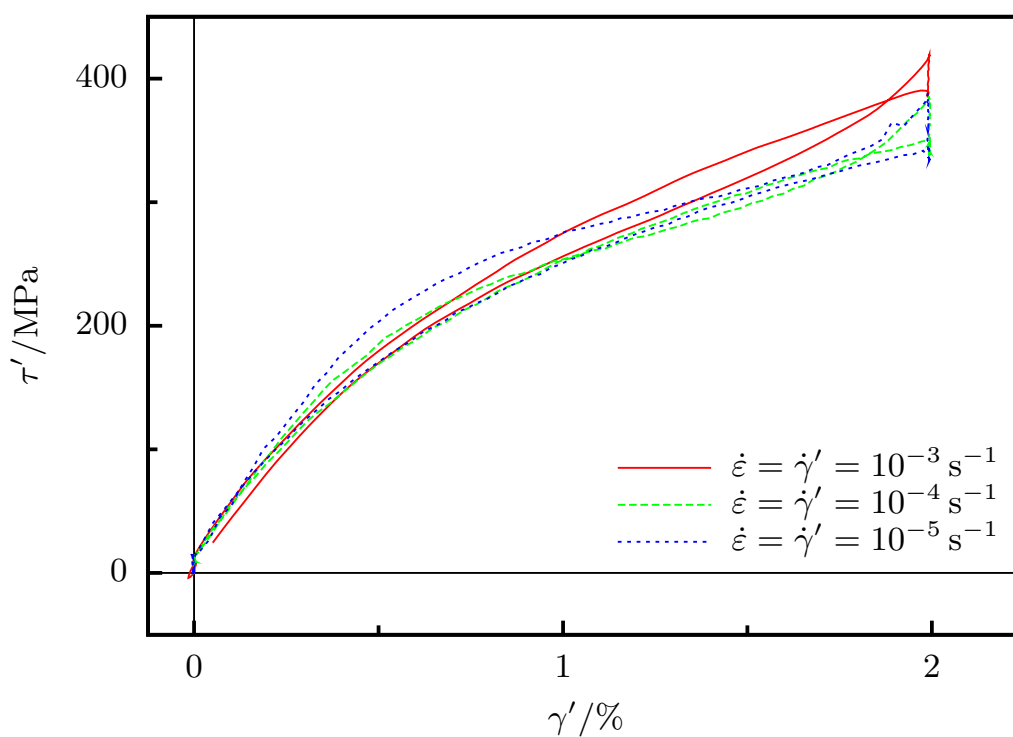


(b) Stress-stress diagram

Figure 6.18: Combined box test for different strain rates, starting at room temperature; strain-strain and stress-stress diagram

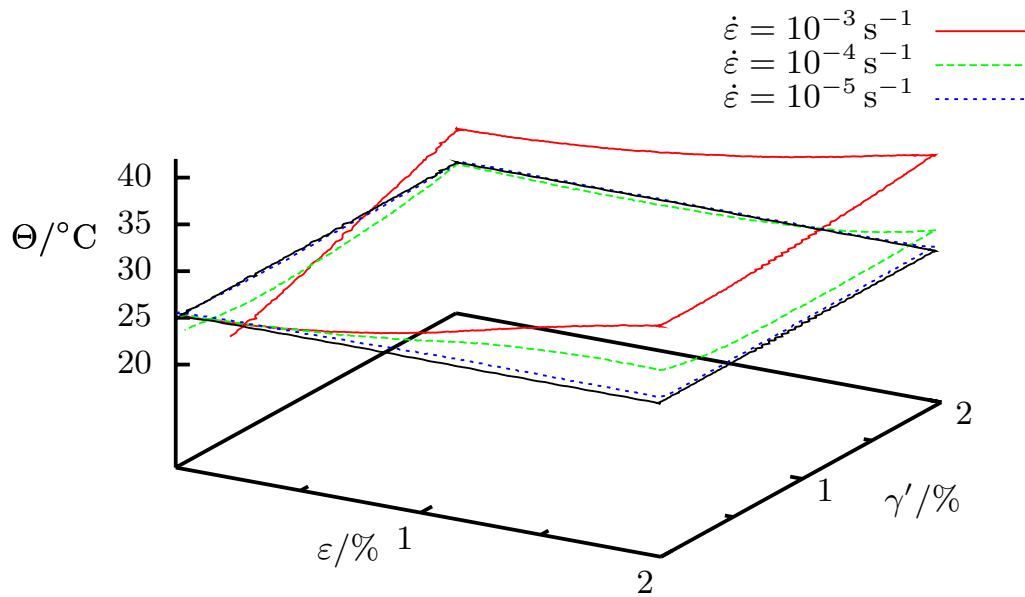


(a) Axial stress-strain diagram

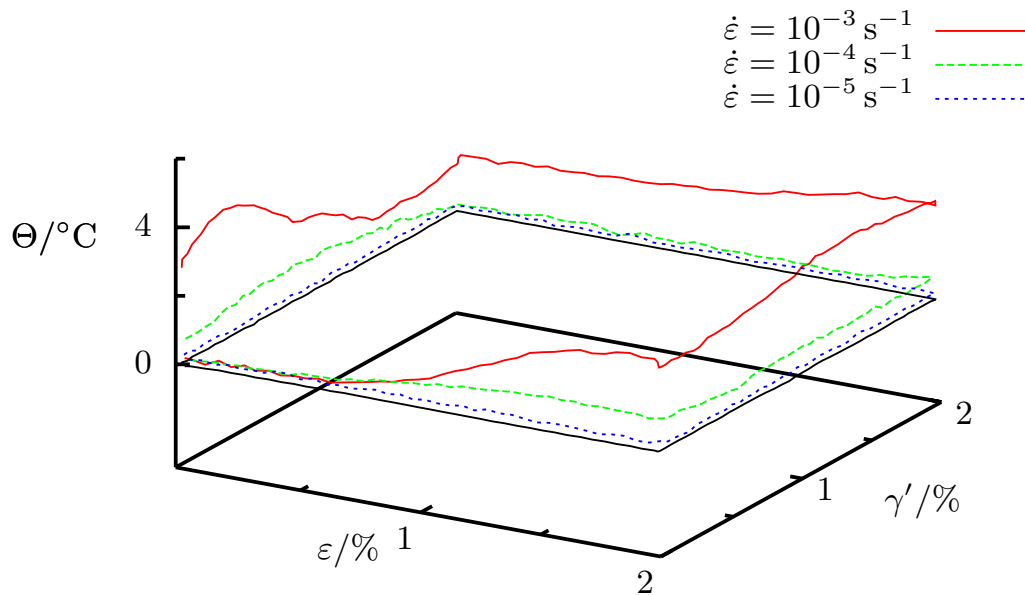


(b) Torsional stress-strain diagram

Figure 6.19: Combined box test for different strain rates, starting at room temperature; axial and torsional stress-strain diagram

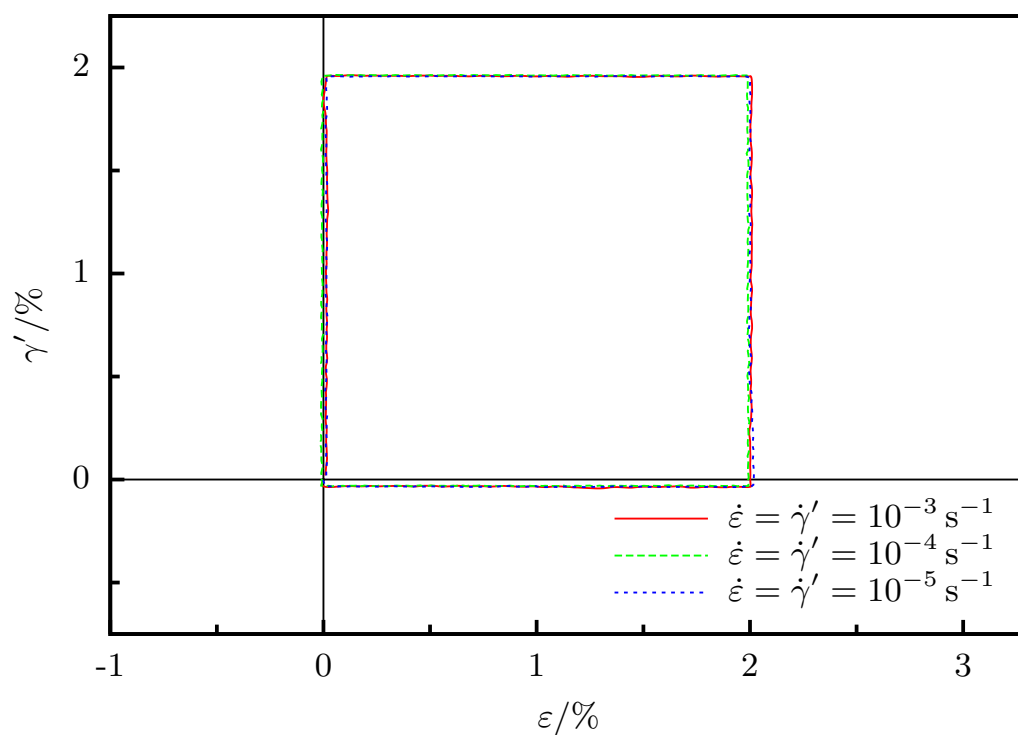


(a) Temperature-strain diagram

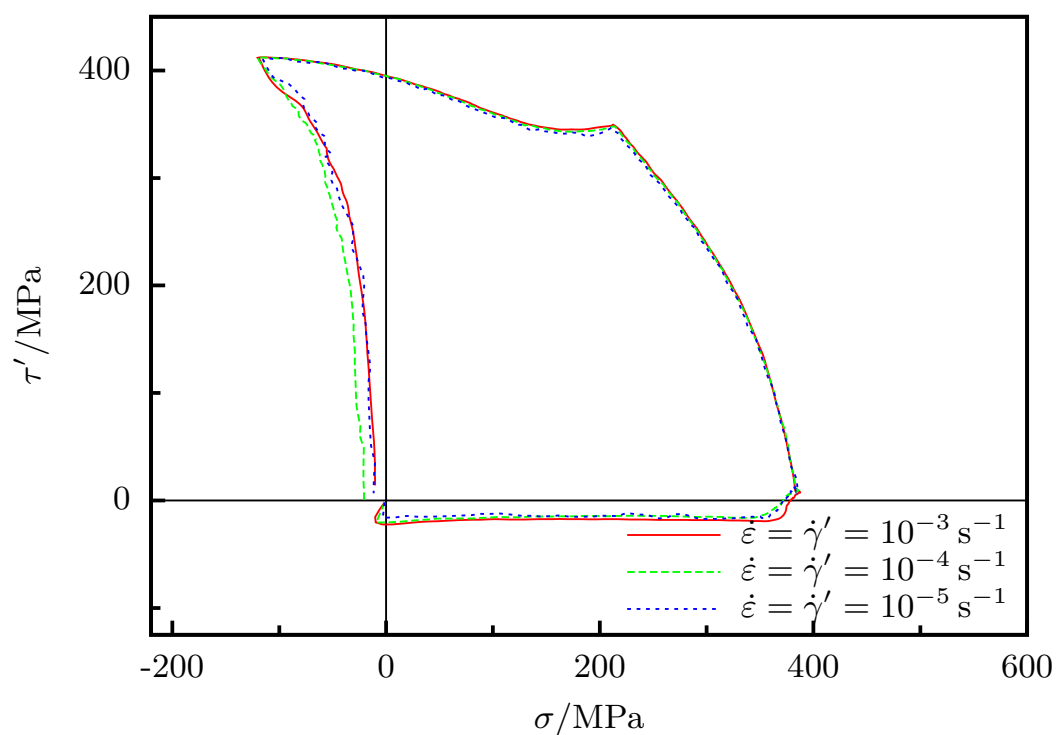


(b) Temperature heterogeneity-strain diagram

Figure 6.20: Temperature response for the combined box test for different strain rates, starting at room temperature

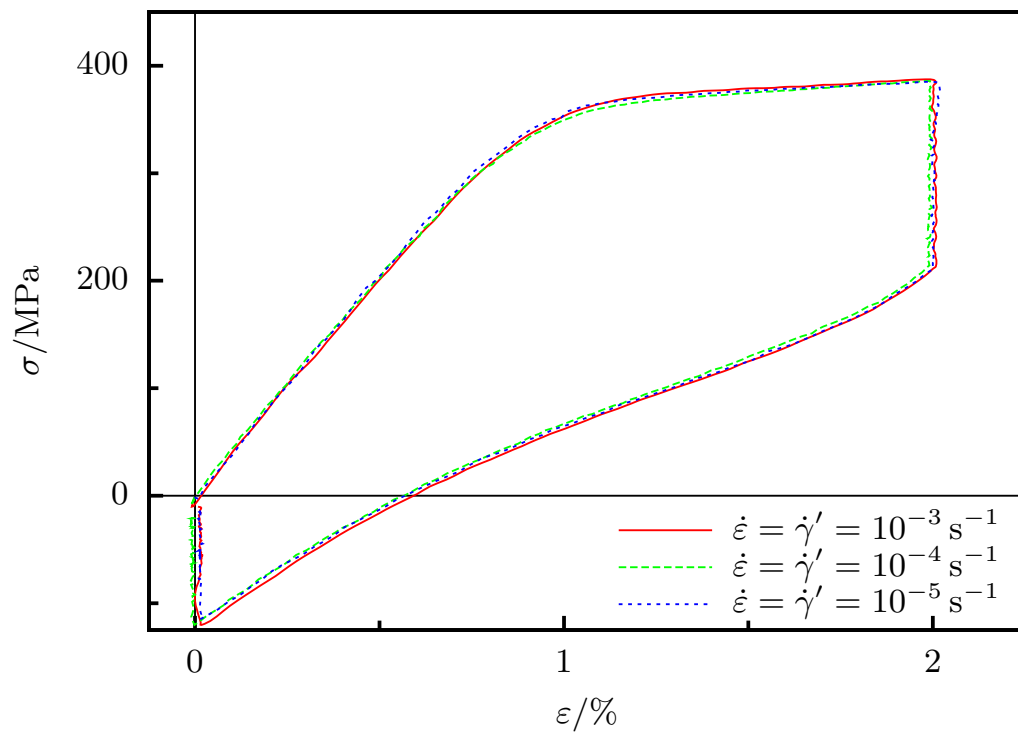


(a) Strain-strain diagram

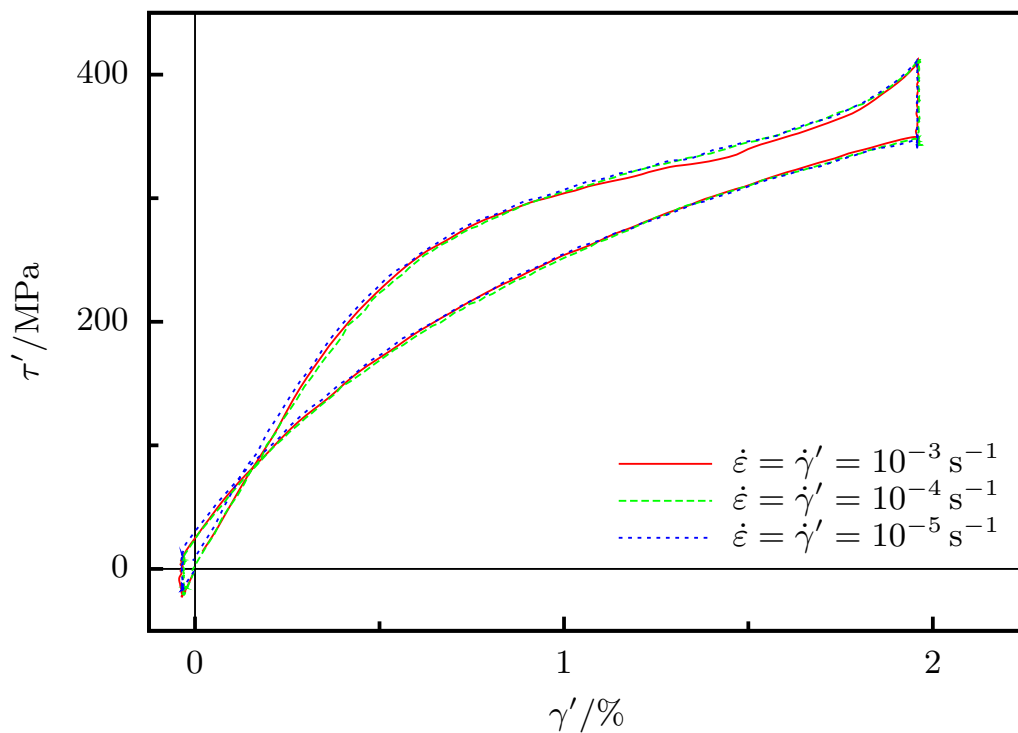


(b) Stress-stress diagram

Figure 6.21: Combined isothermal box test for different strain rates; strain-strain and stress-stress diagram

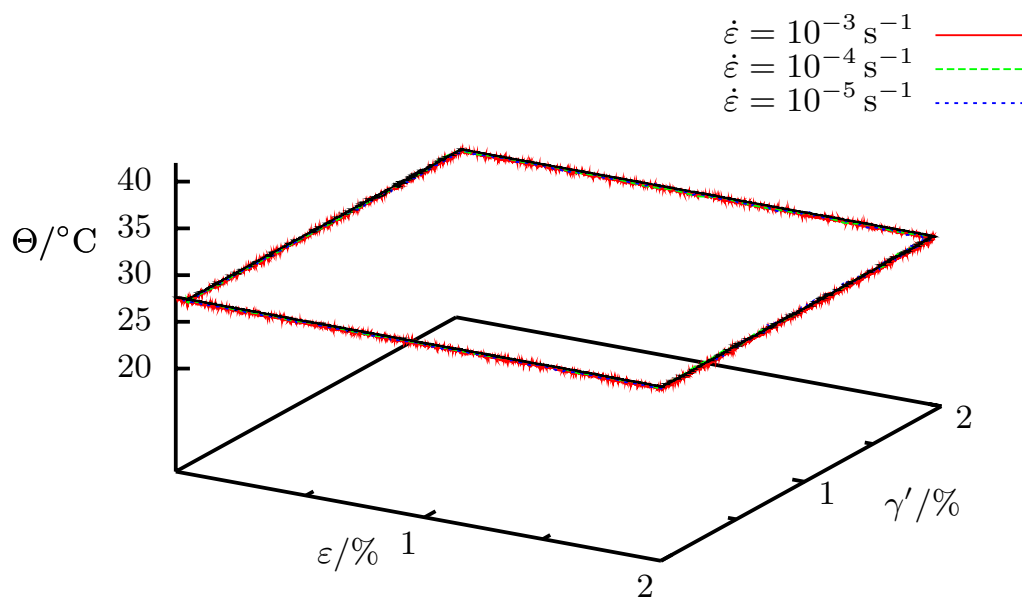


(a) Axial stress-strain diagram

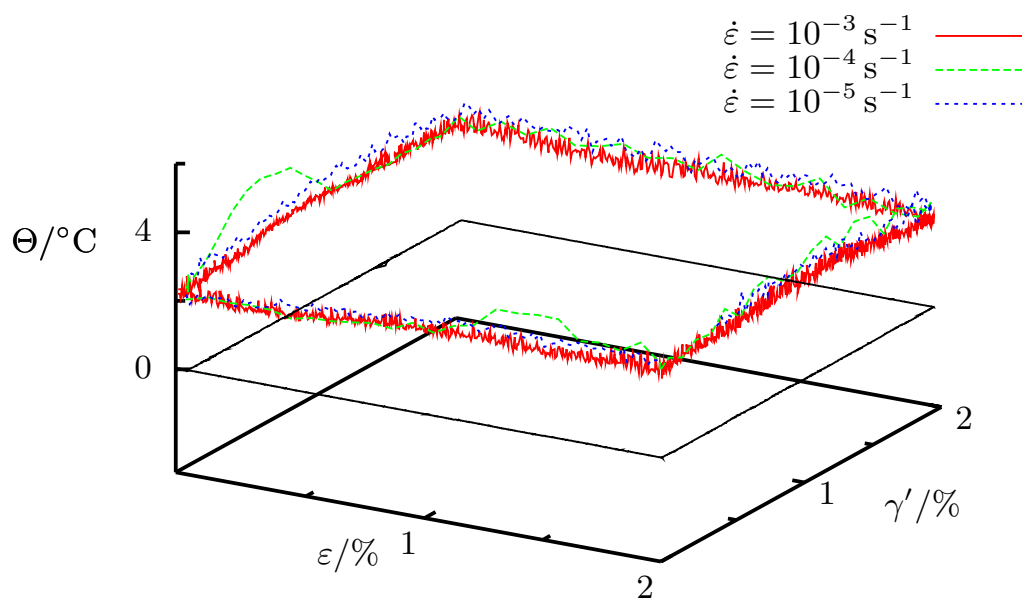


(b) Torsional stress-strain diagram

Figure 6.22: Combined isothermal box test for different strain rates; axial and torsional stress-strain diagram



(a) Temperature-strain diagram



(b) Temperature heterogeneity-strain diagram

Figure 6.23: Temperature response for the isothermal combined box test for different strain rates

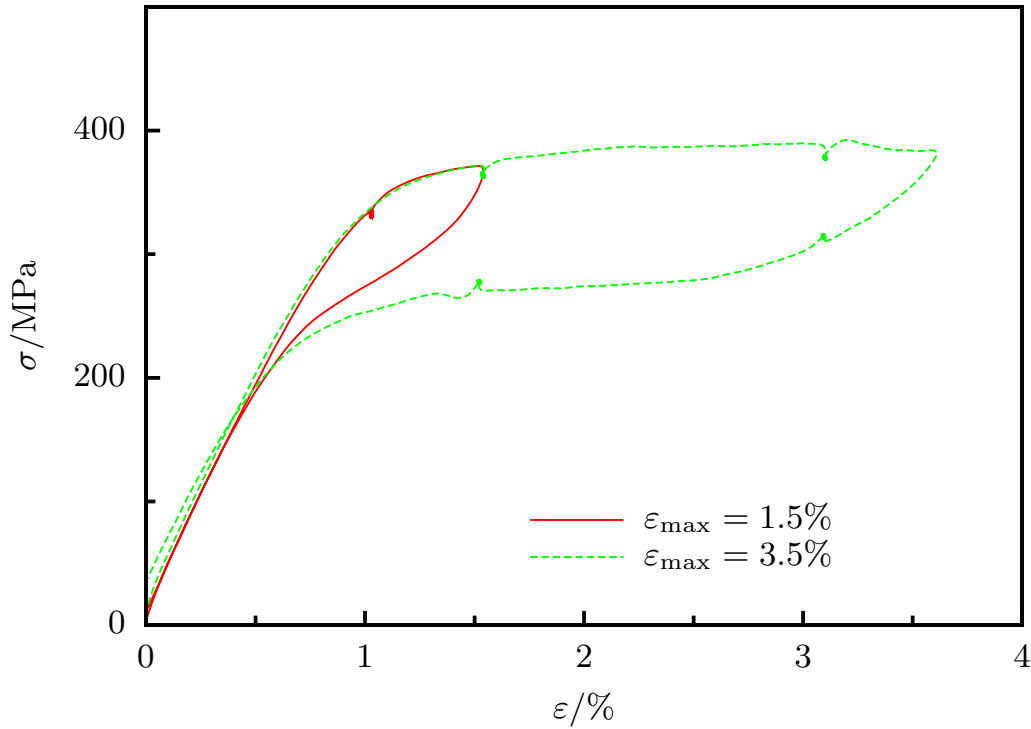


Figure 6.24: Stress-strain diagram for isothermal relaxation tests

boundary conditions, which prove effectively isothermal for the transformation process.

6.2.2 Relaxation behavior

As announced at the beginning of this section, relaxation experiments are conducted under isothermal conditions in order to identify the origin of a relaxation-like material behavior observed on non-temperature controlled relaxation tests, see for instance Helm, D. (2001); Lim, T.J. & McDowell, D.L. (1999). In this context, it is important to decouple the viscous and the temperature induced material behavior. Simple strain controlled tension tests are performed, which are interrupted by strain-hold periods, i.e., the strain is maintained at a constant value. Each strain-hold period takes 900 s. The stress-strain behavior for two of those experiments is shown in Figure 6.24. The applied strain rate is 10^{-3} s^{-1} and the experiment temperature is 27.5°C . Figure 6.25 illustrates the temperature proceeding for the simple relaxation test with a maximum strain of 3.5 % whose stress response is presented in Figure 6.24.

It is obvious (Figure 6.25) that the mean temperature is constant during the whole experiment and that the local temperature difference is constant, too, apart from the first hold period where a very slight increase in the local temperature heterogeneity can be observed. At a first glance, a stress drop is evident

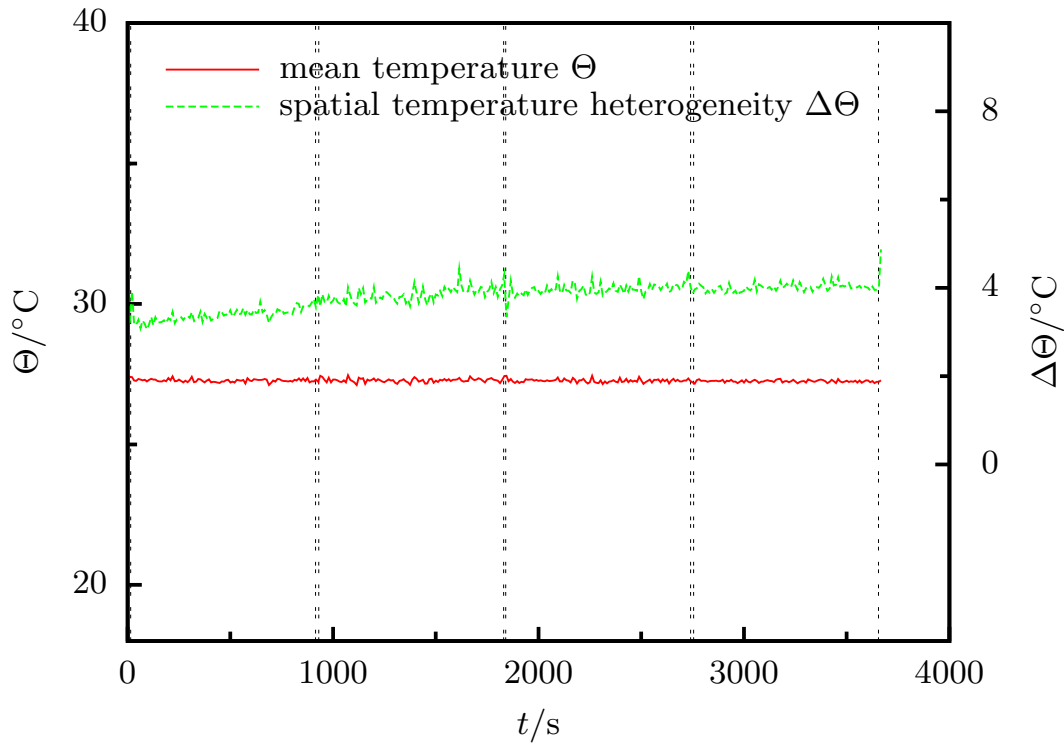


Figure 6.25: Temperature and local heterogeneity of temperature as a function of time for the isothermal relaxation test with $\varepsilon_{\max} = 3.5\%$

in the stress-strain curve (Figure 6.24) for the strain-hold periods, substantiating the notion of a viscous relaxation material response even under isothermal conditions. In order to examine the material behavior more thoroughly, and to elucidate this stress drop, a further postprocessing of the acquired data is mandatory. On this account, stress and strain are plotted as functions of time, Figure 6.26.

Here, as already pointed out, the strain curve is the path of the control variable whereas the stress proceeding represents the material response. The different strain steps are evident with the strain being kept constant at multiples of 1.5%. Consequently, the strain is held at the forward and reverse transformation at strains of 1.5% and 3.0% for 900s each. Since in Figure 6.26 the scale of the stress axis is too large for an estimation of the degree of the viscous material behavior, the stress responses for the strain-hold periods are drawn on a larger scale in figure 6.27.

From upper left to lower right, this figure shows the consecutive strain-hold periods as fluctuations with respect to distinct, appropriately chosen stress reference values. Consequently, the upper diagrams represent strain-hold periods within the forward transformation path while the lower two diagrams show the respective curves for the reverse phase transformation. That way, the stress curves for the four different hold periods can be directly compared on a large stress

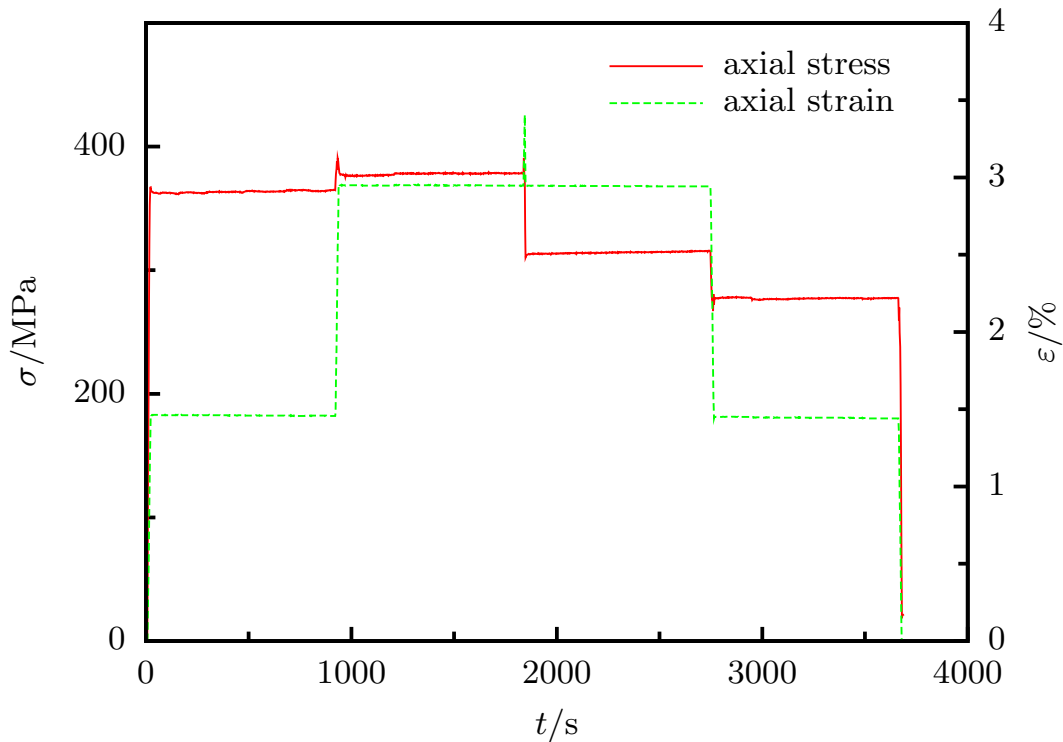


Figure 6.26: Stress and strain as a function of time for the isothermal relaxation test with $\varepsilon_{\max} = 3.5\%$

scale although the stress level of each curve is inherently different. This results from the fact that strain hold periods within the forward and reverse phase transformation are realized.

At first sight, the four distinct stress overshootings at the beginning of each strain-hold period catch the observer's eye. This phenomenon has to be ascribed to the overshooting of the actual strain value, which results from the machine control. Since the machine is electromechanically driven¹², a slight overshooting is inevitable unless a very sluggish control behavior is approved. Consistently, the overshootings correspond to the direction of the changing of strain, leading to a positive overshooting for the two strain hold periods within the forward and a negative overshooting for the two strain hold periods within the reverse phase transformation. Besides, this is the reason why the first impression is when Figure 6.24 is regarded that the material might indeed exhibit some kind of stress relaxation. Moreover, those very small abrupt stress changes in the range of 1-2 MPa during the strain-hold periods have to be attributed to the control action as well. That is, since a digital measuring amplifier¹³ is used, the measuring/control resolution is not infinite. Once these control artifacts are disregarded, it is obvious that a distinctive decrease/increase of the stress level for the strain-

¹²Cf. Section 5.6 for a detailed description of the machine concept.

¹³See Section 5.6 for further details.

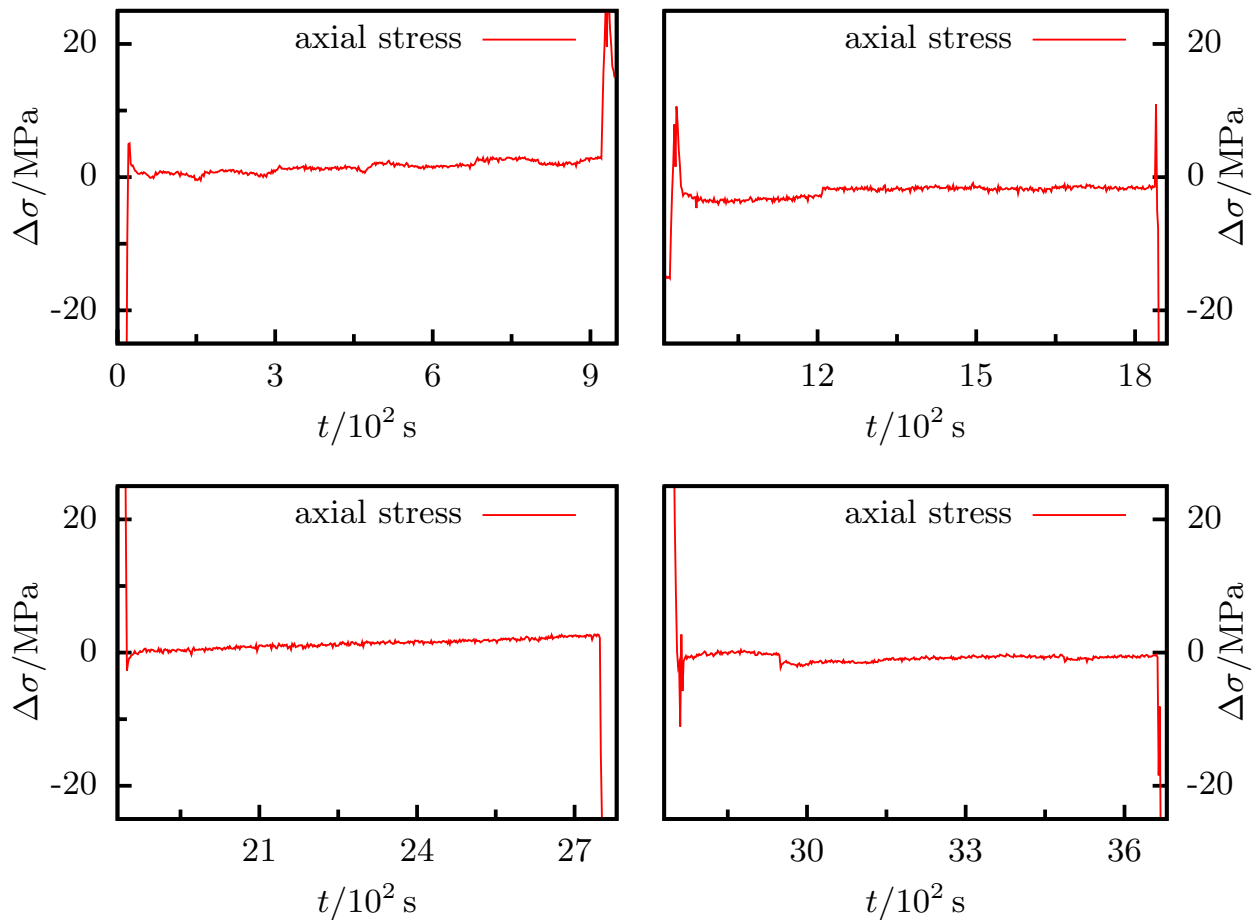


Figure 6.27: Magnified view at the stress progressions during hold times of the relaxation test; stresses are given as fluctuations with respect to a chosen stress reference value, i.e. $\sigma = \sigma_0 + \Delta\sigma$; upper left: first hold period with $\sigma_0 = 362$ MPa; upper right: second hold period with $\sigma_0 = 380$ MPa; lower left: third hold period with $\sigma_0 = 313$ MPa; lower right: fourth hold period with $\sigma_0 = 278$ MPa

hold periods within the loading/unloading path (upper/lower diagrams) due to a viscous relaxation of the specimen material is lacking. Finally, a viscous material behavior, which might be attributed to stress relaxation cannot be observed under isothermal conditions.

6.2.3 Creep behavior

In order to investigate a potential creep behavior of the alloy, simple isothermal tension tests are carried out on different specimens. All these experiments are performed under stress control utilizing a stress rate of 2 MPa/s , which allows for a careful examination of the stress plateau. In this context, it is of special interest to look at the creep behavior within the transformation region, which is

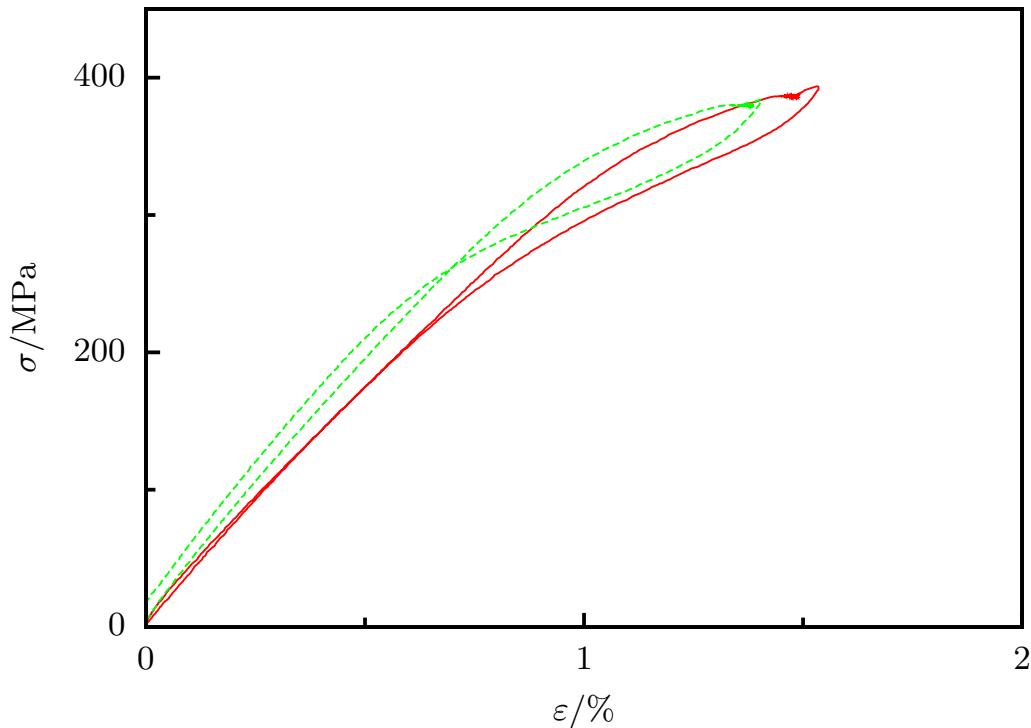


Figure 6.28: Stress-strain diagram for two isothermal creep tests on two different specimens; stress-hold periods at 380 MPa and 387 MPa

why the stress-hold stresses are chosen to be located in the direct vicinity of the transformation start stress.

Figure 6.28 shows the stress-strain behavior of two such simple tension experiments with test temperatures of 27.5°C . The hold stresses of 380 MPa and 387 MPa are kept constant for 600 s and 900 s, respectively. Figure 6.29 presents the corresponding stress and strain progressions as functions of time. In this vein, the chronological order of events is exemplified. Naturally, the stress curves are represented by straight lines, since stress is the control variable, which is set by the controller. After a first increase of the load, the stress is held constant. Subsequently, the specimens are further loaded up to the maximum stress followed by the final unloading. Consequently, stresses and strains of the different experiments can be assigned to one another by their respective experiment durations, which results from the different stress-hold periods of the two experiments. Since the temperature profile is of paramount importance for the development of strain within the transformation region, the temperature progressions, which are measured by all eight thermocouples, are given separately in Figure 6.30 for the 387 MPa hold stress case. Moreover, the calculated mean temperature is depicted as well. Vertical dotted lines mark the beginning and end of the stress-hold periods. Evidently, steady state conditions are realized within the stress-hold period.

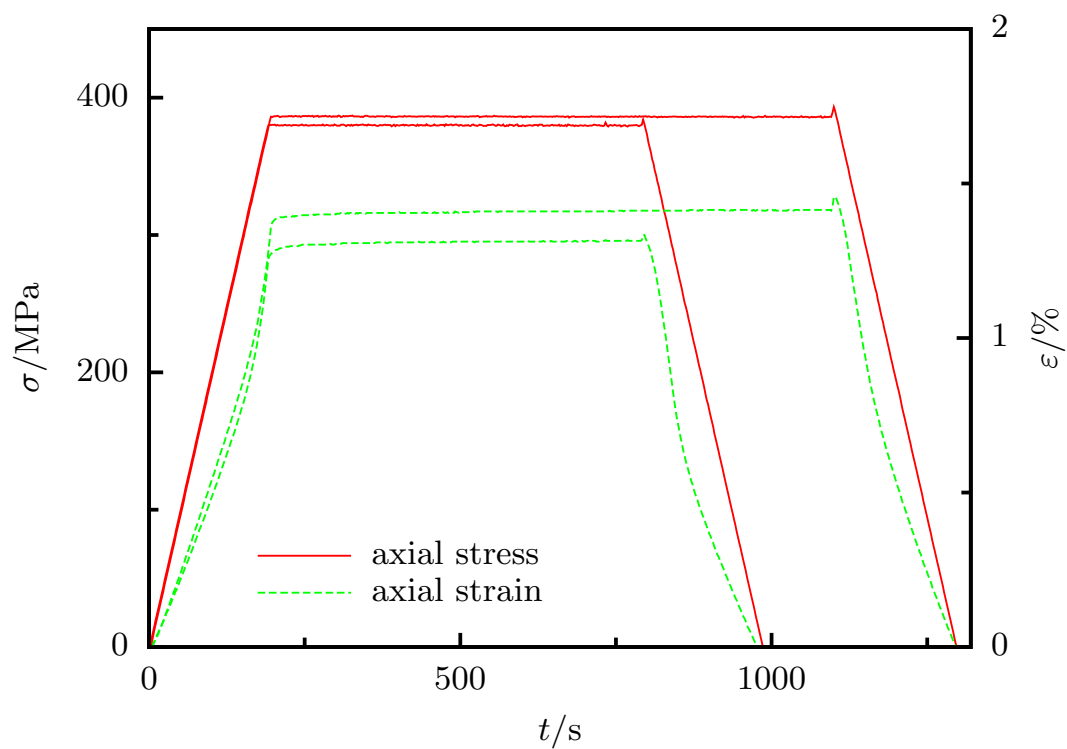


Figure 6.29: Stress and strain as a function of time for the isothermal creep tests

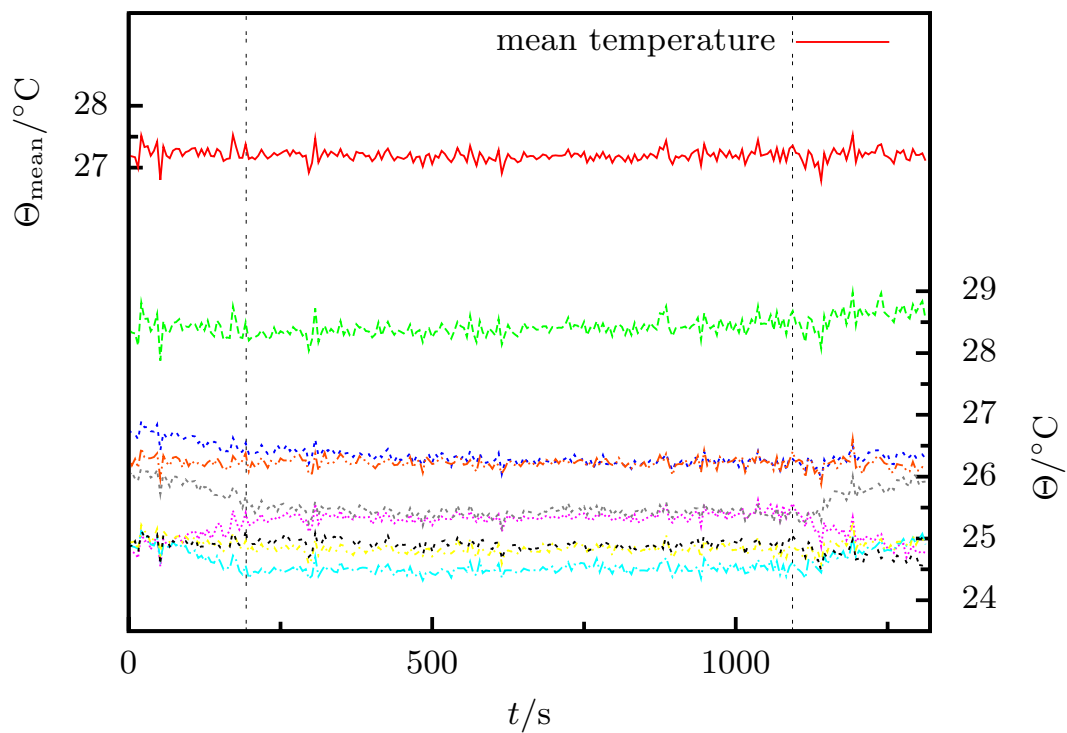


Figure 6.30: Specimen temperatures as functions of time for the case of the 387 MPa hold stress tension test

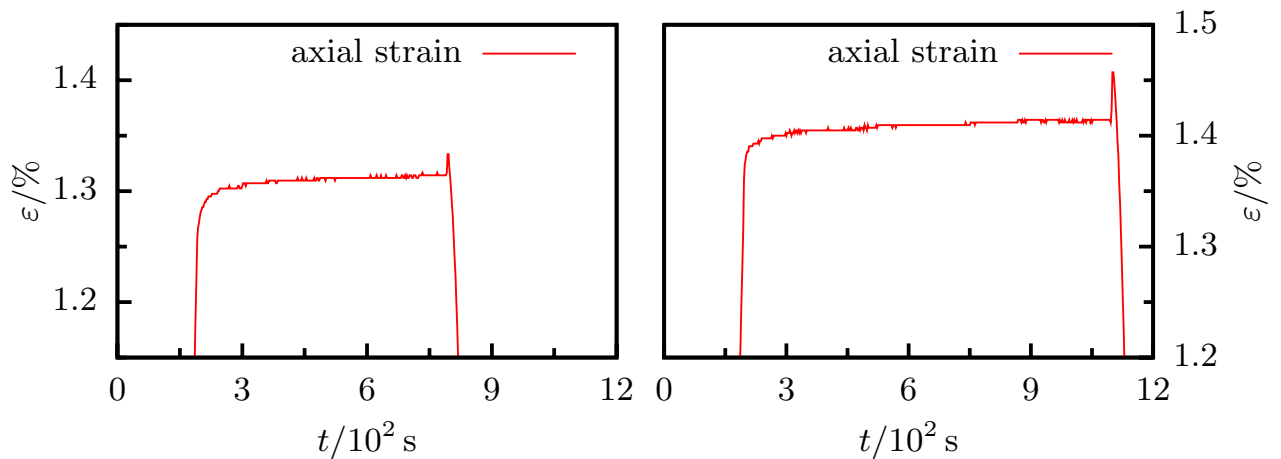


Figure 6.31: Magnified view at the strain progressions during hold times of the creep tests

Figure 6.31 allows a more detailed insight into the respective strain behavior showing the same strain progressions as in Figure 6.29, but plotted on a larger scale, so that only the strain development during the stress-hold periods is presented. It is evident that a certain strain drift is existent. This strain drift, in the order of only a few hundredth of one percent strain, is however relatively small, compared to measurements conducted during non-isothermal experiments commonly found in the literature. [Tobushi, H. et al. \(2003\)](#) report, for instance, that the specimen material transforms for a constant stress under non-isothermal conditions until the end of the hysteresis is reached leading to a pseudo-creep behavior. Furthermore, it is stated that the only reason for this creep-like behavior may be the variation of temperature.

Finally, as repeatedly pointed out before, completely isothermal conditions cannot be realized with the applied setup for the conducted experiments within this work. Fundamentally, even small amounts of heat transfer due to conduction processes are sufficient to shift the local transformation stress to lower values and, hence, to trigger a local transformation of the microstructure, which is embodied by a pseudo-creep behavior of the specimen material. Following this train of thought, the observed strain drift is assumed to be attributed to small local heat transfer processes.

A significantly different behavior can be noted for a third simple tension test whose stress-strain response is given in Figure 6.32. The test temperature is 22°C, and the stress is held constant at multiples of 172.5 MPa with a maximum stress value of 355 MPa. Even in the stress-strain diagram, large pseudo-creep strains are obvious. Again, in order to exemplify the load history, stress and strain are plotted against time in Figure 6.33.

Stress-hold periods are not only inserted during the increase of the loading, as was done in the two already discussed cases, but also in the unloading process.

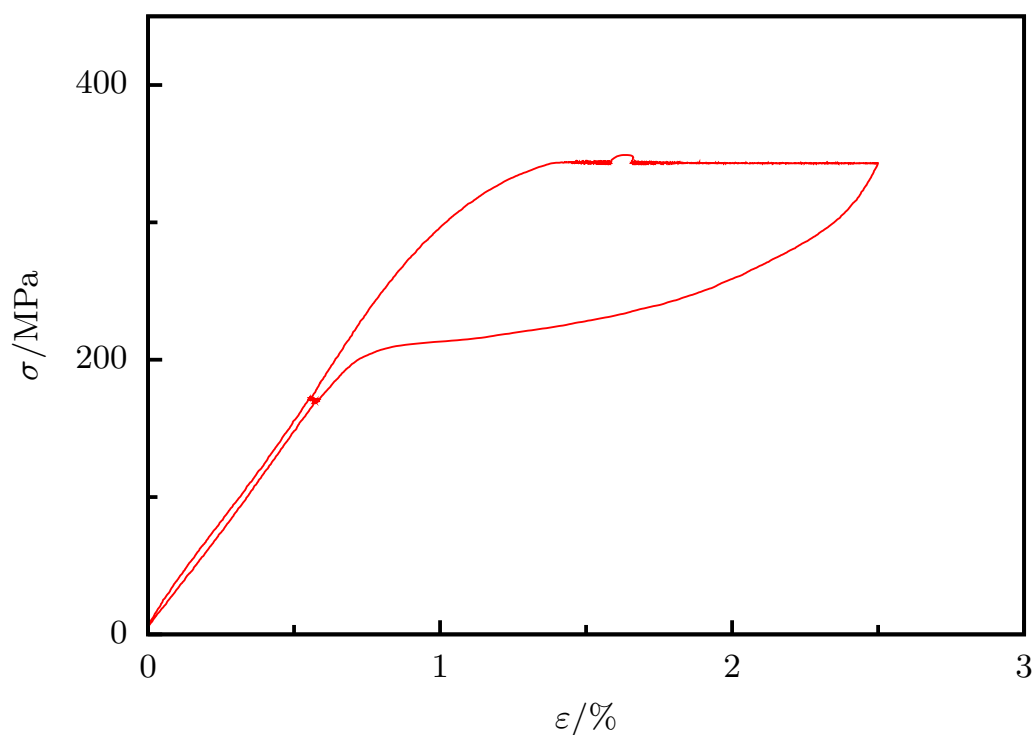


Figure 6.32: Stress-strain diagram for an isothermal creep test; stress-hold periods at multiples of 172.5 MPa; maximum stress 355 MPa

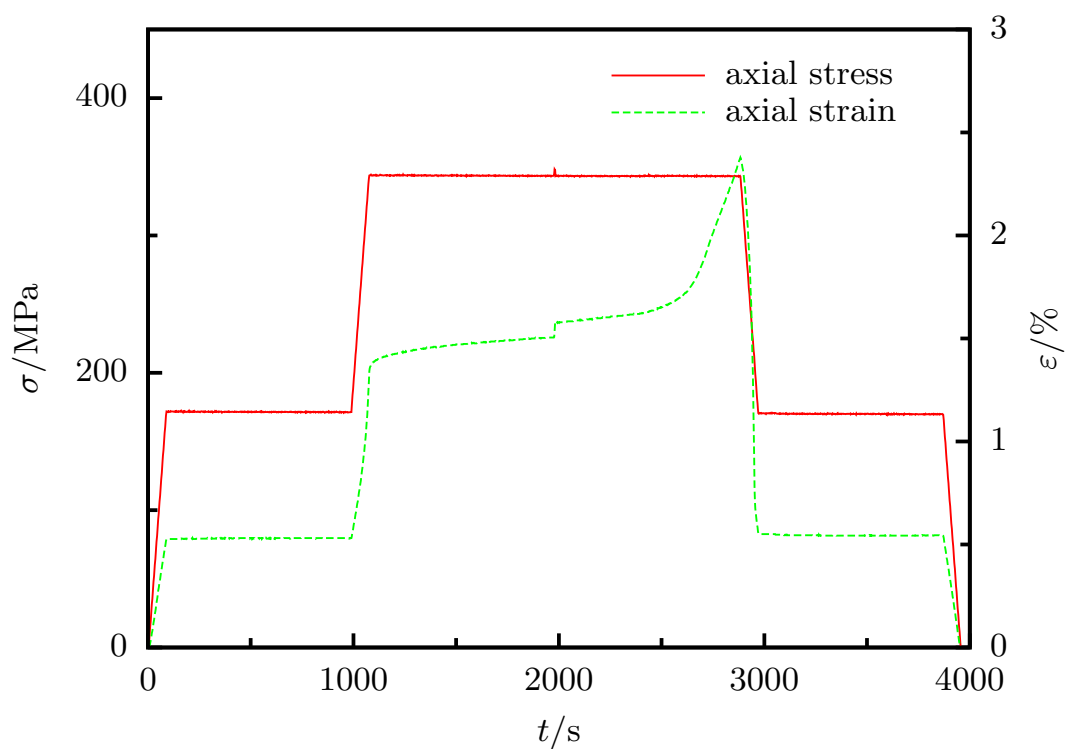


Figure 6.33: Stress and strain as a function of time for the isothermal creep test

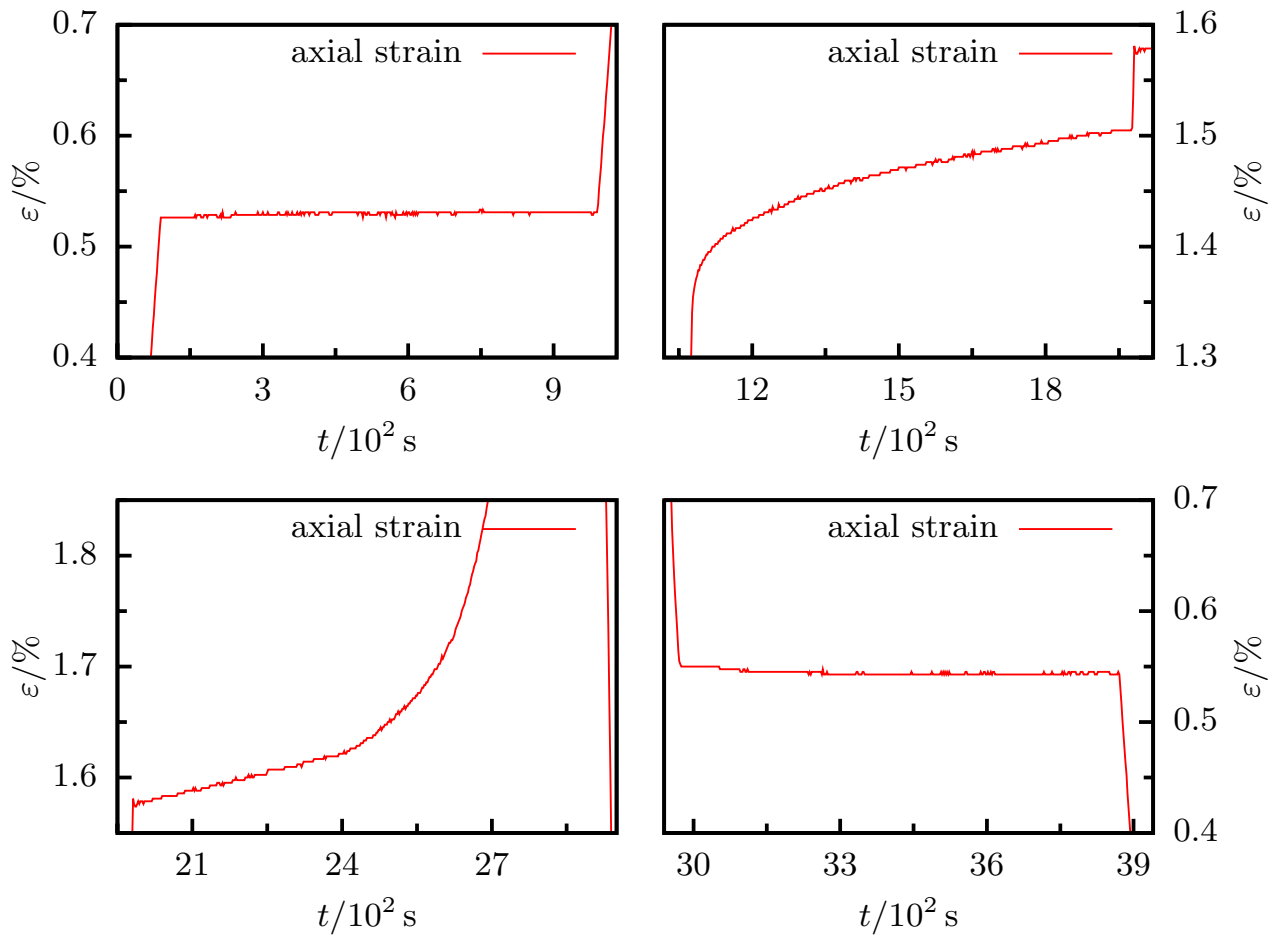


Figure 6.34: Magnified view at the strain progressions during hold times

Concerning the experiment procedure and stress rate, analogous statements hold true with respect to previously made explanations. Even though the scale of Figure 6.33 seems large enough to estimate the creep behavior, in Figure 6.34, the strain development is shown in the same scale as is used for Figure 6.31 to render the different diagrams comparable. Clearly, during the first and the last stress-hold periods a strain drift, which might be ascribed to creep is not existent. Those two stress-hold periods are exemplary for the “elastic” range and the material behavior therein. What is even more intriguing is the strain development during the second and third stress-hold periods, which corresponds to the already shown experiments. Very large strains are accumulated. While the strain development in the second period might look like classical creep, featuring an asymptotic curvature characteristic for primary and steady-state creep, the strain development in the third period is supposed to be attributed to a different cause, since a primary-like creep is absent. Furthermore, the accelerated accumulation of strain, which might look like tertiary creep associated with a self-accelerating softening of the microstructure, does not lead to a damaging

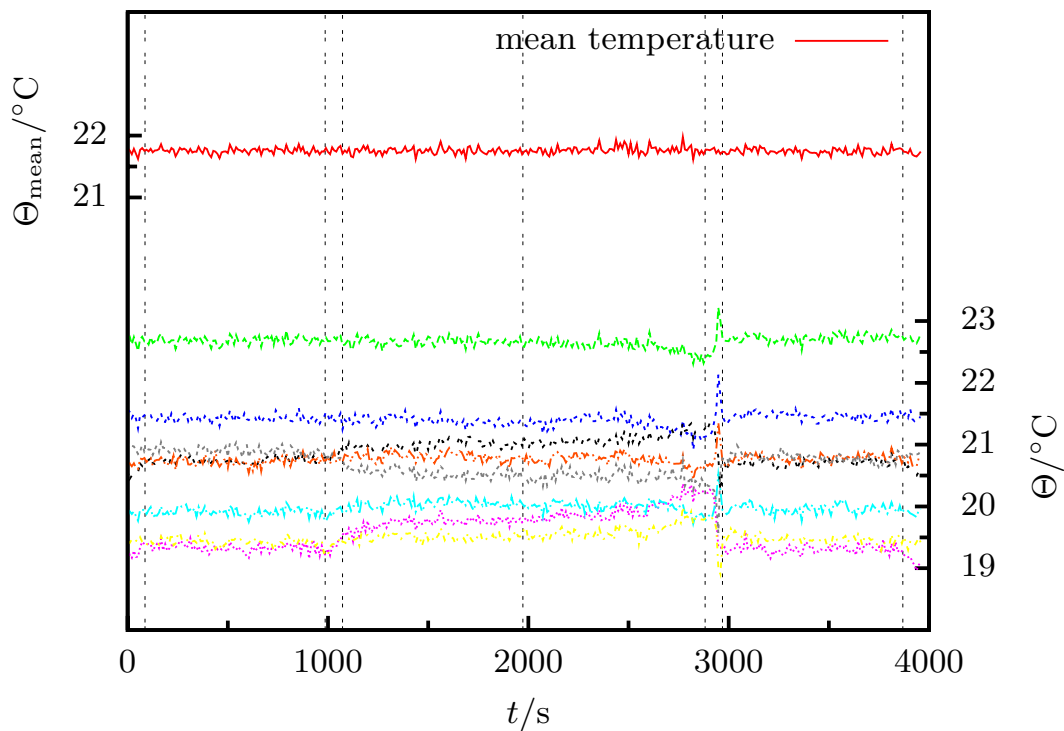


Figure 6.35: Specimen temperatures as functions of time

of the specimen, which is proven by consecutive tests. Apparently, this behavior, which can be observed on other specimens as well, might be triggered by comparably large local temperature fluctuations, which is why the different temperature progressions for this test are presented in Figure 6.35. The same scale as used for Figure 6.30 is utilized. Again, vertical dotted lines mark the stress-hold periods. Fundamentally, time-dependent temperature alterations in the range of 1 K can be observed during the beginning of the second and during the end of the third stress-hold period concurrently representing the periods featuring the largest strain changes. Nevertheless, no such conclusion can be drawn from the progression of the mean temperature exclusively because the mean temperature is constant during the whole experiment. Furthermore, it is impossible to deduce, if there are any even larger time dependent temperature alterations within the specimen, since temperature is measured only at eight distinct locations. Due to the local character of the temperature measuring and control scheme, local effects cannot be neglected, which is why different phenomena can be observed for similar experiment procedures.

Finally, it can be concluded that the findings based on the experiments presented in Figures 6.28 - 6.35 corroborate the notion that the frequently reported creep behavior of nearly equiatomic NiTi may be completely ascribed to the strong interrelation between temperature and transformation stress commonly described by a Clausius-Clapeyron type equation (Ortín, J. & Planes, A. (1989)). Even

though the presented experiments do not represent a direct proof for the absence of a temperature independent creep due to the existence of local temperature variations, a stronger lead than the experiments published in the literature is given concerning the origin of the pseudo-creep behavior.

6.3 Complex loading paths in the tension/compression/torsion subspace

Even though a high interest to model the material behavior of shape memory alloys and NiTi in particular is evident, the experimental data, which is used to fit the material models to, is in most cases associated to simple uniaxial tests or even simple tension experiments. Albeit in some cases the tension/compression asymmetry is incorporated, the tension/torsion asymmetry is in most cases completely neglected. In this regard and in order to allow for the development of reliable models, which may be used to compute complex structures, it is of paramount importance to use multidimensional experiments so that material models can be cross-checked utilizing a high degree of complexity. However, it is quite cumbersome to find nonproportional, multidimensional data in the literature. In this connection, a brief survey of some fundamental experimental works is given in the following. Naturally, this summary is not exhaustive nor it is meant to be.

Fundamentally, most experimental research in the field of shape memory alloys is conducted on Cu-based and NiTi shape memory alloys. As to examine the initial surface of transformation onset, elaborate tests concerning internal pressure and bi-compression experiments on Cu-based shape memory alloys are published, for instance, by the research group around Bouvet (Bouvet, C. et al. (2002a,b, 2004)). Different from that, Jacobus, K. et al. (1996); Gall, K. et al. (1997, 1998) concentrate on the influence of the triaxial compression state on the material behavior of NiTi, analyzing zero hydrostatic pressure, triaxial compression, and hydrostatic compression states. Addressing the tension/torsion behavior, which is of special interest in this work, Šittner, P. et al. (1995, 1996) for example show some box and triangle experiments on Cu-based shape memory alloys in the first axial/torsional stress quadrant. Moreover, the path dependence regarding the loading and unloading sequence is studied there. Similar studies concerning the examination of the path dependence in the first axial/torsional quadrant, but for NiTi, are presented by Rogueda, C. et al. (1996). Also Imbeni, V. et al. (2003); McNaney, J.M. et al. (2003) address the combined tension/torsion behavior for different box tests in the first axial/torsional quadrant varying the aspect ratios of the respective box shape. Extensive biaxial tests are performed by Helm, D. (2001); Helm, D. & Haupt, P. (2003) who present their findings on box and butterfly shaped strain controlled experiments. So far, the accounted publications regarding tension/torsion experiments focus on the material behavior in the first axial/torsional stress or strain quadrant. Yet,

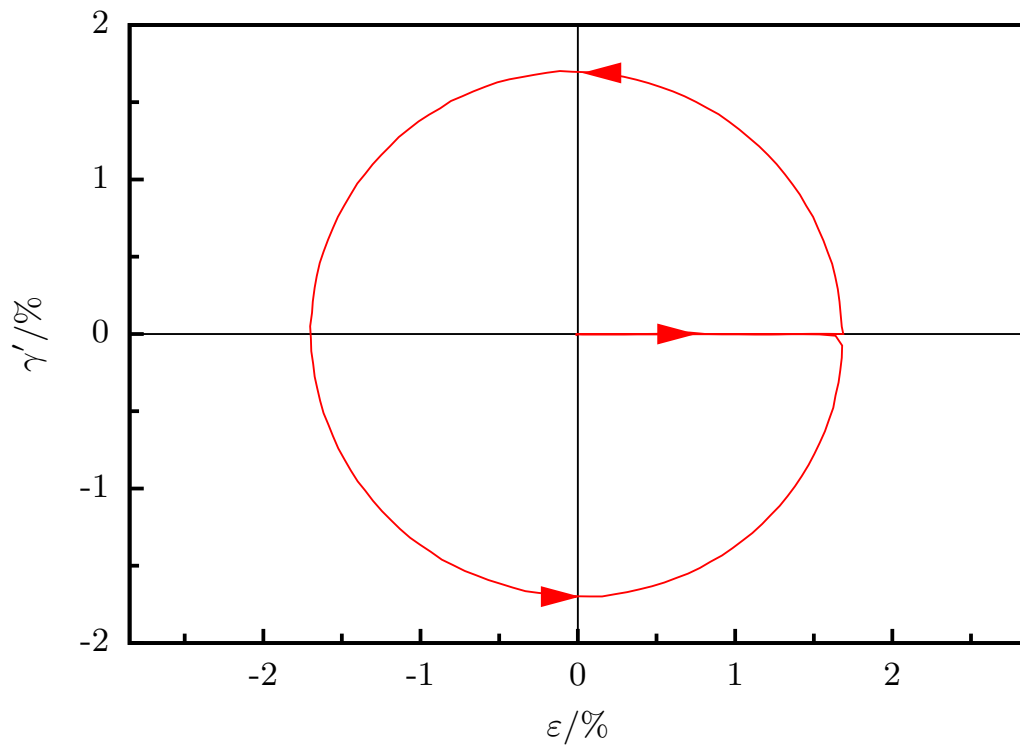
very little has been reported concerning the material behavior in the complete tension/compression/torsion subspace with [Lim, T.J. & McDowell, D.L. \(1999\)](#) being among the very few to present experimental data of that kind, namely the material response to a circular strain path having its center in the origin of the aforementioned subspace.

On this account, some complex biaxial experiments in all four axial/torsional quadrants are discussed in the following. Beginning with the material response to a circular strain path, box and butterfly experiments are shown consecutively. Regarding the latter two types of experiments, special attention is paid to the path dependence and loading/unloading sequence. Again, all experiments are carried out under macroscopically isothermal conditions with a testing temperature of 27.5°C. Since it has been shown in Section 6.2 that the material behavior is independent of the strain rate for constant specimen temperatures, the deformation velocity is chosen to be 10^{-3} s^{-1} .

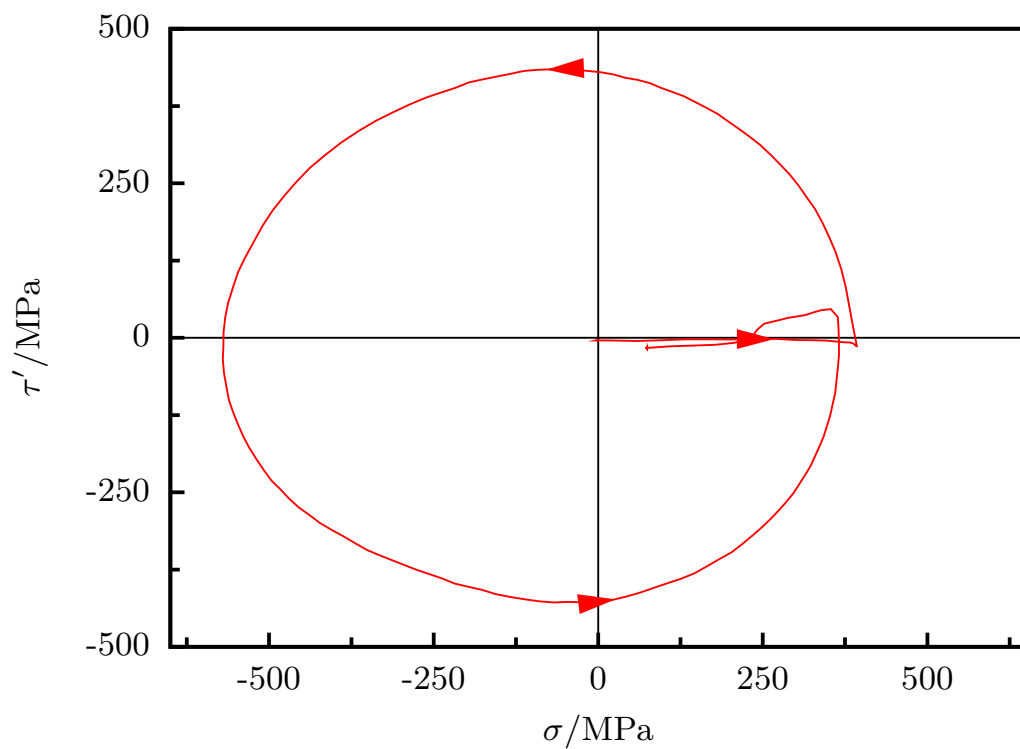
6.3.1 Combined circle test spanning all four axial/torsional strain quadrants

The strain path of the circle experiment is shown in Figure 6.36(a). Arrows indicate the loading direction. First, the specimen is loaded in simple tension in order to get from a state of zero strain to the maximum von-Mises equivalent strain value, which is concomitantly the radius of the circle ($r = 1.7\%$). Due to the accurate shape of the strain path, it can be stated that the quality of the strain control is satisfactory.

The second diagram in Figure 6.36, namely 6.36(b), contains the stress data as the material response to the given strain path. Again, arrows signify the stress change direction. Here and subsequently, the respective arrows characterize the same points in time or points of loading referring to different representations of the material behavior. Hence, each arrow in the stress-stress diagram can be directly associated to a corresponding arrow in the strain-strain diagram. In this way, it can be observed that the stress-stress curve is rotated with respect to the strain-strain curve, since, at particular points, negative axial stresses exist while the specimen is still positively elongated, see the upper arrows. Besides, at these points the shear strain increases whereas the shear stress decreases. This is further substantiated by the respective locations of the circle endpoints. Naturally, within the strain-strain diagram the endpoint exhibits a zero shear strain whereas in the stress-stress diagram a shear stress of substantial magnitude is evident for the corresponding circle endpoint. Similar results concerning a rotated stress-stress curve with reference to a circular strain control path were reported by [Lim, T.J. & McDowell, D.L. \(1999\)](#). In anticipation of the later presented stress-strain diagrams, all this is synonymous with the stress-strain curves intersecting the strain axes upon unloading at an other position than the origin. The same can be observed for a classically plastic material behavior. Finally, upon axial unloading, the shear stress reduces so that, as the origin of



(a) Strain-strain diagram



(b) Stress-stress diagram

Figure 6.36: Combined isothermal circle test spanning all axial/torsional quadrants; strain-strain and stress-stress diagram

the strain-strain diagram is reached, the residual shear stress is nearly zero.

Regarding further the stress-stress diagram, the observer's eye is caught by the asymmetric shape of the curve with respect to the ordinate. This is obviously attributed to the well-known tension/compression asymmetry, and will be evident for all further complex strain paths spanning the complete axial-torsional subspace.

Figure 6.37 features the stress-strain behavior in axial and torsional direction. Clearly, at the very beginning, the axial stress-strain curve resembles the simple tension case, since the first loading is indeed purely tension, as mentioned before. It can be recognized that, in compression, almost directly after the onset of phase transformation, the specimen is unloaded again. This transformation region is significantly smaller than in the tension case. That effect is ascribed to the tension/compression asymmetry with higher compressive stresses requisite for the triggering of phase transition and the fact that Young's modulus is identical for the two loading directions. However, phase transition does take place even for the compression part of the strain path. As can be already assessed from the stress-stress curve, the specimen is still loaded in tension when a zero strain state is attained upon completion of the experiment.

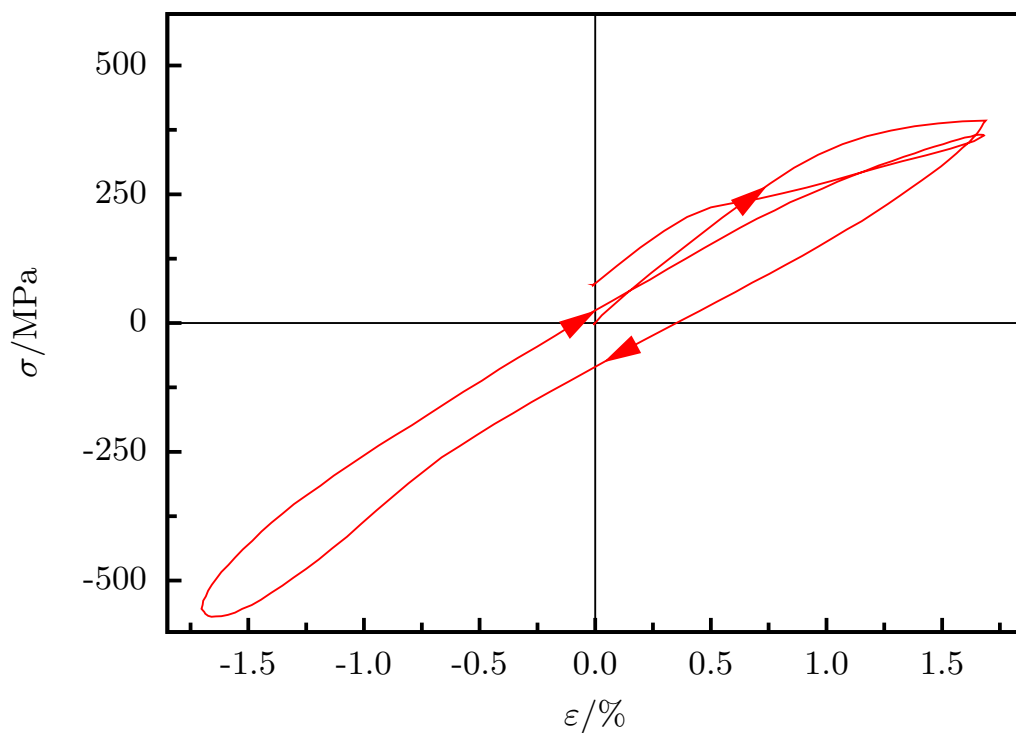
In Figure 6.37(b), the arrows are omitted as they would be located at the very small vertical segments of the torsional stress-strain curve and, thus, have limited informative value. However, it is clear that the chronology of the loading leads to a clockwise progression of the stress-strain points. As a matter of course, the onset of phase transformation cannot be spotted as clearly as in the axial case.

6.3.2 Combined box tests spanning all four axial/torsional strain quadrants

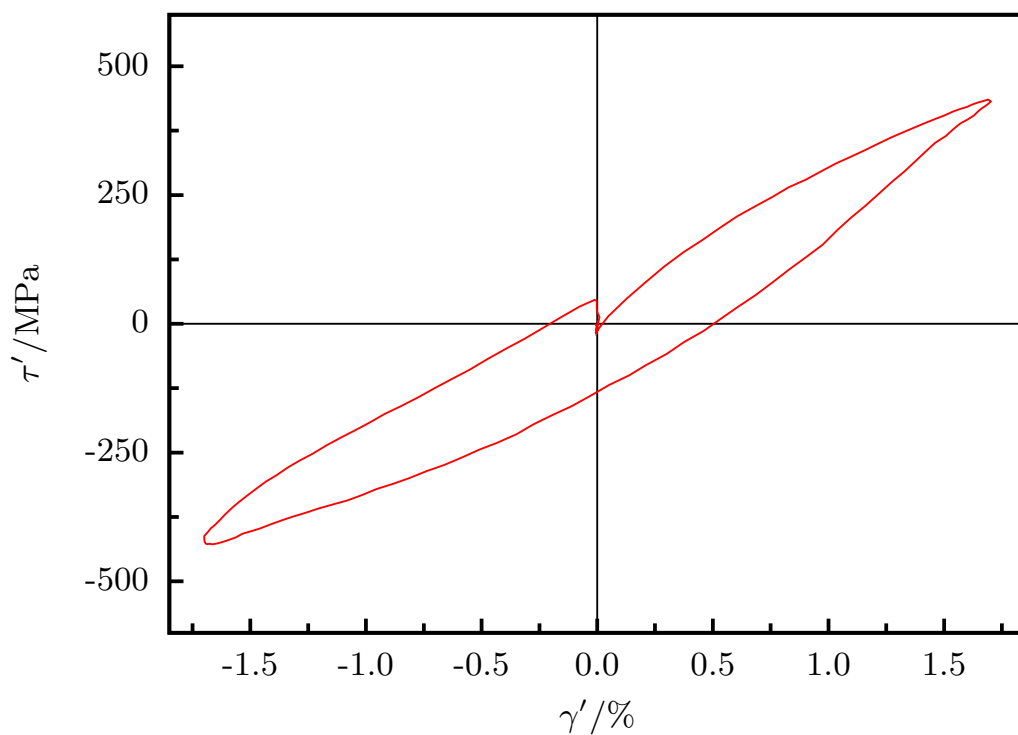
On the following pages, the material response to two different box tests, spanning the complete tension/compression/torsion subspace, is reviewed. Here, special attention is turned on the path dependence of the specimen material. For this reason and in order to investigate the tension/compression asymmetry, the two strain paths differ in the initial loading direction. For each experiment type, the complete loading from and unloading to the origin of the strain space is shown. This is further illustrated by the strain control path depicted in Figure 6.38(a). The maximum von-Mises equivalent strain is $\varepsilon_{eq} = 1.5\%$.

Again, the loading direction is indicated by arrows. Moreover, the distinct experiment curves are plotted using different line types. Obviously, the box test starting in simple tension runs through the box path in counterclockwise direction. Complementary, the other loading path is clockwise oriented.

Figure 6.38(b) shows the respective stress-stress curves. Again, the rotation of the curves and the pronounced tension/compression asymmetry is evident for both experiments. Furthermore, the overall shape of the two distinct curves is qualitatively similar, which is why the two curves are discussed as a whole.

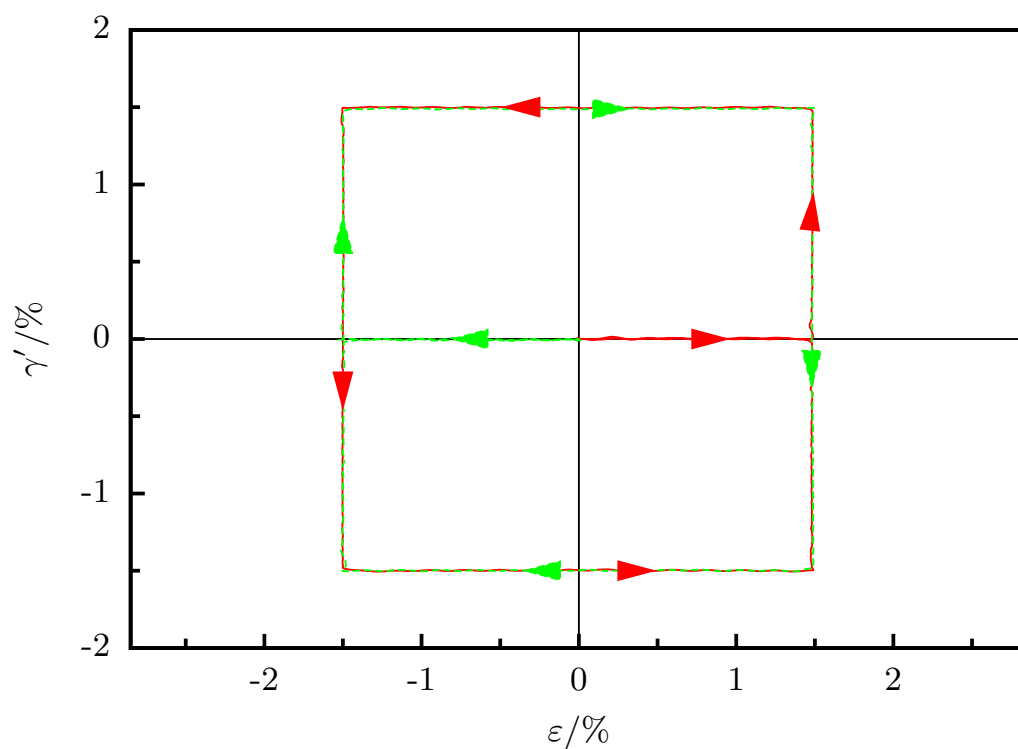


(a) Axial stress-strain diagram

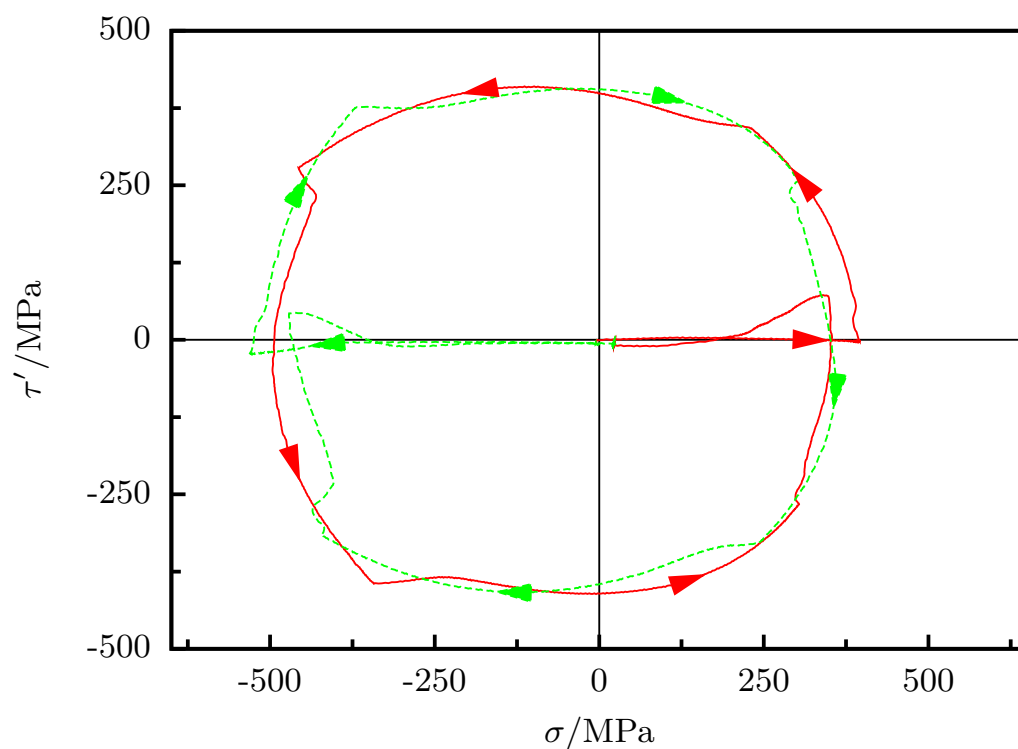


(b) Torsional stress-strain diagram

Figure 6.37: Combined isothermal circle test spanning all axial/torsional quadrants; axial and torsional stress-strain diagram



(a) Strain-strain diagram



(b) Stress-stress diagram

Figure 6.38: Combined isothermal box tests spanning all axial/torsional quadrants; examination of path dependence

Clearly, after loading in torsional direction, a small shear stress dip can be discovered upon unloading in axial direction. This was already discussed in Section 6.2.1.3 for the box test in the first axial/torsional strain-strain quadrant only. It is absorbing that a similar behavior can be recognized for the complementary box test and even for the case of a torsional unloading after an axial loading. Fundamentally, it can be noted that, after the deformation direction is changed, keeping the strain in the other direction constant, a stress dip followed by a renewed increase in the stress associated with the constant strain is existent regardless of the sequence of torsional and axial loading and unloading.

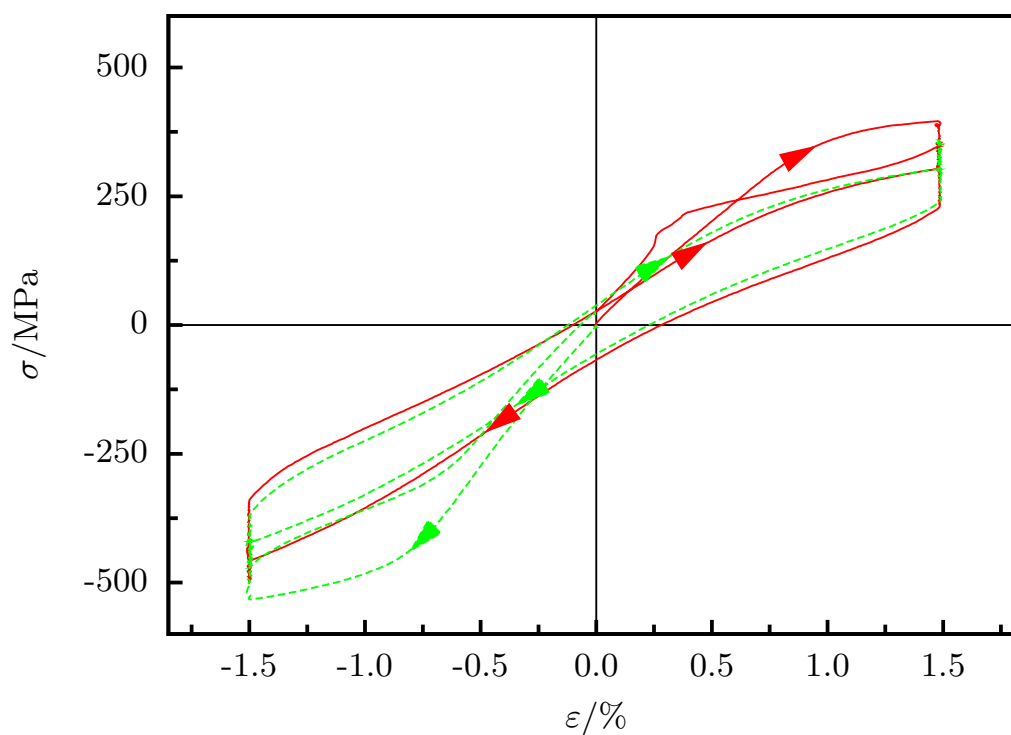
Regarding the stress-strain diagrams in Figure 6.39, a smaller number of arrows can be remarked. The reason is that the arrows pointing in direction of the abscissa are left out because of the limited size of the vertical curve segments and the altering stress change direction there. The reason for the alteration of the stress change direction lies in the interrelation between axial and torsional stress. As a rule of thumb, it can be accounted that one stress component increases as the other one decreases under the condition of one strain component being held constant. This does not hold true perfectly as the already discussed stress dips and the rotation of the stress-stress curves exist. Fundamentally, qualitatively similar progressions referring to the two distinct experiment types may also be noted for the stress-strain diagrams. The slight difference between two torsional stress-strain curves might be attributed to effects concerning the specific microstructure and not to the general material behavior.

6.3.3 Combined butterfly tests spanning all four axial/torsional strain quadrants

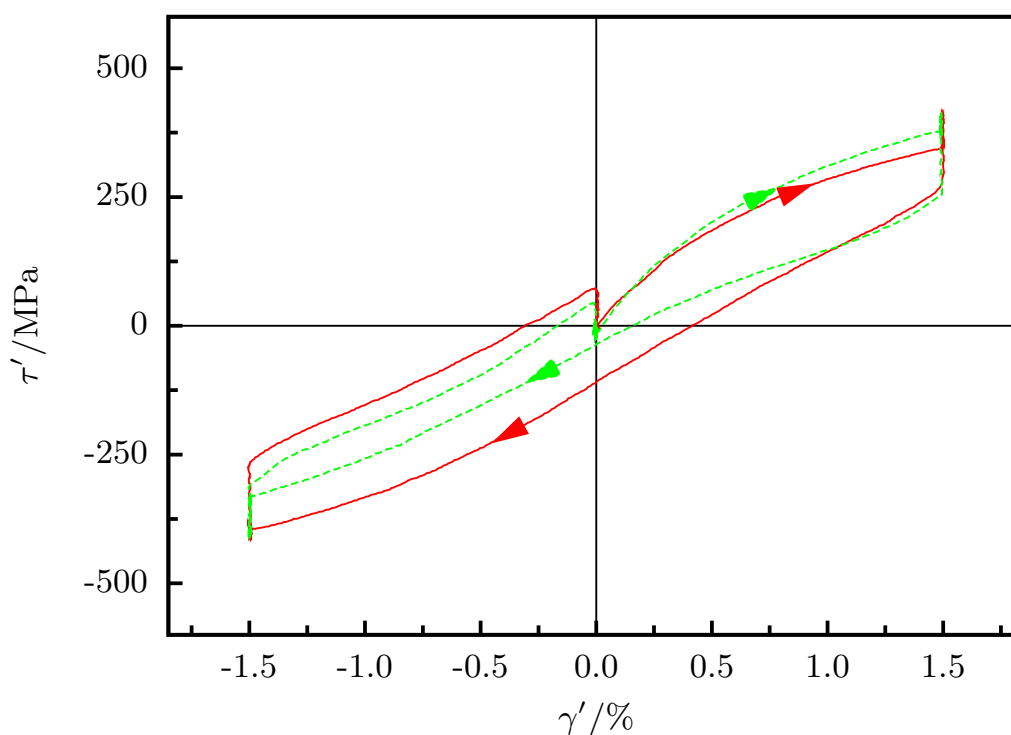
Compared to circle and box tests, the butterfly shaped strain path constitutes a more complex experiment type as it pertains as well proportional as non-proportional strain path segments, and it traverses several times the axial-torsional strain space origin. Consequently, the overall loading is repeatedly reduced to and increased from a state of zero strain.

Again, special focus is on the path dependence of the material behavior with two distinct strain paths starting in tension and torsion direction, respectively. Arrows signify the deformation direction. The maximum von-Mises equivalent strain is chosen to be $\varepsilon_{\text{eq}} = 1.5\%$. Figure 6.40(a) pictures the respective strain control paths. Evidently, in this case, the very first loading step is a proportional step with the origin of the strain space being part of the butterfly shape. This is different from the already discussed biaxial strain paths, namely circle and box, for which uniaxial loading and unloading steps are used in order to get to the actual circular or box shape.

At first sight, the stress-stress diagram (Figure 6.40(b)) comprehends two significantly different stress-stress curves. Apparently, the difference between the two experiments is larger than the difference that was noted for the box tests. Nevertheless, a large part of the discrepancies between the two curves may again

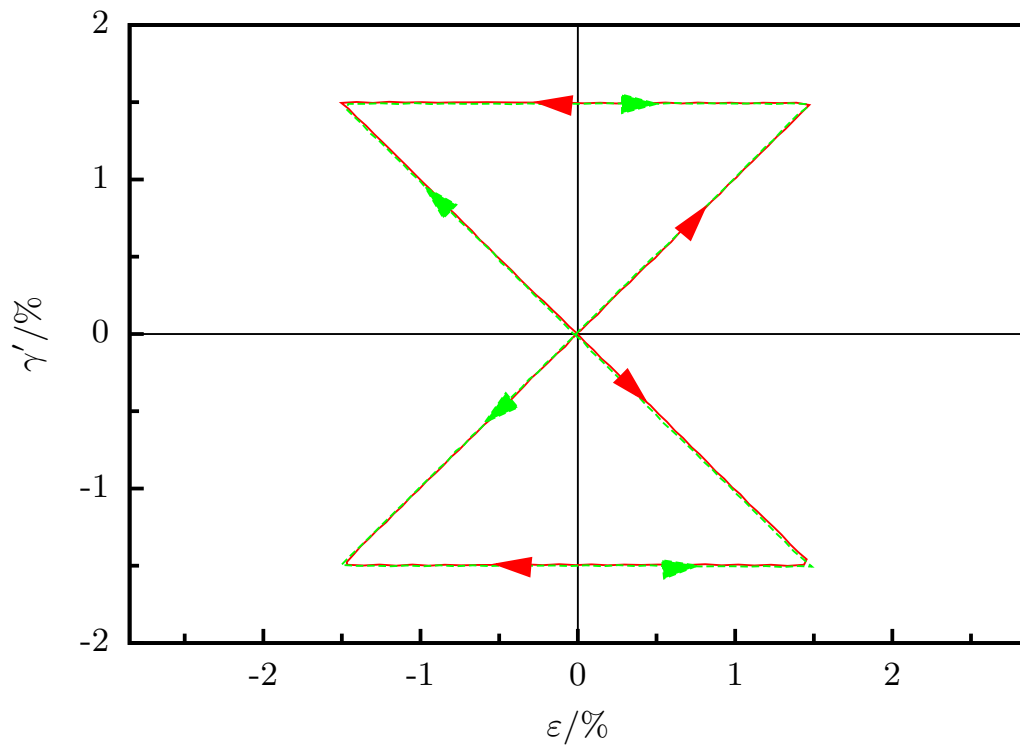


(a) Axial stress-strain diagram

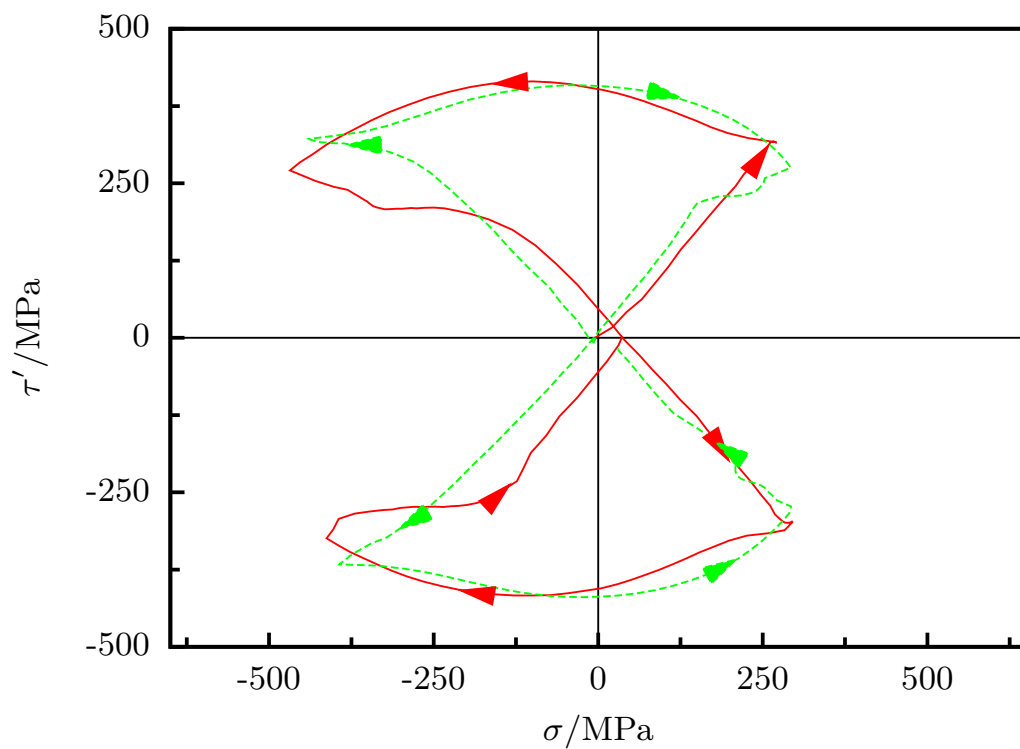


(b) Torsional stress-strain diagram

Figure 6.39: Combined isothermal box tests spanning all axial/torsional quadrants; examination of path dependence



(a) Strain-strain diagram



(b) Stress-stress diagram

Figure 6.40: Combined isothermal butterfly tests spanning all axial/torsional quadrants; examination of path dependence

be attributed to the tension/compression asymmetry. Non-proportional strain path segments are preceded and followed by a proportional loading and unloading step. The enclosed angle between the adjacent stress progression segments is highly dependent on the tension/compression asymmetry, leading to significantly smaller angles in the compression half-space at the change of the deformation direction. Consequently, this results in the impression that the stress-stress curves are highly different.

Contemplating the proportional unloading segments, winding stress-stress progressions can be observed. These conclusions can be equivalently made for both experiment types. Basically, angles between the non-proportional and the proportional unloading segments are much larger than in the cases of proportional loading. Once more, with the shear strain component held constant, i.e., within the non-proportional segments, the shear stress increases as the absolute value of the normal stress decreases.

The stress-strain diagrams for the two butterfly tests are depicted in Figure 6.41. Only three different arrows are plotted in Figure 6.41(b) due to the aforementioned reasons, see Sections 6.3.1 and 6.3.2. Consequently, as a continuous evolution of the axial strain takes place, all arrows are given in the axial stress-strain diagram. Concerning this axial stress-strain diagram, it is interesting to see that almost identical curve segments are revisited in the tension half-space whereas the corresponding observation cannot be made for the compression half-space, as an evolution of the stress-strain curve is evident upon a repeated loading in compression. However, this does not hold true for all tested specimens in general.

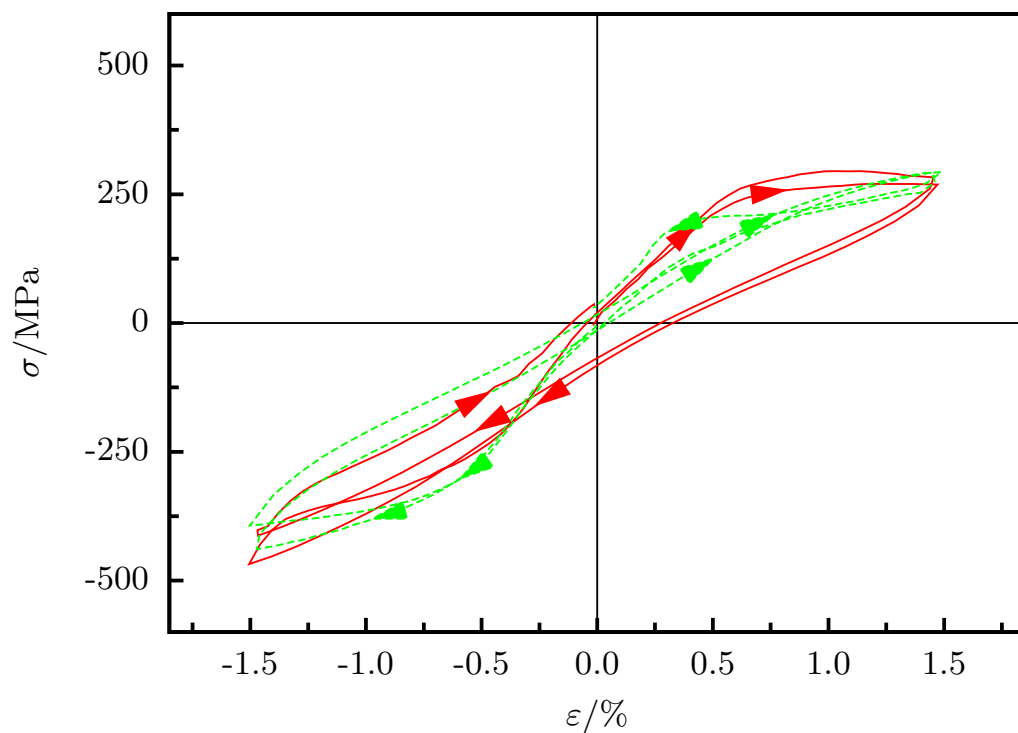
6.4 One-way effect under different loading conditions

This section treats the one-way shape memory effect under different loading conditions. For the sake of completeness, the well-known uniaxial cases of simple tension and simple torsion are presented first. Subsequently, different complex loading paths in the tension/compression/torsion region are accounted with the respective unloading being performed as well in the martensitic as in the austenitic state. In addition to the experiments in this chapter, some further experiments are given in Appendix B.

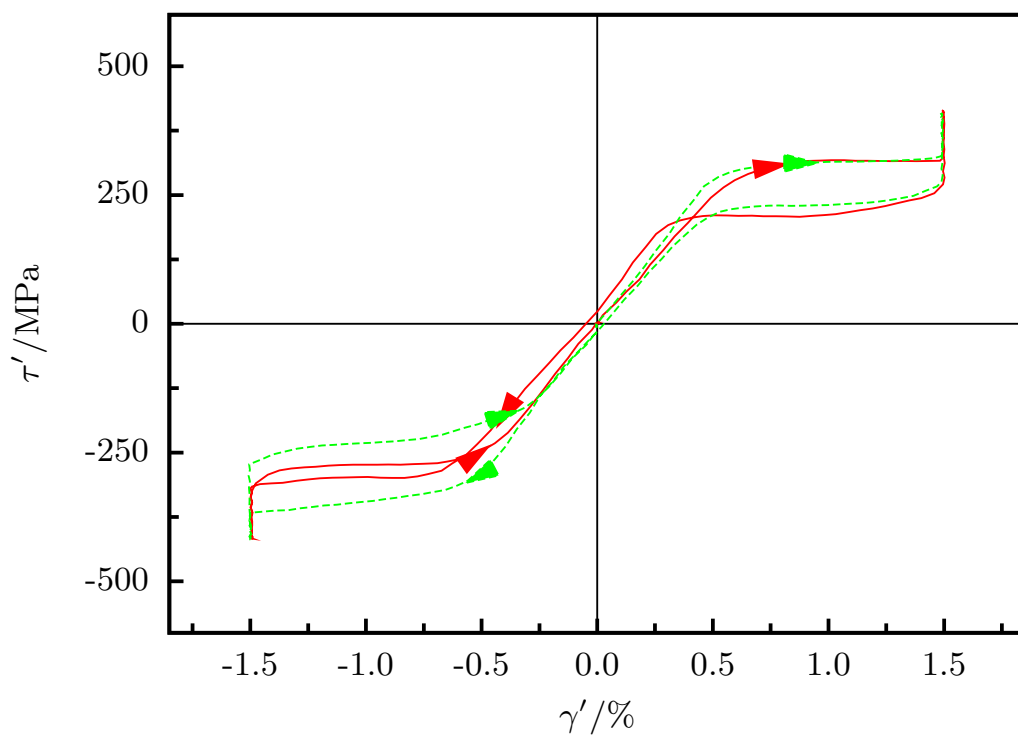
Clearly, since a temperature range of nearly 150 K¹⁴ has to be covered by the strain measuring device, the temperature effect on the system cannot be neglected for the measurement of axial strain¹⁵. Two distinct effects are evident. On the one hand it is the drift of the zero signal of the inductive displacement transducers as these sensors are permanently exposed to the temperature changes within the temperature chamber. On the other hand it is the thermal

¹⁴This temperature range results from the requirement of thermally inducing phase transitions between the austenitic and martensitic microstructure and vice versa.

¹⁵As the measuring of the relative distortion within the gage length is based on a differential measuring of distortion, the temperature effect on the determination of torsional strain can be disregarded.



(a) Axial stress-strain diagram



(b) Torsional stress-strain diagram

Figure 6.41: Combined isothermal butterfly tests spanning all axial/torsional quadrants; examination of path dependence

expansion of the transducer holder system, thus, moving the transducer body relatively to the transducer plunger. On this account, the axial system has to be temperature calibrated in order to account for the measurement error due to the thermal effects. Fundamentally, this is realized by performing a complete temperature cycle between highest and lowest applied temperature. Here, the measuring device is clamped onto the specimen and the specimen is kept free of axial stress during the whole calibration run. Using these data, for all subsequent experiments, each measured data value is offset-compensated to yield the calibrated axial strain values. That way, the thermal expansion of the specimen and the volume change due to a phase transition of the specimen material are also eliminated for all in the following presented axial strain curves. This has to be kept in mind when comparing the given experimental data with respective data in the literature. However, in this manner, the shown strain response of the material can be directly connected to the shape memory effect.

6.4.1 One-way effect under uniaxial loading conditions

Two different simple uniaxial tests are performed, which are simple tension and simple torsion. Both experiment types are stress controlled. Loading and unloading takes place at a temperature of -30°C , having the specimen cooled down below the martensite finish temperature to guarantee an initially martensitic microstructure for the tests. For the remainder of the experiments, the loading is controlled so that the specimen is free of axial and torsional stress. After completion of the unloading process, the specimen is heated up to a temperature of 60°C , which is supposed to be well above the austenite finish temperature A_f , see the respective DSC measurements in Figure 6.7. Hence, an austenitic microstructure is realized. Thereafter, in order to generate a martensitic microstructure, the specimen is cooled down again to a temperature, which is below the martensite finish temperature M_f . Here, a temperature of -85°C is chosen, refer to Figure 6.7 for an estimation of M_f . Subsequently, the temperature is raised to the initial temperature (-30°C) so that a complete temperature cycle is realized.

6.4.1.1 One-way effect for simple tension

Figure 6.42 shows the coupled stress-strain-temperature behavior for the complete simple tension experiment incorporating the already mentioned sequence of mechanical and thermal loading and unloading. For the sake of clarity, the two-dimensional projections on the temperature-strain and stress-strain space of this diagram are shown in Figures 6.43 and 6.44.

Clearly, a pseudoplastic material behavior can be observed at the initial temperature of -30°C , since a residual strain in the order of 2% axial strain is evident on mechanical unloading. In the following, the initially remaining strain is completely recovered as the specimen is heated up. This process is concluded around

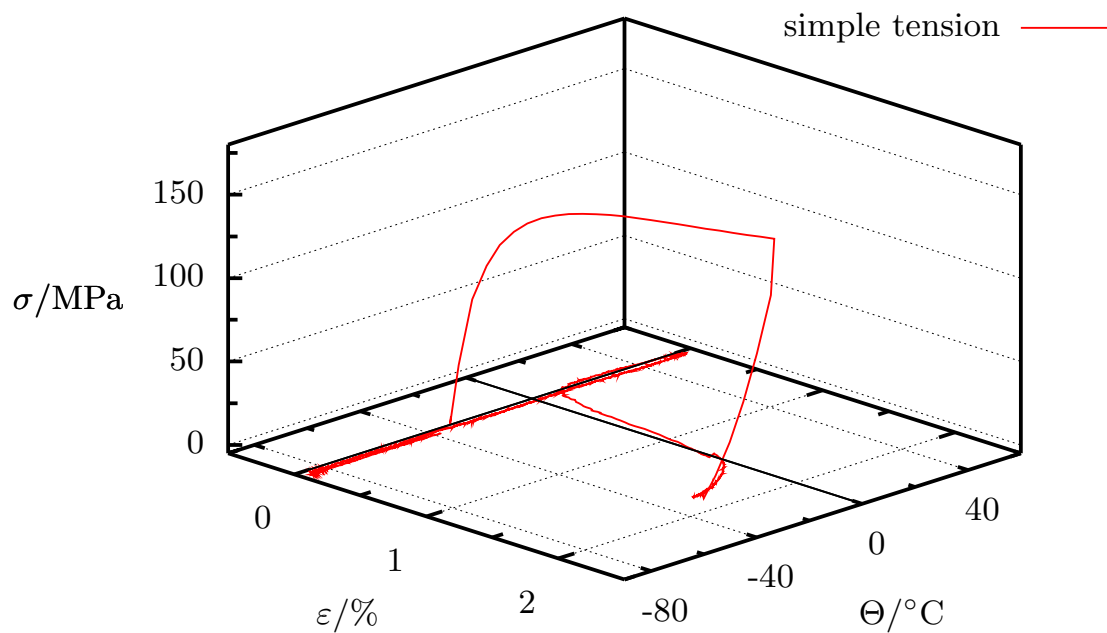


Figure 6.42: One-way effect for simple tension; stress-strain-temperature diagram

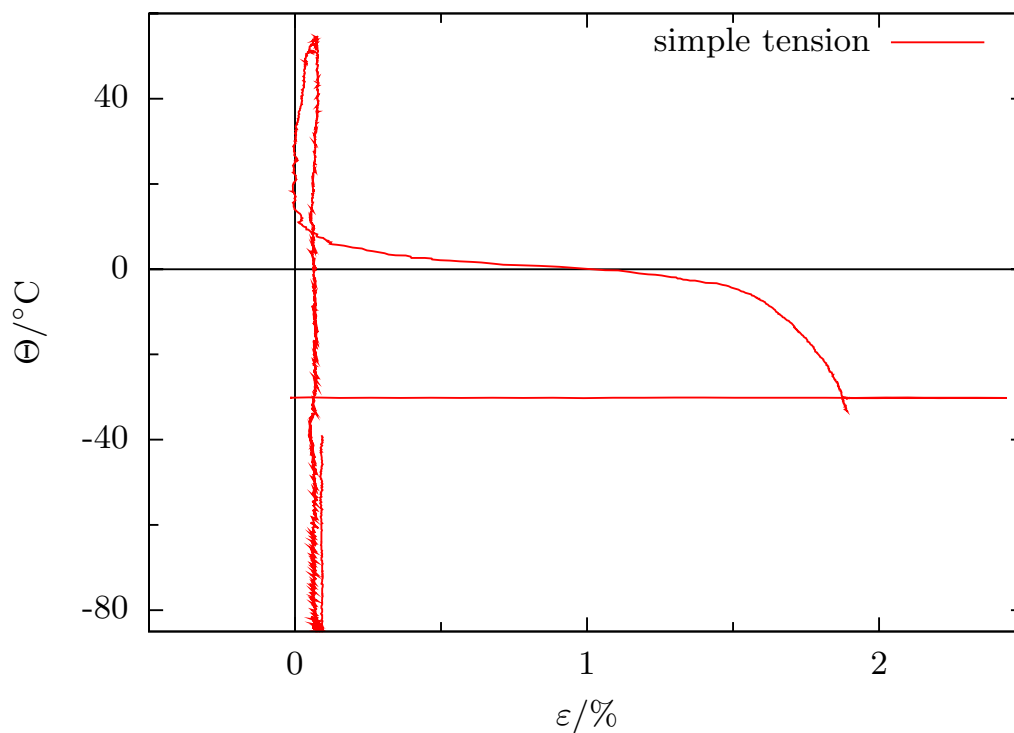


Figure 6.43: One-way effect for simple tension; strain-temperature diagram

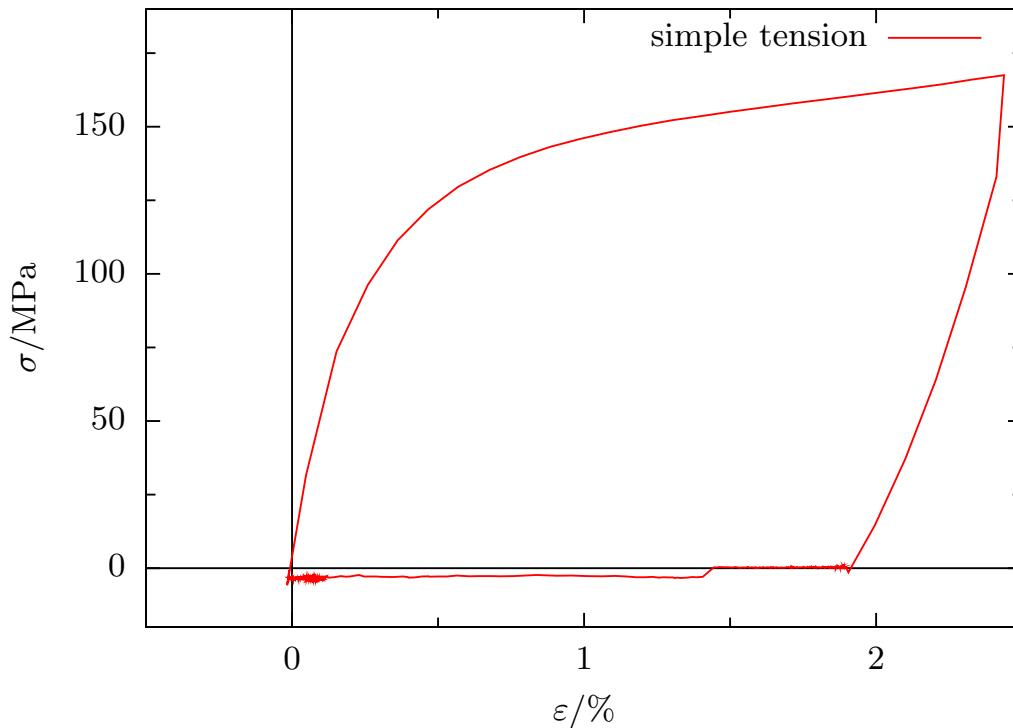


Figure 6.44: One-way effect for simple tension; stress-strain diagram

a specimen temperature of 20°C, which is in good accord with the DSC measurements, since the first endothermic peak has its finish temperature around that particular value. In this connection, [Tanaka, K. et al. \(1999\)](#), for instance, report consistently with the findings in this work that almost all of the residual strain is recovered after the first endothermic peak on heating. During the further heating, cooling, and re-heating procedure, the magnitude of the axial strain is permanently negligible so that any residual strain can also be considered absent as the starting temperature is reached again. Furthermore, a second phase transformation, as anticipated due to the existence of a second endothermic peak in the DSC curve, cannot be observed, possibly because of the small magnitude of strain that is commonly associated with a second phase transformation ([Tanaka, K. et al. \(1999\)](#)).

6.4.1.2 One-way effect for simple torsion

Analogous to the last paragraph, the simple torsional experiment concerning the one-way shape memory effect is discussed here. According to the aforementioned succession of mechanical and thermal loading and unloading steps, the strain response of the specimen material is shown in Figure 6.45 as a function of the control variables, namely torsional stress and specimen temperature. Consequently, von-Mises equivalent stress and strain are used again.

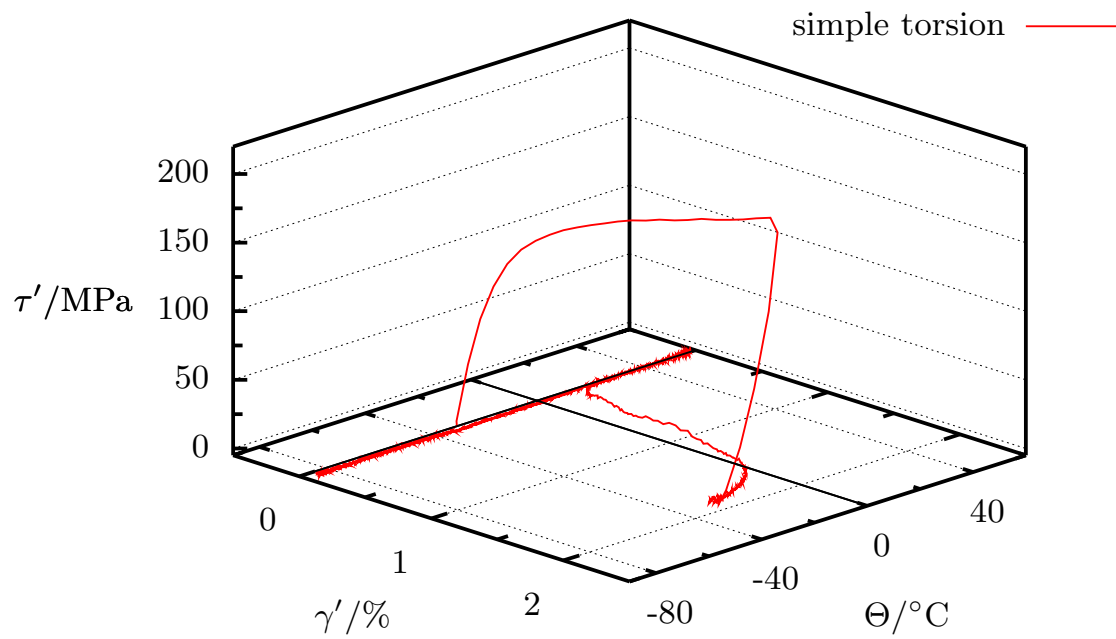


Figure 6.45: One-way effect for simple torsion; stress-strain-temperature diagram

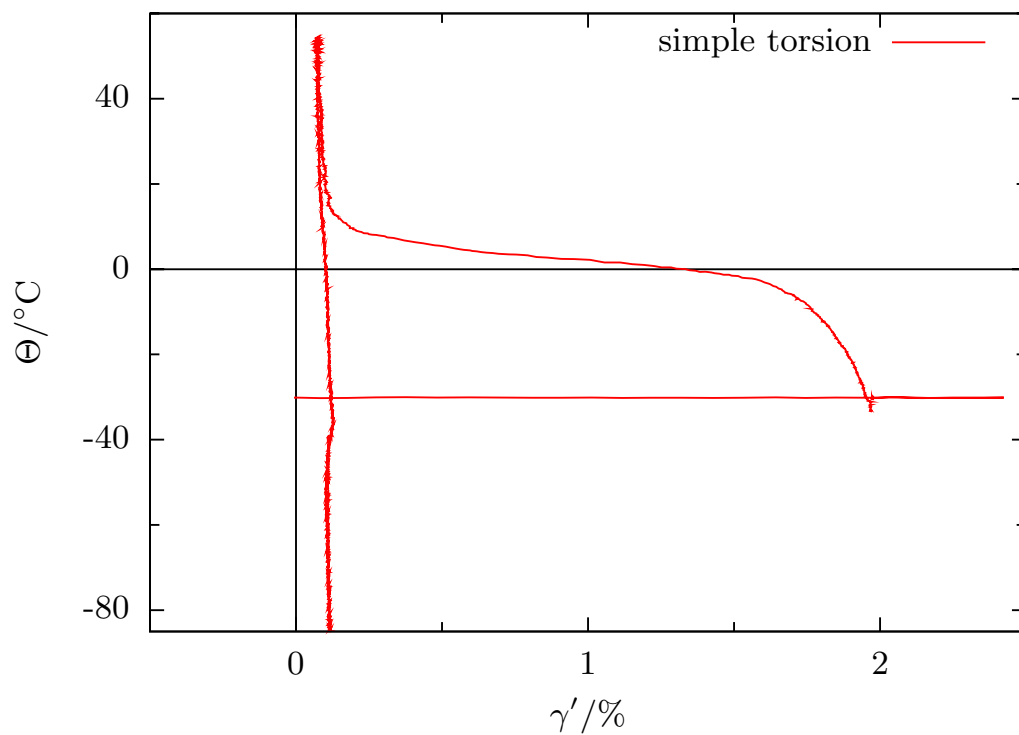


Figure 6.46: One-way effect for simple torsion; strain-temperature diagram

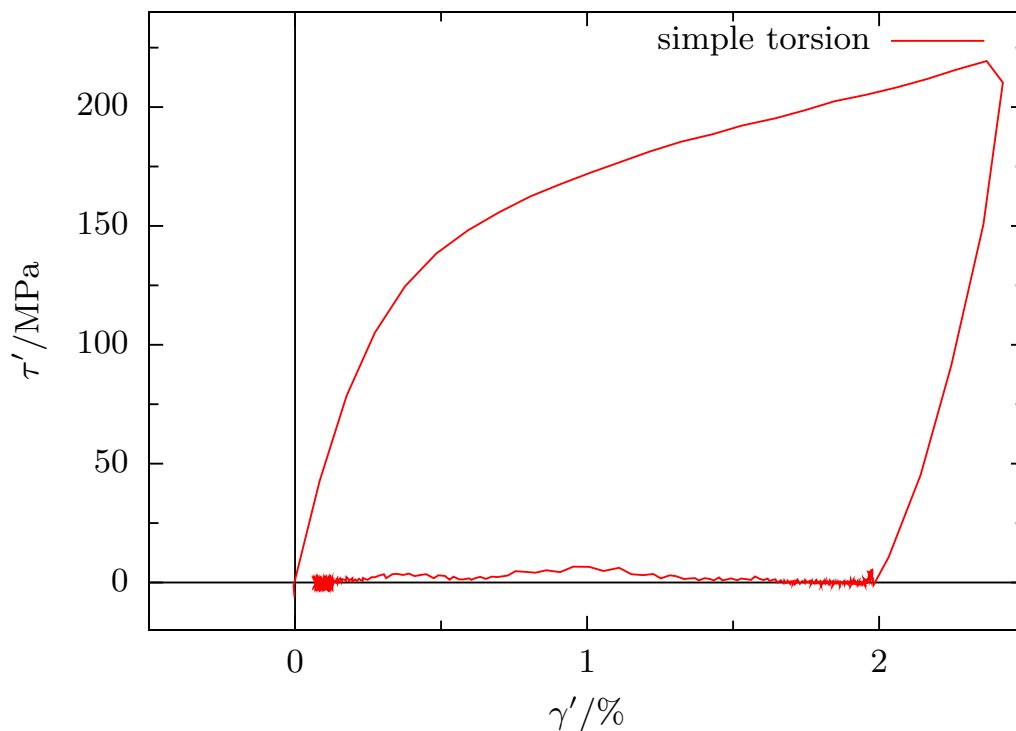


Figure 6.47: One-way effect for simple torsion; stress-strain diagram

Figures 6.46 and 6.47 present a two-dimensional view at the strain behavior as a function of the two independent variables torsional stress and specimen temperature. The qualitative behavior is the same as in the simple tension case. First, in the martensitic state, a pseudoplastic material response featuring a residual strain after mechanical unloading can be clearly observed. Upon heating above a specific limit temperature, the strain is almost completely recovered without any subsequent change in the state of torsional strain on the further thermal cycling. Again, the phase transformation, which is associated with the strain recovery is concluded at 20°C.

The small remnant torsional strain in the order of 0.1% may be attributed to the foregoing generation of the martensitic microstructure. The reason is that, upon transforming into martensite, the specimen material is extremely sensitive to actually smallest external loads, see Tanaka, K. et al. (1999), so that even stresses in the order of only a few megapascals are sufficient to trigger the generation of a small amount of favored martensite variants yielding strains in the observed magnitude.

6.4.2 One-way effect under complex loading conditions

The focus of the following part is on the strain response of the specimen material under combined tension/compression/torsion loading in the martensitic state.

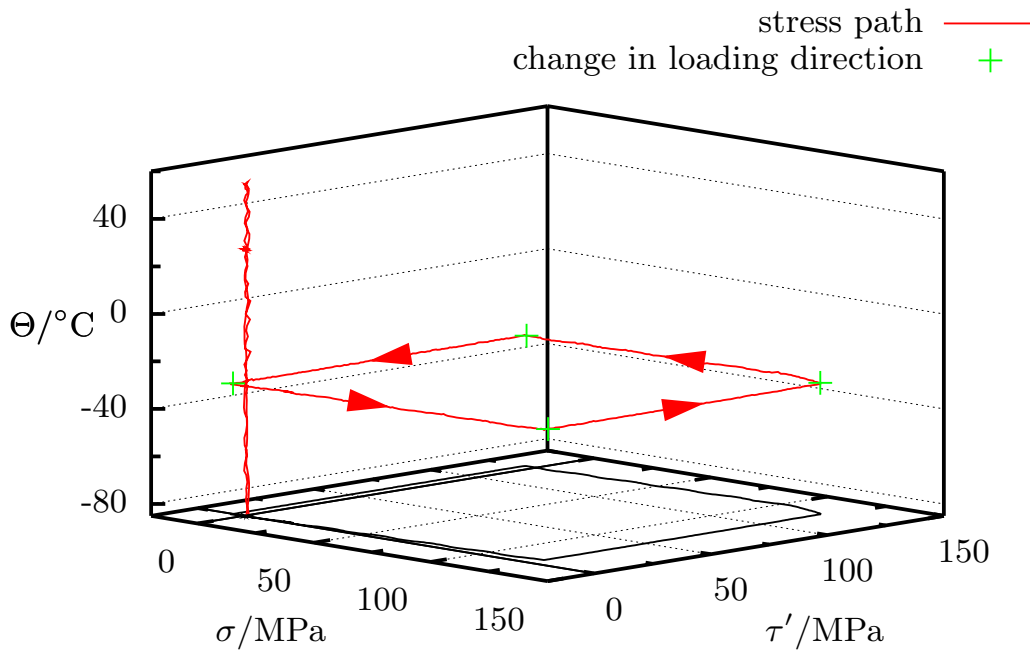


Figure 6.48: Control path of a box test in the pseudoplastic temperature regime

This section is further subdivided with reference to the unloading process and the respective microstructure of the material. The foregoing generation of martensite as explained in the preceding paragraph and the initial temperature of -30°C are common to all experiments in this section.

6.4.2.1 Unloading in the martensitic state

The subsequently discussed experiment can be considered the logical extrapolation of the uniaxial tension and torsion tests onto the two-dimensional tension/compression/torsion space. Once more, the mechanical loading and unloading takes place at the initial temperature of -30°C . Hence, the same microstructure is existent for loading and unloading. Stress control is applied.

As a simple biaxial stress path, a box path in the first axial/torsional stress quadrant is chosen starting with simple tension. Consecutive to the mechanical loading/unloading, the specimen is heated, cooled, and re-heated in the same manner with the same limiting temperatures (60°C , -85°C) as in the uniaxial cases, refer to the previous section (6.4.1) for a detailed discussion on the chosen temperatures. In this vein, a complete temperature cycle is realized and the microstructure is rearranged from martensite to austenite and back to martensite. The respective control path in dependence of all three control variables, namely temperature, normal stress, and shear stress is given in Figure 6.48.

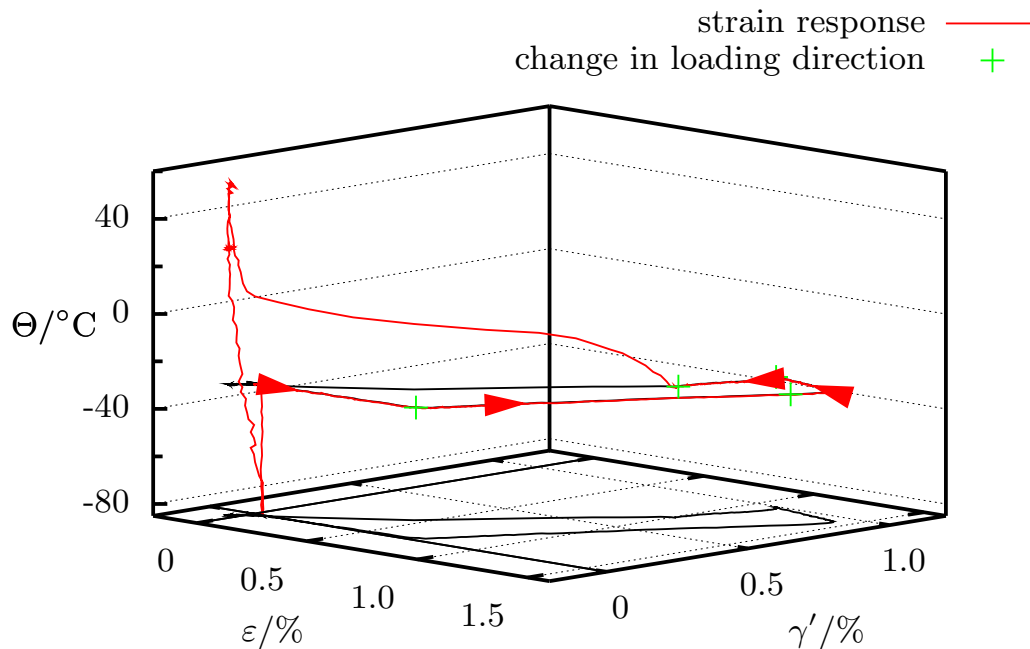


Figure 6.49: Pseudoplastic strain response as a function of temperature on the box stress path in the first axial/torsional stress quadrant

In this and the following diagrams, the loading direction is indicated by arrows when appropriate. Arrows are omitted wherever the respective curve features a change of direction for a consistent loading direction or the curve segment is too small for the applied arrow size. Then again, the arrows signify the same points in the loading history, irrespective of the specific diagram type. Furthermore, crosses label the change of the loading direction so that different curve segments can be doubtlessly ascribed to the different mechanical steps of the experiment. Figure 6.49 shows the strain response on the stress path pictured in Figure 6.48. Here, the strain response is given as a function of the temperature. In order to facilitate the interpretation of the diagram, the two-dimensional projection onto the normal/shear strain space is plotted additionally in Figure 6.49 and separately in Figure 6.50. At the beginning of tensile unloading, normal and shear strain increase simultaneously, followed by a consecutive decrease and increase of normal and shear strain, respectively, at the end. Subsequently, upon further unloading, the strains in both directions diminish resulting in residual strains in the order of 1.0% and 0.75%. The recovery of the residual strains is obvious in the last segment of the strain-strain curve. Furthermore, the strain recovery is also shown as a function of temperature in Figure 6.51. Here, temperature is plotted against equivalent strain as defined in Footnote 2 on page 29. In this manner, normal and shear strain are depicted in one single diagram. Clearly,

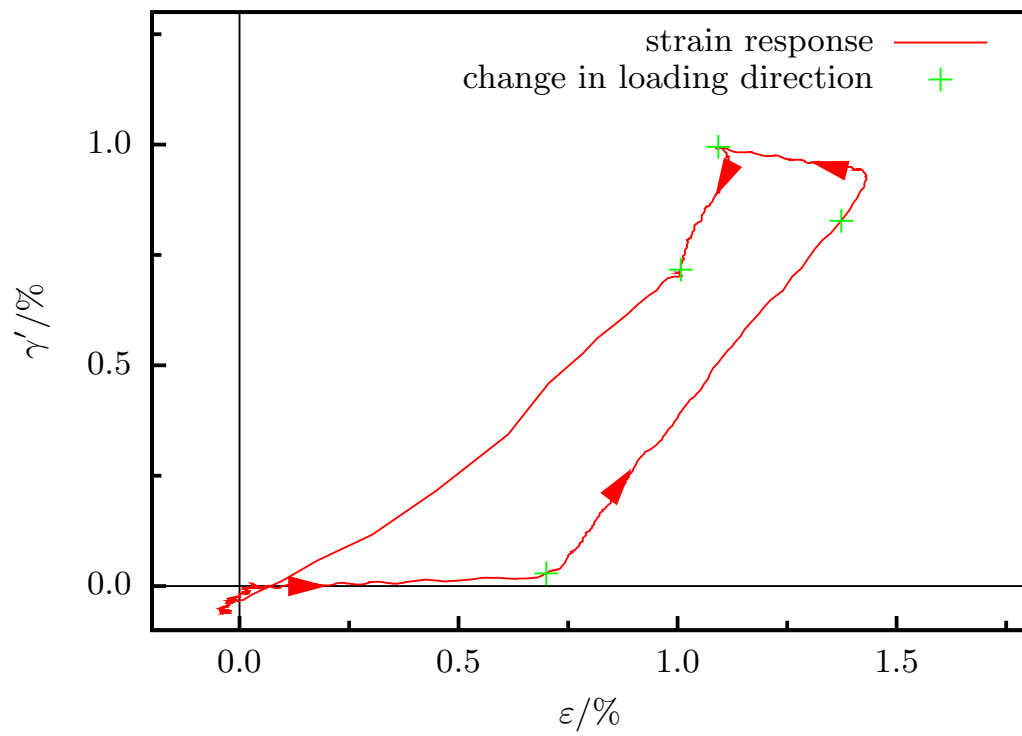


Figure 6.50: Pseudoplastic strain response on the box stress path

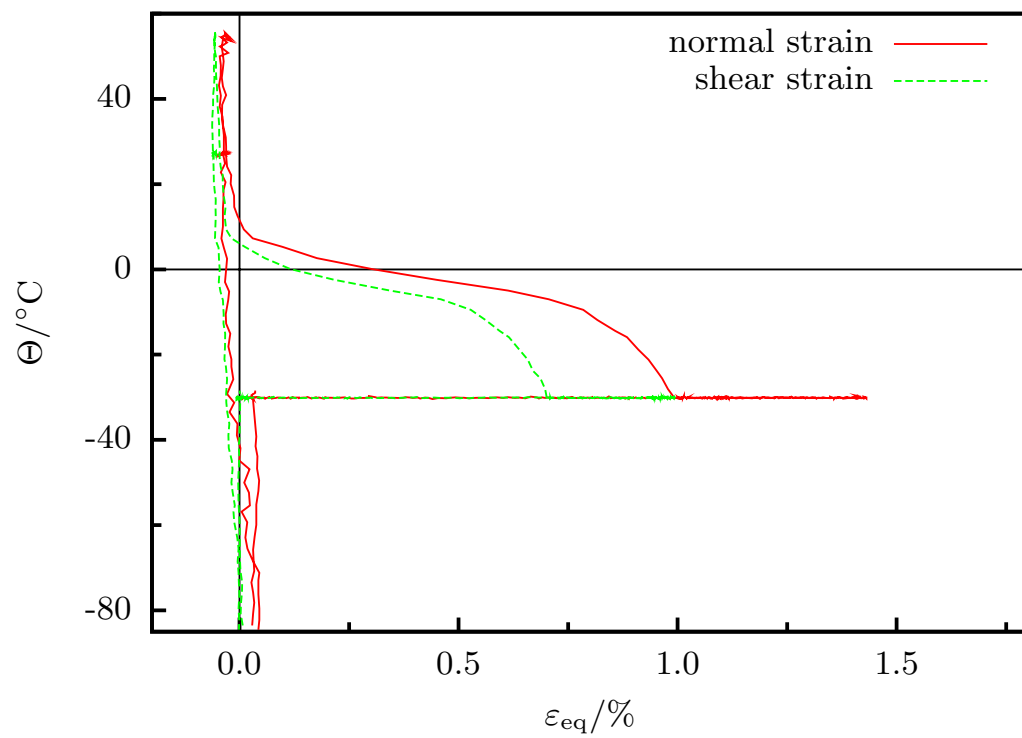


Figure 6.51: Strain recovery of the pseudoplastic box test

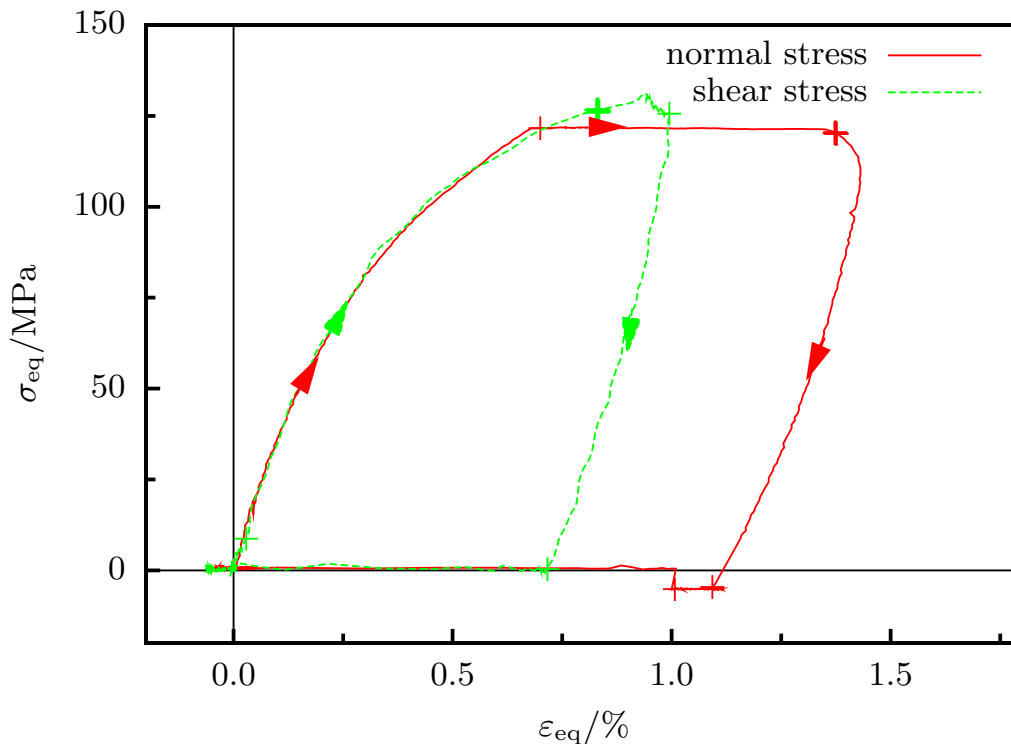


Figure 6.52: Stress-strain diagrams for the pseudoplastic box test

the strain curves resemble the uniaxial cases exhibiting *S*-shaped progressions and a completion of the strain recovery around 20°C. Apparently, the strain recoveries in the distinct directions are independent of one another.

In order to draw a complete picture of the material behavior for the pseudoplastic box test, the respective stress-strain curves are given in Figure 6.52. Once more, equivalent measures are utilized. Here, some shortcomings of the analog machine control are evident. This can be recognized in particular by the inspection of the torsional stress curve as the stress is not perfectly constant during the stress-hold periods upon the first loading step and during heating of the specimen. Especially as the specimen temperature is raised, and phase transition occurs, the strain rate gets extremely large. This poses a big challenge on the machine control. Furthermore, on tensile unloading a compressive stress of -5 MPa is reached. This is readjusted after torsional unloading so that the normal stress vanishes as well. A similar control behavior can be discovered for the following pseudoplastic experiments, too.

It is noteworthy that the stress progressions are identical during the loading process. However, it has to be kept in mind that, upon torsional loading, the specimen is already stressed in axial direction. Moreover, the identity of the stress-strain curves upon loading cannot be observed in this clarity comparing the respective stress-strain curves for the uniaxial cases. There, the torsional stress curve exhibits a steeper slope for larger stress values featuring an identical stress-

strain behavior only up to stress, strain values of 80 MPa, 0.2 %, respectively. Accordingly, the torsional stress-strain slope is reduced due to the distinctly oriented pre-stressing of the specimen. As a matter of fact, an identity of the stress-strain curves will not be existent for different values of the normal stress prior to torsional loading.

6.4.2.2 Unloading in the austenitic state

Different from the presented pseudoplastic experiments, the unloading of the specimen in this section is carried out as the specimen features an austenitic microstructure. First, the specimen is loaded at the same initial temperature (-30°C). Consecutively, the temperature is raised above 90°C . Here, the specimen is unloaded. The temperature is increased up to a higher temperature than before in order to account for the stress-induced shift of the transformation temperatures, see for example [Tanaka, K. et al. \(1999\)](#). [Ortín, J. & Planes, A. \(1989\)](#) point out that “temperature and applied stress play equivalent thermodynamic roles” concerning the process of phase transition, hence, yielding the consequence that for higher applied stresses higher transformation temperatures are existent. Two different experiments are discussed both being stress controlled.

Regarding the first of the two experiments, the stress path is identical to the box path already discussed in Section 6.4.2.1 but with the unloading steps being performed on the austenitic microstructure, see Figure 6.53 for the control path. Again, arrows and crosses are used to facilitate the interpretability of the diagrams when appropriate. From Figure 6.53, it is clear that the unloading is implemented at a different temperature level than the loading.

Thereupon, Figure 6.54 shows the strain response of the material as a function of temperature. These data are further processed to yield the two-dimensional projections in the strain-strain and the temperature-equivalent-strain space, Figures 6.55, 6.56. Clearly, the phase transition is shifted due to the applied stress. In comparison to the phase transformations without external stresses, refer to the preceding sections¹⁶, the onset of the phase transformation is shifted about 40 K, simultaneously reducing the width of the transformation region to about 30 K. A second phase transformation, which is suggested by the shape of the DSC-curves, cannot be observed though the highest applied temperature is supposed to be well above the finish temperature of the second peak. This is corroborated by the fact that the strain recovery is concluded around a temperature of 50°C . Moreover, the temperature range between the completion of loading and the onset of phase transformation into the parent phase is particularly absorbing. Here, the strain significantly increases in loading direction. Further research might be necessary to explain this particular material behavior. Finally, the stress-strain curves are given in Figure 6.57. Clearly, the unloading is completely

¹⁶Beware of the different scales of the temperature strain diagrams resulting from the different temperature ranges.

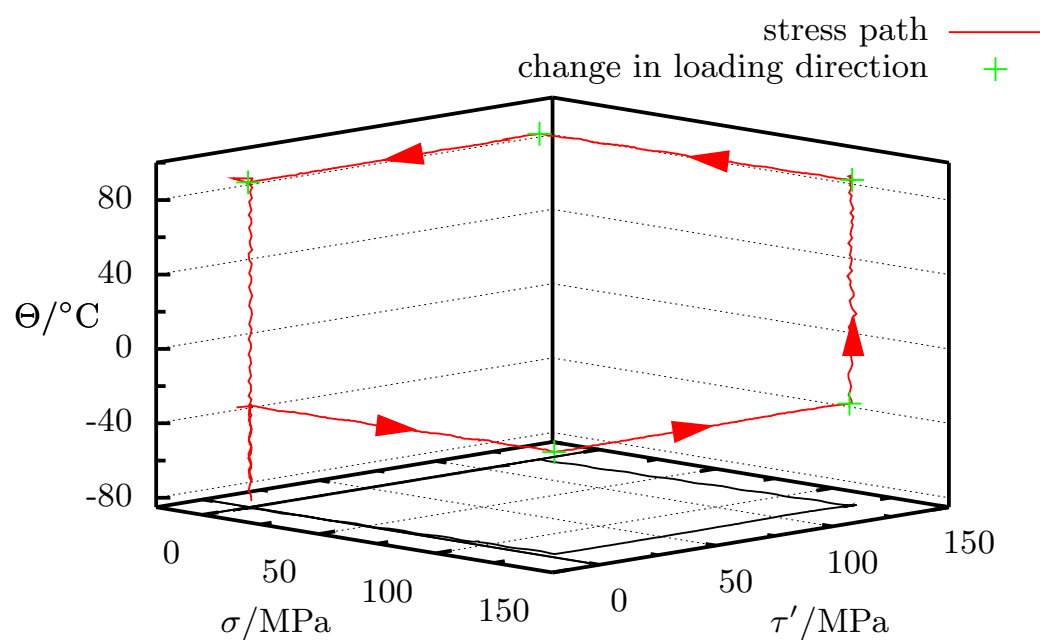


Figure 6.53: Pseudoplastic control path of an interrupted box test

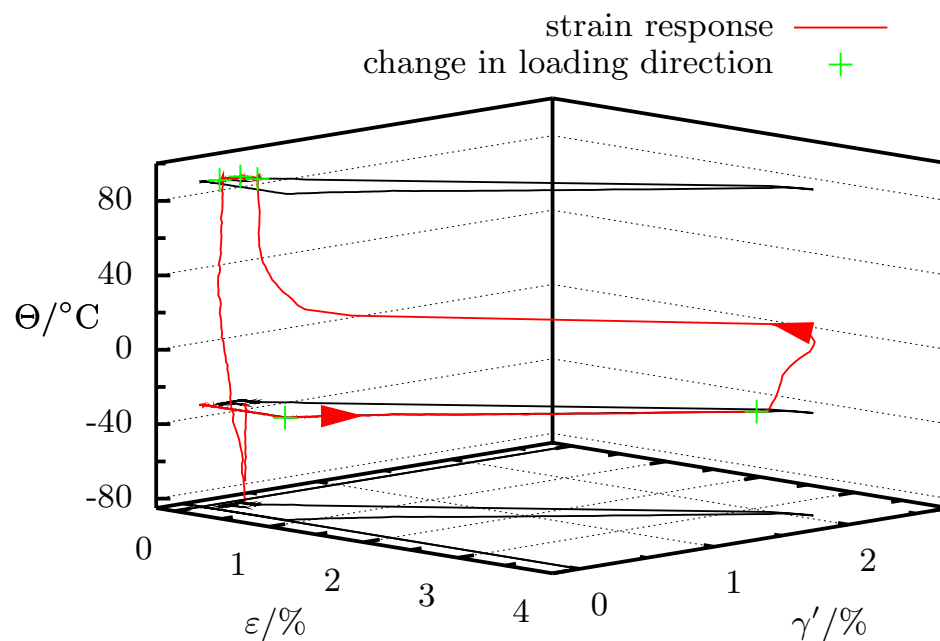


Figure 6.54: Pseudoplastic strain response as a function of temperature on the interrupted box stress path

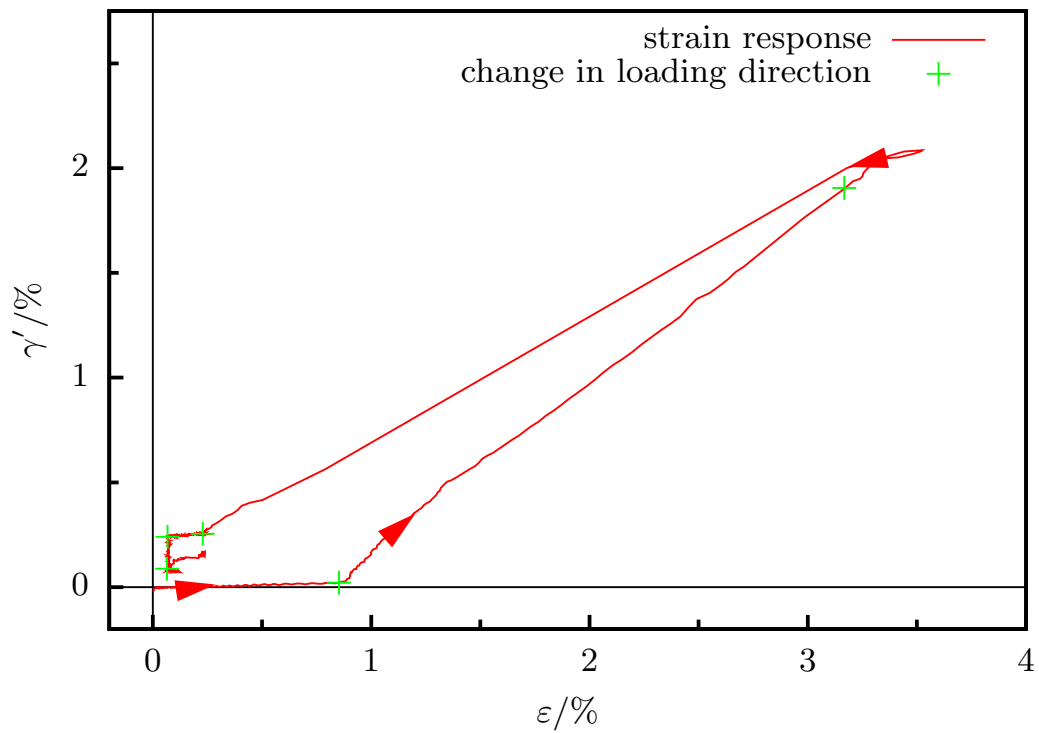


Figure 6.55: Pseudoplastic strain response on the interrupted box stress path

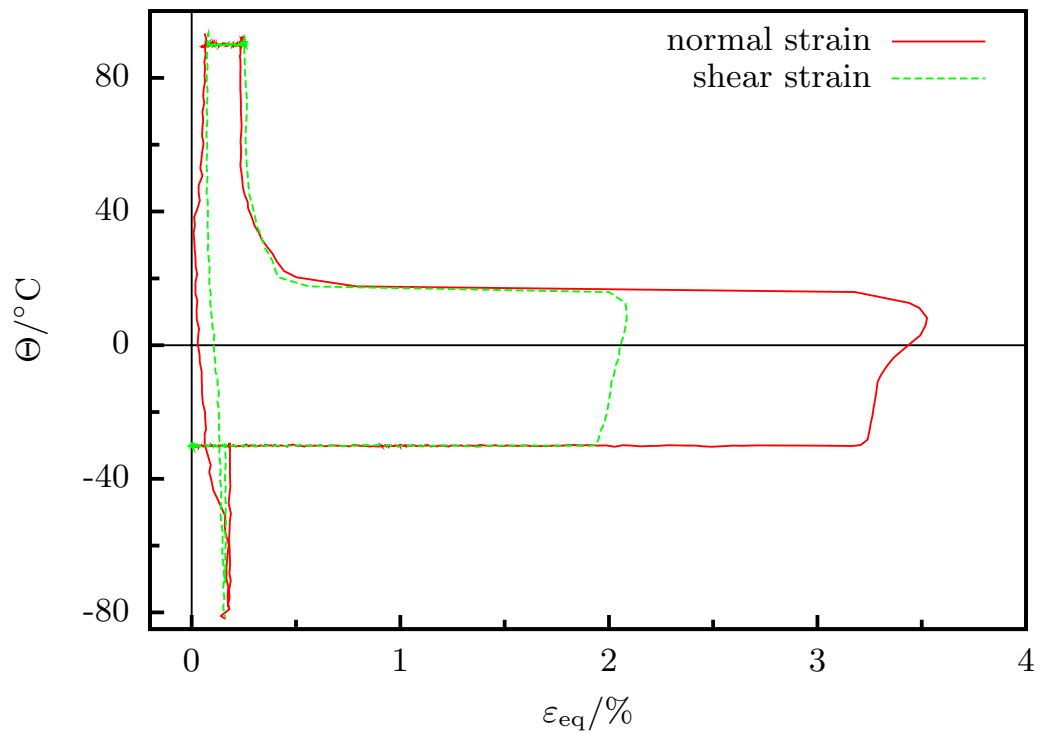


Figure 6.56: Strain as function of temperature for the interrupted pseudoplastic box test

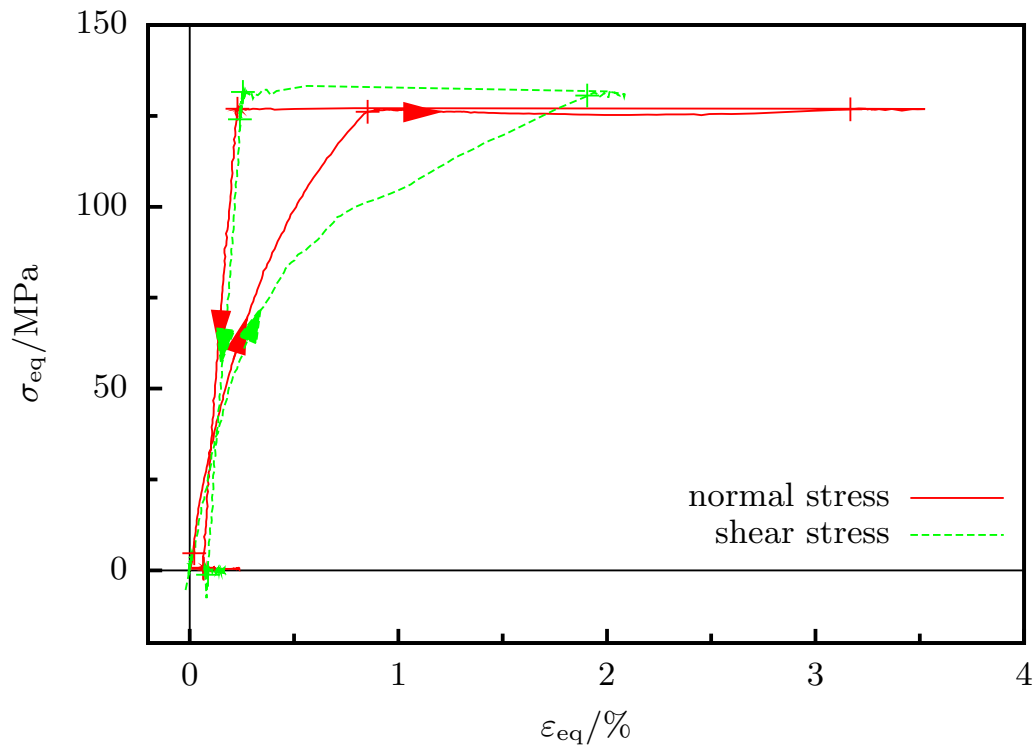


Figure 6.57: Stress-strain diagrams for the interrupted pseudoplastic box test

elastic as the transformation stress at a temperature of 90°C is substantially larger than the applied stress.

So far, the pseudoplastic material behavior has been investigated only in the first axial/torsional stress quadrant of the tension/compression/torsion subspace. In the following, a third multiaxial experiment is discussed, now, exhibiting a compressive stress component, see Figure 6.58 for the control path. The loading and unloading temperatures stay the same (-30°C , 90°C) as in the preceding experiment. Unlike before, after an identical loading process the axial stress is reduced from tension to a zero axial stress state and increased in compressive direction up to the same absolute value as in tension before.

Figures 6.59, 6.60, and 6.61 present the strain response of the specimen material on the accounted control path. While Figure 6.59 represents a three-dimensional temperature strain diagram featuring all interrelations between temperature, axial and torsional strain, Figures 6.60 and 6.61 give the two-dimensional projections into the axial-torsional strain and temperature-equivalent-strain space. With respect to the shear strain curves, it has to be noted that a small offset strain is existent due to the foregoing generation of the martensitic microstructure. It was pointed out before that even small stresses, which are below the control accuracy of the testing machine, may lead to a slightly larger amount of preferentially oriented martensite variants in comparison to other variants. This phenomenon leads to the observed offset strain. However, it is found intriguing

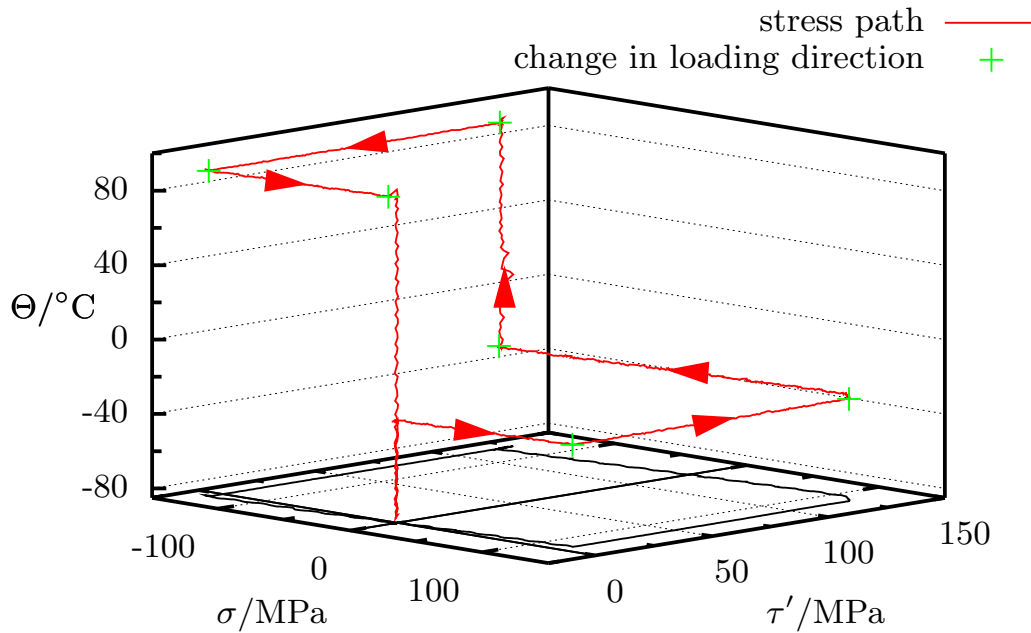


Figure 6.58: Pseudoplastic control path of an interrupted box test with compression

that the shear strain increases as well for loading in tension direction as for unloading and further loading in compression direction. This is accompanied by an increase of the axial strain upon tension and a subsequent reduction of axial strain as the tensile load is reduced followed by a compressive loading.

Again, similar to the conclusions for the preceding experiment, the axial strain component proceeds in loading direction at the beginning of the heating process directly after the completion of the mechanical loading. This process is reversed as the phase transformation sets in. By contrast, this effect cannot be observed for the shear strain. Whether this phenomenon has to be attributed to time dependent creep-like effects, may be subject to further research.

Figure 6.62 contains the respective stress-strain behavior of the specimen material. Consequently, unloading is again completely elastic. The pseudoplastic material behavior is obvious upon axial unloading and further loading in the reverse direction.

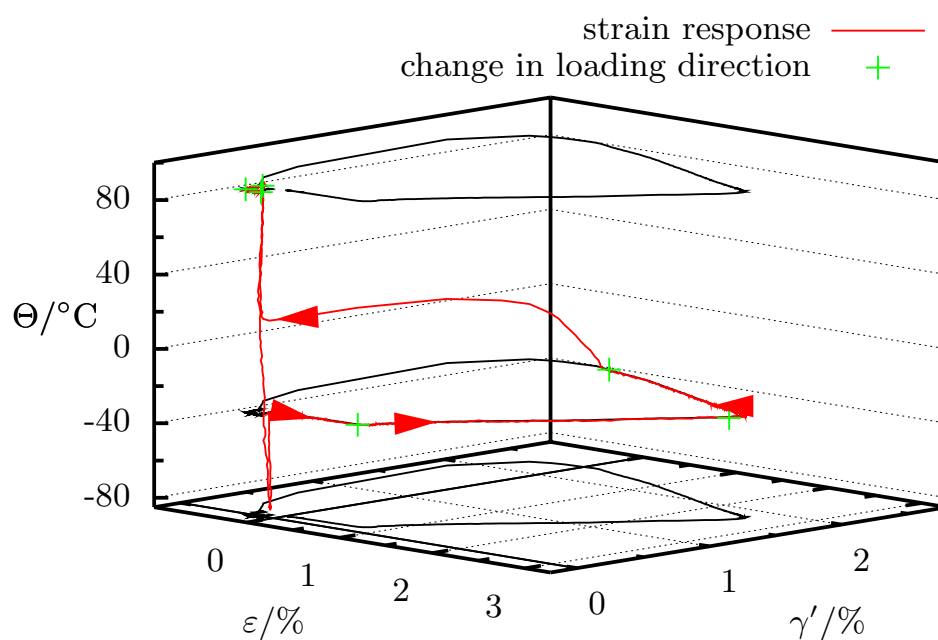


Figure 6.59: Pseudoplastic strain response as a function of temperature on the interrupted box stress path with compression

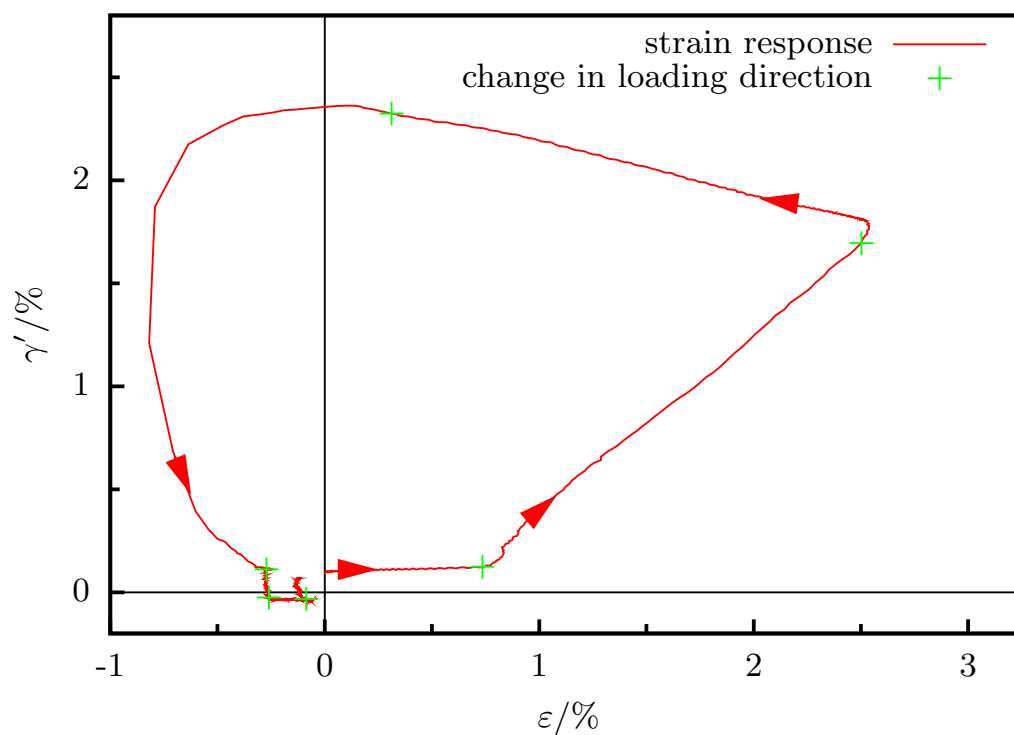


Figure 6.60: Strain response on the interrupted box stress path with compression

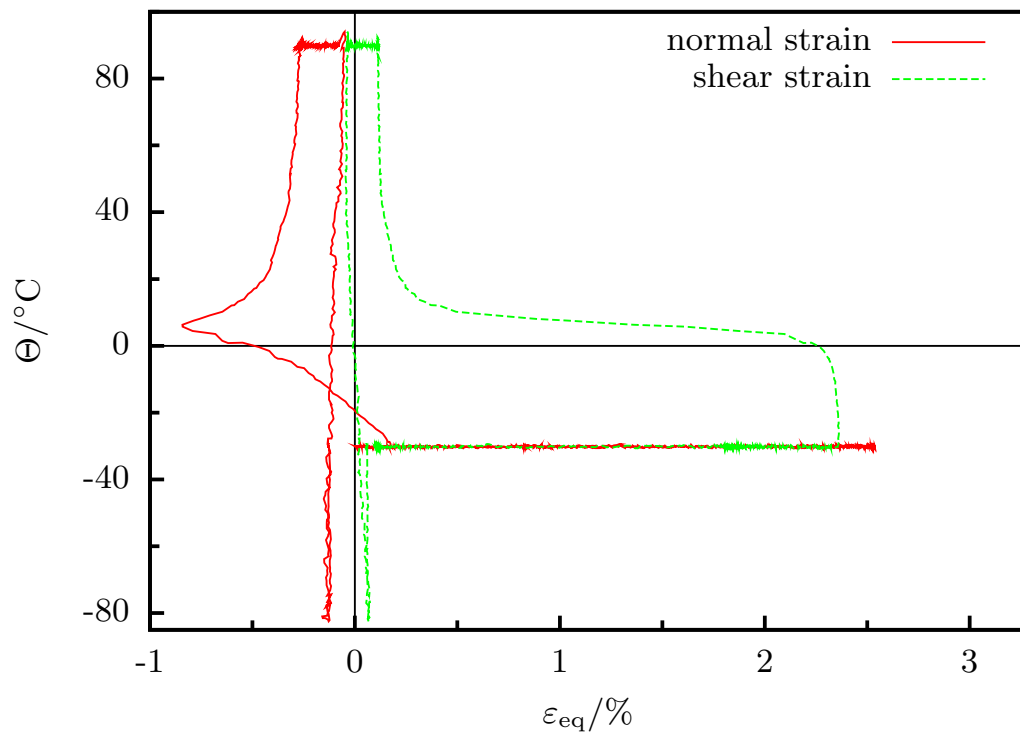


Figure 6.61: Strain as function of temperature for the interrupted pseudoplastic box test with compression

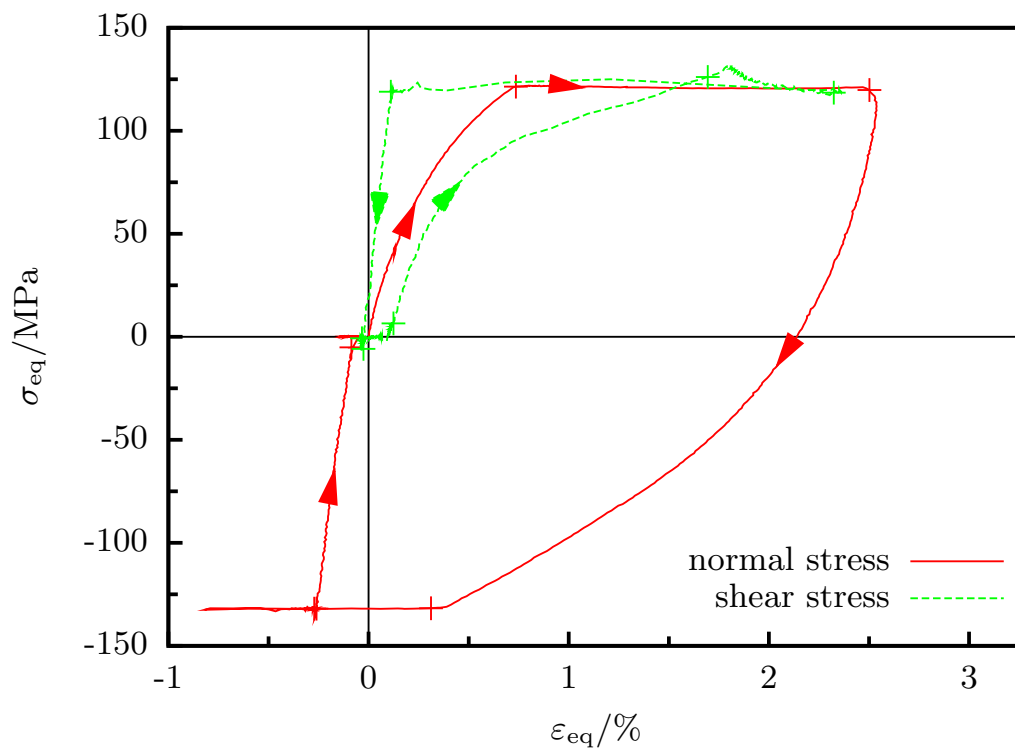


Figure 6.62: Stress-strain diagrams for the interrupted pseudoplastic box test with compression

7 Numerical methods for the parameter identification

In the context of parameter identification, the concepts of forward and inverse problems are frequently utilized.

Fundamentally, these concepts characterize on the one hand side the problem of identifying the output of a given model for a known parameter set and on the other side the inference of a model parameter set from a given observed data set. In the following, this concept is further elucidated and specified to fit the needs of this work.

7.1 Direct problem

If a physical system is to be described, the common scientific practice is to parametrize the systems. Once this is done, usually, efforts are conducted to model the system behavior, i.e., to specify the physical laws. In this account, it is important to mention that the set of parameters consists of observable and model parameters, which are mutually interrelated. This results in the fact that for a completely known set of model parameters some of the observable parameters can be predicted as a result of measurements. This is termed *forward* or *direct* problem, cf. [Tarantola, A. \(1987\)](#) for a detailed insight.

For the special case of thermomechanical material modeling, some observable parameters are, for instance, deformation and temperature. As the modified R_L -model is considered, the constitutive equations represent a system of ordinary differential equations and thus, an initial boundary value problem.

As pointed out in Section 5.8, it is quite cumbersome, if not even impossible, to deduce actual stress and actual strain from measurements on thin-walled tubular specimens within the presented experimental setup. Accordingly, actual stress and strain cannot be considered as observable parameters. Moreover, only engineering stress and strain can be inferred from the measured quantities. As a consequence, if observable parameters shall be used as input of the material model, the modified R_L -model presented in Section 4.2 should be specified for small deformations. This results in a material model relating engineering stress and strain. A summary of the fundamental governing equations of this modified R_L -model for small deformations is given in Figure 7.1. Here, the linearized strain tensor ε and the engineering stress σ are introduced. Furthermore, all stress quantities, which are denoted by the greek symbol τ in Section 4.2, are now substituted by the respective small deformational quantities labeled by the

Tension:	$\boldsymbol{\sigma} = \sigma_{11} \mathbf{e}_1 \otimes \mathbf{e}_1$ $\boldsymbol{\sigma}' = \frac{\sigma_{11}}{3} (2\mathbf{e}_1 \otimes \mathbf{e}_1 - \mathbf{e}_2 \otimes \mathbf{e}_2 - \mathbf{e}_3 \otimes \mathbf{e}_3)$ $\sigma_{11}^* = \frac{2}{3} \sigma_{11}, \quad \sigma_{22}^* = \sigma_{33}^* = \left(\frac{2}{3} - b^2 \right) \sigma_{11}$ $\hat{\sigma} = \sigma = \sqrt{\frac{2}{3}} \sigma_{11}$
Torsion:	$\boldsymbol{\sigma} = \boldsymbol{\sigma}' = \sigma_{12} (\mathbf{e}_1 \otimes \mathbf{e}_2 + \mathbf{e}_2 \otimes \mathbf{e}_1)$ $\sigma_{12}^* = b^2 \sigma_{12}$ $\sigma = \sqrt{2} \sigma_{12}$ $\hat{\sigma} = b \sigma$

Figure 7.2: Specification of stress quantities for special load cases

Consequently, for the case of single tensile or torsional forces with respect to the longitudinal axis, a state of plane stress can be adopted as no external forces impede a deformation in radial and circumference direction. Hence, the basic stress quantities can be calculated for the cases of simple tension and simple torsion, which is shown in compact form in Figure 7.2.

Because of the complexity of the material model, the system of differential equations eludes any direct analytical integration, which is why time integration has to be performed numerically. Different procedures, such as single-step and multi-step, multi-value algorithms, exist, cf. for example [Press, W.H. et al. \(2001\)](#). According to the considered system of differential equations, only single-step algorithms are of further interest. However, time integration can be realized using explicit or implicit approaches. A prominent one-parameter class of integration schemes is according to [Simo, J.C. & Hughes, T.J.R. \(1998\)](#) the generalized midpoint rule

$$\begin{aligned}
 x_{n+1} &= x_n + \Delta t f(x_{n+\vartheta}) \\
 x_{n+\vartheta} &= \vartheta x_{n+1} + (1 - \vartheta)x_n, \quad \text{with } \vartheta \in [0, 1].
 \end{aligned}
 \tag{7.1}$$

Here, x and $f(x)$ respectively denote the independent variable and function value at discrete points in time. Δt represents the time increment. For the limiting cases of the class parameter ϑ , the well-known *Euler* integration schemes are

deduced,

$$\begin{aligned}\vartheta = 0 &\Rightarrow \text{explicit forward Euler} \\ \vartheta = 1 &\Rightarrow \text{implicit backward Euler.}\end{aligned}\tag{7.2}$$

Generally speaking, implicit integration schemes are the method of choice due to their superior stability behavior, cf. [Press, W.H. et al. \(2001\)](#); [Anding, D.K. \(1997\)](#). One benefit is that significantly larger step-sizes can be realized without resulting in convergence problems. Nevertheless, in certain cases, for instance time critical ones, such as crashworthiness computations, or intrinsically parallelized applications, explicit time integration algorithms may prove advantageous.

In this regard some convergence tests were conducted on the implicit and mixed¹ implementations of the R_L -model coded by [Müller, C. \(2003\)](#). It turned out that comparable increment sizes are requisite for the implicit as well as the mixed integration scheme in order to guarantee solutions of equal accuracy. Because of that, together with the fact that the mixed integration algorithm converges within one single iteration step², and because an implicit implementation leads to highly complex derivatives and equations, a mixed integration scheme is used for formulating the forward problem.

The so obtained system of nonlinear equations can be solved, for example, by using *Newton's* method, see Section [7.3.1](#) and Appendix [A](#).

7.2 Inverse problem

Let a physical system be considered, which can be described in part by a mathematical model and the corresponding model parameters. The inverse problem is to derive the “true” model parameters for a given set of observable data, provided that the model is “correct” itself. Usually, the number of observed data is higher than the number of model parameters so that [Tarantola, A. \(1987\)](#) concludes that the inverse problem is as well overdetermined as concomitantly underdetermined. Overdetermination in this case results from the fact that more data values are given than needed for the identification of a certain set of model parameters. Hence, data redundancy exists. While on the one hand overdetermination of model parameters is typically unproblematic, on the other hand an inherent lack of data is present, which is why the complementary set of model parameters is kept underdetermined. The reason is that some “observable” data might not be measurable, or intrinsically different combinations of model parameters might exist, which lead to similar observable parameters. Yet, another

¹The implementation is neither completely implicit nor completely explicit, thus, allowing for a higher accuracy than purely explicit implementations on the one side and a considerable speedup in comparison to implicit implementations on the other side.

²Computation time is a paramount parameter for the identification of material parameters as can be seen in the further sections of this chapter.

point, which adds to the topic of underdetermination, are the experimental uncertainties, like those due to measurement errors, for example. Because of the propagation of errors, the quality of the identified model parameters is thus deteriorated.

Then, some of the model parameters, being in a state of underdetermination, leads to the notion of an ill-posed problem, which is used in the context of model parameter identification synonymously with the term “inverse problem”. According to Hadamard’s definition, a problem is called “ill-posed”, if the solution is not unique, or if it is not a continuous function of the given data, [Tarantola, A. \(1987\)](#).

7.2.1 Probability density and l_p -norm

As mentioned above, it is impossible to infer a set of discrete model parameters, which are taken from a continuous model parameter space from uncertain data. Even the “true” model exhibiting the “true” model parameters will not produce exactly the observed data. On this account, it has to be dealt with probabilities. The challenge is to determine a set of model parameters so that the observable data are the most likely, hence, the likelihood is to be maximized. Consequently, also model parameters are supposed to be given within error bars. Since the exact probability density of the parameters is not known, it has to be estimated. This yields in the notion of error estimators and *maximum likelihood estimation* as stated above.

In this regard, the one-parameter *generalized Gaussian* probability density is frequently used and can be formulated as follows,

$$f_p(y_i) = \frac{p^{(1-1/p)}}{2S_{p_i} \Gamma(1/p)} \exp\left(-\frac{1}{p} \left(\frac{y_i - y(x_i, a_i)}{S_{p_i}}\right)^p\right), \quad (7.3)$$

with $y(x_i, a_i)$, y_i , S_{p_i} being calculated data values, measured data values, and the respective estimators of dispersion. Furthermore, x_i and a_i denote the model input observable parameters and model parameters while $\Gamma(\cdot)$ and p are the *Gamma* function and the generalized Gauss parameter.

In this context, the *weighted l_p -norm* is of further interest being defined as

$$\|\mathbf{z}\|_p = \sum_i^N \left(\frac{|z_i|}{d_i}\right)^p, \quad (7.4)$$

with z_i indicating the components of \mathbf{z} and the weighting factors d_i .

Now, for specific values of p , the generalized Gaussian leads to

$$f_1(y_i) = \frac{1}{2S_{1_i}} \exp\left(-\frac{|y_i - y(x_i, a_i)|}{S_{1_i}}\right), \quad (7.5)$$

being the symmetric exponential probability density for $p = 1$,

$$f_2(y_i) = \frac{1}{\sqrt{2\pi}S_{2_i}} \exp\left(-\frac{1}{2}\left(\frac{y_i - y(x_i, a_i)}{S_{2_i}}\right)^2\right), \quad (7.6)$$

being the well-known normal (Gaussian) distribution for $p = 2$, and

$$f_\infty(y_i) = \begin{cases} 1/(2S_\infty) & \text{for } y(x_i, a_i) - S_\infty \leq y_i \leq y(x_i, a_i) + S_\infty \\ 0 & \text{otherwise,} \end{cases} \quad (7.7)$$

being the box-car probability density for $p = \infty$ with the respective estimators of dispersion, namely the *mean deviation* S_1 , *standard deviation* S_2 , and *mid range* S_∞ . Moreover, the choice of the probability density type is crucial for the further estimation of model parameters. Frequently, a normal error distribution is assumed for measurement and modelization errors, which is motivated by the fact that the sum of a very large number of small random deviations almost always converges to a normal distribution, [Press, W.H. et al. \(2001\)](#).

Now, specifying the condition for a maximum likelihood of the observed data set, the cumulative probability of the measured data has to be maximized, which leads for the case of a normal distribution to

$$P \propto \exp\left(-\frac{1}{2}\sum_{i=1}^N\left(\frac{y_i - y(x_i, a_i)}{S_{2_i}}\right)^2\right) \longrightarrow \max. \quad (7.8)$$

This maximization problem can be further simplified so that for a maximization of the overall probability P , the following relation has to be minimized,

$$\chi^2 := \sum_{i=1}^N\left(\frac{y_i - y(x_i, a_i)}{S_{2_i}}\right)^2 \longrightarrow \min. \quad (7.9)$$

This sum is frequently referred to as *chi-square* whereas the minimization problem as a whole is called *weighted least squares*. In terms of the notion of an l_p -norm with the Gauss parameter p , Equation (7.9) represents the weighted sum of the l_2 -norm.

For the case of a constant standard deviation with $S_2^i = S_2$, the problem of weighted least squares collapses to the problem of least squares, which is consequently the minimization of the cumulated l_2 -norm of the measurement errors, i.e.,

$$\sum_{i=1}^N (y_i - y(x_i, a_i))^2 \longrightarrow \min. \quad (7.10)$$

As this derivation is based on the assumption of normally distributed measurement errors, strictly speaking, normally distributed errors are implicitly supposed for every minimization using least squares. Moreover, it is evident that

the probability of the *mean* or *mathematical expectation* of each measured datum, being the central estimator of the normal distribution, is maximized, cf. [Tarantola, A. \(1987\)](#).

Nevertheless, in many cases, the normal distribution is a rather poor estimation of measurement or modelization errors as for a normal distribution the probability of the occurrence of very large outliers is null without a significant adjustment of the standard deviation. The reason is that the variance of a normal distribution is limited. That is why a small number of outliers is capable of corrupting the parameter identification on a set of otherwise adequate data.

A significantly more robust type is the Cauchy probability density function as it features infinite variance,

$$f_c(y_i) = \frac{1}{\pi S_{c_i}} \frac{1}{1 + \left(\frac{y_i - y(x_i, a_i)}{S_{c_i}} \right)^2}. \quad (7.11)$$

Additionally, it is also bell-shaped like the normal distribution. However, it does not lead to a minimization of an l_p -norm. By contrast, also more robust than the normal Gaussian, the symmetric exponential distribution (Equation (7.5)) can be utilized to reduce the inverse problem to a minimization of the l_1 -norm leading to the *least-absolute-value* criterion, [Tarantola, A. \(1987\)](#).

If different types of error are considered, which result, for instance, from rounding of the last digit of the measurement reading, the box-car distribution associated with the l_∞ -norm comes into play, which yields the *minmax* criterion. Here, the maximum absolute value of the error is minimized.

Infinitely many error distributions can be imagined leading to a minimization of an l_p -norm. Here, it is emphasized that the higher the order of l_p -norm, the higher is the sensitivity to large errors. In this context and in consideration of modelization errors, it is always possible, unless known otherwise, to drop the assumption of a normal error distribution in favor of a different probability density type. However, keeping the drawbacks of a normal distribution in mind, and not knowing any better, a first guess might always be the normal distribution. For an evaluation of the *goodness-of-fit* of a normal distribution with reference to the adopted model, the chosen model parameters, and the chosen probability density type, the weighted least squares can be used as well, [Press, W.H. et al. \(2001\)](#). Here, the calculated chi-square has to be compared with the *chi-square distribution for $N - M$ degrees of freedom*, with N and M respectively being the number of measured data and model parameters.

As pointed out at the beginning of this section, the respective estimator of dispersion of the model parameters is of paramount interest not only for an assumed normal distribution but also for all probability density types. For complicated mathematical models, it can be quite cumbersome to calculate this measure, as such the standard deviations being the main diagonal elements of the covariance matrix in the case of a normal distribution. [Anding, D.K. \(1997\)](#), for example, adopts a different path with respect to the propositions made by [Press, W.H.](#)

et al. (2001). Here, once the validity of the error distribution is verified, multiple sets of “observed” data are *Monte Carlo*³ generated in the vicinity of the originally measured data values using the assumed error distribution. Then, utilizing this vast set of generated data recalculating the model parameters, the standard deviation of each model parameter is estimated.

7.3 Optimization procedures

As the inverse problem for the identification of material parameters represents an optimization problem, and several systems of nonlinear equations exist within this work, which can be reformulated yielding optimization problems, such as the direct problem pertaining the problem of plane stress and the calculation of internal variables, attention is drawn to the field of optimization procedures. In general, optimization problems can be solved analytically and numerically. As problems get more complicated, typically, there remains no choice anymore as to what road is to be taken. That together with the fact that computing power is still increasing abets the application of numerical procedures.

Different types of optimization procedures can be classified utilizing the order of information needed for the respective calculation. In this regard, the order of the optimization method complies to the order of derivatives that are incorporated within the algorithm. In [Vogelsang, H. \(2001\)](#), a classification of some well-known optimization methods is carried out, see [Table 7.1](#). Hereof, it is ob-

Procedure	Order	Information	Convergence	Effort
Newton	2	$f, \nabla f, \nabla^2 f$	■ ■ ■	■ ■ ■
quasi-Newton	1	$f, \nabla f$	■ ■	■ ■
conj. gradient	1	$f, \nabla f$	■ ■	■ ■
Gauss-Seidel	0	f	■	■
stochastic	0	f	□	■

Table 7.1: Computation effort and convergence for several optimization procedures according to [Vogelsang, H. \(2001\)](#)

vious that the higher the order of the optimization algorithm, the better is the convergence rate. Concomitantly, a high order implying high derivatives leads to a significant raise of the computational costs as the computation of derivatives is usually very expensive. Sometimes, the calculation of derivatives is not even possible at all. In this regard, the convergence rate has to be weighed against the computational costs in order to minimize the overall computation time.

However, the overall convergence behavior is additionally of further interest. Newton’s method for example converges only locally quadratically, meaning that,

³see [Section 7.3](#) or [Press, W.H. et al. \(2001\)](#); [Tarantola, A. \(1987\)](#) for a description of Monte Carlo methods

dependent on the starting values, it is possible that Newton's method converges only subquadratically or does not converge at all. Moreover, for multimodal objective functions, gradient based methods, although more robust than Newton's method, cf. [Geiger, C. & Kanzow, C. \(1999\)](#), i.e., a minimum is always found, converge usually to local minima.

In this connection, iterative optimization procedures can be further subdivided to give the categories of deterministic and stochastic approaches, Table 7.2.

iterative/numerical		analytical
stochastic	deterministic	
Monte Carlo trial & error evolutionary algorithms	Newton methods gradient based	extreme value problem

Table 7.2: Classification of optimization algorithms

The main difference between stochastic and deterministic approaches is the scope of information. Fundamentally, deterministic algorithms seek locally for a minimum. As long as the objective function is sufficiently smooth or the starting values are chosen luckily, a deterministic algorithm delivers the global minimum. By contrast, in case of multimodal or noisy objective functions, deterministic algorithms typically get stuck within local minima as stated before.

Eventually, because of the random component, stochastic methods represent intrinsically parallel search algorithms whereas deterministic procedures are based on an inherently sequential search.

Evolutionary algorithms are specifically intriguing, since, herewith, it is tried to combine the advantages of both categories of iterative optimization procedures. On the one hand a global search is guaranteed by use of a random search component while on the other hand, similar to deterministic approaches, the incorporation of the last ameliorating steps leads to a significant acceleration of convergence with respect to purely stochastic algorithms. In this regard, it is dealt with evolutionary algorithms in detail in Section 7.3.3.

However, as deterministic algorithms are very important also for the solution of optimization problems within this work, Newton's method and the *NEWUOA*⁴ algorithm, explained in detail in [Powell, M.J.D. \(2004a\)](#), are shortly presented in the next sections.

7.3.1 Newton's and damped Newton method

The basic problem of an optimization is the minimization problem. Also problems of maximization can be reformulated to yield minimization problems. Con-

⁴NEW Unconstrained Optimization Algorithm

sequently, for a given objective function

$$f : \begin{cases} \mathbb{R}^n & \rightarrow \mathbb{R} \\ \mathbf{x} & \mapsto f(\mathbf{x}) \end{cases} \quad (7.12)$$

the problem reads

$$f(\mathbf{x}) \longrightarrow \min. \quad (7.13)$$

The idea behind Newton's method is to approximate the objective function by the respective second-order Taylor expansion, see [Nocedal, J. & Wright, S.J. \(1999\)](#),

$$q_k(\mathbf{x}) := f(\mathbf{x}_k) + \nabla f(\mathbf{x}_k)^T(\mathbf{x} - \mathbf{x}_k) + \frac{1}{2}(\mathbf{x} - \mathbf{x}_k)^T \nabla^2 f(\mathbf{x}_k)(\mathbf{x} - \mathbf{x}_k). \quad (7.14)$$

Here, $\nabla f(\cdot)$ and $\nabla^2 f(\cdot)$ denote the gradient vector and Hessian of the objective function, \mathbf{x}_k being the independent variables at iteration step k . Subsequently, the approximated function q_k is minimized instead of the objective function itself,

$$q_k(\mathbf{x}) \longrightarrow \min. \quad (7.15)$$

As the calculation of the inverse of the Hessian is usually expensive, the following system of linear equations is solved for \mathbf{z}_k ,

$$\nabla^2 f(\mathbf{x}_k)\mathbf{z}_k = -\nabla f(\mathbf{x}_k). \quad (7.16)$$

As a direct consequence of the minimization of q_k , \mathbf{x}_{k+1} can be taken as

$$\mathbf{x}_{k+1} := \mathbf{x}_k + \mathbf{z}_k. \quad (7.17)$$

But as already mentioned, sometimes Newton's method does not yield a minimum according to the specific objective function. Then, it proves useful in certain cases to take a different governing equation for \mathbf{x}_{k+1} , resulting in the damped Newton method with

$$\mathbf{x}_{k+1} := \mathbf{x}_k + t_k \mathbf{z}_k, \quad (7.18)$$

which is subject to an additional condition specifying t_k . [Verfürth, R. \(2005\)](#) for example suggests

$$|f(\mathbf{x}_k + t_k \mathbf{z}_k)|^2 \leq \left(1 - \frac{t_k}{2}\right) |f(\mathbf{x}_k)|^2 \quad (7.19)$$

in order to find the adequate damping parameter t_k .

7.3.2 The NEWUOA algorithm

One of the major advantages of the NEWUOA approach is that no derivatives of the objective function $f(\mathbf{x})$ are needed. The only requirement is that the function may be calculated for every vector of variables \mathbf{x} . Again, the aim is to find the minimum of the objective function defined in Equation (7.12), i.e.,

$$f(\mathbf{x}) \longrightarrow \min. \quad (7.20)$$

Based on m interpolation points, a quadratic model $q(\mathbf{x})$ of the function $f(\mathbf{x})$ is generated so that the following identity holds for the interpolation points \mathbf{x}_k^i ,

$$q_k(\mathbf{x}_k^i) = f(\mathbf{x}_k^i), \quad i = 1, 2, \dots, m \quad \text{with} \quad n+2 \leq m \leq \frac{1}{2}(n+1)(n+2), \quad (7.21)$$

and n being the number of independent variables. It is noteworthy that, generally, the number of interpolation points is well below the number of independent parameters of the quadratic model, $\frac{1}{2}(n+1)(n+2)$. Consequently, there is some freedom in the independent parameters, which is taken up for the initial model by setting all undefined elements of the Hessian $\nabla^2 q_0(\mathbf{x})$ to zero.

Subsequently, the minimum of the so obtained quadratic approximation of the objective function can be approximated by means of a trust region subproblem,

$$q_k(\mathbf{x}_k^{\text{opt}} + \mathbf{v}_k) \longrightarrow \min, \quad \text{subject to} \quad |\mathbf{v}_k| \leq \Delta, \quad (7.22)$$

with the parameter Δ characterizing the trust region. Here, $\mathbf{x}_k^{\text{opt}}$ is defined by

$$f(\mathbf{x}_k^{\text{opt}}) = \min\{f(\mathbf{x}_k^i)\}, \quad i = 1, 2, \dots, m. \quad (7.23)$$

If the minimum of $f(\mathbf{x})$ is not satisfactorily approximated, the quadratic model has to be modified. This is realized by altering one single interpolation point according to

$$\mathbf{x}_{k+1}^t := \mathbf{x}_k^{\text{opt}} + \mathbf{v}_k, \quad t \in \{1, 2, \dots, m\}, \quad (7.24)$$

and

$$\mathbf{x}_{k+1}^i := \mathbf{x}_k^i, \quad i \in \{1, 2, \dots, m\} \setminus \{t\}. \quad (7.25)$$

Analogous to Equation (7.21), the new quadratic model $q_{k+1}(\mathbf{x})$ has to fulfill the respective interpolation conditions for $k+1$. Nevertheless, since fewer interpolation conditions than independent parameters are given, some parameters stay undefined. On this account, the difference function d_k is introduced, i.e.,

$$d_k(\mathbf{x}) = q_{k+1}(\mathbf{x}) - q_k(\mathbf{x}). \quad (7.26)$$

The undefined independent parameters are thereupon determined by minimizing the Hessian of the Frobenius-norm of the difference function $d_k(\mathbf{x})$,

$$\|\nabla^2 d_k(\mathbf{x})\|_F \longrightarrow \min \quad (7.27)$$

subject to

$$d_k(\mathbf{x}_{k+1}^i) = (f(\mathbf{x}_{k+1}^t) - q_k(\mathbf{x}_{k+1}^t)) \delta_{it}, \quad i = 1, 2, \dots, m, \quad (7.28)$$

with δ_{it} representing the Kronecker delta. Consequently, $d_k(\mathbf{x}_{k+1}^i)$ vanishes for $i \neq t$.

For a more detailed introduction of the NEWUOA algorithm the interested reader is referred to [Powell, M.J.D. \(2002, 2004a,b\)](#) and the references cited therein.

7.3.3 Evolutionary algorithms

As pointed out in the beginning of Section 7.3, evolutionary algorithms are conceptually different from strictly deterministic approaches, such as Newton's method and the NEWUOA algorithm presented in Sections 7.3.1 and 7.3.2. Furthermore, they are supposed to be better suited to cope with multimodal, noisy, and rugged shaped objective functions. In this section, a short introduction to evolutionary algorithms is given in order to clarify the used procedures and nomenclature.

Nowadays, the term evolutionary algorithms combines three similar but traditionally and historically separated schools, which are respectively known as *evolutionary programming*, *evolution strategies*, and *genetic algorithms*. According to [Pohlheim, H. \(1999\)](#), the first works in those fields can be attributed to [Fogel, L.J. et al. \(1966\)](#); [Rechenberg, I. \(1973\)](#); [Holland, J.H. \(1975\)](#). Although the differences of those three approaches were highlighted in the past in order to explain its respective right to exist, now, it is common understanding to emphasize the similarities, and to profit from each other's findings.

In this regard, the basic principle of evolutionary algorithms is to mimic and to adapt successful procedures of nature. In this context, it is important to distinguish between a one-to-one copy and an adaptation and abstraction of natural methods, which is the procedure of choice.

Again, as in the preceding sections, the objective is to solve a problem as formulated by Equations (7.12) and (7.13). As the consecutive steps of evolutionary algorithms can be attributed or compared to natural processes, biological notions are oftentimes used for describing the working principles. In [Vogelsang, H. \(2001\)](#), for example, a correspondence table is given in reference to a day-to-day engineering language. There, some fundamental terms are specified that are frequently used in connection with evolutionary algorithms. A partly amended version is shown in Table 7.3.

7.3.3.1 Simple evolutionary algorithm

As shown in Figure 7.3, a typical simple evolutionary algorithm comprises three distinct and evolutionary algorithm specific steps, which are termed *selection*, *recombination*, and *mutation* in analogy to evolutionary biology. While selection

gene	→	single parameter e.g. Young's modulus
individual	→	vector of parameters
genotype	→	general set of distinct parameters within a parameter vector
population	→	set of all parameter vectors
generation	→	population at a specific point in time
habitat	→	objective function
chance of survival, fitness	→	value of objective function

Table 7.3: Correspondence table specifying some fundamental terms in reference to evolutionary algorithms

is used in all evolutionary algorithms, the two latter steps are utilized in varying degrees, sometimes, even completely left out depending on the specific algorithm. Moreover, some additional tasks have to be performed one of which is the crucial assignment of each individual's fitness.

At the start of each evolutionary optimization, an initial population, being the first generation, has to be generated. That is, a predefined and throughout the whole optimization constant number of parameter vectors is created. Here, the initialization can be performed uniformly at random or with reference to some chosen parameter vectors, which are supposed to be good starting guesses, meaning that on the one hand the chosen parameter vectors themselves can be incorporated into the initial population, or uniformly at random distributed vectors around the starting guesses can be used. With reference to deterministic approaches, which use in general a much smaller number of initial parameter vectors, the starting point for evolutionary algorithms is, hence, much more diverse.

Subsequently and within each further iteration step, the value of the objective function has to be calculated for each parameter vector. As soon as all objective values are known, the goodness of each parameter vector has to be estimated, i.e., fitness has to be assigned. As is the case for all single steps of the simple evolutionary algorithm, several approaches exist as how to assign fitness in the most efficient way. Prominent methods are, for instance, proportional⁵ and rank-based fitness assignment. Pohlheim ([Pohlheim, H. \(1999\)](#)) points out that due to several reasons⁶, it can be shown that a rank-based fitness assignment outperforms other fitness assignment approaches.

Once the fitness and the fitness distribution is known, it can be decided, which parameter vectors should be utilized for the creation of even better parameter vectors, thus, resulting in a new generation. In analogy to evolutionary biology,

⁵The fitness of each individual is proportionally assigned with reference to its own objective value and the objective value of the others.

⁶Proportional fitness assignment may lead to premature convergence or stagnation.

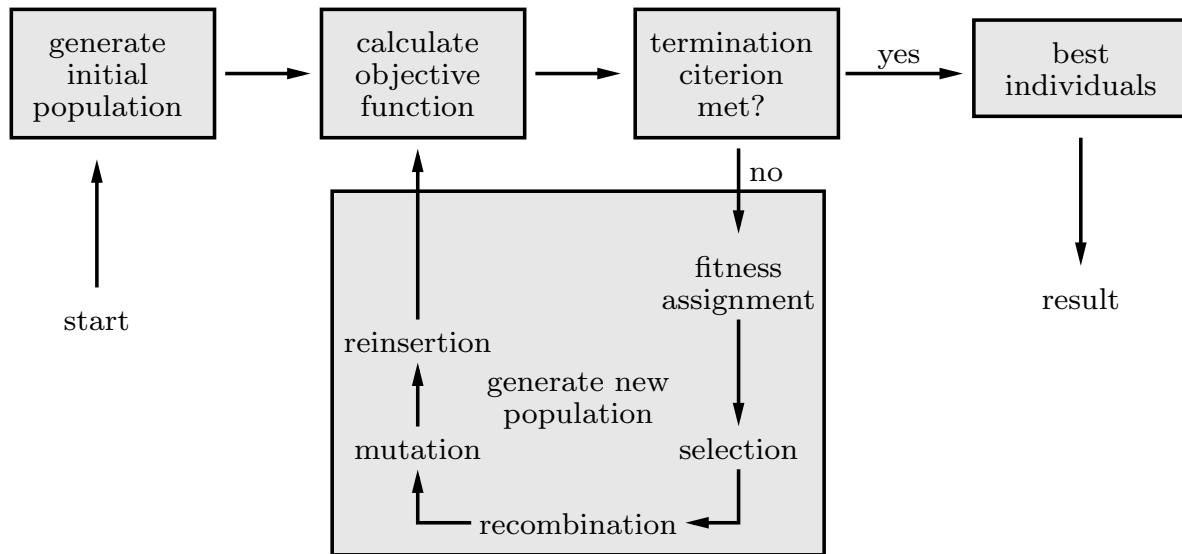


Figure 7.3: Structure of the simple evolutionary algorithm according to [Pohlheim, H. \(1999\)](#)

it is determined, which individuals should become parents, i.e., are used for mating. This process is known as selection. Consequently, individuals exhibiting a higher fitness are supposed to be chosen with a higher probability. Nevertheless, truncation selection, which neglects all individuals that feature a fitness below a well-defined threshold value is not always the appropriate method. Furthermore, stochastic universal sampling, roulette wheel selection, and tournament selection might prove advantageous in multiple cases, see [Pohlheim, H. \(1999\)](#) for a detailed review on this topic.

The actual process of mating and reproduction of offspring is a combination of recombination and mutation. The former is characterized by an interpolation or discrete interchange of single parameters between several⁷ selected parent parameter vectors.

Following the recombination step, each newly created parameter vector is mutated. In so doing, small statistical fluctuation terms with a zero mean are added to the parameters. As evident, the variance of the stochastic mutation is a crucial parameter of the specific evolutionary algorithm as such governing the coarseness of the search. With reference to deterministic optimization algorithms, which often work with a step-size adaptation, see [Geiger, C. & Kanzow, C. \(1999\)](#), algorithms for adaptive step-size control can also be incorporated into evolutionary algorithms, then adapting the mutation variance, see [Ostermeier, A. et al. \(1994\)](#); [Hansen, N. \(2005\)](#). Albeit possible, [Pohlheim, H. \(1999\)](#) suggests a different methodology, which will be revisited in Section 7.3.3.2. The main drawback of an adaption of the mutation step is correspondingly the ten-

⁷Different from biological evolution, the number of parents who are used for mating is not necessarily two within evolutionary algorithms.

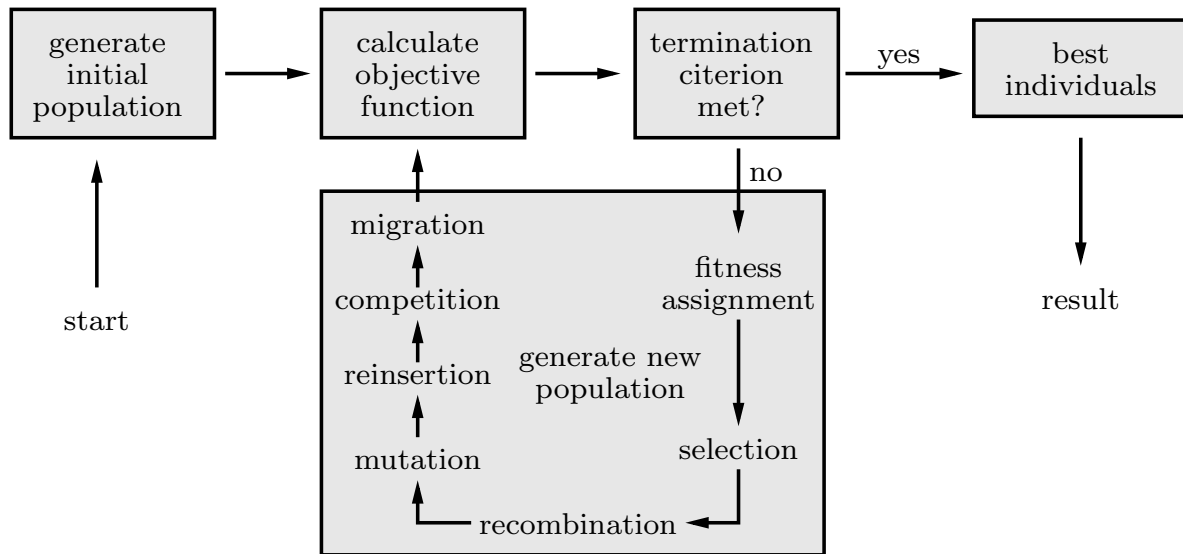


Figure 7.4: Structure of the extended evolutionary algorithm according to [Pohlheim, H. \(1999\)](#)

dency to converge to local minima.

As already mentioned, the total size of the population is kept constant. Consequently, due to the generation of offspring, a larger pool of individuals compared to the fixed population size is existent after recombination. On this account, only a part of all parameter vectors is reinserted into the new generation. This leads, for example, to the concepts of elitest or pure reinsertion, cf. [Pohlheim, H. \(1999\)](#). At this point the new generation has been created and the next iteration can be conducted.

7.3.3.2 Extended evolutionary algorithm

In contrast to Section [7.3.3.1](#), now, the constraint that only one single homogeneous population may be existent is abandoned. It can be shown that, hereby, a significant enhancement of the convergence behavior is attained in most cases. Furthermore, by using this amendment of the simple algorithm, evolution is modeled in a way that is significantly more similar to biological evolution. The structure of the extended version of the simple evolutionary algorithm is given in Figure [7.4](#).

In the following, the special case of a regional model featuring competition and migration is accounted. Nevertheless, Figure [7.4](#) also applies to the general case of an extended evolutionary algorithm. The interested reader is once more referred to the excellent monograph by [Pohlheim, H. \(1999\)](#).

The regional model concept is based on the notion of multiple subpopulations. In the general case, different populations coexist without any interrelation. That means, different evolutionary algorithms with respect to different feasible oper-

ators⁸ can be realized. In so doing, it can be surveyed to what extent different strategies are appropriate for solving the optimization problem. As this information is indeed interesting but does not directly lead to an improvement of the convergence rate, the concept of competing subpopulations is added. Here, after each iteration step the success⁹ of the different populations is compared. This together with the possibility of individuals leaving and joining specific subpopulations according to the respective success of the subpopulations, known as migration, yields a powerful optimization tool. Thus, it is feasible to reallocate the computational resources of the subpopulations. The practical realization is that the subpopulation size is changing, concomitantly keeping the overall population size constant. Accordingly, “successful” subpopulations are subject to immigration processes from less successful subpopulations resulting in a growth of the respective population size.

In this regard, it is important that the subpopulations are separated from each other most of the time, and, only occasionally, migration is possible. Furthermore, a lower limit of the subpopulation size is mandatory in order to inhibit the complete annihilation of a subpopulation.

In this manner, it is possible and highly probable that different subpopulations are dominant referring to the population size at distinct points in time. The reason is that, as different operators may be used, distinct strategies prove successful at different points in time during the optimization process. A typical example is the use of different mutation variances. In this vein, one subpopulation seeks after an optimum very coarsely within the search space while the other performs a very fine search. It is evident that the coarse search will be more successful in most cases at the beginning of an optimization run while a finer search will be more promising later on as most parameter vectors are in the vicinity of the optimum.

In the light of step size adaptation, the regional approach incorporating competition and migration is considered more robust, since, as a minimum subpopulation size is immanent so that subpopulations are not annihilated, larger step sizes are more likely even if a subpopulation with a very small mutation variance is dominant. By this means, the probability of a premature convergence can be efficiently reduced.

7.3.3.3 Classification of evolutionary algorithms

Generally speaking, the only way to assure the finding of the optimum of a multimodal, rugged shaped, and noisy objective function is to perform a systematic exploration of the model space. However, this proves impossible due to the extremely high computational costs for a high-dimensional model space. Because of this, stochastic methods have been developed.

⁸fitness assignment, selection, recombination, mutation, reinsertion

⁹for example the best parameter vector of every subpopulation

In this section, it is tried to classify the distinct steps of a simple¹⁰ evolutionary algorithm with respect to stochastic and deterministic methods. The same can be done for general evolutionary algorithms in a straightforward manner.

Starting with the generation of an initial population, it can be stated that the procedure is very similar to deterministic approaches. As long as “good” solutions of a problem are known, those are used as a first guess. The subsequent calculation of the objective values for the parameter vectors and the fitness assignment are as well straightforward and strictly deterministic. Accounting selection as being the consecutive step within evolutionary algorithms, this step can also be regarded as deterministic, albeit with some exceptions. In the case of a truncation selection procedure, the first part of the just mentioned statement holds true without any restrictions while for the case of different selection methods, a stochastic component is introduced and the latter restriction is evident. Nevertheless, a selection of parameter vectors with lower objective values is even in the other cases more likely and the reason for using a stochastic component within the selection step is just to guarantee a higher diversity of the solutions. With respect to the recombination process, it is pointed out that the interchange or interpolation is also considered mainly deterministic. Indeed, what makes the family of evolutionary algorithms belong partly to stochastic methods is the occurrence of mutation. Here, irrespective of the earlier iteration progression, single parameters of the parameter vectors are altered. As already mentioned in Section 7.3.3.2, this step is responsible for an ongoing iteration even if local minima are detected. In general, this holds true for a finite period of time, which, in particular, can be very long though.

7.4 Implementation and realization

7.4.1 Formulation of the objective function

The main idea behind the applied concept of parameter identification is to reduce the parameter identification problem to an optimization problem, see Section 7.2. Consequently, the objective function has to be formulated.

An appropriate measure of the goodness of the fit seems to be naturally the error between observed and modeled data using an adequate l_p -norm, Section 7.2.1. In the case of a continuum mechanics, material model, this leads to the comparison of measured and computed stress values for distinct strain values. This means that the objective function value depending on the independent variables, namely the material parameters, is the accumulated stress error. Hence, for the computation of each single objective value, the direct problem as shown in Section 7.1 has to be solved. In this context, it is obvious that an analytical evaluation of the derivatives of the objective function with respect to the independent variables is impossible, since only discrete objective values can be

¹⁰This specialization is made without loss of generality.

computed. Furthermore, it turns out that the objective function is multimodal, noisy, and rugged shaped. These points together with the considerations concerning optimization methods in Section 7.3 and the proceedings in Anding, D.K. (1997); Vogelsang, H. (2001) lead to the consequence of using an evolutionary algorithm in order to find the global minimum of the cumulative stress error. The general realization thereof is presented in the following.

In order to be able to give a stochastically funded estimation of the true parameters, the same experiments have to be performed repeatedly using different specimens from one single charge. As several distinct experimental data are used, different sample points exist in each data set so that it is impossible to directly compare two sample points belonging to two distinct experiments. Nevertheless, a direct comparison between two experiments is actually not necessary on a point-by-point base. It is rather important to compare the experimentally observed and computed stress values at the same sample points. In this regard, two imaginable proceedings are either to compute the stress values at the measured strain values and thus to alter the step size for the computation permanently, or to interpolate the measured stress values so that a constant step size can be used for the computation of the model stresses. As the latter procedure is common practice in the field of parameter identification, see for instance Vogelsang, H. (2001), and as it can be shown that the former procedure leads to profound computation problems, the interpolation procedure is chosen within this work. Consequently, an even noisier and more rugged shape of the objective function is prevented.

As evident from Section 7.3.3, the estimation of the objective function leading to the computation of the direct problem (Section 7.1) and thus, the calculation of the material law has to be performed repeatedly within the optimization run. Based on the work of Müller, C. (2003) who implemented the R_L -model presented in Section 4.1 using a user subroutine of the commercial finite element software MSC.Marc¹¹, the modified version of the R_L -model according to Section 4.2 is realized yielding a modified subroutine. Here, as mentioned before, the time integration is performed using a mixed Euler scheme resulting in a system of linear equations, which can be solved efficiently. By this means, the calculation of the material model, giving the engineering stress and thus, the applied axial and torsional load ((5.14), (5.15)), is realized at one single Gauss point in reference to a finite element approach, which was shown to be sufficient in Section 7.1. Recapitulating the just stated, the respective stress state is evaluated for a given strain state.

As mentioned in Section 7.1, a plane stress state is existent so that the respective strain state is not known in advance. Hence, the complete stress and strain state have to be calculated outside but incorporating the actual evaluation of the material law. This is performed utilizing an iterative approach by means of an additional damped Newton iteration. Finally, this implementation yields the

¹¹Co. MSC Software Corporation, MSC.Marc, nonlinear finite element analysis (FEA) program incorporating geometric and material nonlinearities

stand alone program for calculating the objective value for a given set of material parameters and experimental data, which is constitutive for the realization of the evolutionary algorithm.

7.4.2 Implementation of the evolutionary algorithm

The actual evolutionary optimization is implemented using the *Genetic and Evolutionary Algorithms Toolbox* (GEATbx) for MATLAB¹² by Pohlheim, H. (2005a,b,c). Herewith, it is possible to realize a vast number of different evolutionary strategies, and to incorporate the different methods presented in Section 7.3.3. Furthermore, the progress of the optimization run is visualized very concisely so that the actual state of the population is known to the user at every point in time. Since a FORTRAN and C software interface is integrated part of the MATLAB software, external user subroutines can be directly incorporated into the MATLAB code. However, precompiled stand alone executable programs can be utilized even more easily.

7.4.3 Parallelization of the evolutionary algorithm

It was emphasized in Section 7.3 that the downside of stochastic algorithms is the significantly larger number of calculations with respect to deterministic approaches. Even though by use of evolutionary algorithms the effective number of calculations can be efficiently reduced in comparison to purely stochastic procedures, the computational costs are still noticeably higher than for the deterministic algorithms. At this point, the intrinsic parallelism of evolutionary algorithms comes into play. In this context, parallelism has a double meaning according to Vogelsang, H. (2001). On the one side it is the parallel structure on the population level using temporarily separated subpopulations. On the other hand it is the independence of the calculation of two objective values for two distinct parameter vectors.

Vogelsang, H. (2001) and Anding, D.K. (1997) showed that a parallelization of evolutionary algorithms is straightforward and that a significant speedup can be realized though different proceedings were chosen in the two works. In this regard, it is essential to know the bottleneck of the sequential implementation. In most cases, the performance of the objective function realization slows down the overall computation so that it proves most efficient to perform a parallelization on this stage of the program. First tests with the sequential version of the evolution algorithm and the stand alone objective function evaluation application featuring, for a typical setup, a run-time¹³ of 1.3 s, will subsequently substantiate this first estimation. Since the evaluation of the objective function values is

¹²Co. The MathWorks, Inc., MATLAB, short for MATrix LABoratory, is a numerical computing environment and programming language written in C.

¹³CPU, Intel Pentium IV 3.2 GHz with 2 Gbyte RAM

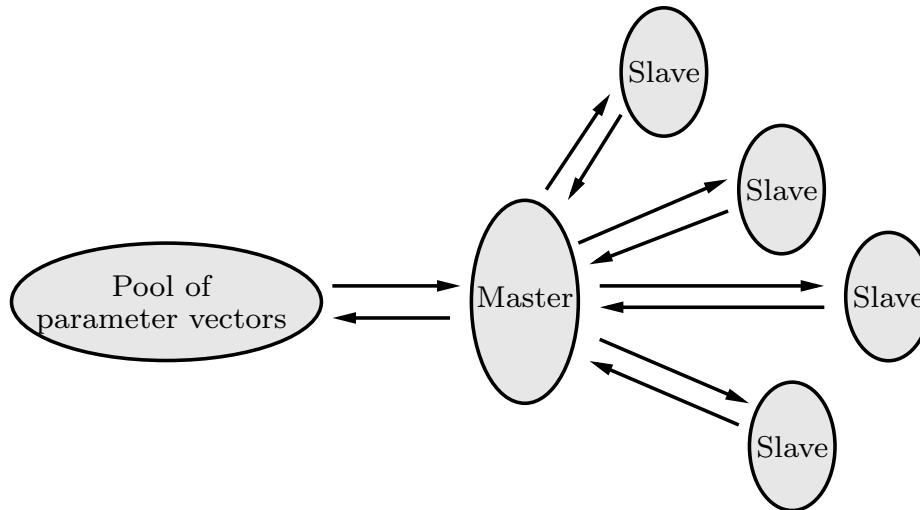


Figure 7.5: Master-slave paradigm

anyway inherently parallel, as just mentioned, the program can be parallelized at that stage without large effort in general.

The actual realization of a parallelized MATLAB code using different computers is nevertheless quite complicated. In fact, different toolboxes exist for the parallelization of MATLAB, such as the *Distributed Computing Toolbox* by MathWorks or the *Distributed and Parallel Application (DP) toolbox* by Pawletta, S. et al. (2005). But all of them require one single independent MATLAB license for each computer, cf. for instance Kempner, J. & Travinin, N. (2003); Levy, S.D. et al. (2005); Pohlheim, H. et al. (1999), which proves extremely expensive. In this regard, a different custom-tailored approach is used for the parallelization, which is based on the aforementioned DP toolbox. As this toolbox is funded on the message-passing system *Parallel Virtual Machine (PVM)*, cf. Geist, A. et al. (1994) for further details, two layers corresponding to two different abstraction levels are existent. Pawletta, S. et al. (2005) describe the lower layer as having an “abstraction level that is too low to meet the productivity requirements of a ‘real’ MATLAB user”. Nevertheless, by a modification of this low layer, special parallel applications can be realized so that only one single MATLAB license is needed for the given parameter identification problem.

The parallel system that is used for the computations is based on a *Beowulf*¹⁴ cluster¹⁵. The parallel setup follows the *master-slave paradigm*, see Figure 7.5 and Geist, A. et al. (1994); Vogelsang, H. (2001).

Here, the server termed *master* assigns tasks to the nodes, which are called *slaves*. An efficient dynamic load balancing can be attained that way so that for

¹⁴A cluster consisting of several similar or identical commercial-off-the-shelf (COTS) computers which use as operating system a free and open source software.

¹⁵The cluster consists of the server which exhibits an Intel Pentium IV 3.2 Ghz CPU and 13 nodes featuring 1 Intel Pentium IV 3.2 Ghz, 1 AMD Athlon 2600+, 6 Intel Pentium III 700 Mhz, 2 Intel Pentium III 650 Mhz, and 3 Intel Pentium III 550 Mhz CPUs.

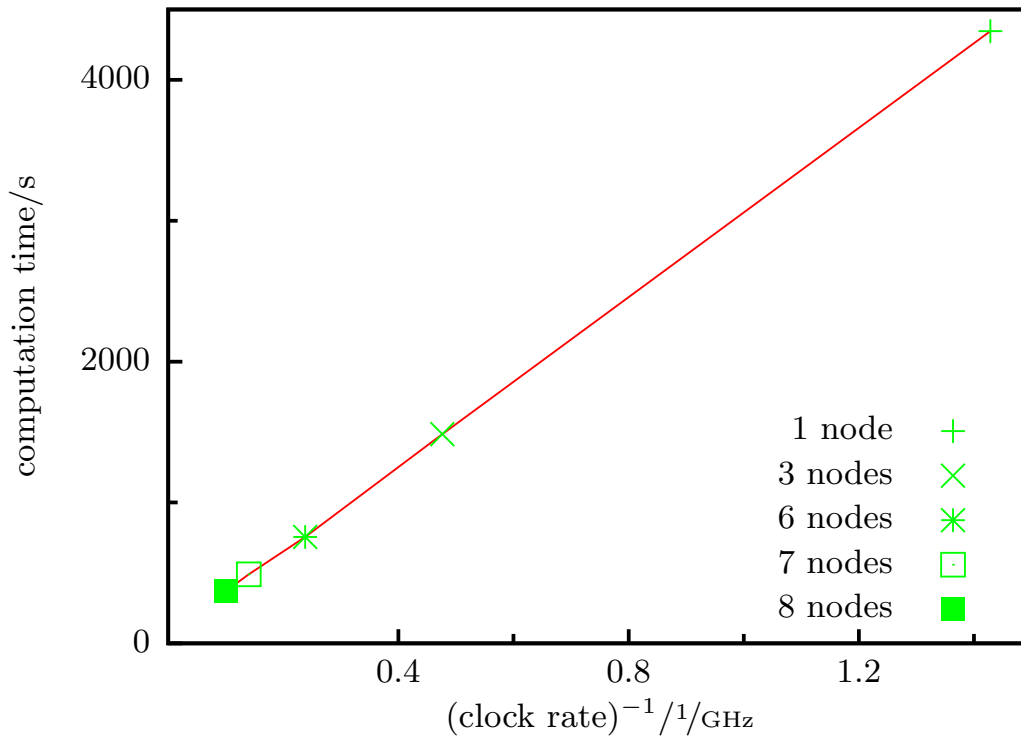


Figure 7.6: Speedup due to a parallelization of the algorithm

a large number of objective function evaluations and a heterogeneous system, as given, the overall performance is not slowed down by single slow CPUs.

Vogelsang, H. (2001) estimates in his work the potential speedup for a parallel setup like the one used here, as follows

$$\frac{t^{\text{parallel}}}{t^{\text{serial}}} = \frac{\frac{n}{l}t_{\text{obj}} + \frac{t_{\text{obj}}}{2} + nt_{\text{adm}}}{nt_{\text{obj}}} = \frac{1}{l} \left(1 + \frac{l}{2n} + l \frac{t_{\text{adm}}}{t_{\text{obj}}} \right)$$

$$\approx \frac{1}{l}$$

under the assumptions that

$$n \gg l \geq 1 \quad \text{and} \quad t_{\text{adm}} \ll t_{\text{obj}}.$$

Here, n , l , t_{obj} , and t_{adm} respectively represent the number of tasks, the number of identical nodes, the period of time that is necessary to compute the objective function value, and the period of time required for administration and communication purposes. Consequently, an almost linear speedup can be expected under the given assumptions.

The resulting speedup is surveyed for the implemented parallel evolutionary algorithm using eight nodes calculating the same objective function value over and over in order to guarantee comparability. Using the server, the computation

time of one single objective function evaluation is 0.1 s. The achieved speedup is shown in Figure 7.6.

Since different CPUs of a similar type are used, the cumulated clock rate is utilized to estimate the overall computing power. It is evident that the computation time scales almost perfectly linearly with the cumulated computation power of the single nodes. For more complex computations leading to larger computation times it proves reasonable to additionally use the master itself for the evaluation of the objective function values.

8 Determination of material parameters

8.1 Basic considerations

Before the actual parameter identification can be initialized, the admissible domain of the material parameters has to be accurately defined. It is of paramount importance for the computation time to reduce the size of the search space appropriately. Then again, it has to be large enough so that good or optimal solutions are not excluded. On this account, the meaning of the different material parameters is summarized in the following. In this regard, Table 8.1 gives a brief survey of the different material parameters that are included in the material model. Evidently, fifteen distinct material parameters are used. Müller, C.

Symbol	Material parameter	Measuring unit
E	Young's modulus	MPa
ν	Poisson's ratio	–
α_0	thermal expansion coefficient	1/K
ρ_0	density	kg/m mm ²
c_p	isobaric specific heat	J/kg K
Δu^*	phase specific internal energy difference	J/kg
Δs^*	phase specific internal entropy difference	J/kg K
\bar{u}_0	configurational internal energy	J/kg
\bar{s}_0	configurational internal entropy	J/kg K
η	amplitude of pseudoelastic strain	–
a_1	slope parameter forward transformation	–
a_2	slope parameter reverse transformation	–
r_1	radius parameter forward transformation	–
r_2	radius parameter reverse transformation	–
b	tension/torsion asymmetry parameter	–

Table 8.1: Material parameters of the modified R_L -model

(2003) takes the values for three of those from Hodgson, D.E. & Brown, J.W. (2000), namely the thermal expansion coefficient, the isobaric specific heat, and the mass density. In particular, the values of the former two parameters cannot be measured by means of the earlier described experimental setup, refer to Chap-

ter 6 for more details thereof. Consequently, these two¹ are adopted as reported by Hodgson, D.E. & Brown, J.W. (2000). By contrast, the assessment of the material density is straightforward and can be conducted without much effort². In this vein, those three material parameters are set prior to the optimization so that the respective values can be considered constant for the later identification process. They are shown in Table 8.2.

Parameter	Value
$\alpha_0/1/K$	$8.8 \cdot 10^{-6}$
$\rho_0/kg/m\ mm^2$	$6.5 \cdot 10^{-3}$
$c_p/J/kg\ K$	837.36

Table 8.2: Material parameters that are taken from the literature and identified in advance

As a consequence, only twelve variables are left over whose values are to be identified by the calculation of the inverse problem. In this connection, it is well known that Young's modulus and Poisson's ratio characterize the apparently elastic region of the material with Young's modulus representing the slope of the tensile stress-strain curve in the elastic region and Poisson's ratio embodying the parameter to yield the respective slope upon shear loading³. Furthermore, it was pointed out in Chapter 4 that the amplitude of pseudoelastic strain or pseudoelastic flow, namely η , can be interpreted as the length of the pseudoelastic stress-strain hysteresis in tension. In this regard, the tension/torsion asymmetry coefficient b furnishes by means of Equation (4.71) the respective hysteresis length in torsion or shear. Moreover, this asymmetry coefficient additionally deforms the shear stress-strain curve with respect to the tension stress-strain curve as illustrated in Figure 4.1⁴.

As clearly suggested by the respective names, a_1 , a_2 , r_1 , r_2 are purely phenomenological parameters adjusting the plateau slopes and the radii between the end of transformation and the further elastic loading or unloading depending on the transformation direction.

¹In accord with the proceeding in Müller, C. (2003), the arithmetic mean of the thermal expansion coefficients of austenite and martensite is utilized.

²A graduated beaker filled with water is positioned on a set of scales. Subsequently, a small NiTi specimen, irrespective of its shape, is put into the beaker. The volume of the displaced amount of water and the additional weight can be measured directly so that the density of the specimen material follows from the quotient of the two measurements.

³According to Hooke's law, the elastic slope for simple shear, namely the shear modulus G , is given by

$$G = \frac{E}{2(1 + \nu)}$$

so that the elastic slope is defined by a combination of Poisson's ratio and Young's modulus.

⁴It was shown that for $b = 1$ the stress-strain curves in simple tension and simple shear coincide.

While the effect of most of the material parameters on the stress-strain diagram is elucidated by now, the interpretation of the remaining four model parameters, which govern the transformation process is not as obvious at first sight. In this connection it is instructive to take a closer look at the driving force as defined in Equation (4.68), which is to be specified for the onset of the forward and reverse phase transition. It can be inferred from Equations (4.34) and (4.36) that the driving force vanishes at the beginning of the phase transformation with the martensite mass fraction being identical to zero or one referring to the particular transformation direction. Hence, Equation (4.68) collapses to yield clear equations for the transformation stresses

$$\sigma = \frac{\rho_0}{\hat{\eta}} [(\bar{u}_0 - \Delta u^*) + (\Delta s^* - \bar{s}_0) \Theta] \quad (\text{forward transformation}) \quad (8.1)$$

$$\sigma = -\frac{\rho_0}{\hat{\eta}} [(\bar{u}_0 + \Delta u^*) + (\Delta s^* + \bar{s}_0) \Theta] \quad (\text{reverse transformation}) \quad (8.2)$$

and thus, for the hysteresis height $\Delta\sigma$ and level $\bar{\sigma}$ as functions of the four considered material parameters and the specimen temperature,

$$\Delta\sigma = \rho_0 \frac{2(\bar{u}_0 - \Theta\bar{s}_0)}{\hat{\eta}}, \quad (8.3)$$

$$\bar{\sigma} = -\rho_0 \frac{\Delta u^* - \Theta\Delta s^*}{\hat{\eta}}. \quad (8.4)$$

Figure 8.1 illustrates schematically these interrelations and delivers a phenomenological interpretation of the material parameters, which affect the onset of the transformation process. This figure displays a modified version of a similar diagram taken from Luig, P. et al. (2006), which addressed the R_L -model as derived by Müller, C. (2003). Here, it is adapted to the modified R_L -model using small deformations⁵. It follows from Equations (8.3) and (8.4) that at least two different experiments, which are to be conducted at distinct temperatures, are necessary for the definite identification of the four parameters \bar{u}_0 , \bar{s}_0 , u^* , s^* . Moreover, those two experiments must cover the whole hysteresis so that the microstructure is almost completely martensitic exhibiting a martensite mass fraction that is approximately equal to one⁶ at the onset of reverse phase transformation. Referring to simple tension tests, the transition region between the phase transformation domain and the elastic/plastic loading of martensite is

⁵The model itself is formulated in large deformations. Nonetheless, due to the measuring conditions only small deformation measures can be acquired so that a small deformation version of the modified R_L -model is enforcedly used for the identification of the model parameters, see Section 7.1 for a more detailed discussion on this topic.

⁶It is well-known today that the microstructure of the shape memory alloy is not completely martensitic at the end of the mechanical hysteresis, cf. Brinson, L.C. et al. (2004). However, it is rather complicated to determine the exact martensite mass fraction, since intricate methods like neutron deflection or synchrotron radiation examinations are mandatory. Thus, a completely martensitic microstructure is just a first guess until the true microstructure is measured and can be adopted in the model.

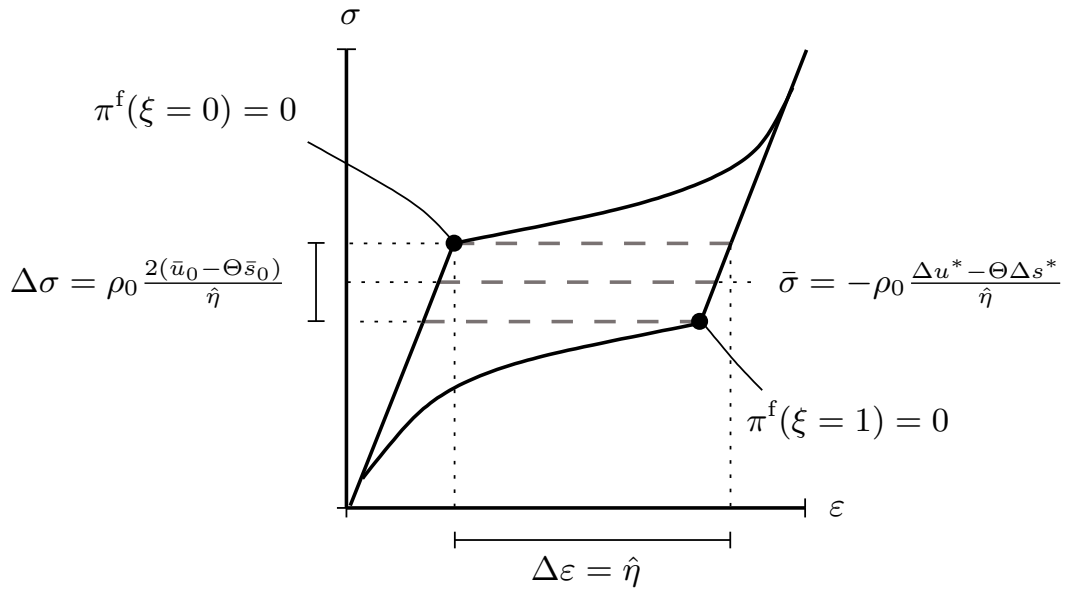


Figure 8.1: Phenomenological interpretation of selected material parameters, utilizing equivalent quantities as defined in Equations (4.49), (4.50) and specified for small deformations

very distinctive in the stress-strain diagram. On this account, at least two simple tension tests are used as input data for the identification process. All material parameters, apart from Poisson's ratio and the tension/torsion asymmetry coefficient, may be identified using these data. As emphasized before, Poisson's ratio and the tension/torsion asymmetry coefficient characterize the material behavior upon shear with respect to simple tension. Consequently, experiments that feature a shear component, like simple torsion experiments, are to be realized, too. Therefore, two simple torsion tests are additionally performed at the same distinct temperatures as in the simple tension cases. Altogether, four experiments at two different temperature levels are conducted. 500 independent sample points per experiment are then used for the subsequent parameter identification.

By means of one set of above stated experiments it is possible to calculate a rough estimate of the “true” material parameters by hand, which may be used as initial guess and starting point for the consecutive, numerical optimization run. Besides, the limits of the search space may be assessed. Consequently, the search space as depicted in the course of this paragraph might prove suitable only for the utilized specimen material and heat treatment. Table 8.3 lists the various domains of the material parameters that are left over for the evolutionary optimization.

In addition to the search space limits, some other constraints are existent, which pose restrictions on specific combinations of material parameters. Similar to the search space limits themselves, these constraints are not imperative for the pa-

Parameter	Domain
E	[25000, 47000]
ν	[0, 0.35]
Δu^*	[0, 30000]
Δs^*	[0, 100]
\bar{u}_0	[0, 17000]
\bar{s}_0	[0, 50]
η	[0, 0.055]
a_1	[0, 1.1]
a_2	[0, 15]
r_1	[0, 10]
r_2	[0, 10]
b	[0.75, 1]

Table 8.3: Admissible domain of the material parameters for the modified R_L -model

parameter identification but may lead to a much faster convergence rate. [Pohlheim, H. \(1999\)](#) concludes that every inch of previous knowledge is to be used for the identification process in order to get the best solution taking the shortest computation time.

[Ortín, J. & Planes, A. \(1989\)](#) showed that an interrelation between transformation start, finish temperatures and the applied external stress exists, which may be formulated by means of a Clausius-Clapeyron-like equation. In this regard, it appears fruitful to inspect the governing equation for the driving force, Equation (4.68), in detail. Under the assumption that the driving force is a function of the martensite mass fraction only, cf. Equation (4.34), the slopes of the start and finish lines of the transformation temperatures can be inferred straightforward as functions of the externally applied stress to yield

$$\left. \frac{d\sigma}{d\Theta} \right|_{M_s^\sigma} = \left. \frac{d\sigma}{d\Theta} \right|_{A_f^\sigma} = \frac{\rho_0}{\hat{\eta}} (\Delta s^* - \bar{s}_0) \quad (8.5)$$

and

$$\left. \frac{d\sigma}{d\Theta} \right|_{A_s^\sigma} = \left. \frac{d\sigma}{d\Theta} \right|_{M_f^\sigma} = \frac{\rho_0}{\hat{\eta}} (\Delta s^* + \bar{s}_0). \quad (8.6)$$

Here, the martensite mass fraction is set to $\xi = 0$ for M_s^σ and A_f^σ and $\xi = 1$ for A_s^σ and M_f^σ , see Footnote 6 on page 158 for a discussion on the martensite mass fraction at the end of the hysteresis. These interrelations are illustrated in Figure 8.2, taken in an adapted version from [Müller, C. \(2003\)](#) to suit the modified R_L -model. Since only pseudoelastic material behavior is accounted,

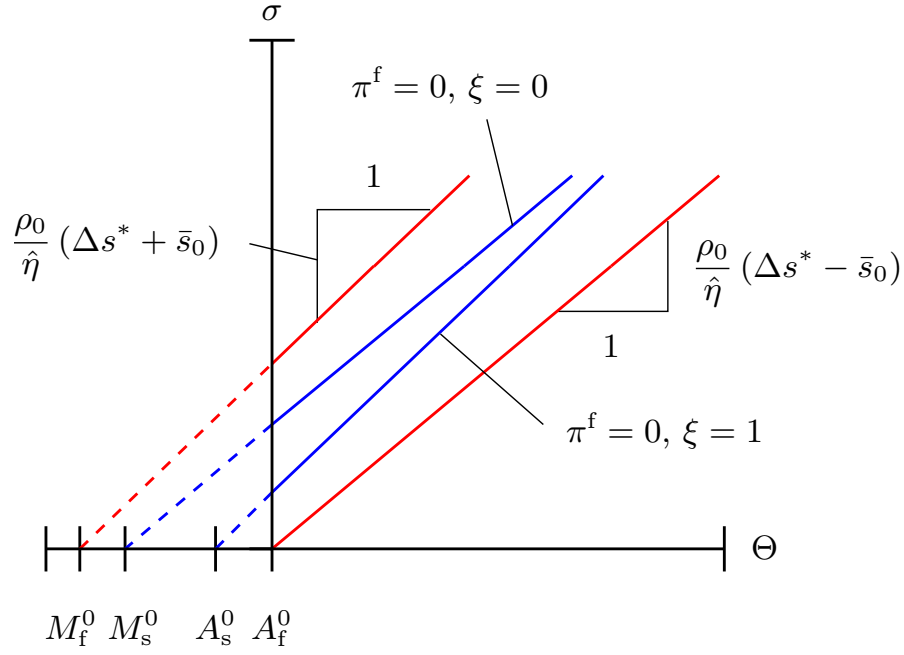


Figure 8.2: Physical interpretation of selected material parameters

and temperatures below A_f^0 are beyond the scope of the considered material model⁷, those parts of the curves which are below that particular temperature are denoted by dashed lines, see Müller, C. (2003) for further details.

As known from the literature (Shaw, J.A. & Kyriakides, S. (1995); Tanaka, K. et al. (1995)), the start lines of forward and reverse transformation as depicted in Figure 8.2 feature positive slopes. Consequently, Equation (8.5) leads to the requirement

$$\bar{s}_0 < \Delta s^*. \quad (8.7)$$

Moreover, it may be deduced from experimental data that the austenite start line proceeds within the pseudoelastic temperature range below the martensite start line resulting in the fact that the reverse transformation stress exhibits a lower value than the forward transformation stress. With Equations (8.1) and (8.2) this constraint reads

$$\bar{s}_0 \Theta < \bar{u}_0. \quad (8.8)$$

Finally, the values of the transformation stresses have to be positive so that,

⁷Even though it is supposed that the parent phase is mainly R-phase (Section 6.1), the material behavior might be described very well by the considered material model. The reason is that the microstructural difference between austenite and R-phase is relatively small compared to the B19'-microstructure so that the stress-strain curves for $B2 \rightarrow B19'$ and $R \rightarrow B19'$ look very similar. Naturally, the strong temperature dependence of the apparent Young's modulus as reported in Section 6.1.5 is not implemented as this effect is inexistent for an austenitic microstructure.

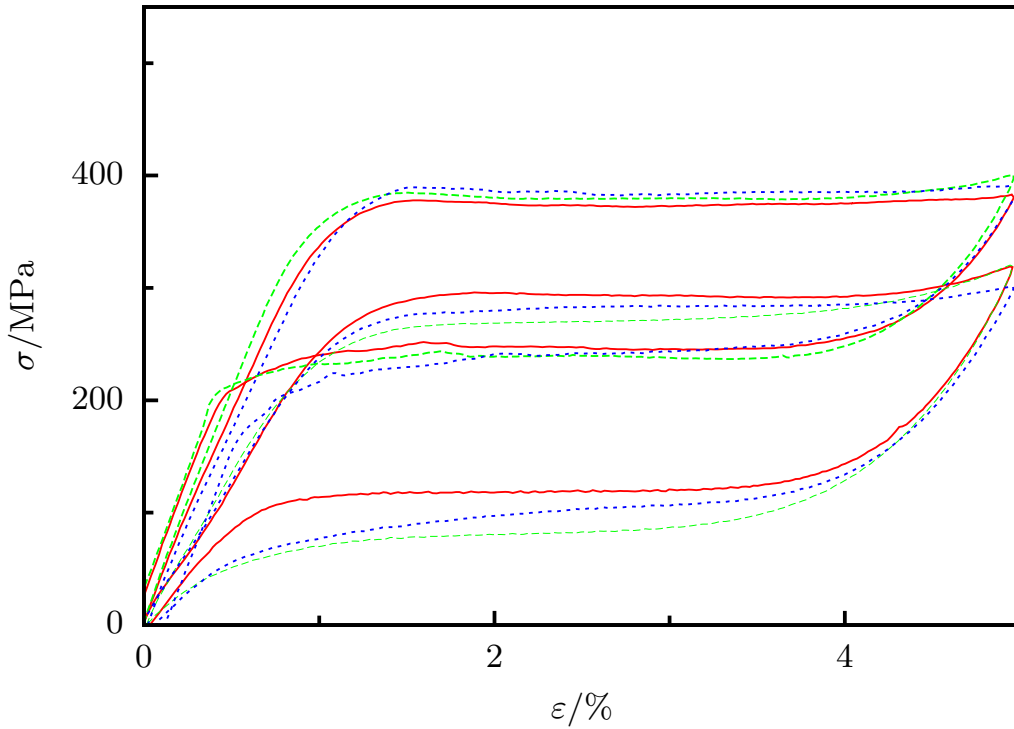


Figure 8.3: Typical simple tension stress-strain progressions measured on three different specimens at two distinct temperatures (10°C , 27.5°C)

based on Equations (8.1) and (8.2), the following relations have to hold

$$\Delta u^* < (\Delta s^* - \bar{s}_0)\Theta + \bar{u}_0 \quad (8.9)$$

$$\Delta u^* < (\Delta s^* + \bar{s}_0)\Theta - \bar{u}_0. \quad (8.10)$$

8.1.1 Results of the parameter identification

Seven sets of four experiments each are conducted on seven different specimens. As mentioned in the last paragraph, two simple tension and two simple torsion tests at two different temperatures are chosen as parameter identification input data. The maximum strains are $\varepsilon = 5\%$ and $\gamma' = 3.5\%$ with testing temperatures of 10°C and 27.5°C . Each test is strain and temperature controlled so that macroscopically isothermal conditions are warranted.

Figures 8.3 and 8.4 show a selection of some typical stress-strain progressions of the conducted experiments. Clearly, for the higher temperature the respective curves correspond very well while for 10°C the spreading is significantly larger. The impact thereof on the parameter identification is discussed later in this section.

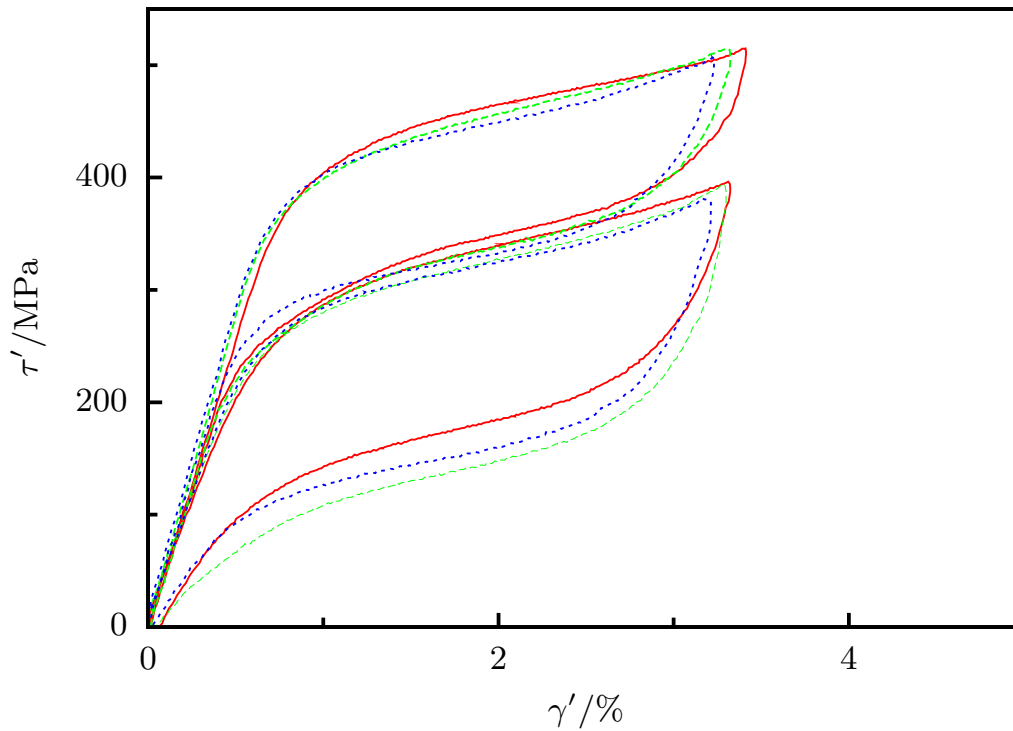


Figure 8.4: Typical simple torsion stress-strain progressions measured on three different specimens at two distinct temperatures 10°C, 27.5°C)

Having started the formulation of the objective function in terms of the l_2 -norm and having tested different other l_p -norms for the given problem, it emerges that the assumption of normally distributed errors leads to reasonable optimization results. Consequently, an objective function based on the l_2 -norm is used in the following, see Section 7.4.1 for further details. Referring to computation time, it was argued in Section 7.4.3 that a considerable speedup of evolutionary algorithms can be achieved by means of a parallelization implemented on a Beowulf cluster. For the subsequently presented parameter identification, such a cluster is utilized containing four 3 GHz- and eleven 650 MHz-class CPUs. The applied evolutionary algorithm uses a regional model featuring four competing subpopulations with initial subpopulation sizes of 25 individuals. Hence, the overall population consists of 100 individuals in total. In this context, the concept of subpopulation migration is implemented exhibiting a minimum subpopulation size of seven individuals and a migration interval of ten generations. Four distinct search strategies with varying mutation parameters are realized for the different subpopulations in order to allow for a coarse as well as a fine examination of the search space.

Subsequent to the evolutionary parameter identification, the parameter values are taken as input data for a further optimization by means of the NEWUOA algorithm, which was briefly sketched in Section 7.3.2. It turns out that an

appreciable, further improvement of the material parameters cannot be achieved by the application of this deterministic approach. This might be ascribed to the rugged shape of the objective function, see Section 7.3.

Parameter	Mean	Standard deviation	Normalized standard deviation
E	33194	1051	0.03
ν	0.064	0.04	0.65
Δu^*	10297	715	0.07
Δs^*	40.9	2.4	0.06
\bar{u}_0	1622	571	0.35
\bar{s}_0	4.3	2.0	0.46
η	0.0499	0.0016	0.03
a_1	0.45	0.03	0.06
a_2	0.45	0.23	0.51
r_1	0.70	0.16	0.22
r_2	0.96	0.23	0.24
b	0.82	0.01	0.01

Table 8.4: Identified material parameters, mean, standard deviation, and normalized standard deviation

Table 8.4 specifies the mean values of the material parameters and the respective standard deviations. It has to be emphasized that these values are calculated from the seven optimized material parameter sets. The particular parameter sets are listed in Appendix C.1. Due to the complexity of the material model and the applied identification procedure, the individual standard deviations are not computed separately for each parameter set. Furthermore, the simulation of synthetic data sets, as proposed in Press, W.H. et al. (2001) and as applied by Anding, D.K. (1997) in order to corroborate the statistical significance of the identification, proves impracticable because of the high computational costs⁸ associated with this procedure.

Even though the number of experimental data is limited to seven sets of experiments due to the high computation, material, and machining costs, the spreading of the different parameter values is comparably small. However, the amendment of the experimental database might be subject to further research.

With reference to the standard deviations, some particular material parameters are to be discussed in more detail. These are ν , \bar{u}_0 , \bar{s}_0 , a_2 , r_1 , r_2 . In addition to the standard deviation of Poisson's ratio the mean value itself is especially noteworthy, since it is far-off the expected value, which is in the vicinity of 0.33.

⁸Computation times of 24 hours or longer are typical for the parameter identification on one single set of experiments in the described manner. Parallelization is already considered therefor by means of the aforementioned Beowulf cluster.

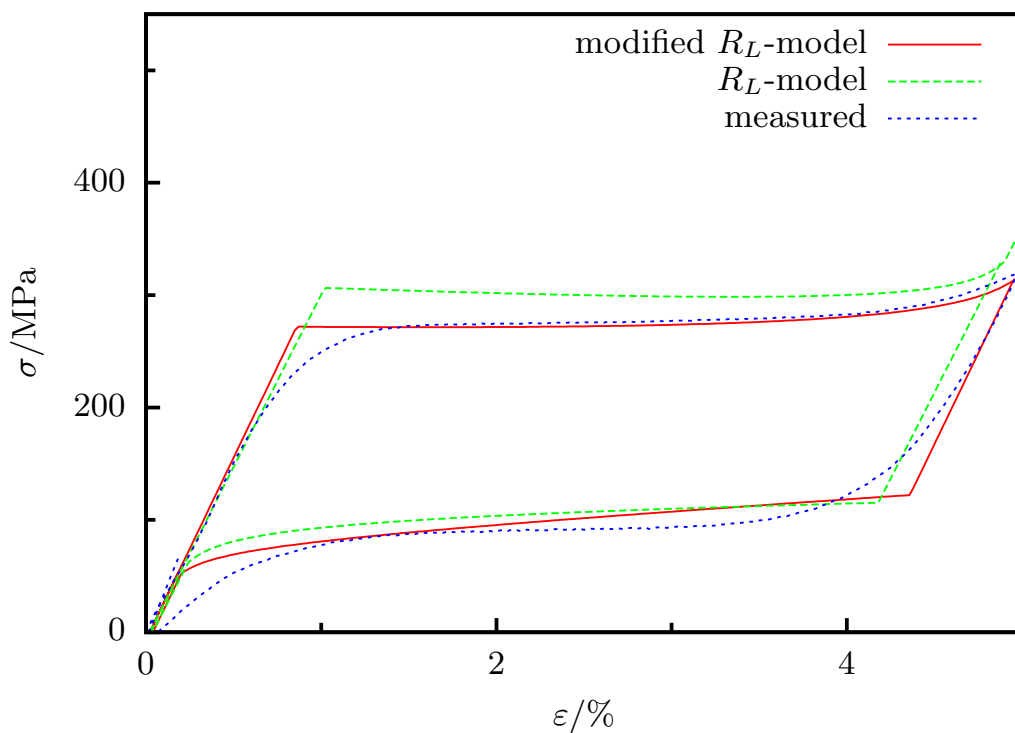
The reason for this shift lies in the existence of the R -phase. It is evident (Figures 8.3, 8.4) that such strong temperature dependence of the apparently elastic slope cannot be observed in the stress-strain diagram upon shear compared to the normal stress-strain curves. Consequently, as the elastic region is superimposed with an additional effect, which, apparently, depends strongly on the loading direction, the original meaning of the elastic parameters is considerably obscured. Clearly, the shear modulus G is almost constant for the different experiments. Hence, even relatively small deviations of Young's modulus lead to extremely large relative deviations of Poisson's ratio. The reason is the special relationship between the shear modulus, Young's modulus, and Poisson's ratio.

By contrast, if \bar{u}_0 and \bar{s}_0 are considered, it is instructive to recall Equation (8.4). Basically, those two material parameters govern the height of the hysteresis. In this regard, the aforementioned spreading of the stress-strain curves at 10°C has to be revisited, cf. Figure 8.3. Since, at low temperatures, the reverse transformation clearly shows a larger spread than the forward transformation segment of the stress-strain curves including different levels, slopes, and radii, the deviation of the respective material parameters, namely \bar{u}_0 , \bar{s}_0 , a_2 , r_2 is relatively large, too. Referring to the forward transformation, the reason why r_1 exhibits a standard deviation of the same order lies in the different development of the transition region between phase transformation and elastic/plastic loading of martensite as illustrated in the stress-strain diagram.

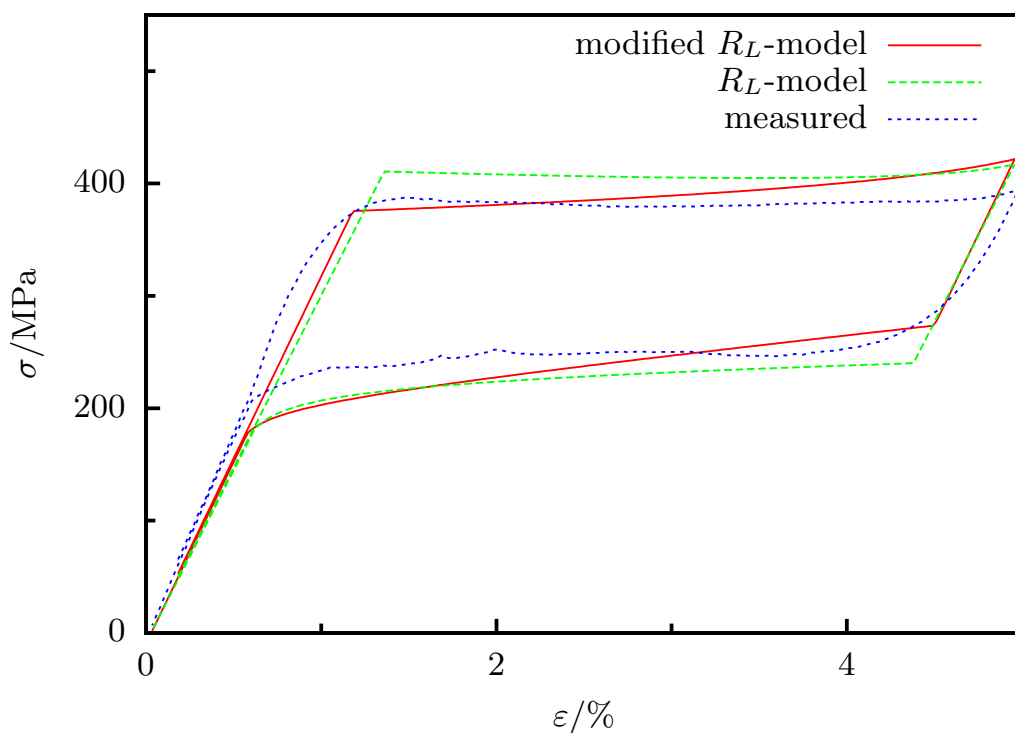
Figures 8.5 and 8.6 contain measured and computed stress-strain curves for the chosen parameter identification input tests. Here, the experimental data of one specific set of experiments is shown. Furthermore, material parameters have been identified using these data both for the R_L -model as described by Müller, C. (2003) and for the modified R_L -model as derived in Section 4.2. For comparison, the calculated material response using the two distinct models and the just mentioned material parameters is depicted as well. Consequently, the mean values evaluated from all parameter identifications are not utilized here. The intention is to illustrate the capacity of each model to predict the material behavior and to show the differences that result from the models.

First, the simple tension curves are regarded as given in Figure 8.5. Inherent in the material models, the smooth transition between the apparently elastic and the phase transformation regions is not modeled. However, the modified model fits the experimental data better, meaning that stress deviations with respect to the measurements are smaller. Moreover, the hysteresis height is predicted more accurately. Notwithstanding the better overall performance of the modified approach, it is noteworthy that for the higher temperature, namely 27.5°C , an unnatural, positive slope can be noted. This behavior originates from the identification process, since experimental data associated with torsion is also used featuring a positive slope within the transformation region.

In this connection, it is imperative to address the simple torsion curves, which are plotted in Figure 8.6. Here, the better performance of the modified model is evident. The reason is that the stress levels of the stress-strain curves in the shear



(a) Testing temperature 10°C



(b) Testing temperature 27.5°C

Figure 8.5: Computed and measured simple tension tests

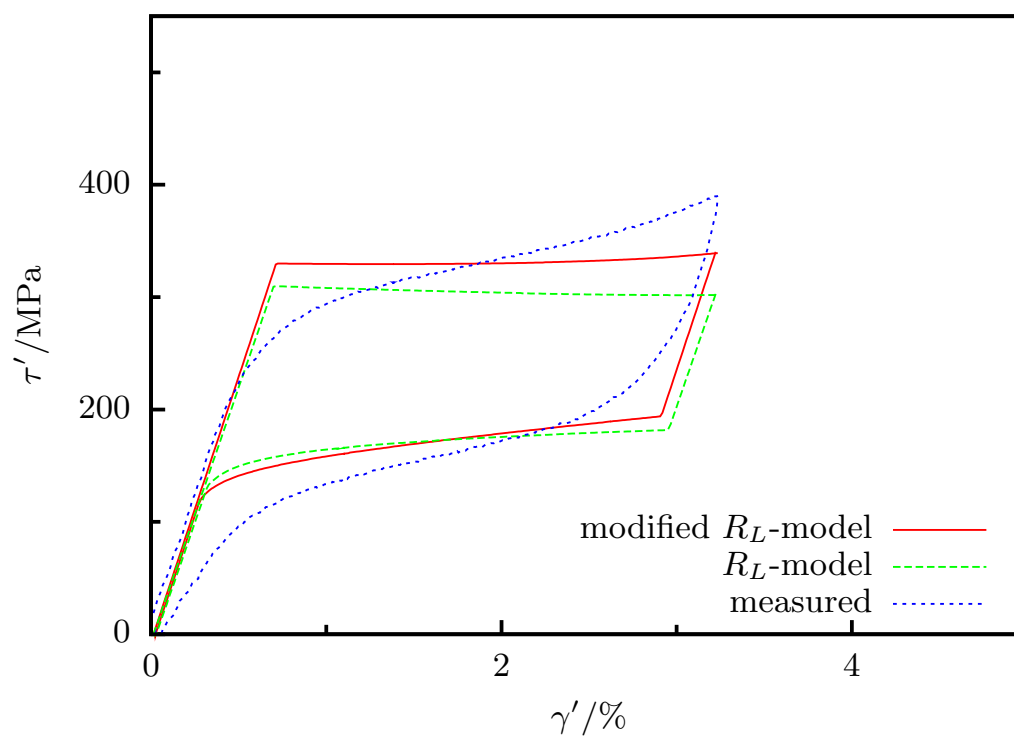
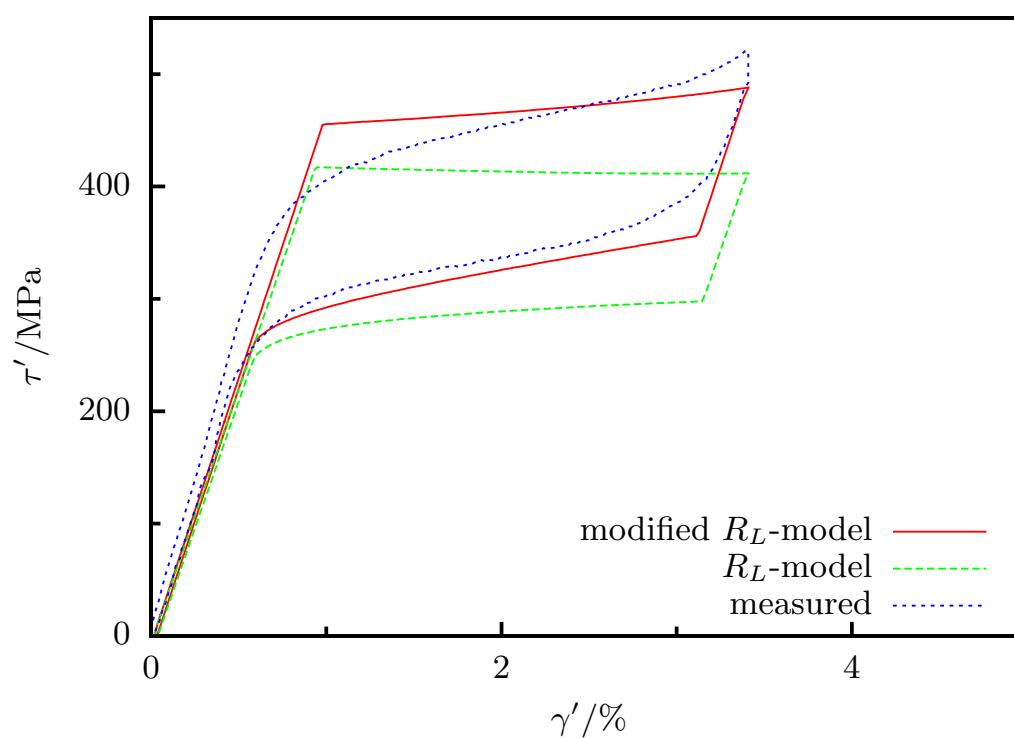
(a) Testing temperature 10°C (b) Testing temperature 27.5°C

Figure 8.6: Computed and measured simple torsion tests

space cannot be predicted appropriately by the original R_L -model. Although, the stress-strain curve of the modified approach is not forecast as accurately as in the simple tension case within the forward transformation region, the R_L -model shows a considerably worse approximation of the material behavior.

Altogether, it has to be stated that the modified R_L -model is capable of better reproducing the measured stress-strain behavior compared to the original R_L -model. Even though this modified approach features some shortcomings referring to experiments with reorientation of the microstructure⁹ it is obvious that the original model is not better suited for complex experiments, since the relation between tension and torsion is not modeled accurately. Nonetheless, for a further improvement of the description of the tension/torsion asymmetry it proves mandatory to incorporate additionally some asymmetry into the phenomenological material parameters which govern the slopes of the transformation regions.

8.2 Comparison between calculated and measured data sets

In this section, experimental and calculated data are compared. Only results from the modified R_L -model are presented. Different from the last section, the experimental data, which is utilized here, is not taken for the parameter identification. Consequently, it can be evaluated in what extent the material model can be applied to problems, to which the model is not fitted to. In this regard, it is noteworthy that only experiments in the first axial/torsional strain quadrant are chosen because the tension/compression asymmetry is not modeled. Hence, the calculated stress response in the compression region would be inherently less accurate than the respective response in the tension region anyway.

Again, all experiments are performed under strain and temperature control leading to macroscopically isothermal conditions. The von-Mises equivalent strain rates are chosen as $\dot{\varepsilon}_{\text{eq}} = 10^{-4} \text{ s}^{-1}$. First, proportional experiments are presented, since the Clausius-Duhem inequality is fulfilled a priori in that case, refer to Section 4.2 for a discussion on this topic. Subsequently, some experiments with reorientation of the microstructure are treated, see also Appendix C.2.

8.2.1 Proportional experiments

Two distinct proportional tests are considered in the following. For each experiment the maximum von-Mises equivalent strain is chosen as $\varepsilon_{\text{eq}_{\text{max}}} = 3.5\%$. The particular experiments are characterized by the ratio between axial and shear strain, which is defined by

$$\alpha = \frac{\gamma'}{\varepsilon}. \quad (8.11)$$

⁹This topic is discussed in detail in Section 8.2.2.

The two experiments feature proportionality coefficients of $\alpha = 0.5$ and $\alpha = 2$. The strain control paths and the respective stress-stress response are plotted in Figure 8.7. For clarity, a circle exhibiting a radius of $\varepsilon_{\text{eq}_{\text{max}}} = 3.5\%$ is drawn in order to exemplify the identical maximum equivalent strains. Obviously, the material returns to a state of zero stress upon completion of the experiments whereas the model predicts residual stress components.

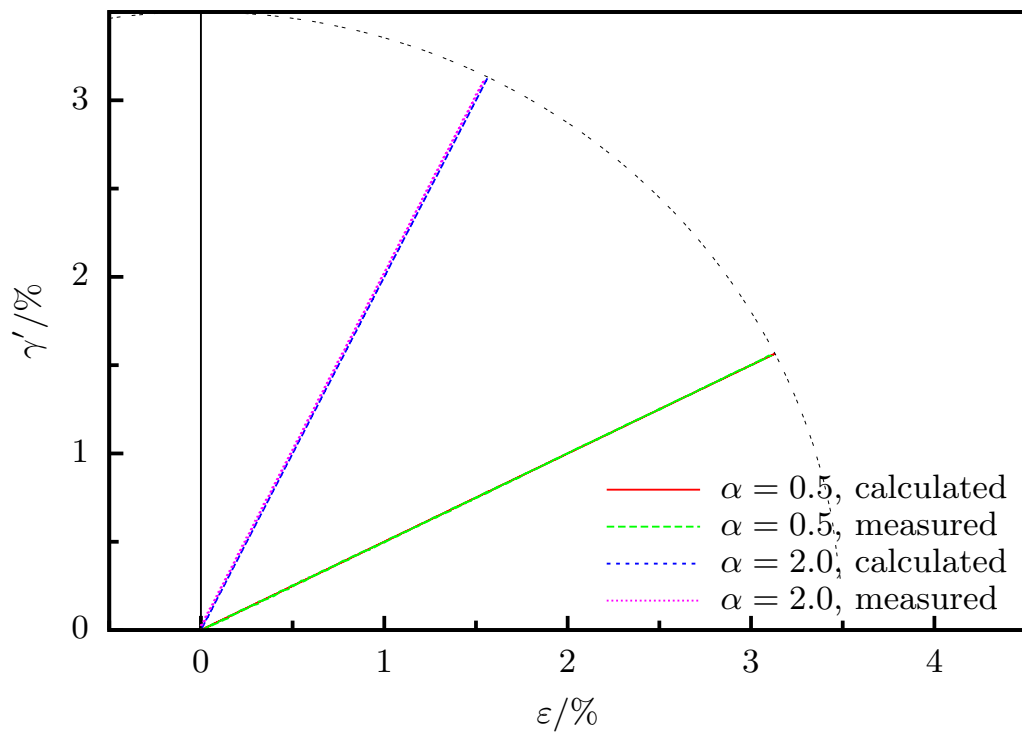
However, it can be concluded that the material behavior is predicted considerably well by the modified R_L -model. This is further corroborated by the diagrams in Figure 8.8. The overall stress levels are in good accord with the measurements and the shape of the computed curves is mostly consistent with the measured progressions. As mentioned before, the slope of the forward transformation segment in the axial stress-strain diagram is slightly overestimated. Besides, for the case of predominantly tensile loading, the shear stress level is underestimated. Simultaneously, within the shear stress forward transformation region, the model predicts decreasing stress values while, in fact, the measured shear stress is still increasing. The contrary is true for the case of primarily torsional loading. Here, the normal stress is decreasing for a forward phase transformation whereas a positive slope is computed using the material model.

8.2.2 Nonproportional experiments

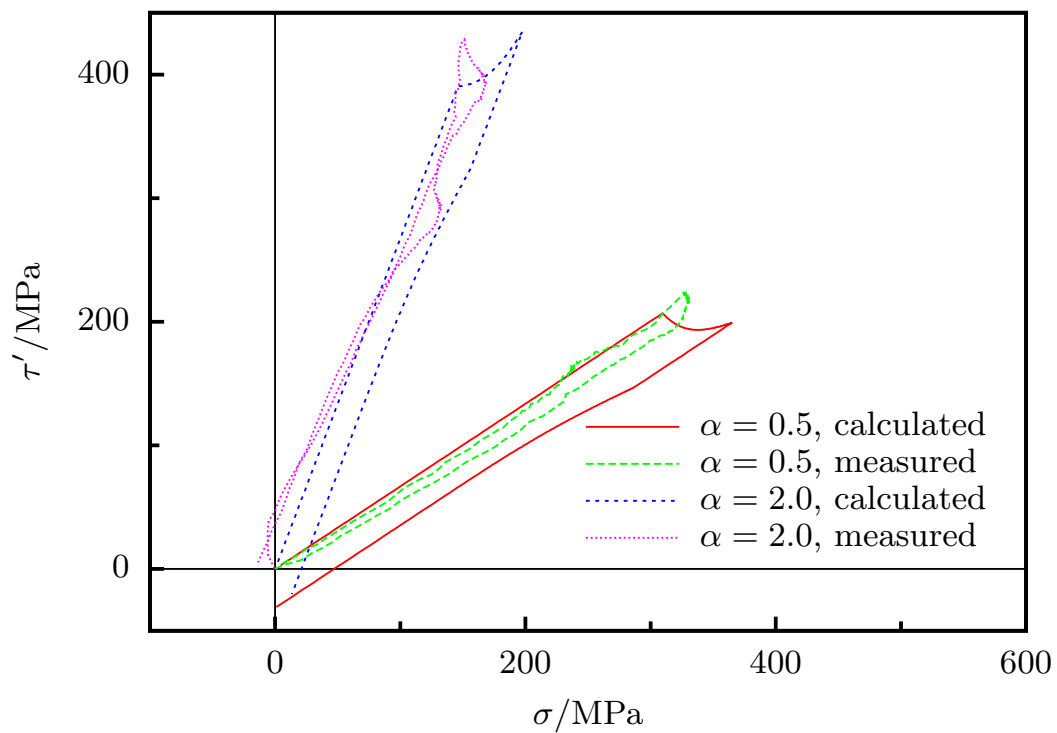
The aim of this section is to assess the applicability of the modified R_L -model with reference to nonproportional experiments. Here, only the box test as discussed in the context of strain rate dependence in Section 6.2.1.3 is treated. One further experiment, namely a butterfly test, is presented in Appendix C.2. Naturally, the basic conclusions are identical for the two different cases. The maximum strains for the box test are $\varepsilon = 2\%$ and $\gamma' = 2\%$ starting in simple tension. Subsequently, special focus is on the development of the entropy production rate, which is to be non-negative according to the Clausius-Duhem equation (4.29). However, it was stated in Section 4.2 that for loadcases featuring reorientation the Clausius-Duhem inequality is not fulfilled a priori. Consequently, the entropy production rate is evaluated and the compliance with the Clausius-Duhem inequality is inspected after each computation step.

Figure 8.9 shows the strain control path and the stress response of the material. Crosses indicate the violation of the Clausius-Duhem inequality. Evidently, as the specimen is loaded above the onset of phase transformation and the loading direction is changed, the Clausius-Duhem inequality is immediately violated. This is also the case during unloading in axial direction until a state of zero normal stress is reached. If the stress-stress curves are regarded, it is especially intriguing that upon the final torsional unloading the calculated normal stress proceeds in the wrong direction accumulating compressive stresses. In contrast to the measurements, residual stresses are still existent when all strains are completely reduced.

The stress-strain curves are depicted in Figure 8.10. If the final unloading step is

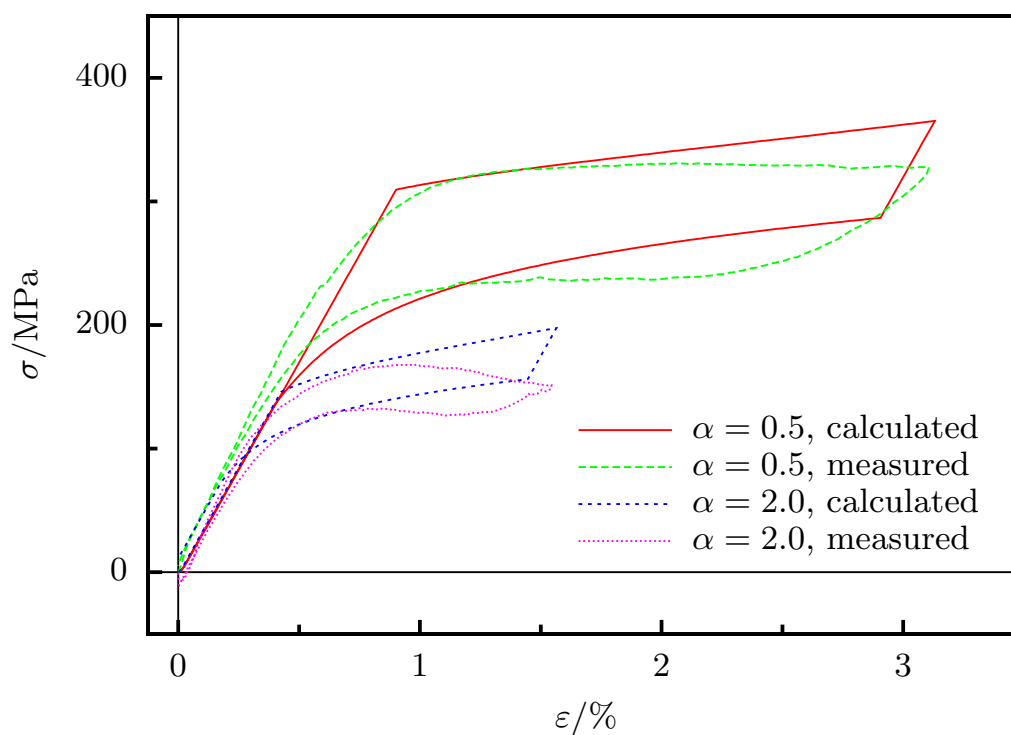


(a) Strain-strain diagram

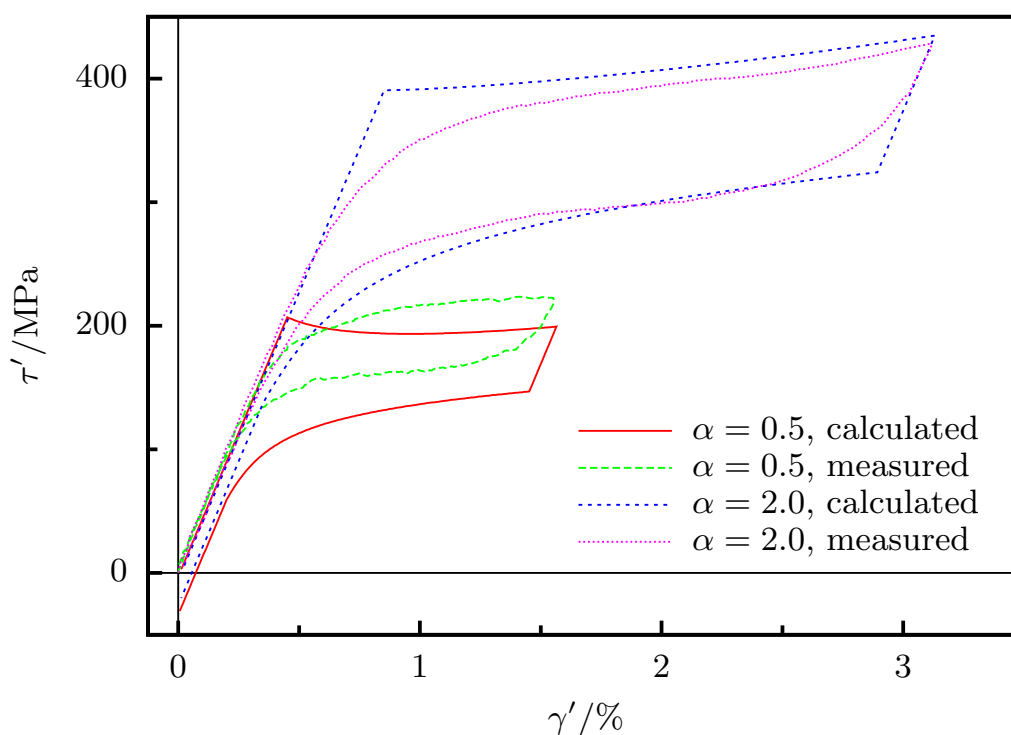


(b) Stress-stress diagram

Figure 8.7: Combined proportional tests for different ratios between axial and torsional strain; strain-strain and stress-stress diagram

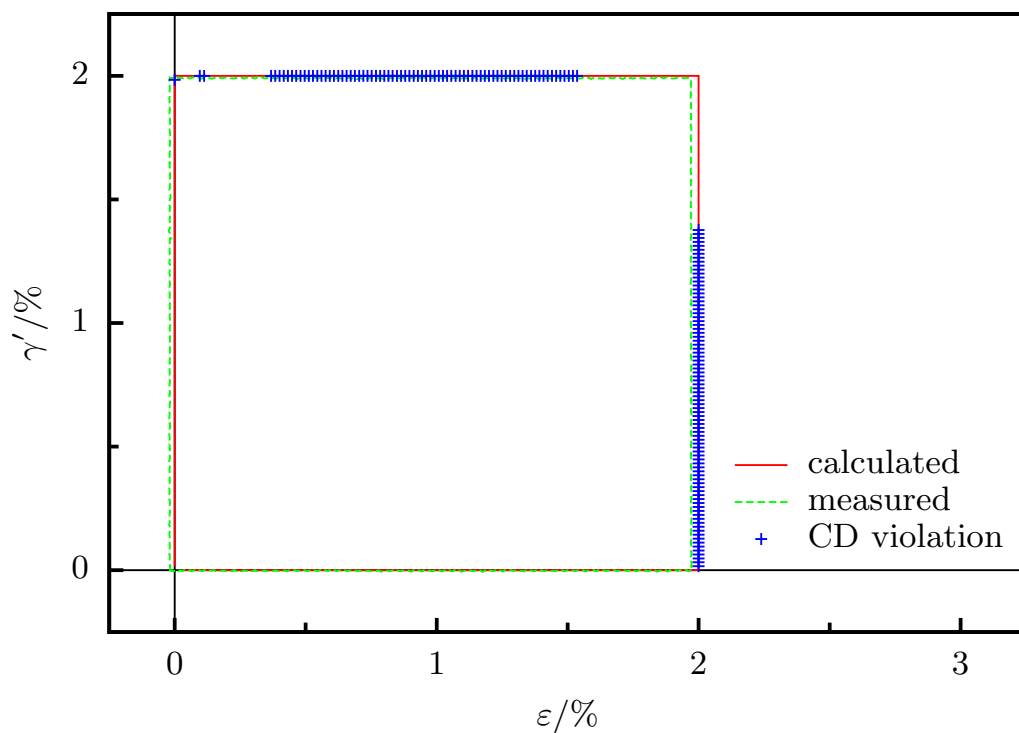


(a) Strain-strain diagram

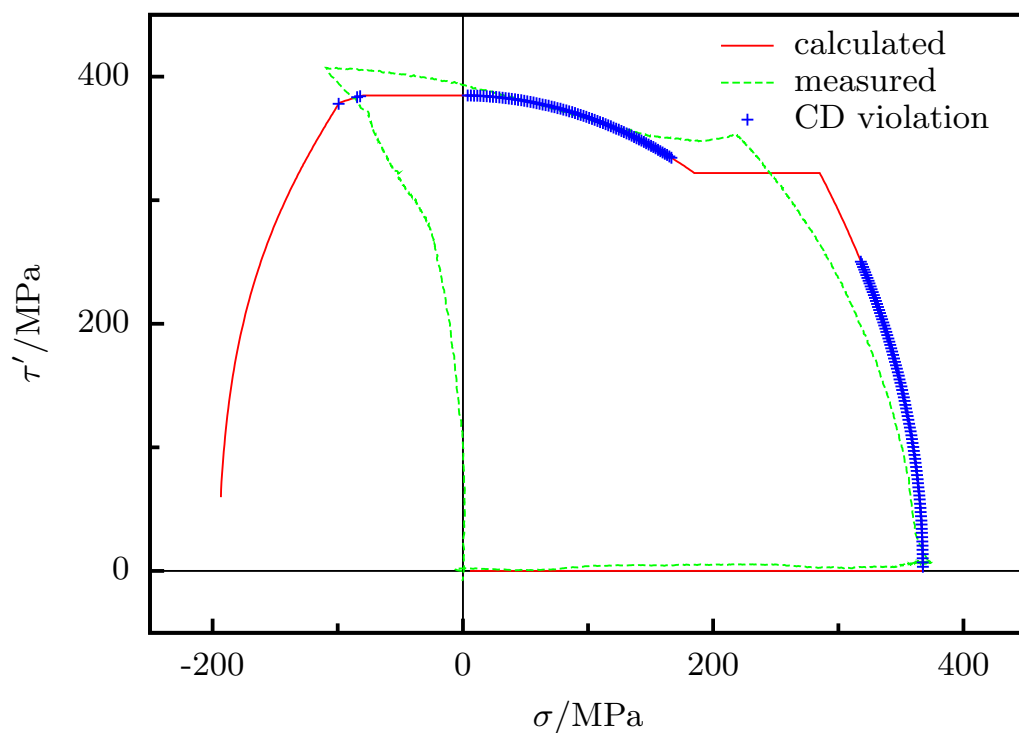


(b) Stress-stress diagram

Figure 8.8: Combined proportional tests for different ratios between axial and torsional strain; axial and torsional stress-strain diagrams

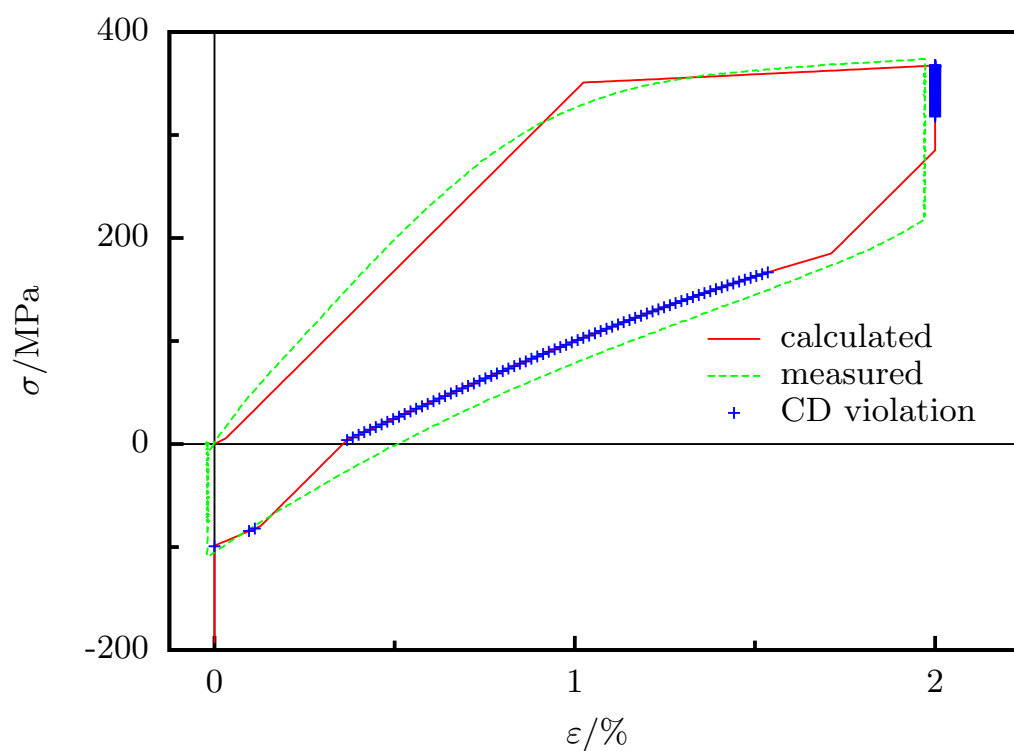


(a) Strain-strain diagram

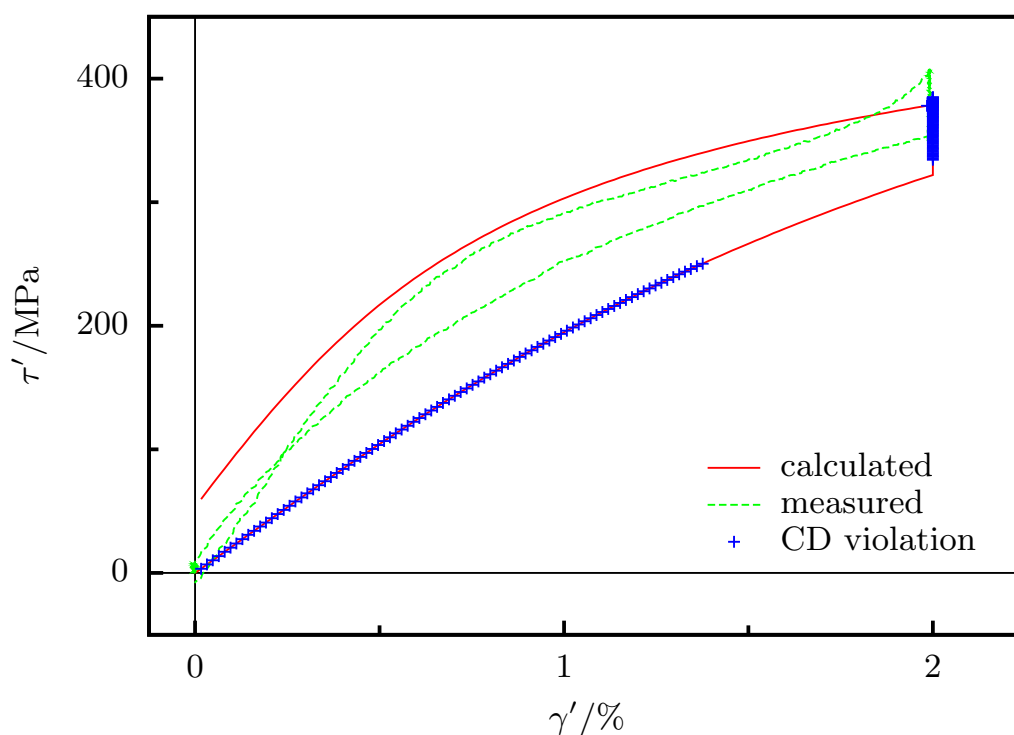


(b) Stress-stress diagram

Figure 8.9: Combined box test, measured and calculated; strain-strain and stress-stress diagram



(a) Strain-strain diagram



(b) Stress-stress diagram

Figure 8.10: Combined box test, measured and calculated; axial and torsional stress-strain diagrams

disregarded, the material behavior is qualitatively well approximated by the material model. However, the Clausius-Duhem relation is infringed for the largest part of the experiment and the final unloading cannot even qualitatively be predicted accurately. As a concluding remark, it has to be mentioned that as stated in Section 4.2 the applicability of the modified R_L -model has to be restricted to proportional loadcases only.

9 Conclusions and possible extensions

9.1 Summary

The key issues in this thesis were the identification of model parameters for the R_L - and modified R_L -model, respectively, and the examination of multidimensional experiments in order to enlighten the thermomechanical coupling inherent in the material behavior of polycrystalline NiTi shape memory alloys.

After an introduction comprising the motivation and outline of the present work, the basic shape memory effects were elucidated on the micro- and macroscale. Here, just a simplified overview was presented. Thereafter, the focus was on the establishment of the continuum mechanical and thermodynamic framework used in this treatise, followed by a presentation and brief deduction of the R_L -model as derived by Müller, C. (2003). Finally, Chapter 4 was concluded by the introduction of a modification of the afore-discussed R_L -model and a survey of several existing approaches to model the tension/torsion asymmetry.

Addressing the experimental part of this work, the experimental setup was illustrated subsequently. On the one hand, the existing basic configuration was shown, while on the other, several newly developed devices and novel concepts were presented. Thereafter, an extensive characterization of the utilized shape memory alloy was performed. The idea was both to identify some key properties of the given material and to find an appropriate heat treatment. The first mechanical main experiments were meant to discover, if the pseudoelastic material behavior is rate dependent. This was viewed apart from possible temperature effects, which potentially were the result of specific geometries and heat transfer conditions. On this account, uniaxial and biaxial, macroscopically isothermal tests were conducted. Moreover, some isothermal uniaxial relaxation and creep experiments were performed with time constants in the order of decades of minutes. In the case of relaxation tests, considerably large strain rates could be applied for the loading and unloading processes. A second, major topic of the experiments was the assessment of the biaxial material behavior in all four axial/shear strain quadrants containing the tension/compression/torsion subspaces. In this connection, special attention was drawn on the path and direction dependence of the loading and unloading of the specimen. The third and last part of the material testing dealt with the one-way shape memory effect. The classical uniaxial tests were conducted first. Consecutively, biaxial experiments in the first axial/torsional stress quadrant featuring the unloading of the specimen on a martensitic as well as on an austenitic microstructure were shown. This section was completed by a biaxial experiment in the first

two axial/torsional quadrants with loading and unloading of the specimen being performed at different crystallographic microstructures.

The other principal topic, apart from the examination of multidimensional material testing, was the identification of material model parameters. In this connection, Chapter 7 gave a brief introduction to the concepts of direct and inverse problems. Furthermore, the direct formulation was specified to the given problem in terms of the applied material model. In the course of that chapter, different numerical optimization procedures were presented with special attention to the comparison between deterministic and partly stochastic methods. Besides, some considerations concerning the formulation of the objective function referring to different probability densities were given. Finally, the implementation of the parameter identification was exemplified, followed by a discussion of the practical realization thereof. Subsequently, the material parameters were identified and, for comparison, the experimental data, which was used for the identification process, was recalculated using the identified parameters and the given material models. In the end of that chapter, some multidimensional experimental data were compared to calculated data utilizing the identified model parameters.

9.2 Conclusions

Referring to the experimental setup, it can be stated that the developed new strain measuring and temperature control configuration is capable of realizing macroscopically isothermal conditions as well as biaxial strain states with considerably large specimen distortions. Here, it is important that the strain state is measured locally at the gage length contrary to the frequently utilized concept of deducing the strain state from the movement of the crosshead. Furthermore, the realized temperature control setup is one of the first to guarantee macroscopically isothermal conditions for three-dimensional specimens as opposed to thin wire samples. Due to the active control scheme, even very fast temperature variations can be compensated.

Resulting from the uniaxial tension and torsion and the biaxial box tests with different strain rates under isothermal and non-isothermal conditions, it is evident that the considered shape memory alloy does not exhibit any strain rate dependence within the pseudoelastic regime. Moreover, the relaxation experiments show that the effect of stress relaxation is absent under the applied conditions. Concerning the creep behavior, it is difficult to draw a final conclusion, nevertheless, strong cues are given, which imply that a potentially noted pseudocreeep behavior may be the result of temperature effects.

The box and butterfly experiments are to the author's knowledge and apart from circle tests the first multidimensional experiments on NiTi to cover all four axial/torsional strain quadrants. In this connection, explanations for the observed direction dependence of the loading were presented and the tension/compression asymmetry was assessed. It is inferred that the apparent direction dependence of

the measurements associated with the two experiment types may be elucidated by the tension/compression asymmetry.

Some new types of experiments were discussed in connection to pseudoplasticity and the one-way shape memory effect. The classical behavior is also observed under combined stress states without any measurable interrelation between the different loading axes as the specimen temperature is increased. However, some interesting material behavior can be noticed for biaxially loaded specimens upon heating, which could not be explained in the course of this work.

Referring to the parameter identification, it has to be concluded that adequate parameter sets were found. Besides, it is noteworthy that a further improvement of the identified parameter sets cannot be achieved by means of the applied deterministic optimization approach. Additionally, the comparison between the R_L - and the modified R_L -model shows that the measured tension/torsion asymmetry, which can also be deduced from several experimental data published in the literature, is accurately predicted by the modified approach in opposition to the original R_L -model. Nevertheless, it is left to mention that the modified approach appears impracticable for the prediction of loading paths incorporating reorientation of the microstructure by virtue of a violation of the second law of thermodynamics in form of the Clausius-Duhem relation.

Concluding this treatise, the principal new contributions of this work are concisely highlighted.

- An effective digital temperature control scheme for three-dimensional specimens was implemented on the base of Joule heating, convective cooling by means of liquid nitrogen, and a temperature measuring by the use of a set of multiple thermocouples.
- A biaxial strain measuring device capable of measuring strains resulting from considerably large distortions was developed, which minimizes cross-talk, and which can readily be used within a large temperature region.
- According to the isothermal and non-isothermal experiments, it was shown that the material does not exhibit any strain rate dependence for pseudoelasticity.
- Evidence was presented that stress relaxation is absent for pseudoelasticity under macroscopically isothermal conditions.
- Biaxial tests were performed, which are the first nonproportional tests on NiTi, apart from circular strain paths, covering all four axial/torsional strain quadrants.
- Multidimensional experiments on different microstructures were conducted with reference to pseudoplasticity and the one-way shape memory effect, which are the first of this kind for NiTi specimens.

- Model parameters were systematically identified for the R_L - and the modified R_L -model followed by a validation of the models utilizing data associated with uniaxial and biaxial experiments.

9.3 Outlook

Some fundamentally new experiments and experiment types were performed in the present work. Besides, the parameter identification was realized in a concise and stringent way. Nevertheless, the execution of further experiments could prove fruitful in order to allow for a deeper understanding of the transformation progress and the point of transformation onset for different thermomechanical loading conditions.

With reference to the realized parameter identification and the further identification of model parameters for other material models, it is mandatory to know the martensite mass fraction and the proceeding of the martensitic transformation. On this account, some neutron deflection examinations are to be carried out for the shown multidimensional experiments. That way, the material modeling is facilitated, as the onset and progress of the phase transition are of paramount importance for the calculation of the material response.

Clearly, the effect of reorientation should be incorporated in a continuum mechanical material model. At that time, it seems extremely difficult to adapt the existing R_L - or modified R_L -model to reorientation processes concomitantly allowing for a modeling of the axial/shear asymmetry. In this regard, it has to be assessed to what extent some new considerations are to be integrated in an amended material model and if the basic structure of the existent model can be maintained.

Readdressing the presented creep experiments, it is necessary to extend the experimental database. In this connection, it might be sufficient to perform uniaxial tests on thin wire samples whose temperature is kept constant by means of a passive temperature control system as described in [Shaw, J.A. & Kyriakides, S. \(1995\)](#). However, it appears necessary to utilize a local strain measuring device in order to prevent the system from any deterioration of the measurement results as a consequence of the gripping and the sample geometry within the gripping. Furthermore, the viscous material behavior within the pseudoplastic temperature regime is of special interest. Some effects, which could be observed on the experiments concerning the one-way shape memory, may be elucidated thereby. Due to the same reason, more extensive testing with reference to the one-way effect in the described manner seems appropriate.

A Implementation of the modified R_L -model

In this section, the material model is implemented by recourse to time discretization, see Section 7.3.1. The task is to compute the martensite mass fraction and the stress state for every time step. Consequently, the system of equations has to be solved with respect to the unknowns \mathbf{x} as defined by

$$\mathbf{x}_{k+1} = \begin{pmatrix} \boldsymbol{\sigma}_{k+1} \\ \xi_{k+1} \end{pmatrix} \quad (\text{A.1})$$

with

$$\mathbf{x}_{k+1} = \mathbf{x}_k + \mathbf{z}_k \quad (\text{A.2})$$

and

$$\mathbf{z}_k = \begin{pmatrix} \Delta\boldsymbol{\sigma}(\boldsymbol{\sigma}_{k+1}) \\ \Delta\xi(\xi_{k+1}) \end{pmatrix}. \quad (\text{A.3})$$

Basically, \mathbf{z}_k has to be determined in order to get \mathbf{x}_{k+1} . On this account, Newton's method is applied to the following function

$$\mathbf{R} = \begin{pmatrix} \boldsymbol{\sigma}_{k+1} - \boldsymbol{\sigma}_k - \Delta\boldsymbol{\sigma}(\boldsymbol{\sigma}_{k+1}) \\ \xi_{k+1} - \xi_k - \Delta\xi(\xi_{k+1}) \end{pmatrix} \quad (\text{A.4})$$

with

$$\Delta\boldsymbol{\sigma}(\boldsymbol{\sigma}_{k+1}) = \mathbb{C}_0 : (\Delta\boldsymbol{\varepsilon} - \Delta\boldsymbol{\varepsilon}^{\text{tr}} - \Delta\Theta\boldsymbol{\alpha}_0) \quad (\text{A.5})$$

and

$$\begin{aligned} \Delta\xi &= \frac{\frac{\eta}{\sigma_k^2} [\boldsymbol{\sigma}'_k : \mathbb{Z}_k(\boldsymbol{\sigma}_k) + \hat{\sigma}_k \boldsymbol{\sigma}'_k] : \Delta\boldsymbol{\sigma} + \rho_0 (-\Delta s^* + (1 - 2\xi_k) \bar{s}_0) \Delta\Theta}{\rho_0 \left(\frac{\partial k^\alpha}{\partial \xi} \right)_k - \left(\frac{\partial \pi^f}{\partial \xi} \right)_k} \\ &= \mathbf{w}_k : \Delta\boldsymbol{\sigma} + K \Delta\Theta. \end{aligned} \quad (\text{A.6})$$

Here, \mathbf{w}_k and K are defined as

$$\mathbf{w}_k = \frac{\frac{\eta}{\sigma_k^2} [\boldsymbol{\sigma}'_k : \mathbb{Z}_k(\boldsymbol{\sigma}_k) + \hat{\sigma}_k \boldsymbol{\sigma}'_k]}{\rho_0 \left(\frac{\partial k^\alpha}{\partial \xi} \right)_k - \left(\frac{\partial \pi^f}{\partial \xi} \right)_k} \quad (\text{A.7})$$

and

$$K = \frac{\rho_0 (-\Delta s^* + (1 - 2\xi_k) \bar{s}_0)}{\rho_0 \left(\frac{\partial k^\alpha}{\partial \xi} \right)_k - \left(\frac{\partial \pi^f}{\partial \xi} \right)_k}. \quad (\text{A.8})$$

Furthermore, the transformation strain increment is specified from Equation (4.65)

$$\begin{aligned}\Delta\boldsymbol{\varepsilon}^{\text{tr}} &= \frac{\eta}{\sigma_k^2} [\Delta\xi \hat{\sigma}_k \boldsymbol{\sigma}'_k + \xi_k \mathbb{Z}_k(\boldsymbol{\sigma}_k) : \Delta\boldsymbol{\sigma}] \\ &= \Delta\xi \mathbf{r}_k + \mathbb{Y}_k : \Delta\boldsymbol{\sigma}\end{aligned}\quad (\text{A.9})$$

with the \mathbf{r}_k and \mathbb{Y}_k being given by

$$\mathbf{r}_k = \frac{\eta}{\sigma_k^2} \hat{\sigma}_k \boldsymbol{\sigma}'_k \quad (\text{A.10})$$

and

$$\mathbb{Y}_k = \frac{\eta}{\sigma_k^2} \xi_k \mathbb{Z}_k(\boldsymbol{\sigma}_k). \quad (\text{A.11})$$

\mathbf{z}_k is inferred as the system of equations,

$$\nabla\mathbf{R} \mathbf{z}_k = -\mathbf{R}, \quad (\text{A.12})$$

is solved. Consequently, $\nabla\mathbf{R}$ reads

$$\nabla\mathbf{R} = \begin{pmatrix} \frac{\partial\mathbf{R}}{\partial\boldsymbol{\sigma}_{k+1}} & \frac{\partial\mathbf{R}}{\partial\xi_{k+1}} \end{pmatrix} \quad (\text{A.13})$$

with

$$\frac{\partial\mathbf{R}}{\partial\boldsymbol{\sigma}_{k+1}} = \begin{pmatrix} \mathbb{I} + \mathbb{C}_0 : \frac{\partial\Delta\boldsymbol{\varepsilon}^{\text{tr}}}{\partial\boldsymbol{\sigma}_{k+1}} \\ -\frac{\partial\Delta\xi}{\partial\boldsymbol{\sigma}_{k+1}} \end{pmatrix} \quad (\text{A.14})$$

and

$$\frac{\partial\mathbf{R}}{\partial\xi_{k+1}} = \begin{pmatrix} \mathbb{C}_0 : \frac{\partial\Delta\boldsymbol{\varepsilon}^{\text{tr}}}{\partial\xi_{k+1}} \\ 1 \end{pmatrix}. \quad (\text{A.15})$$

The missing derivatives collapse to

$$\frac{\partial\Delta\xi}{\partial\boldsymbol{\sigma}_{k+1}} = \mathbf{w}_k : \mathbb{I} \quad (\text{A.16})$$

and

$$\frac{\partial\Delta\boldsymbol{\varepsilon}^{\text{tr}}}{\partial\boldsymbol{\sigma}_{k+1}} = \mathbb{Y}_k : \mathbb{I} \quad (\text{A.17})$$

Finally, with

$$\frac{\partial\Delta\boldsymbol{\varepsilon}^{\text{tr}}}{\partial\xi_{k+1}} = \mathbf{r}_k \quad (\text{A.18})$$

the gradient of the function \mathbf{R} can be calculated to yield

$$\nabla \mathbf{R} = \begin{pmatrix} \mathbb{I} + \mathbb{C}_0 : (\mathbb{Y}_n : \mathbb{I}) & \mathbb{C}_0 : \mathbf{r}_n \\ -\mathbf{w}_n : \mathbb{I} & 1 \end{pmatrix}. \quad (\text{A.19})$$

After solving the system of linear equations as presented in Equation (A.12) the problem can be considered as solved, since the stress state and the martensite mass fraction are known for the next time step.

B Additional experiments concerning the one-way effect

This section is meant as an addendum to Section 6.4. Two experiments are considered which feature different microstructures for loading and unloading. The tests are conducted under stress and temperature control. Loading is performed in the martensitic state of the specimen. This is realized by cooling down the specimen below -85°C . Afterwards, the specimen is heated up to a temperature of -30°C . Common to both experiment types are the first two loading steps. The experiments are treated consecutively.

The first experiment type is an interrupted box test in the first axial/torsional stress quadrant. At the beginning of the experiment, the specimen is loaded in tension followed by a loading in torsion concomitantly keeping the axial stress constant. The maximum stresses are $\sigma = 127\text{ MPa}$ and $\tau' = 127\text{ MPa}$. Subsequently, the specimen is heated above 60°C which is supposed to be below the $R \rightarrow B2$ phase transformation under the considered stress state. As soon as the specimen is cooled down to 27.5°C , it is unloaded in the reverse loading order. Similar diagrams to Section 6.4.2.1 are presented in Figures B.1 - B.5. The most interesting parts of the diagrams are the segments which cover the cooling from 60°C and the subsequent unloading. In this region, the temperature dependence of Young's modulus is evident as the strain is continuously decreased and increased depending on the direction of the temperature change. Finally, the strain is almost completely reduced after unloading. The residual strains are of the same order as for the aforementioned tests and might be neglected. The reason is that on cooling even smallest stresses are sufficient to trigger strains in the considered order, see Section 6.4.

The second experiment type which is treated in this section is similar to the first one concerning the temperature cycle and the respective temperatures for loading and unloading. The only difference is that the tensile stress is reduced to zero followed by a loading in compression after the two initial loading steps. The compressive stress is $\sigma = 127\text{ MPa}$. Axial and shear stress are kept constant for the subsequent temperature changes. Again, the most interesting parts of the diagrams in Figures B.6 - B.10 are related to the heating and cooling above 27.5°C . In this context, it is instructive to compare those curve segments as shown in Figures B.6 - B.10 and 6.58 - 6.62.

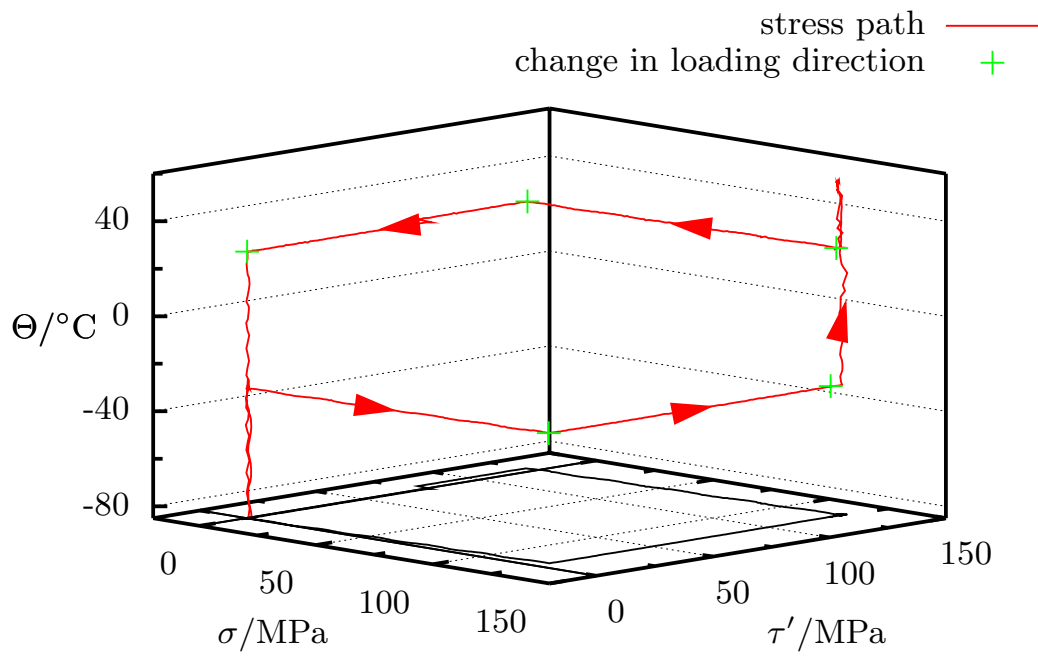


Figure B.1: Pseudoplastic control path of an interrupted box test

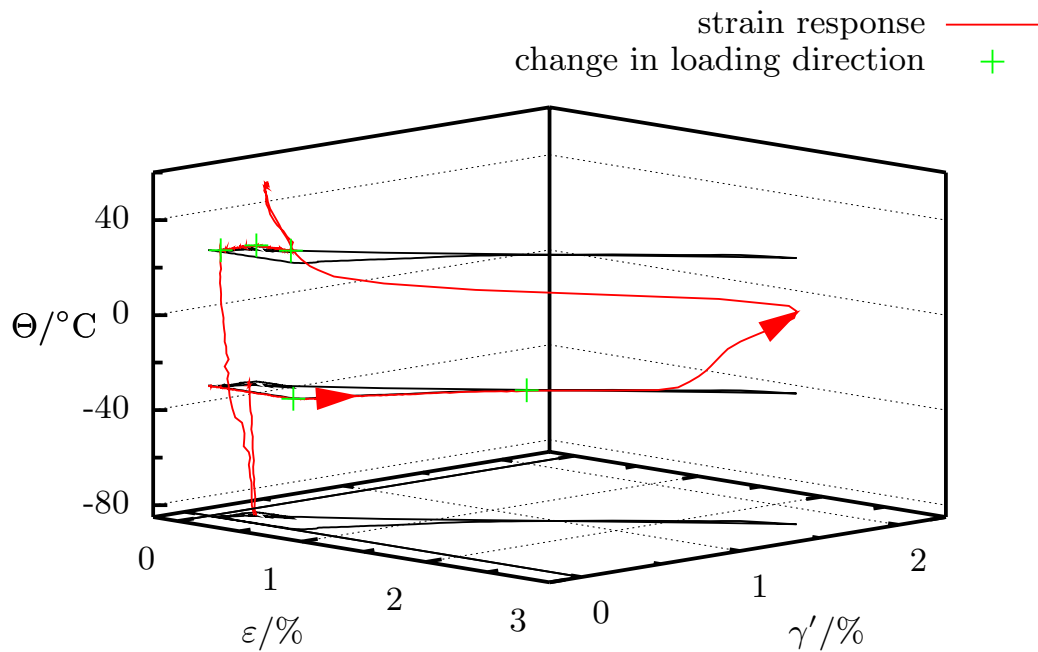


Figure B.2: Pseudoplastic strain response as a function of temperature on the interrupted box stress path

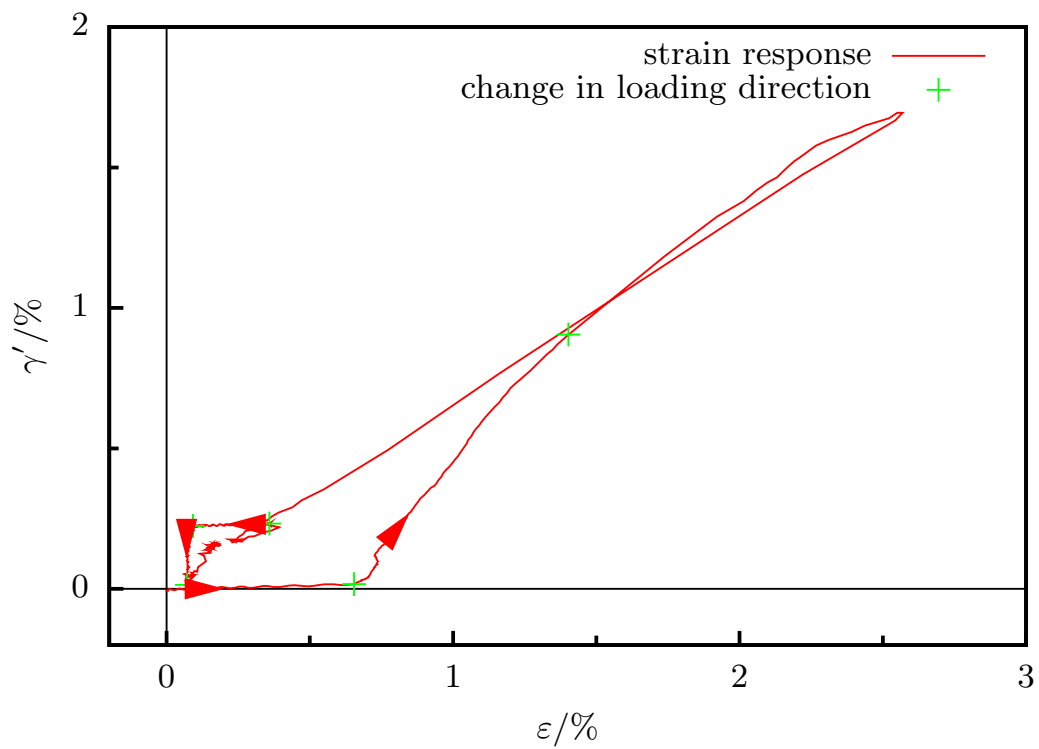


Figure B.3: Pseudoplastic strain response on the interrupted box stress path

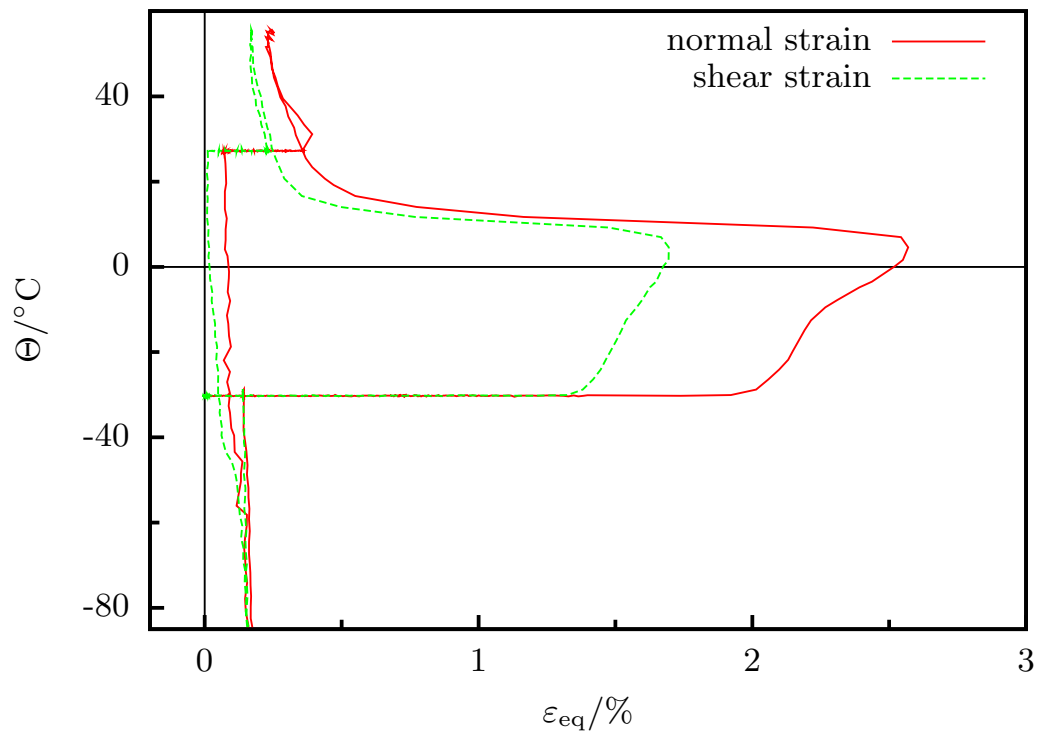


Figure B.4: Strain as function of temperature for the interrupted pseudoplastic box test

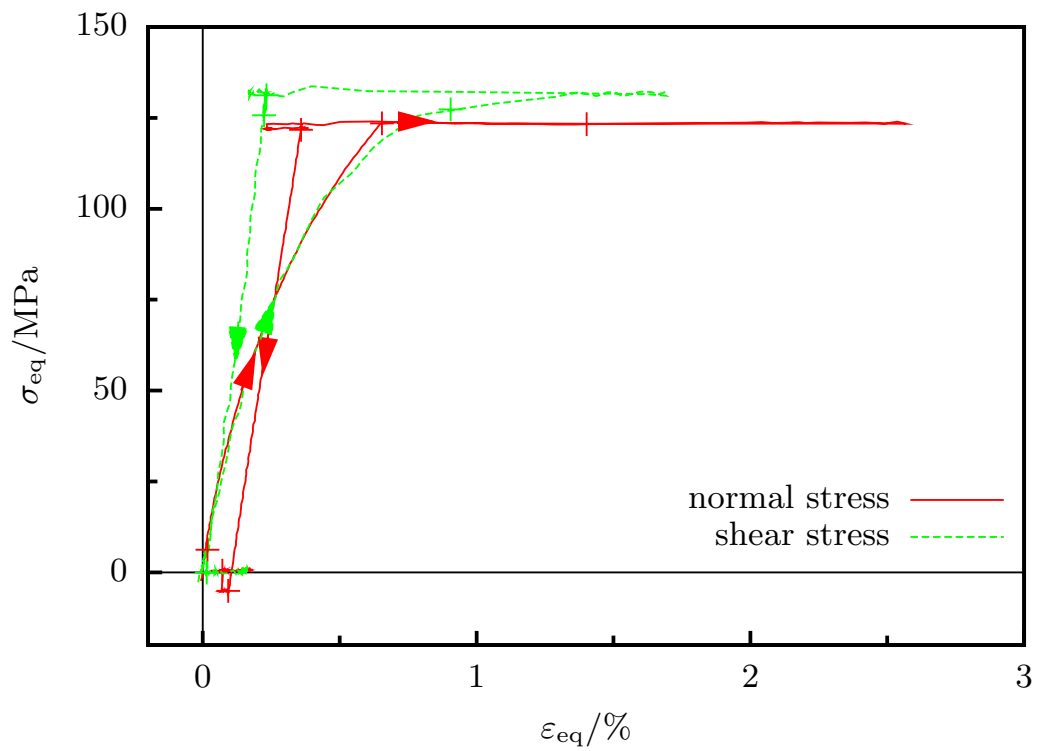


Figure B.5: Stress-strain diagrams for the interrupted pseudoplastic box test

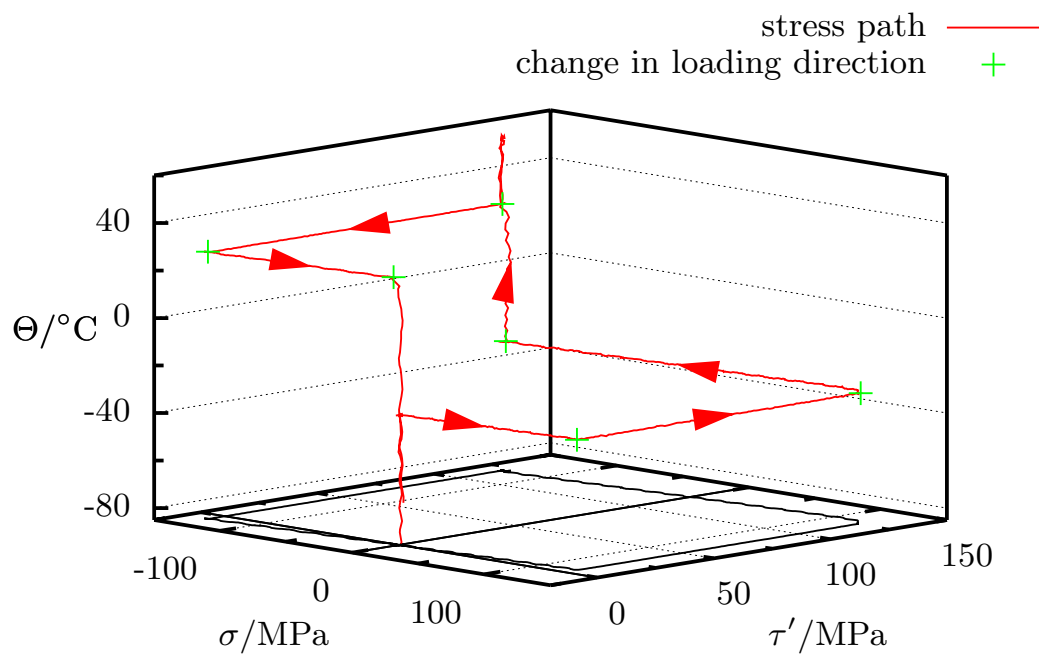


Figure B.6: Pseudoplastic control path of an interrupted box test with compression

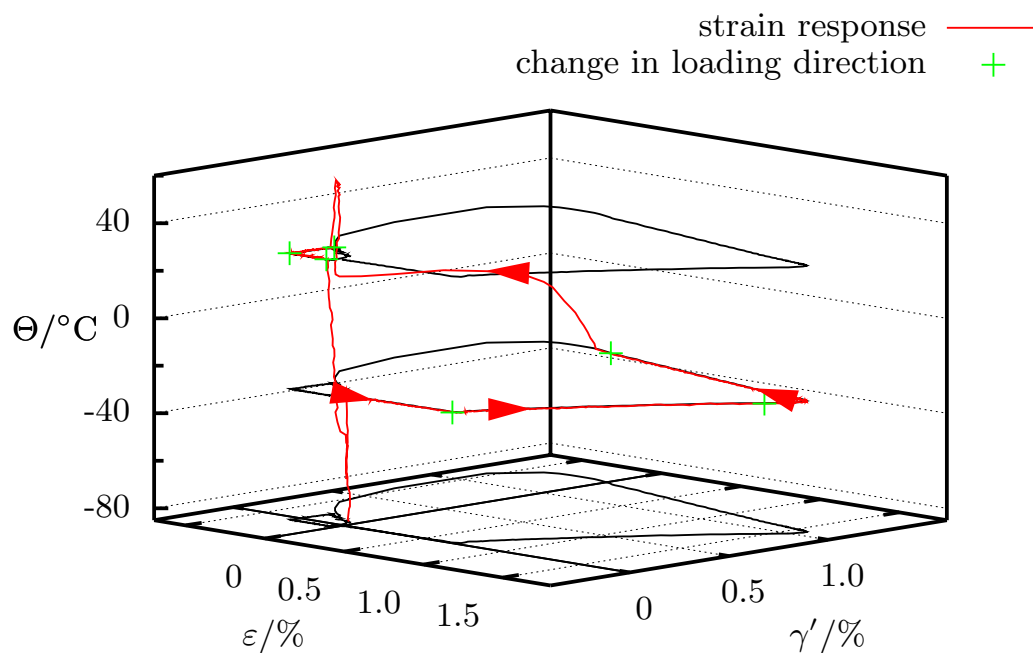


Figure B.7: Pseudoplastic strain response as a function of temperature on the interrupted box stress path with compression

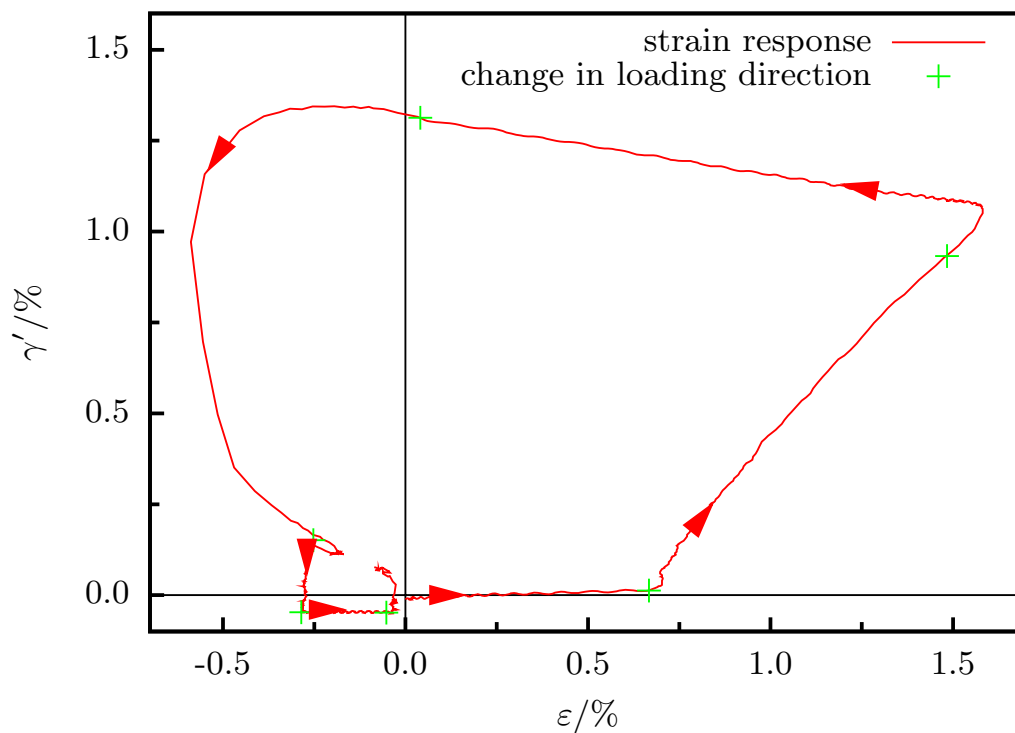


Figure B.8: Strain response on the interrupted box stress path with compression

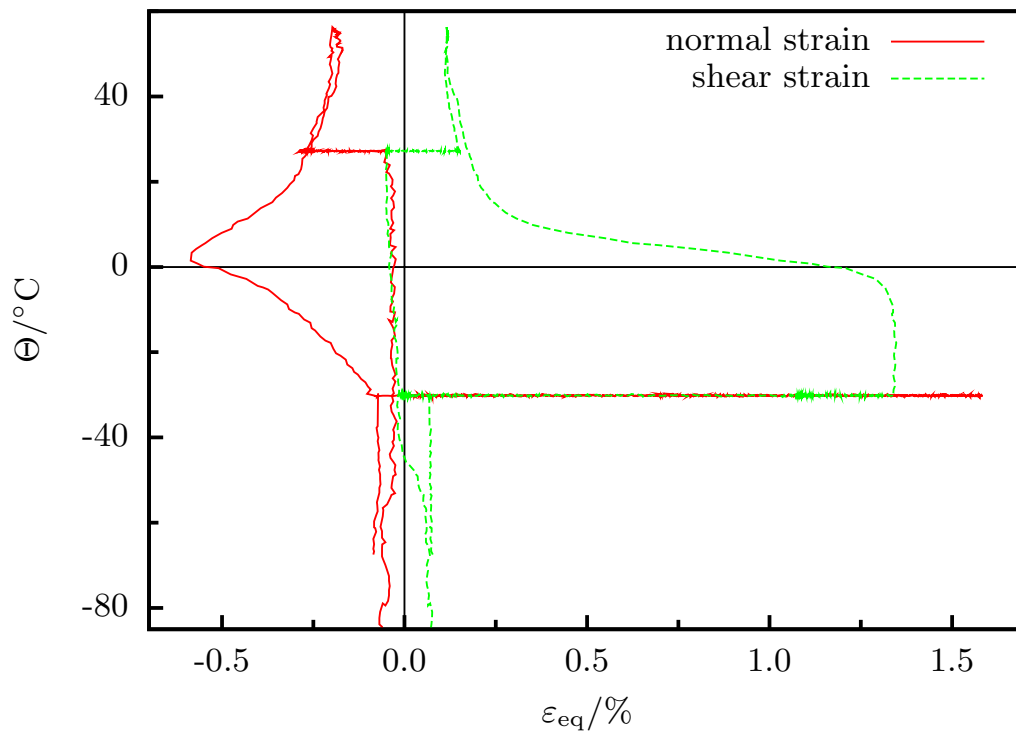


Figure B.9: Temperature/strain for the pseudoplastic box test with compression

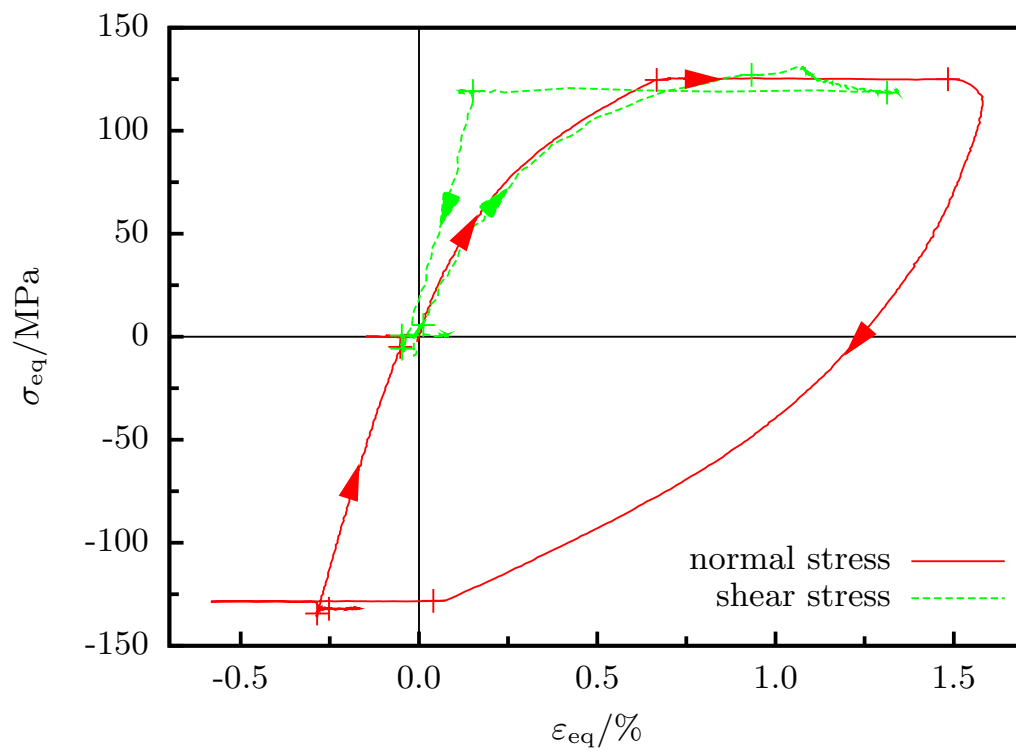


Figure B.10: Stress/strain for the pseudoplastic box test with compression

C Results of the parameter identification

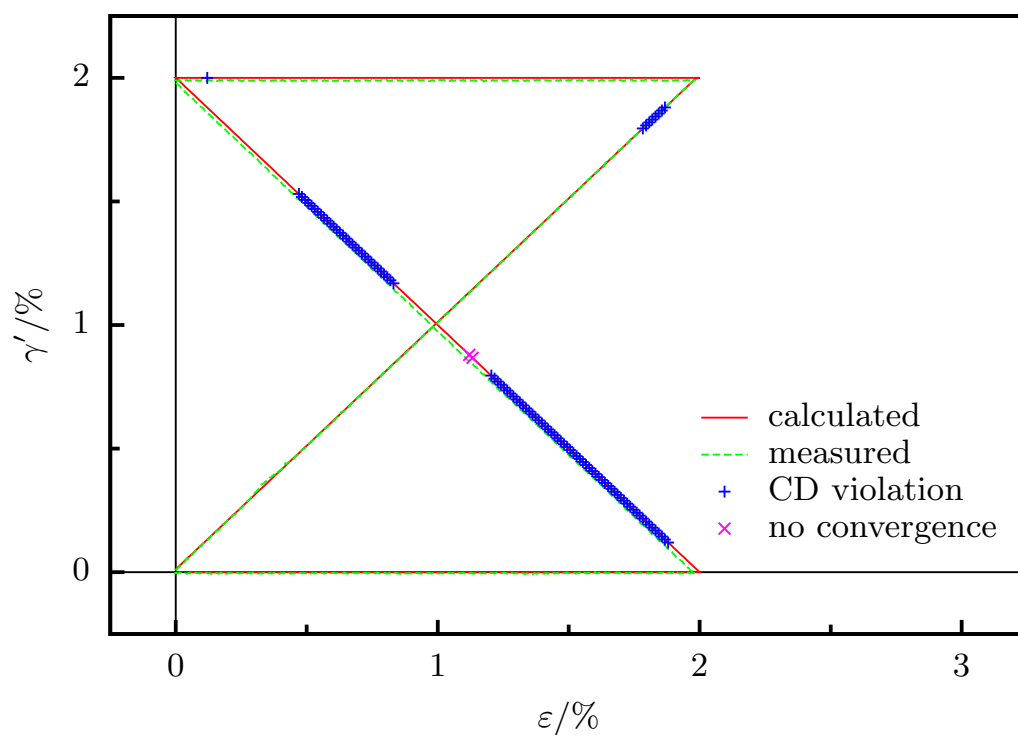
C.1 Identified material parameters

Parameter	1	2	3	4	5	6	7
E	34762	34857	33068	32540	32315	32585	32237
ν	0.157	0.074	0.053	0.066	0.023	0.032	0.039
Δu^*	10539	9610	11005	9662	11016	9241	11012
Δs^*	41.8	38.2	43.2	38.9	43.3	37.3	43.4
\bar{u}_0	1595	2254	1997	847	2012	688	1967
\bar{s}_0	4.4	6.6	5.5	1.5	5.4	1.1	5.4
η	0.0518	0.0464	0.0500	0.0514	0.0498	0.0499	0.0504
a_1	0.47	0.52	0.43	0.47	0.44	0.43	0.44
a_2	0.15	0.19	0.85	0.42	0.69	0.43	0.44
r_1	0.85	0.48	0.60	0.87	0.59	0.90	0.61
r_2	0.56	0.65	1.14	1.12	1.04	1.14	1.01
b	0.80	0.83	0.81	0.80	0.82	0.82	0.83

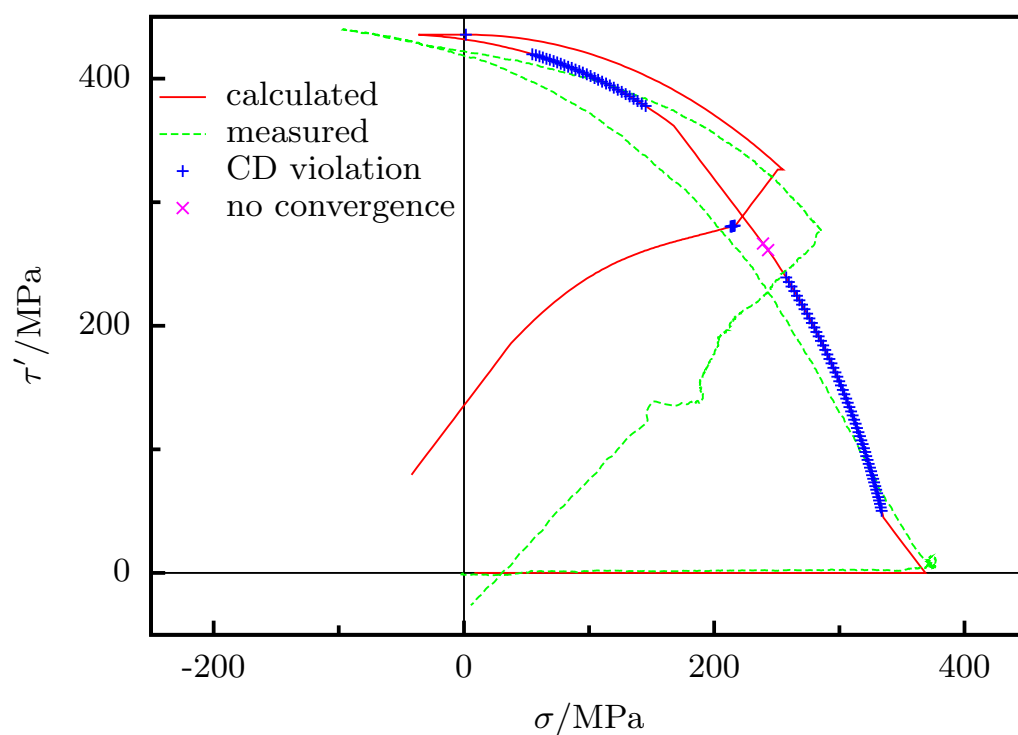
Table C.1: Identified material parameters for seven different specimens

C.2 Additional nonproportional experiments and comparison

In addition to the nonproportional box tests presented in Section 8.2.2, two sets of experimental and calculated data for a butterfly loading path are compared in this section. Again, strain and temperature control is applied. The von-Mises equivalent strain rate is continuous $\dot{\epsilon}_{\text{eq}} = 10^{-4} \text{ s}^{-1}$. Furthermore, the compliance with the Clausius-Duhem relation is inspected after each computation step. For clarity, the violation of the Clausius-Duhem inequality is signified by crosses in all diagrams. Beyond the violation of the Clausius-Duhem relation a second problem comes into play as the butterfly test is considered. That is, the missing convergence of the material model at specific points in the computation process. Naturally, if the computation is pursued beyond a state of non-convergence, all further data are deteriorated. In this connection, it has to be pointed out that the problem of missing convergence depends strongly on the material parameter set and the computation step size.

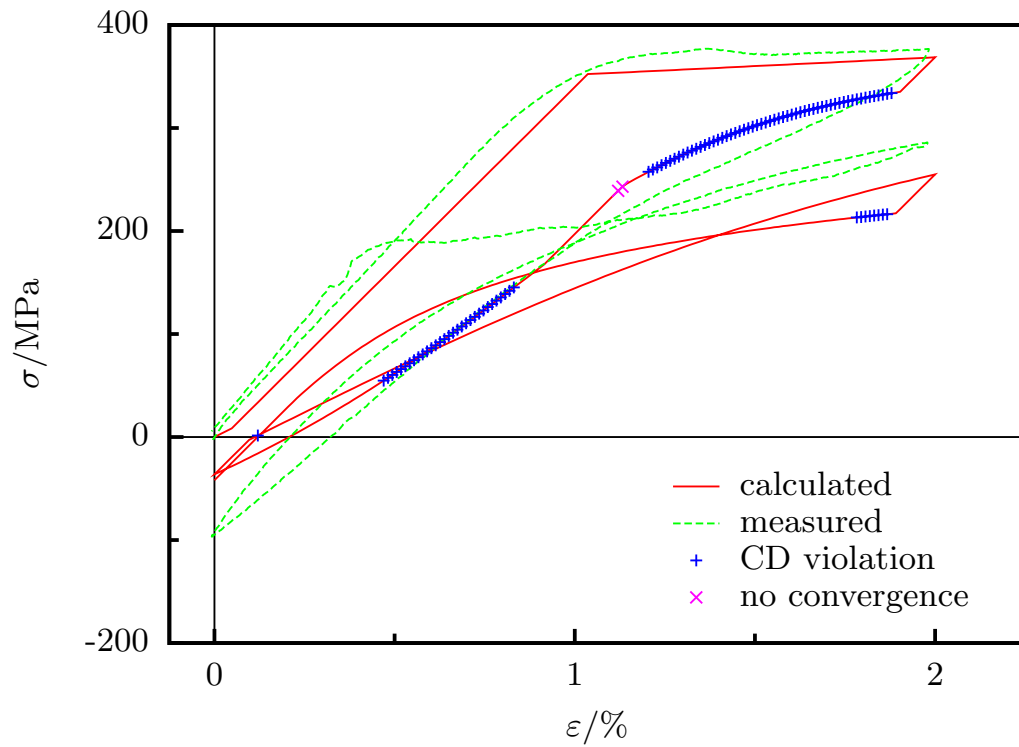


(a) Strain-strain diagram

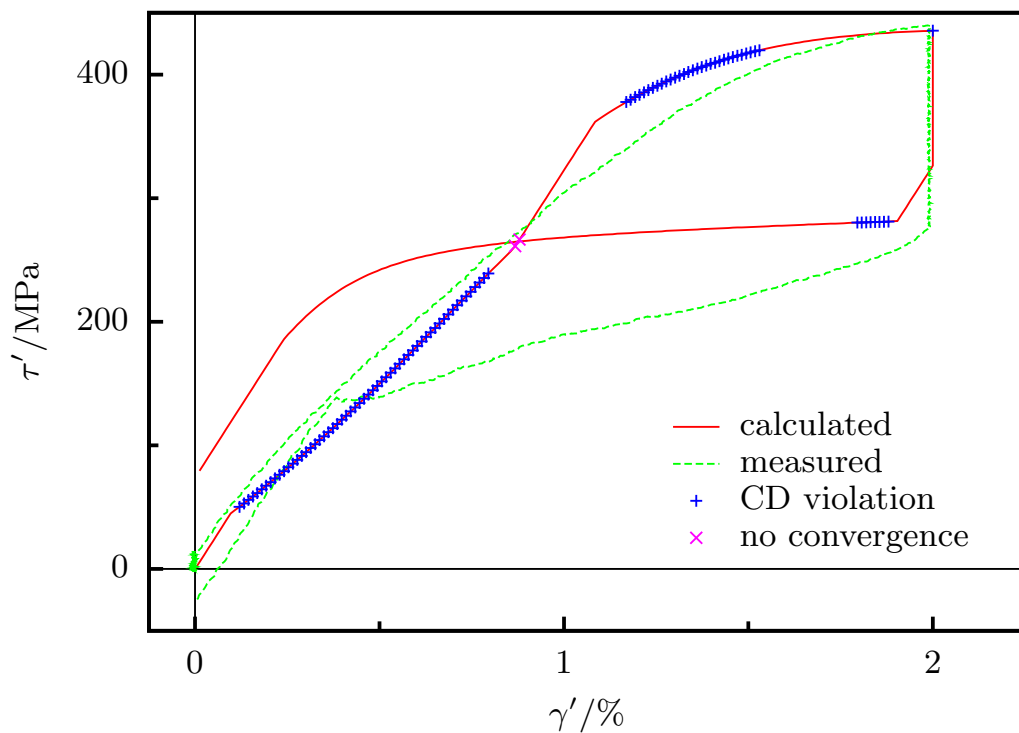


(b) Stress-stress diagram

Figure C.1: Combined butterfly test, measured and calculated; strain-strain and stress-stress diagram



(a) Strain-strain diagram



(b) Stress-stress diagram

Figure C.2: Combined butterfly test, measured and calculated; axial and torsional stress-strain diagrams

The respective diagrams are shown in Figures C.1 and C.2. As the particular diagrams are regarded, it is surprising that the measured material behavior is approximated as accurately albeit all the aforementioned problems.

Bibliography

- ALTENBACH, J. & ALTENBACH, H. (1994): *Einführung in die Kontinuumsmechanik*, B.G. Teubner Stuttgart 1994.
- ANDING, D.K. (1997): *Zur simultanen Bestimmung materialabhängiger Koeffizienten inelastischer Stoffgesetze* 1997, Dissertation, Ruhr-Universität Bochum, Mitteilungen aus dem Institut für Mechanik, Nr. 109.
- BOUVET, C., CALLOCH, S. & LEXCELLENT, C. (2002a): *Approches expérimentale et théorique du comportement thermomécanique sous chargement multiaxial d'alliages à mémoires de forme polycristallins*, in: Journal de Physique IV, Volume 12, Pr 11, 283–290.
- BOUVET, C., CALLOCH, S. & LEXCELLENT, C. (2002b): *Mechanical Behavior of a Cu-Al-Be Shape Memory Alloy Under Multiaxial Proportional and Non-proportional Loadings*, in: Journal of Engineering Materials and Technology - Transactions of the ASME, Volume 124, 2, 112–124.
- BOUVET, C., CALLOCH S. & LEXCELLENT C. (2004): *A phenomenological model for pseudoelasticity of shape memory alloys under multiaxial proportional and nonproportional loadings*, in: European Journal of Mechanics A/Solids, Volume 23, 1, 37–61.
- BRINSON, L.C., SCHMIDT, I. & LAMMERING, R. (2004): *Stress-Induced Transformation Behavior of a Polycrystalline NiTi Shape Memory Alloy: Micro and Macromechanical Investigations via in situ Optical Microscopy*, in: Journal of Mechanics and Physics of Solids, Volume 52, 7, 1549–1571.
- DIN 43722 (1994): *Thermopaare – Teil 3: Thermoleitungen und Ausgleichleitungen, Grenzabweichungen und Kennzeichnungssystem (IEC 584-3: 1989, modifiziert), Deutsche Fassung HD 446.3 S1: 1989*, DIN Deutsches Institut für Normung e.V.
- DIN EN 60584-2 (1994): *Thermopaare – Teil 2: Grenzabweichungen der Thermospannungen (IEC 584-2: 1982 + A1: 1989), Deutsche Fassung EN 60584-2: 1993*, DIN Deutsches Institut für Normung e.V.
- EGGELER, G. (2001a): *Grundlagen Werkstoffe*, Ruhr-Universität Bochum, Fakultät für Maschinenbau, Institut für Werkstoffe, Lehrstuhl Werkstoffwissenschaft.

- EGGELER, G. (2001b): *Untersuchung von Werkstoffen mit Röntgen-, Elektronen- und Neutronenstrahlen - mit einer Einführung in die Durchstrahlungselektronenmikroskopie*, Ruhr-Universität Bochum, Fakultät für Maschinenbau, Institut für Werkstoffe, Lehrstuhl Werkstoffwissenschaft.
- FOGEL, L.J., OWENS, A.J. & WALSH, M.J. (1966): *Artificial Intelligence through Simulated Evolution*, John Wiley New York 1966.
- FUNAKUBO, H. (Ed.) (1984): *Shape Memory Alloys*, Volume 1 of *Precision Machinery and Robotics*, Gordon and Breach Science Publishers 1984.
- GALL, K., LIM, T.J., MCDOWELL, D.L., SEHITOGLU, H. & CHUMLYAKOV, Y.I. (2000): *The role of intergranular constraint on the stress-induced martensitic transformation in textured polycrystalline NiTi*, in: *International Journal of Plasticity*, Volume 16, 1189–1214.
- GALL, K., SEHITOGLU, H. & MAIER, H. (1997): *Asymmetric Stress-Strain Response in Shape Memory Alloys*, in: KHAN, A.S. (Ed.): *Physics and Mechanics of Finite Plastic and Viscoplastic Deformation*, Neat Press Fulton, Maryland 1997, pp. 153–154, *Proceedings of Plasticity '97: The Sixth International Symposium on Plasticity and Its Current Applications*.
- GALL, K., SEHITOGLU, H., MAIER, H.J. & JACOBUS, K. (1998): *Stress-Induced Martensitic Phase Transformations in Polycrystalline CuZnAl Shape Memory Alloys under Different Stress States*, in: *Metallurgical and Materials Transactions A*, Volume 29A, 765–773.
- GEIGER, C. & KANZOW, C. (1999): *Numerische Verfahren zur Lösung unrestringierter Optimierungsaufgaben*, Springer-Verlag Berlin Heidelberg 1999.
- GEIST, A., BEGUELIN, A., DONGARRA, J., JIANG, W., MANCHEK, R. & SUNDERAM, V. (1994): *PVM: Parallel Virtual Machine - A Users' Guide and Tutorial for Networked Parallel Computing*, The MIT Press, Cambridge, Massachusetts, London, England.
- GRABE, C. & BRUHNS, O.T. (2006): *Multidimensional Tests of Superelastic, Polycrystalline NiTi under Isothermal Conditions*, in: *Proceedings of Applied Mathematics and Mechanics*, Volume 6, 373–374.
- GRABE, C. & BRUHNS, O.T. (2007): *Tension/torsion tests of pseudoelastic, polycrystalline NiTi shape memory alloys under temperature control*, in: *Materials Science and Engineering A*, Volume to appear.
- HANSEN, N. (2005): *The CMA Evolution Strategy: A Tutorial*, Technical report, Technische Universität Berlin, Bionik und Evolutionstechnik, URL <http://www.bionik.tu-berlin.de/user/niko/cmatutorial.pdf>, 2005.

- HARA, T., OHBA, T., OKUNISHI, E. & OTSUKA, K. (1997): *Structural Study of R-Phase in Ti-50.23 at.%Ni and Ti-47.75 at.%Ni-1.50 at.%Fe Alloys*, in: Materials Transactions, JIM, Volume 38, 1, 11–17.
- HECKMANN, A. (2003): *Mikrostruktur und Ermüdung von NiTi-Formgedächtnislegierungen 2003*, Dissertation, Ruhr-Universität Bochum.
- HELM, D. (2001): *Formgedächtnislegierungen - Experimentelle Untersuchung, phänomenologische Modellierung und numerische Simulation der thermomechanischen Materialeigenschaften 2001*, Dissertation, Universität Gesamthochschule Kassel.
- HELM, D. & HAUPT, P. (2003): *Shape memory behaviour: modelling within continuum thermodynamics*, in: International Journal of Solids and Structures, Volume 40, 827–849.
- HODGSON, D.E. & BROWN, J.W. (2000): *Using Nitinol Alloys*, Technical report, Shape Memory Applications, Inc., San Jose, CA, USA, 2000.
- HOLLAND, J.H. (1975): *Adaptation in natural and artificial systems*, The University of Michigan Press 1975.
- HONMA, T. (1984): *Types and Mechanical Characteristics of Shape Memory Alloys*, in: FUNAKUBO, H. (Ed.): *Shape Memory Alloys*, Gordon and Breach Science Publishers 1984, Volume 1 of *Precision Machinery and Robotics*, pp. 61–175.
- HORNBOGEN, E. (1995): *On the Term “Pseudo-elasticity”*, in: Zeitschrift für Metallkunde, Volume 86, 5, 341–344.
- IMBENI, V., MEHTA, A., ROBERTSON, S.W., DUERIG, T.W., PELTON, A. & RITCHIE, R.O. (2003): *On the Mechanical Behavior of Nitinol under Multiaxial Loading Conditions and In Situ Synchrotron X-Ray Diffraction*, in: PELTON, A. & DUERIG, T.W. (Eds.): *Proceedings of the Shape Memory and Superelastic Technologies Conference 2003 (SMST-2003)*, SMST Society, Inc., Menlo Park, CA 2003, pp. 267–276.
- INCROPERA, F.P. & DEWITT, D.P. (1996): *Fundamentals of Heat and Mass Transfer*, 4. Edition, John Wiley & Sons New York Chichester Brisbane Toronto Singapore 1996.
- ISERMANN, R. (1988): *Digitale Regelsysteme - Band I - Grundlagen, Deterministische Regelungen*, Springer-Verlag Berlin Heidelberg New York 1988.
- JACOBUS, K., SEHITOGLU, H. & BALZER, M. (1996): *Effect of Stress-State on the Stress-Induced Martensitic Transformation in Polycrystalline Ni-Ti Alloy*, in: Metallurgical and Materials Transactions A, Volume 27A, 3066–3073.

- JUHÁSZ, L., SCHNACK, E., HESEBECK, O. & ANDRÄ, H. (2002): *Macroscopic Modeling of Shape Memory Alloys under Non-proportional Thermo-mechanical Loadings*, in: *Journal of Intelligent Material Systems and Structures*, Volume 13, 825–836.
- KEMPNER, J. & TRAVININ, N. (2003): *Parallel Matlab: The Next Generation*, in: *7th High Performance Embedded Computing Workshop (HPEC 2003)*, 2003.
- KHALIL ALLAFI, J. (2002): *Mikrostrukturelle Untersuchungen zum Einfluss von thermomechanischen Behandlungen auf die martensitischen Phasenumwandlungen an einer Ni-reichen NiTi Formgedächtnislegierung 2002*, Dissertation, Ruhr-Universität Bochum.
- KRONE, L., MENTZ, J., BRAM, M., BUCHKREMER, H.-P., STÖVER, D., WAGNER, M., EGGELER, G., CHRIST, D., REESE, S., BOGDANSKI, D., KÖLLER, M., ESENWEIN, S.A., MUHR, G., PRYMAK, O. & EPPLE, M. (2005): *The Potential of Powder Metallurgy for the Fabrication of Biomaterials on the Basis of Nickel-Titanium: A Case Study with a Staple Showing Shape Memory Behaviour*, in: *Advanced Engineering Materials*, Volume 7, 7, 613–619.
- KÖRTVÉLYESSY, L. (1998): *Thermoelement Praxis: neue theoretische Grundlagen und deren Umsetzung*, 3. Edition, Vulkan-Verlag Essen 1998.
- LEO, P.H., SHIELD, T.W. & BRUNO, O.P. (1993): *Transient heat transfer effects on the pseudoelastic behavior of shape-memory wires*, in: *Acta metall. mater.*, Volume 41, 8, 2477–2485.
- LEVY, S.D., DJALALIEV, P.L., SHRESTHA, J.M., KHASYMSKI, A. & CONNORS, C.D. (2005): in: *Proceedings of the 18th International Conference on Parallel and Distributed Computing Systems*, International Society for Computers and their Applications, Las Vegas, Nevada 2005.
- LEXCELLENT, C., BOUBAKAR, M.L., BOUVET, C. & CALLOCH, S. (2006): *About modelling the shape memory alloy behaviour based on the phase transformation surface identification under proportional loading and anisothermal conditions*, in: *International Journal of Solids and Structures*, Volume 43, 613–626.
- LEXCELLENT, C. & REJZNER, J. (2000): *Modeling of the strain rate effect, creep and relaxation of a Ni-Ti shape memory alloy under tension (compression) – torsional proportional loading in the pseudoelastic range*, in: *Smart Materials and Structures*, Volume 9, 613–621.
- LEXCELLENT, C. & TOBUSHI, H. (1995): *Internal Loops in Pseudoelastic Behaviour of Ti-Ni Shape Memory Alloys: Experiment and Modelling*, in: *Mechanica*, Volume 30, 459–466.

- LI, Z.Q. & SUN, Q.P. (2002): *The initiation and growth of macroscopic martensite band in nano-grained NiTi microtube under tension*, in: International Journal of Plasticity, Volume 18, 1481–1498.
- LIM, T.J. & MCDOWELL, D.L. (1995): *Path Dependence of Shape Memory Alloys during Cyclic Loading*, in: Journal of Intelligent Material Systems and Structures, Volume 6.
- LIM, T.J. & MCDOWELL, D.L. (1999): *Mechanical Behavior of an Ni-Ti Shape Memory Alloy Under Axial-Torsional Proportional and Nonproportional Loading*, in: Journal of Engineering Materials and Technology, Volume 121, 1, 9–18.
- LIN, P., TOBUSHI, H., TANAKA, K., HATTORI, T. & IKAI, A. (1996a): *Influence of Strain Rate on Deformation Properties of TiNi Shape Memory Alloy*, in: JSME International Journal Series A – Mechanics and Material Engineering, Volume 39, 1, 117–123.
- LIN, P., TOBUSHI, H., TANAKA, K. & IKAI, A. (1996b): *Deformation Properties of TiNi Shape Memory Alloys*, in: JSME International Journal Series A – Mechanics and Material Engineering, Volume 39, 1, 108–116.
- LUIG, P., KNOPIK, A., OBERSTE-BRANDENBURG, C., GRABE, C., BRUHNS, O.T. & PREDKI, W. (2006): *Damping couplings with elements of pseudoelastic NiTi shape memory alloys*, in: Archive of Applied Mechanics, Volume 76, 75–87.
- MATSUI, R., TOBUSHI, H. & IKAWA, T. (2004): *Transformation-induced creep and stress relaxation of TiNi shape memory alloy*, in: Proceedings of the Institution of Mechanical Engineers – Part L – Journal of Materials: Design & Applications, Volume 218, L4, 343–353.
- MCCORMICK, P.G., LIU, Y. & MIYAZAKI, S. (1993): *Intrinsic thermal-mechanical behaviour associated with the stress-induced martensitic transformation in NiTi*, in: Materials Science and Engineering A, Volume 167, 51–56.
- MCCORMICK, P.G., MIYAZAKI, S. & LIU, Y. (1992): *Intrinsic transformation influenced mechanical behaviour in a Ni-Ti alloy*, in: Proceedings of the International Conference on Martensitic Transformations, 1992.
- MCNANEY, J.M., IMBENI, V., JUNG, Y., PAPADOPOULOS, P. & RITCHIE, R.O. (2003): *An experimental study of the superelastic effect in shape-memory Nitinol alloy under biaxial loading*, in: Mechanics of Materials, Volume 35, 969–986.
- MELTON, K.N. (1998): *General applications of SMA's and smart materials*, in: OTSUKA, K. & WAYMAN C. M. (Eds.): *Shape Memory Materials*, Cambridge University Press 1998.

- MICHUTTA, J. (2005): *Metallkundliche Untersuchungen zum Einfluss von Ni_4Ti_3 -Teilchen auf die martensitische Umwandlung in Ni-reichen NiTi-Einkristallen* 2005, Dissertation, Ruhr-Universität Bochum, fortschritt-Berichte VDI, Reihe 5, Grund- und Werkstoffe/Kunststoffe, Nr. 712.
- MILLS, A.F. (1999): *Heat Transfer*, 2. Edition, Prentice Hall 1999.
- MIYAZAKI, S. (1996): *Development and Characterization of Shape Memory Alloys*, in: KALISZKY, S., SAYIR, M., SCHNEIDER, W., BIANCHI, G. & TASSO, C. (Eds.): *Shape Memory Alloys*, International Centre for Mechanical Sciences 1996, Number 351 in CISM Courses and Lectures.
- MIYAZAKI, S. (1998): *Medical and dental applications of shape memory alloys*, in: OTSUKA, K. & WAYMAN C. M. (Eds.): *Shape Memory Materials*, Cambridge University Press 1998.
- MIYAZAKI, S., IMAI, T., IGO, Y. & OTSUKA, K. (1986): *Effect of Cyclic Deformation on the Pseudoelasticity Characteristics of Ti-Ni Alloys*, in: Metallurgical Transactions A, Volume 17A, 115–120.
- MIYAZAKI, S., OHMI, Y., OTSUKA, K. & SUZUKI, Y. (1982): *Characteristics of Deformation and Transformation Pseudoelasticity in Ti-Ni Alloys*, in: Journal de Physique, Colloque C4, supplement to no. 12, Volume 43, C4–255–C4–260.
- MÜLLER, C. (2003): *Thermodynamic modeling of polycrystalline shape memory alloys at finite strains* 2003, Dissertation, Ruhr-Universität Bochum, Mitteilungen aus dem Institut für Mechanik, Nr. 132.
- MÜLLER, C. & BRUHNS, O.T. (2004): *An Eulerian Model for Pseudoelastic Shape Memory Alloys*, in: Materialwissenschaft und Werkstofftechnik, Volume 35, 5, 260–271.
- MÜLLER, C. & BRUHNS, O.T. (2006): *A thermodynamic finite-strain model for pseudoelastic shape memory alloys*, in: International Journal of Plasticity, Volume 22, 1658–1682.
- MUKHERJEE, K., SIRCAR, S. & DAHOTRE, N.B. (1985): *Thermal Effects Associated with Stress-induced Martensitic Transformation in a Ti-Ni Alloy*, in: Materials Science and Engineering, Volume 74, 75–84.
- NOCEDAL, J. & WRIGHT, S.J. (1999): *Numerical Optimization*, Springer series in operations research, Springer-Verlag New York, Inc. 1999.
- OGDEN, R.W. (1997): *Non-linear elastic deformations*, Dover Publications, Inc., Mineola, New York 1997.
- ORTÍN, J. & PLANES, A. (1989): *Thermodynamics of thermoelastic martensitic transformations*, in: Acta metall., Volume 37, 5, 1433–1441.

- OSTERMEIER, A., GAWELCZYK, A. & HANSEN, N. (1994): *Step-size Adaption Based on a Non-local Use of Selection Information*, in: DAVIDOR, Y., SCHWELFEL, H.-P. & MÄNNER, R. (Eds.): *Proceedings of the Third Conference on Parallel Problem Solving from Nature - PPSN III*, Jerusalem, Springer 1994, pp. 189–198.
- OTSUKA, K. (1990): *Introduction to the R-Phase Transition*, in: DUERIG, T.W., MELTON, K.N., STÖCKEL, D. & WAYMAN, C.M. (Eds.): *Engineering Aspects of Shape Memory Alloys*, Butterworth-Heinemann 1990, pp. 36–45.
- OTSUKA, K. & WAYMAN C. M. (Eds.) (1998): *Shape Memory Materials*, Cambridge University Press 1998.
- PAWLETTA, S., FINK, R., PAWLETTA, T., DREWELOW, W. & DUENOW, P. (2005): *Distributed and Parallel Application Toolbox (DP Toolbox) for use with MATLAB(R) Version 1.7*, Department of Electrical Engineering, University of Wismar, Germany.
- POHLHEIM, H. (1999): *Evolutionäre Algorithmen: Verfahren, Operatoren und Hinweise für die Praxis*, Springer-Verlag Berlin; Heidelberg; New York 1999.
- POHLHEIM, H. (2005a): *GEATbx Introduction – Evolutionary Algorithms: Overview, Methods and Operators, version 3.7*, URL <http://www.geatbx.com>.
- POHLHEIM, H. (2005b): *GEATbx Options – Parameter Options, version 3.7*, URL <http://www.geatbx.com>.
- POHLHEIM, H. (2005c): *GEATbx Tutorial – Genetic and Evolutionary Algorithm Toolbox for use with Matlab*, Genetic and Evolutionary Algorithm Toolbox for use with Matlab, version 3.7.
- POHLHEIM, H., PAWLETTA, S. & WESTPHAL, A. (1999): *Parallel Evolutionary Optimization under Matlab on standard computing networks*, in: BANZHAF, W. (Ed.): *GECCO'99 - Proceedings of the Genetic and Evolutionary Computation Conference - Workshop program*, Kaufmann, M. 1999, pp. 174–176.
- POWELL, M.J.D. (2002): *Least Frobenius norm updating of quadratic models that satisfy interpolation conditions*, Technical Report DAMTP 2002/NA08, Department of Applied Mathematics and Theoretical Physics, Centre for Mathematical Sciences, Wilberford Road, Cambridge CB3 0WA, England, 2002.
- POWELL, M.J.D. (2004a): *The NEWUOA software for unconstrained optimization without derivatives*, Technical Report DAMTP 2004/NA05, Department of Applied Mathematics and Theoretical Physics, Centre for Mathematical Sciences, Wilberford Road, Cambridge CB3 0WA, England, 2004a.

- POWELL, M.J.D. (2004b): *On the use of quadratic models in unconstrained minimization without derivatives*, in: Optimization Methods & Software, Volume 19, 3-4, 399–411.
- PRESS, W.H., TEUKOLSKY, S.A., VETTERLING, W.T. & FLANNERY, B.P. (2001): *Numerical Recipes in Fortran 77: The Art of Scientific Computing*, Volume 1, 2nd Edition, Cambridge University Press 2001.
- QIDWAI, M.A. & LAGOUDAS, D.C. (2000): *On thermomechanics and transformation surfaces of polycrystalline NiTi shape memory alloy material*, in: International Journal of Plasticity, Volume 16, 1309–1343.
- RANIECKI, B. & LEXCELLENT, C. (1998): *Thermodynamics of isotropic pseudoelasticity in shape memory alloys*, in: European Journal of Mechanics, A/Solids, Volume 17, 2, 185–205.
- RANIECKI, B., LEXCELLENT, C. & TANAKA, K. (1992): *Thermodynamic models of pseudoelastic behaviour of shape memory alloys*, in: Archives of Mechanics, Volume 44, 3, 261–284.
- RECHENBERG, I. (1973): *Evolutionsstrategie: Optimierung technischer Systeme nach Prinzipien der biologischen Evolution*, Friedrich Frommann Verlag (Günter Holzboog KG.), Stuttgart-Bad Cannstatt 1973.
- ROGUEDA, C., LEXCELLENT, C. & BOCHER, L. (1996): *Experimental study of pseudoelastic behaviour of a Cu Zn Al polycrystalline shape memory alloy under tension-torsion proportional and non-proportional loading tests*, in: Archives of Mechanics, Volume 48, 6, 1025–1045.
- SABURI, T. (1998): *Ti-Ni shape memory alloys*, in: OTSUKA, K. & EAYMAN, C.M. (Eds.): *Shape Memory Materials*, Cambridge University Press 1998.
- SHAW, J.A. & KYRIAKIDES, S. (1995): *Thermomechanical Aspects of NiTi*, in: J. Mech. Phys. Solids, Volume 43, 8, 1243–1281.
- SHIMIZU, K. & TADAKI, T. (1984): *Shape Memory Effect: Mechanism*, in: FUNAKUBO, H. (Ed.): *Shape Memory Alloys*, Gordon and Breach Science Publishers 1984, Volume 1 of *Precision Machinery and Robotics*, pp. 1–60.
- SIMO, J.C. & HUGHES, T.J.R. (1998): *Computational Inelasticity*, Volume 7 of *Interdisciplinary applied mathematics*, Springer-Verlag New-York, Inc. 1998.
- ŠITTNER, P., HARA, Y. & TOKUDA, M. (1995): *Experimental Study on the Thermoelastic Martensitic Transformation in Shape Memory Alloy Polycrystal Induced by Combined External Forces*, in: Metallurgical and Materials Transactions A, Volume 26A, 2923–2935.

- ŠITTNER, P., NOVÁK, V., LUKÁŠ, P. & LANDA, M. (2006): *Stress-Strain-Temperature Behavior Due to B2-R-B19' Transformation in NiTi Polycrystals*, in: *Journal of Engineering Materials and Technology*, Volume 128, 268–278.
- ŠITTNER, P., TAKAKURA, M., HARA, Y. & TOKUDA, M. (1996): *On Transformation Pathways of General Stress Controlled Thermoelastic Martensitic Transformation in Shape Memory Alloys*, in: *Journal de Physique IV*, Volume 6, 1, 357–366.
- ŠITTNER, P., TAKAKURA, M. & TOKUDA, M. (1997): *Shape memory effects under combined forces*, in: *Materials Science and Engineering A*, Volume 234–236, 216–219.
- STEIN, E. & BARTHOLD, F.-J. (1996): *Elastizitätstheorie*, in: MEHLHORN, G. (Ed.): *Der Ingenieurbau, Grundwissen: Werkstoffe, Elastizitätstheorie*, Ernst & Sohn, Berlin 1996.
- SUN, Q.P. & LI, Z.Q. (2002): *Phase transformation in superelastic NiTi polycrystalline micro-tubes under tension and torsion - from localization to homogenous deformation*, in: *International Journal of Solids and Structures*, Volume 39, 3797–3809.
- TANAKA, K., KITAMURA, K. & MIYAZAKI, S. (1999): *Shape memory alloy preparation for multiaxial tests and identification of fundamental alloy performance*, in: *Arch. Mech.*, Volume 51, 6, 785–803.
- TANAKA, K., NISHIMURA, F. & TOBUSHI, H. (1995): *Transformation start lines in NiTi and Fe-based shape memory alloys after incomplete transformations induced by mechanical and/or thermal loads*, in: *Mechanics of Materials*, Volume 19, 271–280.
- TARANTOLA, A. (1987): *Inverse Problem Theory; Methods for Data Fitting and Model Parameter Estimation*, Elsevier Science Publishers B.V. 1987.
- TOBUSHI, H., ENDO, M., IKAWA, T. & SHIMADA, D. (2003): *Pseudoviscoelastic behavior of TiNi shape memory alloys under stress-controlled subloop loadings*, in: *Archives of Mechanics*, Volume 55, 5-6, 519–530.
- TOBUSHI, H., SHIMENO, Y., HACHISUKA, T. & TANAKA, K. (1998): *Influence of strain rate on superelastic properties of TiNi shape memory alloy*, in: *Mechanics of Materials*, Volume 30, 141–150.
- TOBUSHI, H., TAKATA, K., SHIMENO, Y., NOWACKI, W.K. & GADAJ, S.P. (1999): *Influence of strain rate on superelastic behaviour of TiNi shape memory alloy*, in: *Proceedings of the Institution of Mechanical Engineers – Part L – Journal of Materials: Design & Applications*, Volume 213, 2, 93–102.

- TOKUDA, M., ŠITTNER, P., TAKAKURA, M. & HAZE, M. (2002): *Multi-Axial Constitutive Equations of Polycrystalline Shape Memory Alloy (Experimental Background)*, in: JSME International Journal Series A – Solid Mechanics and Material Engineering, Volume 45, 2, 276–281.
- TOKUDA, M., YE, M., TAKAKURA, M. & ŠITTNER, P. (1998): *Calculation of mechanical behaviors of shape memory alloy under multi-axial loading conditions*, in: International Journal of Mechanical Sciences, Volume 40, 2-3, 227–235.
- TREPPMANN, D. & HORNBOGEN, E. (1995): *The Effect of Dislocation Substructure and Decomposition on the Course of Diffusionless Transformations*, in: Journal de Physique IV, Volume 5, 211–216.
- TRUESDELL, C. & NOLL, W. (2003): *The non-linear field theories of mechanics*, 3 Edition, Springer-Verlag Berlin Heidelberg New York 2003.
- UNBEHAUEN, H. (1997): *Regelungstechnik I - Klassische Verfahren zur Analyse und Synthese linearer kontinuierlicher Regelsysteme*, 9. Edition, Friedr. Vieweg & Sohn Verlagsgesellschaft mbH, Braunschweig/Wiesbaden 1997.
- UNBEHAUEN, H. (1997): *Regelungstechnik II - Zustandsregelung, digitale und nichtlineare Regelsysteme*, Friedr. Vieweg & Sohn Verlagsgesellschaft mbH, Braunschweig/Wiesbaden 1997.
- VERFÜRTH, R. (2005): *Einführung in die Numerische Mathematik*, Ruhr-Universität Bochum.
- VOGELANG, H. (2001): *Parameteridentifikation für ein selbstkonsistentes Stoffmodell unter Berücksichtigung von Phasentransformationen* 2001, Dissertation, Ruhr-Universität Bochum, Mitteilungen aus dem Institut für Mechanik, Nr. 129.
- XIAO, H., BRUHNS, O.T. & MEYERS, A. (1999): *Existence and uniqueness of the exactly-integrable hypoelastic equation $\overset{\circ}{\boldsymbol{\tau}}^* = \lambda(\text{tr}\mathbf{D})\mathbf{I} + 2\mu\mathbf{D}$* , in: Acta Mechanica, Volume 138, 31–50.
- XIAO, H., BRUHNS, O.T. & MEYERS, A. (2000a): *The choice of objective rates in finite elastoplasticity: general results on the uniqueness of the logarithmic rate*, in: Proceedings of the Royal Society London A, Volume 456, 1865–1882.
- XIAO, H., BRUHNS, O.T. & MEYERS, A. (2000b): *A consistent finite elastoplasticity theory combining additive and multiplicative decomposition of the stretching and the deformation gradient*, in: International Journal of Plasticity, Volume 16, 143–177.
- XIAO, H., BRUHNS, O.T. & MEYERS, A. (2006): *Elastoplasticity beyond small deformations*, in: Acta Mechanica, Volume 182, 31–111.

Lebenslauf

Name	Frank Christian Grabe
Geburtstag	27.04.1978
Geburtsort	Hagen
Staatsangehörigkeit	deutsch
Familienstand	verheiratet
08/1984 – 07/1988	Grundschule Boloh in Hagen
08/1988 – 07/1997	Theodor-Heuss-Gymnasium in Hagen Abschluss: Allgemeine Hochschulreife
10/1997 – 09/2002	Studium an der Ruhr-Universität Bochum Fachrichtung: Maschinenbau Abschluss: Diplom-Ingenieur
10/1998 – 10/2002	Studentische Hilfskraft am Lehrstuhl für Technische Mechanik der Ruhr-Universität Bochum
11/2002 – heute	Wissenschaftlicher Mitarbeiter am Lehrstuhl für Technische Mechanik der Ruhr-Universität Bochum

**Mitteilungen aus dem Institut für Mechanik
RUHR-UNIVERSITÄT BOCHUM
Nr. 142**

978-3-935892-17-9